Picosecond Third-Order Nonlinearities in Metal-Complexed PDA's and All-Optical Switching Potentiality in Fabry-Perot Devices Containing poly-DCHD

Miguel Angel Camacho-Lopez

Thesis Submitted for the Degree of Doctor of Philosophy in the Department of Physics

Heriot-Watt University August 2002

Table of Contents

List of Figures

List of Tables

Acknowledgements

I would like to thank my supervisors Brian Wherrett and Ajoy Kar for giving me the opportunity of carry out my PhD into the nonlinear optics group (NLO), as well as for their direction and useful suggestions.

I thank all the members of the NLO group, my office mate G. Brown (a very nice guy), Dr. A. Tookey, M. Bakarezos, H.Bookey, G. Papageorgiou, I. Galbraith, and Dr. K. Bindra. I would like to thank in particular Dr. Ian Blewett for the hours he spent teaching me how to operate, align, fix and give some maintenance to the picosecond laser system used in carrying out all the experiments reported in this thesis.

I thank Dr. W E Lindsell, Dr. P N Preston and Dr. C Murray from the Chemistry Department (Heriot-Watt) for preparing and providing the samples studied in Chapter 5. Samples studied in Chapter 6 and Chapter 7 were prepared at the Molecular Photonics Group, Department of Polymer Chemistry, National Institute of Materials and Chemical Research (Tsukuba Japan) by Dr. S Yamada, Dr. H Matsuda, Dr. H Kasai, and Dr. H Nakanishi. The experiments reported in Chapter 6 were carried out by Dr. R Rangel-Rojo. Many thanks to all these people, their contribution was very important.

Many thanks to my wife Zuleyka and my son Miguel Angel for their very important love and support, they have played a very important role during this enjoyable time we have spent in Edinburgh. Also I would like to thank my parents Angela and Santiago, my lovely sisters Alicia and Dolores and my brothers Santiago and Marco for giving me all their love and support.

I met many Mexican people in Edinburgh, all of them were very nice. The Mexican parties are something I will remember forever. Thanks to all these people to be very friendly. In particular I would like to thank Francisco and Myrna Villarreal because they helped me to sort many duties when I moved in Edinburgh to start my PhD. Many thanks to be so kind.

Finally, I want to thank CONACyT-Mexico for providing a scholarship to carry out my PhD.

Abstract

This work reports the experimental study of the third-order nonlinear optical properties of different polydiacetylenes (PDA's) using a tuneable sub-picosecond laser system as the light source. A comprehensive study of their nonlinear response was carried out in order to gain an understanding of the dynamics of the nonlinear optical response, and to evaluate the potential of these polymers for the technological application into the ultra-fast all-optical switching field. The optical switching potential was demonstrated in Fabry-Perot etalons containing poly-1,6-dicarbazolyl-2,4-hexadiyne (poly-DCHD). The techniques employed to measure the nonlinear properties of the materials studied and to characterise the Fabry-Perot devices were z-scan and time-resolved pump-continuum probe techniques respectively.

The third-order nonlinear properties near-resonance (λ = 532 nm) of coordination PDA's containing nickel, copper, ruthenium and molybdenum have been studied by the z-scan technique. Values for the nonlinear absorption coefficient β and the nonlinear refractive index n_2 have been obtained, as well as the figures of merit for the potential for all-optical switching applications. All the samples showed to be suitable to be used in Fabry-Perot geometries.

The on- and near-resonant third-order optical response of poly-DCHD microcrystals (100 nm size) in suspension was studied by the z-scan technique with a tuneable sub-picosecond laser system. The absorptive and refractive contributions to the excitonic-dominated nonlinearity were fully resolved at several wavelengths.

Fabry-Perot etalons containing poly-1,6-dicarbazolyl,2,4-hexadiyne (DCHD) with different concentrations have been fabricated and widely studied in the 700-800 nm range (pumping around the poly-DCHD low-energy peak absorption, λ = 640 nm) on the picosecond time scale using the well-known pump-continuum probe technique. A spectrally-broad "white light" was produced by pumping a de-ionised water cell and used as a probe to monitor the linear and nonlinear Fabry-Perot transmission. Time–resolved fringe-shifts were observed in all the devices. Fringe-shifts up to $\Delta\lambda$ = 6.6 nm were observed in the Fabry-Perot device containing a concentration of 9wt% of poly-DCHD.

Chapter 1

Introduction

1.1 Nonlinear organic materials

Organic materials have emerged during 1980s as an important class of nonlinear optical materials that offers unique opportunities for fundamental research as well as for technological applications [1] [2]. Organic materials are molecular materials that represent an ensemble of chemically bonded molecular units only weakly interacting with each other in the bulk through Van der Waals interactions. In such a case, the nonlinear optical response of organic systems can be described primarily as derived from a deformation of electron clouds within each molecule that arises from the presence of the intense electric field of an applied optical pulse. In other words, the optical nonlinearity is primarily molecular in nature. This behaviour is very different from inorganic semiconductors or ionic crystals in which no single molecular unit in the bulk can be identified; consequently, the nonlinearity in these inorganic systems is a bulk effect [3]. Organic structures also exhibit two different kinds of bonds: σ-and π-types [4]. A σ bond is formed by an overlap of atomic orbitals of two chemically bonded atoms, along the internuclear axes. A single bond formed by a carbon (C) atom is always of σ-type. The π-bonds are formed by a lateral overlap of the transverse $2p$ orbitals on two chemically bonded atoms. Because each carbon atom can form a maximum of four bonds involving one $2s$ and three $2p$ orbitals, it can form multiple bonds in which one bond is of σ-type and the remaining bonds are of π-type. For example, in a $-C\equiv C-$ bond, the two carbon atoms are bonded by a σ-bond that is formed by two σ-electrons, and two π-bonds that

involve four π-electrons. These concepts will be discussed in more detail in sections 3.2 and 3.3.

A distinct class of organic materials is the *conjugated* structures that involve alternate single and multiple bonds. In these structures, the π-electrons are delocalised over an effective conjugation length. The conjugated structures exhibit large optical nonlinearities even under non-resonant conditions (i.e., within the optical transparency regions), the nonlinearity being primarily derived from the delocalised π-electrons [1] [2].

Within the nonlinear optics field, organic materials have attracted a lot of interest, due mainly to their large non-resonant nonlinearities and their fast response time associated with moderately large on-resonance nonlinearities [2]. Molecular materials, in addition to exhibiting a large non-resonant response, also offer tremendous flexibility for optimisation of the nonlinear optical response, and the necessary material fabrication both at molecular and bulk levels. At the molecular level, one can use molecular engineering to design and synthesize structures with enhanced microscopic nonlinearities. Polymeric structures provide the added structural flexibility in that one can make modifications by grafting a nonlinear active group both in the main chain (the polymer backbone) and the side chain. At the bulk level, one can prepare different types of ensembles such as crystals, monolayer and multilayer films of oriented as well as unoriented polymers [1] [5] [6].

Over the last few years, as an extension to studies of conjugated organic systems for potential application in the field of nonlinear optics, conjugated organometallic systems have begun to be investigated [7]. It has been seen that the presence of low oxidation state transition-metals situated in the backbone of a conjugated organic polymer serve to

enhance the polarisability of such systems as compared to purely organic analogues. One family of such organometallic systems is the group 10-transition metal diethynyl polymers first synthesised by Hagihara *et al* [8]. In these polymers, a group 10-transition metal (nickel, palladium or platinum) is σ-bonded to a carbon-carbon triple bond. The coordination geometry with respect to the metal is *trans* square-planar leading to a linear, rigid rod conjugated polymer backbone.

Organic electro-optic materials have many attributes that are suitable for a variety of potential applications in electro-optics. Also optical bistability has been reported in Fabry-Perot cavities filled with organic liquids such as CS_2 [9] and nitrobenzene [10]. A Fabry-Perot interferometer is a high-resolution spectroscopy tool that has many applications. Using inorganic and organic electro-optic materials in Fabry-Perot interferometry, various potential applications have been demonstrated [11] [12]. The nonlinear-optical Fabry-Perot interferometer has been investigated for its potential applications in photonic switching [13], optical signal processing, and optical computing [14].

1.2 Polydiacetylenes in nonlinear optics

Polymers are a large class of materials consisting of many small molecules called monomers (the simple chemical unit which, when many are joined together, form a polymer) that can be linked together to form long chains, thus they are known as macromolecules (very large molecule). A typical polymer may include tens of thousands of monomers.

The conjugated polymers (polymers with long conjugated carbon chains) were a development based on the principle of maximising the conjugation length. The backbones

of these polymers are fully conjugated, although defects tend to limit the actual observed conjugation length. Amongst the most widely studied conjugated polymers are the polydiacetylenes (PDA`s).

Many PDA`s with different side groups, such as urethanes, sulphonates, and carboxylic acid esters, have been explored, with the emphasis on improving nonlinearities and other material properties, such as solubility in organic solvents, used when these have to be processed into particular devices (optical fibres, waveguides, and thin-films, among others). Several ultrafast nonlinear optical signal-processing schemes rely on the material`s intensity-dependent index of refraction as the basic nonlinear mechanism. In order to realise these concepts a material is needed with both a large and a fast (subpicosecond response time) nonlinear optical coefficient. The PDA's have the largest measured nonresonant third-order nonlinear optical susceptibility $\chi^{(3)}$ (Re$\chi^{(3)}$ is proportional to the nonlinear refractive index n_2. and Im$\chi^{(3)}$ is proportional to the two-photon absorption (TPA) coefficient β). The response time of this nonlinearity has been theoretically predicted to be subpicosecond.

PDA's are highly coloured materials, often red, blue or black and usually insoluble but some, including those with urethane [15], sulphonate [16] and ester [17] side-chains, are soluble in common organic solvents. The highly unsaturated conjugated backbone of PDA's imparts unusual physical properties, including relatively large third-order optical nonlinearity [2]. Third-order nonlinear optical interactions yield a rich variety of phenomena that can provide useful fundamental information on the structure and dynamics of molecules and polymers and can be utilised for device concepts. There are numerous third-order processes that can be distinguished on the basis of frequencies of the output and input waves, as well as by the nature of any material resonance

encountered. Consequently, different $\chi^{(3)}$ terms are used to describe the various processes. The intensity dependence of the refractive index provides a basis for all-optical processing of information, which could result in tremendous gain in processing speed. In addition to this important technological thrust, the intensity dependent refractive index also gives rise to a large number of phenomena such as self-focusing or defocusing, four-wave mixing, optical bistability, and the optical Kerr gate effect [18]. Furthermore, the third-order nonlinear response coupled with electronic and vibrational resonances yields phenomena such as two-photon absorption and coherent Raman effects [19].

The large off-resonant nonlinear refractive index along with a subpicosecond response time makes PDAs ideal candidates for application in ultrafast all-optical switching. All-optical phase modulation has been demonstrated using single-crystal channel waveguides of a polydiacetylene [20].

1.3 Some nonlinear polymer materials studied in the past

Some of the PDA's already studied are the *p*-toluene sulphonate (pTS) [21] [22], 3SMBU [23], *n*-butoxycarbonylmethylurethane (4BCMU [24], 9BCMU [23]), 1,6-N-Carbazolyl-2,4-hexadiyne (poly-DCH) [25] and metalised polydiacetylenes [26]. Much of the work into third-order nonlinearities in organic materials has been concerned with such polymer materials. Poly-4BCMU is one of the polydiacetylenes that has been widely studied, it consists of a planar carbon backbone chain with radical side-groups at both ends of the chain. For those properties that have been measured, e.g., the nonlinear absorption (β) and the sign and magnitude of the nonlinear refractive index (n_2), there is a large discrepancy in the reported values. Nunzi and Grec [27] used 33 ps pulses to probe 1.7wt% of powdered polymer crystals which had been dissolved in benzene chloride, and allowed to form a gel. They reported a value of 4.5 x 10^{-2} cmMW^{-1} for the two-photon absorption

(TPA) coefficient for a densely-packed amorphous film. Townsend *et. al.* [28] fabricated directional couplers in thin films of 4BCMU and modelled the transmission through the system based upon a single channel waveguide approximation to determine a TPA coefficient value of the order of 1×10^{-3} $cmMW^{-1}$. Reported values for the nonlinear index of refraction range from $n_2 = -1 \times 10^{-13}$ cm^2W^{-1}, measured by an attenuated total reflection method in conjunction with pump-probe techniques [29], to $n_2 = 5 \times 10^{-10}$ cm^2W^{-1}, derived from optical bistability measurements in nonlinear prism coupling experiments [30]. Nunzi and Charra [31] used a three-level model and picosecond phase conjugation measurements to account for the enhanced irradiance-dependent nonlinearities in 4BCMU solutions contained in a 1mm thick cell. They obtained a value for the nonlinear absorption coefficient of $\beta \sim 5 \times 10^{-2}$ $cmMW^{-1}$, while n_2 changed sign as a function of irradiance, I, ranging from -4.7×10^{-7} cm^2MW^{-1} as I approached zero, to $+7.4 \times 10^{-7}$ cm^2MW^{-1} at $I = 3$ $GWcm^{-2}$. Torruellas *et. al.* [32] used a four-level model calculation and transmission against input intensity measurements to obtain a value of $\beta = 35 \pm 15$ $cmGW^{-1}$ at 1.06 μm wavelengths for ns pulses, and $\beta = 15 \pm 5$ $cmGW^{-1}$ for 30 ps.

Guest-host materials have been less studied for third-order optical nonlinearities. These materials generally consist of a nonlinear chomophore as the active guest and a polymer matrix, such as poly-methyl methacrylate (PMMA), as the passive host. Within a guest-host sample it is not possible to have as high a proportion of the nonlinearly-active material as a conjugated polymer, and hence the nonlinear susceptibilities tend to be smaller. However, the nonlinear properties of the guest and linear optical and material properties of the host may be developed independently, resulting in superior film quality to that of the conjugated polymers. Amongst all the chomophores studied, have been the phthalocyanines [33], 4-(N, N-diethylamino)-β-nitrostyrene (DEANST) [34], 3-(diethylimino)-4-(1-cyano-2-propen-1-yl)phenyl(dicyanomethanide) (DEMI-3CNQ) [35],

3-acetamido-4-dimethylaminonitrobenzene (DAN), as well as charge transfer materials [36].

1.4 PDA's in this thesis

The work reported in this thesis was carried out on some metal-complexated PDA's (Chapter 5) and the PDA known as poly-DCHD (Chapter 6 and Chapter 7). In the past few years, chemists have observed that organometallic compounds can have very intense metal to organic ligand (π-π^* transitions), or organic ligand to metal charge transfer bands in the ultraviolet and visible parts of the spectrum [37]. These intense charge transfer bands arise from an excellent overlap of the diffuse metal *d* orbitals and the ligand π-orbitals. This overlap results in large induced dipole moments for the ground to excited state transition, a pre-requisite for achieving large nonlinearities. In addition, metal centres can be made extremely electron rich or electron deficient by tuning their oxidation state or the ligand environments.

The electronic absorption spectra of the organometallic polymers are broadband and red-shifted compared to the analogous monomer complexes due to an increase in the conjugation length [37]. It is interesting to note that in comparison to related purely organic polymers, the maximum absorption wavelength of these polymers is somewhat shorter [38]. This tends to suggest that at least in the ground state, the presence of a metal centre in the polymer backbone acts as a defect in terms of conjugation length [39]. The principal features of the electronic absorption spectra of the organometallic systems are *a*) absorptions associated with electron transfer within the organic ligand and *b*) absorptions associated with transfer of charge from the metal to the conjugated organic ligand [40].

On the other hand, microcrystals of some diacetylenes, prepared by the reprecipitation method have been studied as dispersions in liquid media [41]. Interesting behaviour has been observed in the solid-state polymerisation of diacetylene monomers and with the optical properties of polydiacetylene microcrystals. First, the polymerisation proceeds perfectly from one end to the other end of the diacetylene microcrystals. Next, the excitonic absorption peak position was found to shift to higher energy with decreasing size of the PDA microcrystals [42]. The size effect was observed even for crystals as large as 100 nm or more, in contrast to the conventional quantum effect of inorganic semiconductors where size effects are observed only for microcrystals of less than about 10 nm [43]. In addition, since the microcrystal dispersions in water have low optical loss, the Kerr shutter response of PDA microcrystals could be measured, and the non-resonant $\chi^{(3)}$ value was estimated to be of the order of 10^{-13} to 10^{-12} esu in very low concentrations (10^{-3} M) [44].

Fabrication and assembly of nanostructured materials are currently of considerable interest from the viewpoint of their unusual properties and their scale of order and structure [45], which permits processing from the molecular level upward by taking advantage of current microfabrication technologies.

Recently, Nakanishi and coworkers established a versatile and easy process to prepare aqueous dispersions of organic micro and nanoparticles by first preparing a finely divided dispersion of the target molecules in an appropriate solvent in water [46]-[49]. Densification and crystallisation may subsequently follow, leading to the specific morphology and structure of the microparticle 'single crystal' [47]. Polymer single particles have been produced using solid-state topochemical polymerisation in single crystalline microparticles of a diacetylene monomer (DCHD) [46]. Poly-DCHD nanocrystals have been obtained in two different sizes: 30 and 100 nm.

These organic molecular and polymeric nano-micro particles have unique electronic and optical properties. An example is the sharp well-defined particle-size dependent excitonic feature in poly-DCHD nanocrystals, not observed in the bulk crystal [42]. It has been shown that the excitonic absorption is attributable to the extension of π-conjugation along the poly-DCHD chain and the increase of absorbance indicates that the dispersed DCHD particles gradually crystallise during a period of about 10 min [43].

1.5 Scope and layout of this thesis

In Chapter 2 is presented a detailed description of the subpicosecond laser system, experimental techniques, equipment and software used in all the experiments. The same laser system is used in all experiments and two well-known techniques are used for carrying out the experimental work of this thesis. The Z-scan technique (Figure 2.3) is used in the experiments of Chapter 5 and Chapter 6 for measuring the nonlinear absorption and refraction coefficients of the corresponding samples. The pump-continuum probe technique is used in the experiments carried out in Chapter 7.

In order to understand the concepts developed in the next chapters, the sections in Chapter 3 provide a very useful introduction to the science of macromolecules and some basic concepts on polymers. Also presented is a brief description of the chemical structure and preparation procedure of these samples.

In Chapter 4 some selected nonlinear optical processes are discussed in order to provide a basis for the understanding of the next chapters. Here also is presented the theoretical description of the z-scan technique used in measuring the nonlinear coefficients (absorption and refraction) of the samples studied in Chapter 5 and Chapter 6. Based on this theoretical description, the experimental data can be analysed.

In Chapter 5, is presented a picosecond study of the third-order nonlinear properties of (diethylamino) alkyl substituted PDA's with some transition metals (copper [Cu], nickel [Ni], ruthenium [Ru] and molybdenum [Mo]). The influence of metal addition to the polymer backbone on the nonlinear optical properties is investigated by using the z-scan technique, which has been described in the previous chapter. Their nonlinear absorption and refraction coefficients near resonance, in particular at λ=532 nm, are measured. These nonlinear coefficients will be determined for all the samples, and their values presented. The figures of merit *W* and *T,* which are important quantities and a very useful criteria in determining whether a particular material is suitable for practical applications, such as in all-optical switching field and directional couplers, are also evaluated.

In Chapter 6, the z-scan studies made with the picosecond laser system described in Chapter 2 on poly-DCHD microcrystals with average particle sizes of 100 nm are described. The third-order nonlinear optical properties near and on resonance are studied, and the values of the nonlinear refractive and absorptive coefficients will be measured at several wavelengths. The results reported in this chapter play an important role as background, which is needed to understand and explain some of the results, reported in Chapter 7

In Chapter 7, I present a systematic study, using a picosecond broadband white-light source [50] [51], of four symmetric (mirrors with the same characteristics) Fabry-Perot devices (etalons) containing poly-DCHD microcrystal thin-films of different concentrations. The principle of such operations is the shifting of the Fabry-Perot transmission peak (probe) in response to control (pump) pulses [52]. The nonlinear medium (poly-DCHD) must be such that the absorption of one control pulse will change its refractive index at the probe wavelength enough to shift the transmission peak of the etalon [53] [54] [55].

A theoretical model for the Fabry-Perot linear transmission is presented. The Fabry-Perot peak-shift produced by pumping the poly-DCHD thin-film with an 800 fs strong beam on its low-energy peak absorption around 640 nm is time-resolved. The refractive index change associated with this fringe-shift is measured in all the devices and their values are presented. The refractive cross section σ_n (change in refractive index per generated excitation per unit volume) is calculated from the maximum refractive index change. The fringe-shift relaxation (recovering) is also investigated; the recovery times are estimated. In order to estimate the potential of these devices within the all-optical switching applications, the two figures of merit W and T are evaluated, as well as the switching energy.

References

[1] P Prasad, *Introduction to nonlinear optical effects in molecules and polymers*, John Wiley & Sons, New York, 1991.

[2] P N Prasad and D R Ulrich, *Nonlinear optical and electroactive polymers*, Plenum Press, NY, 1988.

[3] H Huag, *Optical nonlinearities and instabilities in semiconductors*, Academic Press, London, 1988.

[4] J McMurry, *Organic Chemistry*, Brooks/Cole Publishing Company, 1992.

[5] Seymour, Raymond B. and Charles E. Carraher., *Giant molecules*, John Wiley & Sons, New York, 1990.

[6] Billmeyer, Fred W., *Textbook of polymer science*, John Wiley & Sons, New York, 1984.

[7] W J Blau, H J Byrne, D J Cardin and A P Davey, *J. Mater. Chem.*, **1**, 245, 1991.

[8] N Hagihara, S Takahashi, K Ogha and K Sonagashira, *Journal of Organometallic Chemistry*, **188**, 237, 1980.

[9] W E Williams, M J Soileau and W V Stryland, *Optics Comm.*, **50**, 256, 1984.

[10] T Bischofberger and Y R Shen, *Opt. Lett.* **4**, 40, 1979.

[11] G Hernandez and K H Clark. *Appl. Opt.* **33**, 1989, 1994.

[12] R Lytel and G F Lipscomb. *Appl. Opt.* **25**, 3889, 1986.

[13] J F Heffernan, M H Moloney, J Hegarty and J S Roberts, *Electron. Lett.* **27**, 659, 1991.

[14] See, for example, H M Gibbs, *Optical bistability: Controlling light*, Academic, Orlando, Fla., 1985.

[15] G N Patel, R R Chance and J D Witt, *J. Polym. Sci. Polym. Lett. Ed.*, **16**, 607, 1978.

[16] G Wenz, M A Muller, M Schmit and G Wegner, *Macromolecules*, **17**, 837, 1984.

[17] C Plachetta, N O Rau and R C Schulz, *Mol. Cryst. Liq. Cryst.*, **96**, 141, 1983.

[18] A Yariv, *Quantum Electronics*, John Wiley, 3rd ed., 1988.

[19] R W Boyd, *Nonlinear Optics*, Academic Press, 1992.

[20] M Thakur and D M Krol, *Appl. Phys. Lett.* **56**, 1213 (1990).

[21] G J Blanchard, J P Heritage, G L Baker, and S Etemad, *Chem. Phys. Lett.*, **158**, 329, 1989.

[22] G J Blanchard, J P Heritage, A C Von Lehmen, M K Kelly, G L Baker, and S Etemad, *Phys. Rev. Lett.*, **63**, 887, 1989.

[23] T L Axon, D Bloor, S Molyneux, A K Kar, and B S Wherrett, *SPIE*, **2025**, 376, 1993.

[24] J M Nunzi and F Charra, *Mol. Cryst. Liq. Cryst. Sci. Technol. B*, **2**, 131, 1992.

[25] S Molyneux, H Matsuda, A K Kar, B S Wherrett, S Okada, and H Nakanishi, *Nonlinear Optics*, **4**, 2999, 1993.

[26] M A Camacho, A K Kar, W E Lindsell, C Murray, P N Preston and B S Wherrett, *J. Mater. Chem.*, **9**, 1251, 1999.

[27] J Nunzi and D Grec, *J. Appl. Phys.*, **62**, 2198, 1987.

[28] P Townsend and J Jackel, *Appl. Phys. Lett.*, **55**, 1829, 1989.

[29] M Sinclair, D McBranch, D Moses and A Heeger, *Appl. Phys. Lett.*, 53, 2374, 1988.

[30] B Singh and P Prasad, *J. Opt. Soc. Am.* B, **5**, 453, 1988.

[31] J Nunzi and F Charra, *Nonlinear Optics*, **1**, 19, 1991.

[32] W Torruellas and G Stegeman, *Optics Commun.*, **82**, 94, 1991.

[33] V S Williams, S Mazumdar, R N Armstrong, Z Z Ho and N Peyghambarian, *J. Phys. Chem.*, **96**, 4500, 1992.

[34] T Kurihara, H Kanbara, H Kobayashi, K Kubodera, S Matsumoto, and T Kaino, *Opt. Comm.*, **84**, 149, 1991.

[35] E C Smith, *Ultrafast third-order nonlinearities in novel zwitterionic molecules*, PhD thesis, Heriot-Watt University, Edinburgh, 1998.

[36] B Sipp, G Klein, J P Lavoine, A Penicaud, and P Batail, *Chem. Phys.*, **144**, 299, 1990.

[37] W Blau and A Davey, *J. Matter. Chem.*, **1**, 245, 1991.

[38] N Hagihara and K Sonahashira, *J. Organometallic Chem.*, **188**, 237, 1980.

[39] H Masai and N Hagihara, *J. Organometallic Chem.*, **26**, 237, 1971.

[40] A Dray and F Wittman, *Synthetic Metals*, **41**, 871, 1991.

[41] H Katagi et. al., *Jpn. J. Appl. Phys.*, **35**, 1364, 1996.

[42] A Samson and J Kenneth, *Photonic and optoelectronic polymers*, ACS Symposium Series **672**, Amer. Chem. Soc,, Washington, DC, 191, 1996.

[43] H Kasai et. al., *Jpn. J. Appl. Phys.*, **34**, 1208, 1995.

[44] H Kasai et. al., *Jpn. J. Appl. Phys.*, **35**, 221, 1996.

[45] Nanostructured Materials, *Chem. Mater.* **8**, 1569, 1996.

[46] Hiro Matsuda, Shinji Yamada, Edward Van Keuren, *et al.*, *SPIE Proceedings*, **2998**, 241 (1997).

[47] S Okada, H. Matsuda, H. Nakanishi, *et al.*, *Jpn. J. Appl. Phys.*, **31**, L1132, 1992.

[48] K. Yase, H Nakanishi, *et al.*, *Mol. Cryst. And Liq. Cryst.*, **294**, 71, 1996.

[49] H Katagi, H Matsuda, H Nakanishi, et al., *Jpn. J. Appl. Phys.*, **35**, L1364, 1996.

[50] R Rangel-Rojo, S Yamada, H Matsuda, H Kasai, H Nakanishi, A K Kar and B S Wherrett, *J. Opt. Soc. Am. B*, 15, 2937, 1998.

[51] M Bakarezos, M A Camacho, Ajoy K Kar, Brian S Wherrett, H Matsuda, T Fukuda, S Yamada, R R Rangel-Rojo, H Katagi, H Kasai, S Okada, and H Nakanashi., *Electron. Lett.*, **35**, pp. 1078 (1999).

[52] V S Williams, Z Z Ho and N Peyghambarian, *Appl. Phys. Lett.*, 57, 2399, 1990.

[53] J L Jewell, Y H Lee, M Warren, H M Gibbs, N Peyghambarian, A C Gossard, and W Wiegmann, *Appl. Phys. Lett.*, **46**, 918, 1985.

[54] A Migas, A Antonetti, D Hulin, A Mysyrowicz, H Gibbs, N Peyghambarian, and J L Jewell, *Appl. Phys. Lett.*, **46**, 70, 1985.

[55] H S Loka and W E Smith, *IEEE Photo. Tech. Lett.*, **10**, 1733, 1998.

Chapter 2

Experimental techniques and the laser system

2.1 Introduction

In this chapter is presented a detailed description of the subpicosecond laser system, experimental techniques, equipment and software used in all the experiments. The same laser system was used in all experiments and two well-known techniques were used for carrying out the experimental work of this thesis. Z-scan technique (Figure 2.3) was used in the experiments of Chapter 5 and Chapter 6 for measuring the nonlinear absorption and refraction coefficients of the corresponding samples. Pump-continuum probe was used in the experiments carried out in Chapter 7.

2.2 Subpicosecond laser system

The first stage of this laser system shown in Figure 2.1 is the Antares modelocked Nd:YAG system, the frequency-double output of which pumps the 702 synchronously modelocked dye-jet laser. Both of these are manufactured by Coherent Inc.. The Antares also seeds a regenerative Nd:YAG amplifier (RGA) which pumps the final stage, a pulse-tuneable dye-amplifier (PTA) which amplifies the output from the 702 to produce a 10 Hz train of high-energy pulses. The RGA and PTA are models 60-10 and P60 respectively, manufactured by Continuum Inc..

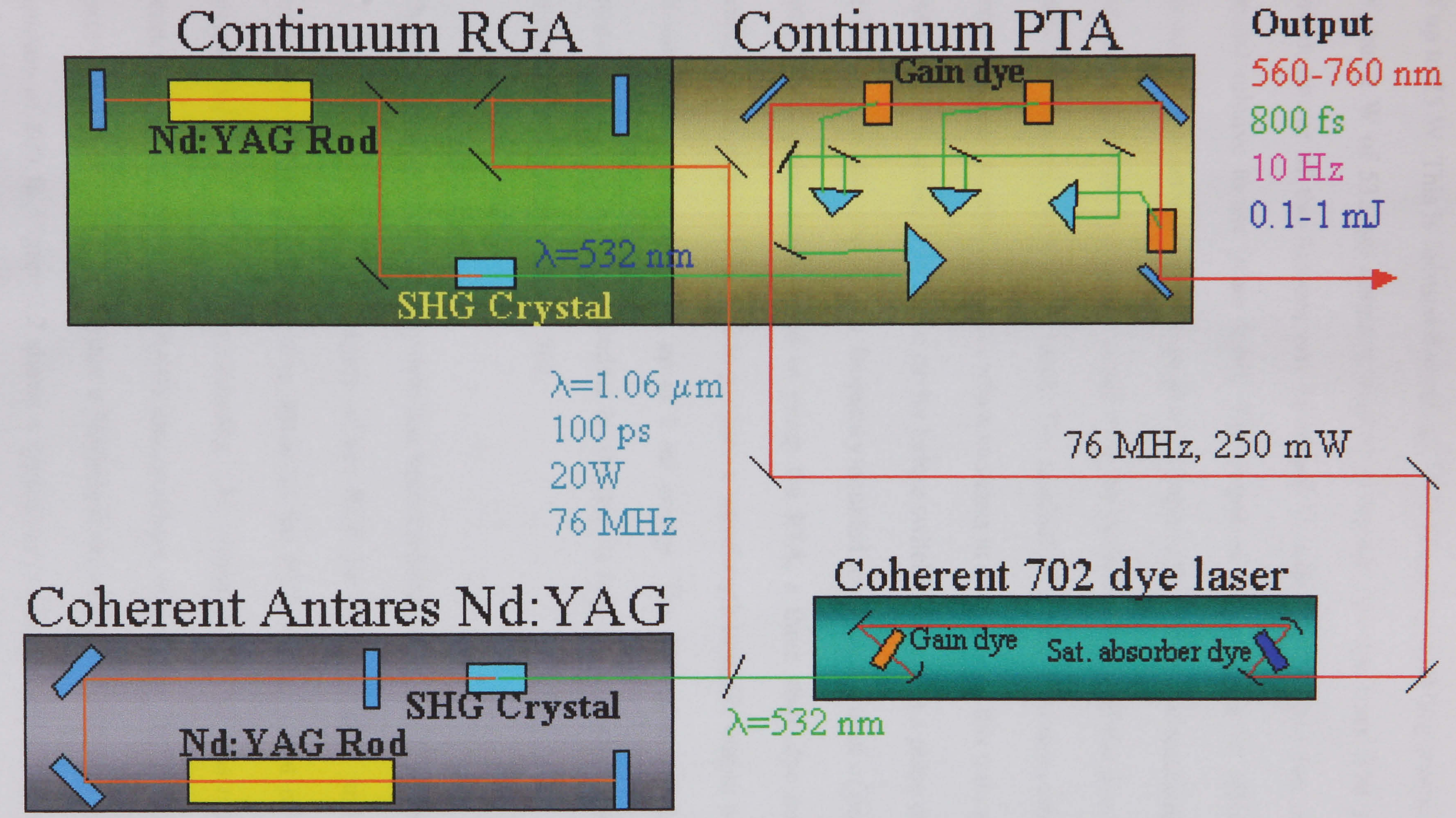

Figure 2.1: Schematic diagram of the sub-picosecond laser system.

The Antares generates a 76 MHz train of 100 ps, 1064 nm pulses with an average power of up to 25 W. This is focused through an LBO frequency doubling crystal to give up to 5 W, but 2 W of 532 nm output is used to pump the 702 dye laser. The green (532 nm) output power of the Antares can be varied by adjusting the position of the doubling crystal relative to the beam focus. The output of the 702 is a 76 MHz train of sub-picosecond pulses with an average power of up to 250 mW whose wavelength depends on the gain dyes used, but can be tuned over the operation range of the dye by rotating the intra-cavity birefringent etalon stack. The residual IR from the Antares after the doubling process is used to seed the RGA, which switches in one pulse of this train and amplifies it with about 10 passes around the cavity before switching out with a pulse energy of 50 mJ at 10 Hz repetition rate. This is frequency-doubled to produce a train of pulses at 532 nm with 25 mJ pulse energy used to pump the PTA, a three stage dye amplifier, which amplifies the output of the 702 to produce a wavelength tuneable output of a 10 Hz train of subpicosecond pulses with up to 1 mJ energy. The PTA also contains an optional saturable absorber which, depending on the dye, is required to remove the residual train of unamplified pulses from the 702.

Characterisation of this laser system has been reported previously [1], the salient results of which are the output energies of the PTA for different dyes and that the best description for the temporal pulse shape of the PTA output is that of a single-sided exponential pulse rather than a Gaussian. The output of the 702 was monitored with a Femtochrome Research Inc. FR-103 autocorrelator, which uses the technique of second harmonic generation (SHG) within a Michelson interferometer and gives a typical pulse duration of 800 fs. Figure 2.2 shows a typical oscilloscope trace of the autocorrelation function from which a pulse duration of 800 fs was calculated.

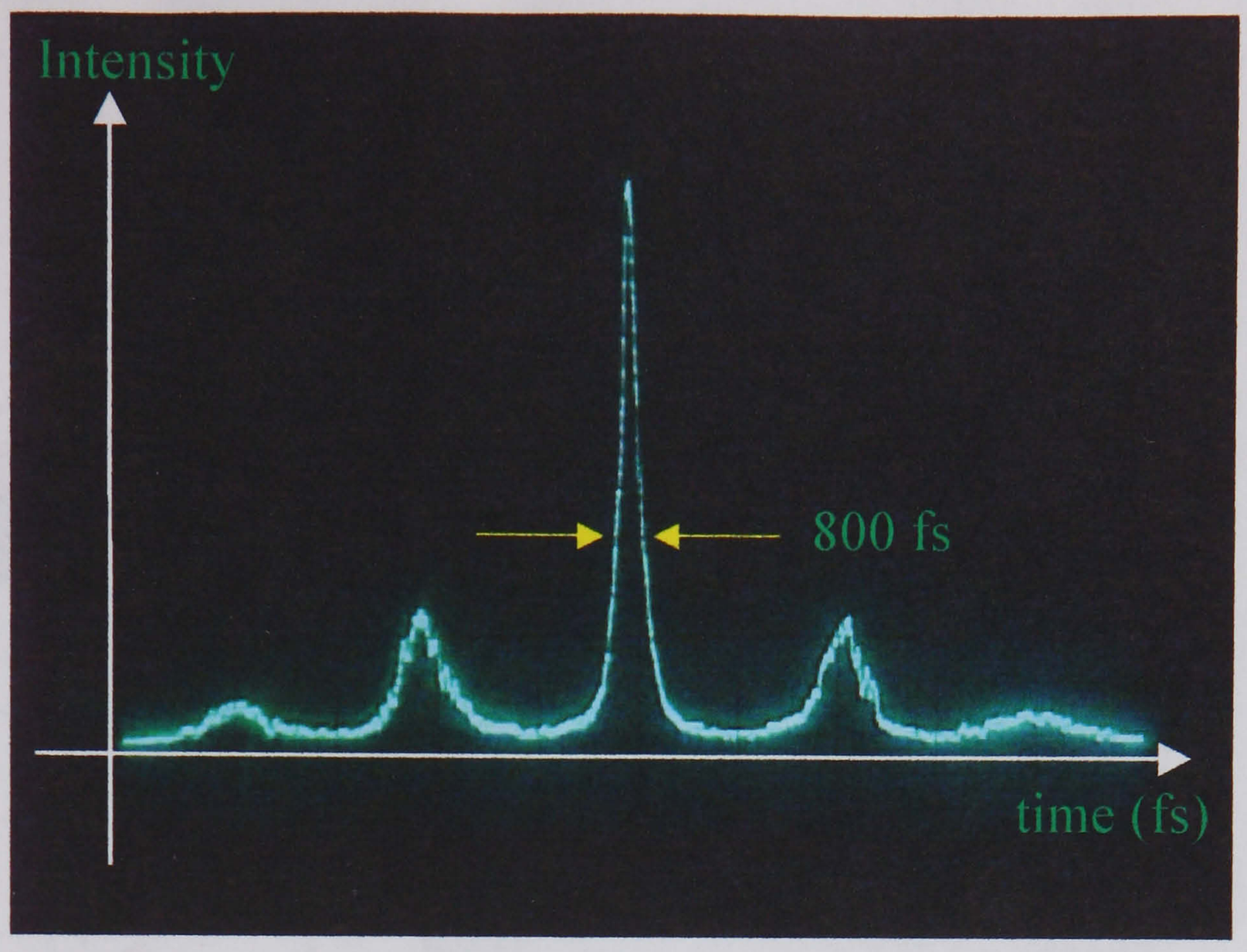

Figure 2.2: Oscilloscope trace showing the output from the autocorrelator.

2.3 Z-scan technique

The Z-scan technique, introduced in 1990 [2], has been used as an accurate method for determining nonlinear refraction and absorption of materials. It is a single beam technique, based on self-focusing or self-defocusing, which can be used to determine the real and imaginary parts of the frequency degenerate third-order susceptibility $\chi^{(3)}$. In this technique the sample is moved in the intensity pattern generated along the z-axis (Figure 2.3) by focusing a laser beam, and the on-axis transmitted signal is measured in the far field by a detector (D_3) placed behind a small aperture (closed-aperture Z-scan). Changes of the refractive index due to optical nonlinearities in the sample are detected as irradiance variations of the transmitted signal as a function of the sample position (z).

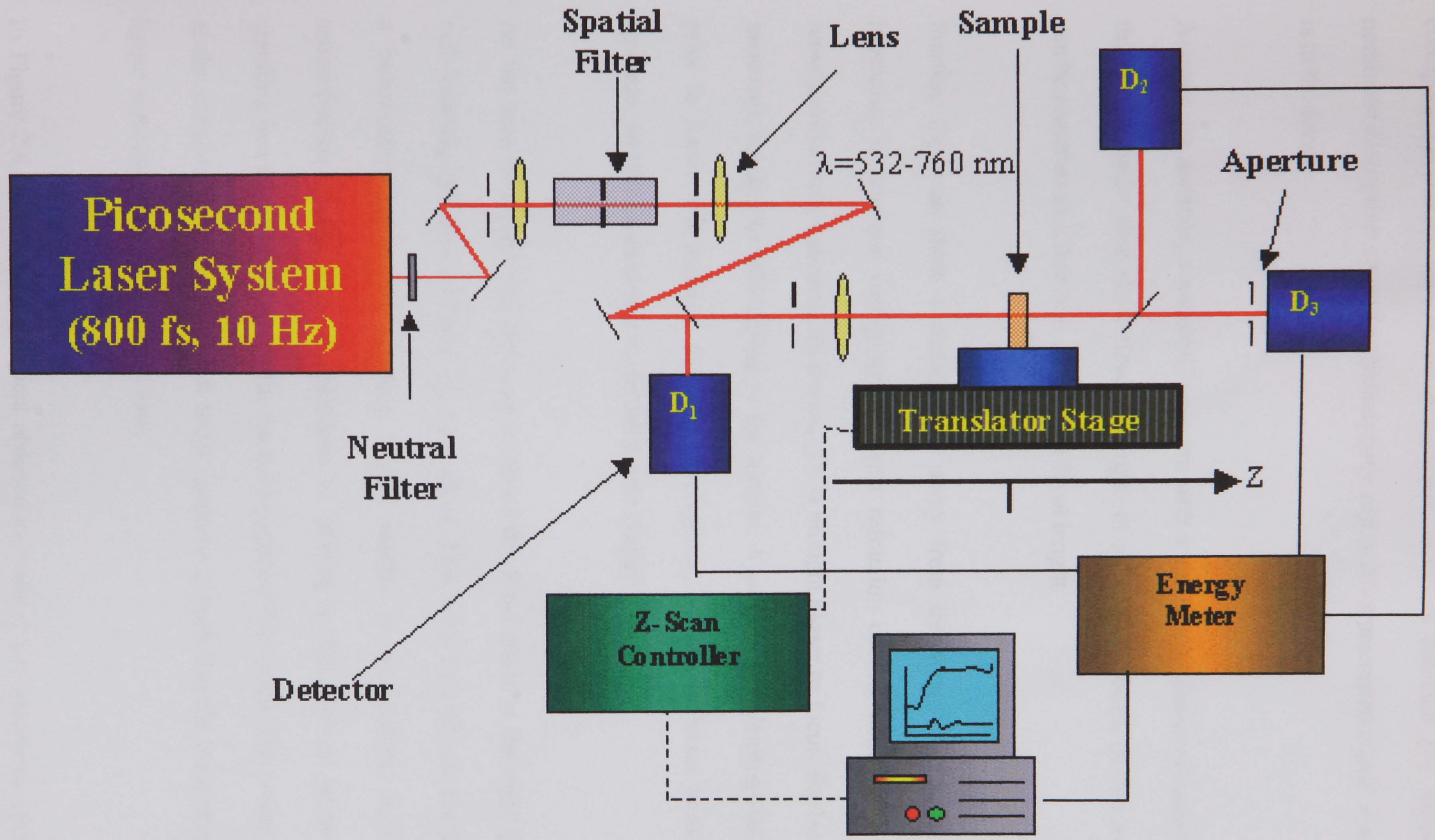

Figure 2.3: Z-scan Setup.

Multiphoton absorption can be measured in the slightly different open-aperture configuration, where the whole transmitted beam is detected (by detector D_2) and nonlinear absorption causes a characteristic dip in the transmitted signal when the sample is in the focus.

Assume, for instance, a material is present with a positive nonlinear refractive index and a thickness smaller than the diffraction length of the focused beam (a thin medium). This can be regarded as a thin lens of variable focal length.

Starting the scan from a distance far away from the focus (negative z), the beam irradiance is low and negligible nonlinear refraction occurs; hence, the transmittance remains relatively constant. As the sample is brought closer to focus, the beam irradiance increases, leading to self-lensing in the sample. A negative self-lensing (self-defocusing) prior to focus will increase the beam divergence, leading to beam broadening at the aperture, and thus a decrease in transmittance (valley).

As the scan continues and the sample passes the focal plane to the right (positive z), a self-focusing (positive self-lensing) takes place. This tends to collimate the beam, causing a beam-narrowing at the aperture, which results in an increase in the measured transmittance (peak). This is analogous to placing a thin lens at or near the focus, resulting in a minimal change of the far field pattern of the beam. The z-scan is completed as the sample is moved away from focus (positive z) such that the transmittance becomes linear since the irradiance is again low.

In Figure 2.4 are shown the typical absorption (valley) and saturation (peak) traces, as well as the trace for the case in which the nonlinear refractive index of the sample is

positive showing a valley-peak feature. A peak-valley feature means that the nonlinear refractive index is negative.

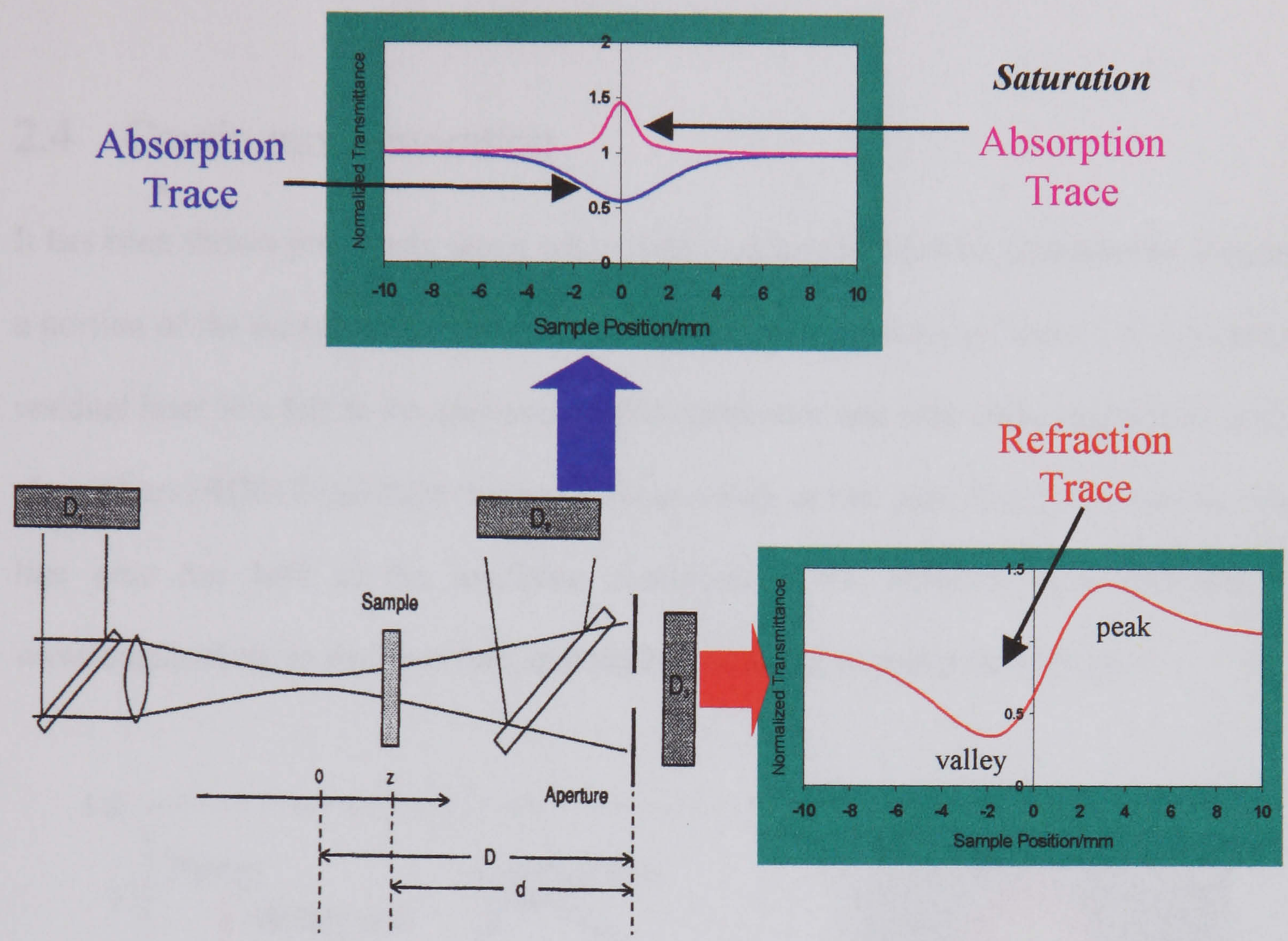

Figure 2.4: Z-scan setup. Typical absorption, saturation absorption and refraction traces. D_1, D_2 and D_3 are the reference, unapertured and apertured detectors, respectively; z is the sample position, d is the distance between the sample and the aperture, which is situated at a distance D from the focal plane ($z = 0$).

Large refractive nonlinearities in materials are commonly associated with a resonant transition, which may be of single or multiphoton nature. The nonlinear absorption in such materials arising from either direct multiphoton absorption, saturation of the single photon absorption, or dynamic free-carrier absorption have strong effects on the measurements of nonlinear refraction using the z-scan technique. Clearly, even with nonlinear absorption, a z-scan with a fully open aperture ($S = 1$) is insensitive to nonlinear

refraction. Such z-scan traces with no aperture are expected to be symmetric with respect to the focus ($z = 0$) where they have a minimum transmittance (e.g., a multiphoton absorption) or maximum transmittance (e.g., saturation of absorption).

2.4 Continuum generation

It has been shown previously that a white light continuum could be generated by focusing a portion of the output of the PTA onto a cell containing de-ionised water [3]. The strong residual laser line left in the spectrum of the continuum was removed using Schott colour glass filters (RG612 and RG615), using either a high or low pass filter to remove the laser line plus one half of the available continuum. This, however, also depleted the wavelengths close to the laser line, making it impossible to probe these regions.

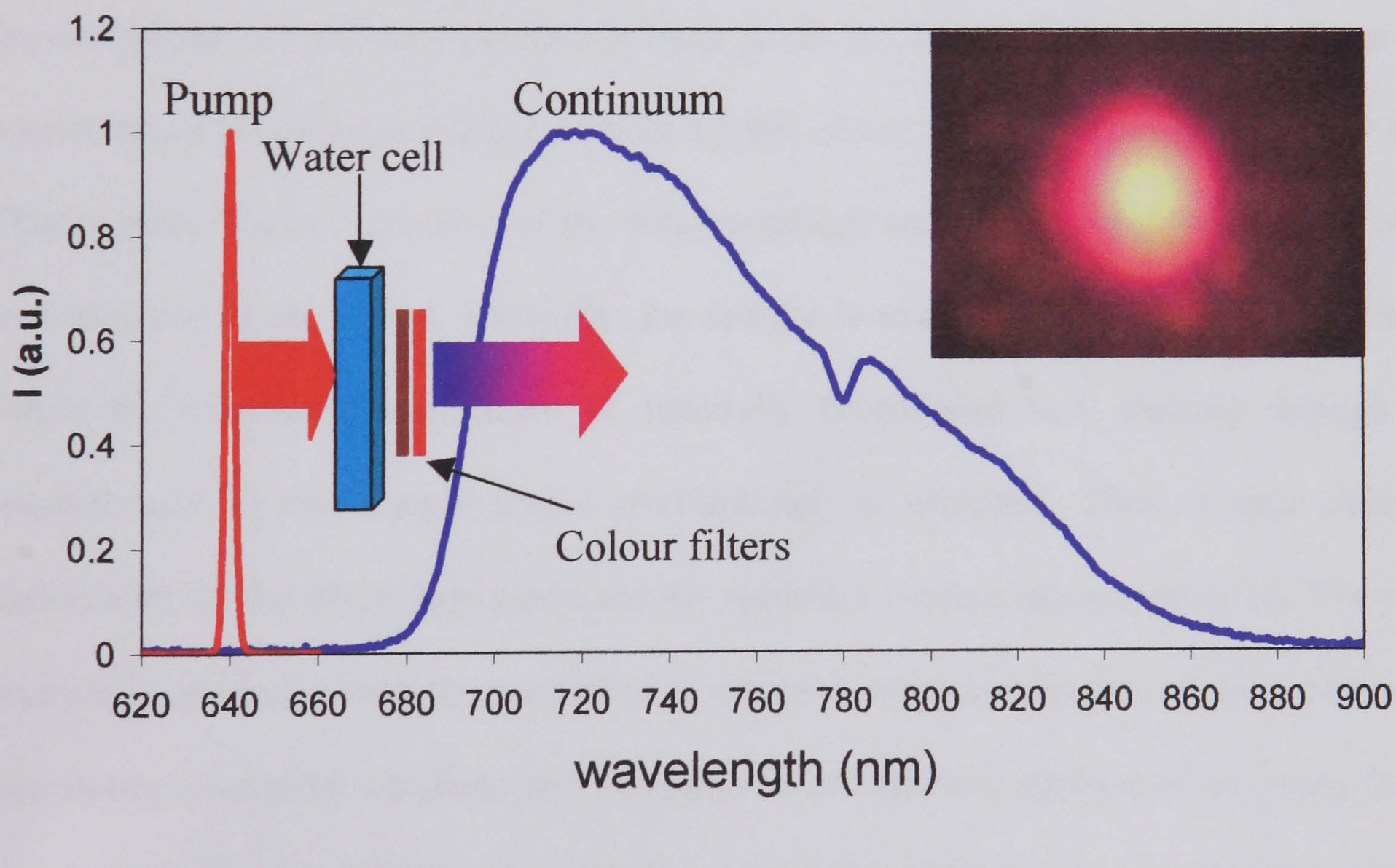

Figure 2.5: White-light continuum spectrum. The inset picture shows how the emanating white-light looks when it is projected onto a white screen.

In our experiments this was not a problem because the pump wavelength was at 640 nm and the interesting probe region was 660-900 nm. Figure 2.5 shows the spectral profiles

of both, pump and continuum light. As we can see in the spectrum, by using the colour filters RG612 and RG615, only wavelengths longer than 640 nm were available. For all pump energies greater than 30 mJ a white-light output was clearly visible, emanating from the sample container. The spatial size and shape of the continuum also varied with time. The inset picture in Figure 2.5 shows how the emanating white-light looks when it is projected onto a white screen (placed before the colour filters). From this picture we can see in the centre of the spot a bright area, which corresponds to the continuum emission, surrounded by a wide red ring coming from the residual pump beam.

2.5 Pump-continuum probe technique

The technique used in the experiments reported in Chapter 7 is known as pump-continuum probe (Figure 2.6) and allows nondegenerate time-resolved measurements to be carried out. As will be described in more detail in Chapter 7, the linear (in absence of excitation) and nonlinear transmission of a Fabry-Perot etalon containing a polymer thin-film is measured as a function of the delay produced between the pump and probe beam arrival times at the etalon. Basically, the sample is excited with an intense laser beam while the transmission spectrum of spectrally broad-band light passing through the excited area of the sample (beam overlapping), is recorded. Then, a time delay is introduced for the white-light pulse and the spectrum is taken again, and so on. The same process is continued until the transmission spectrum taken in presence of the pump beam (excitation) is similar (in shape and intensity) to that taken in absence of the pump beam, in other words, this indicates that the transmission has fully recovered and the nonlinear effect induced by the excitation has already gone.

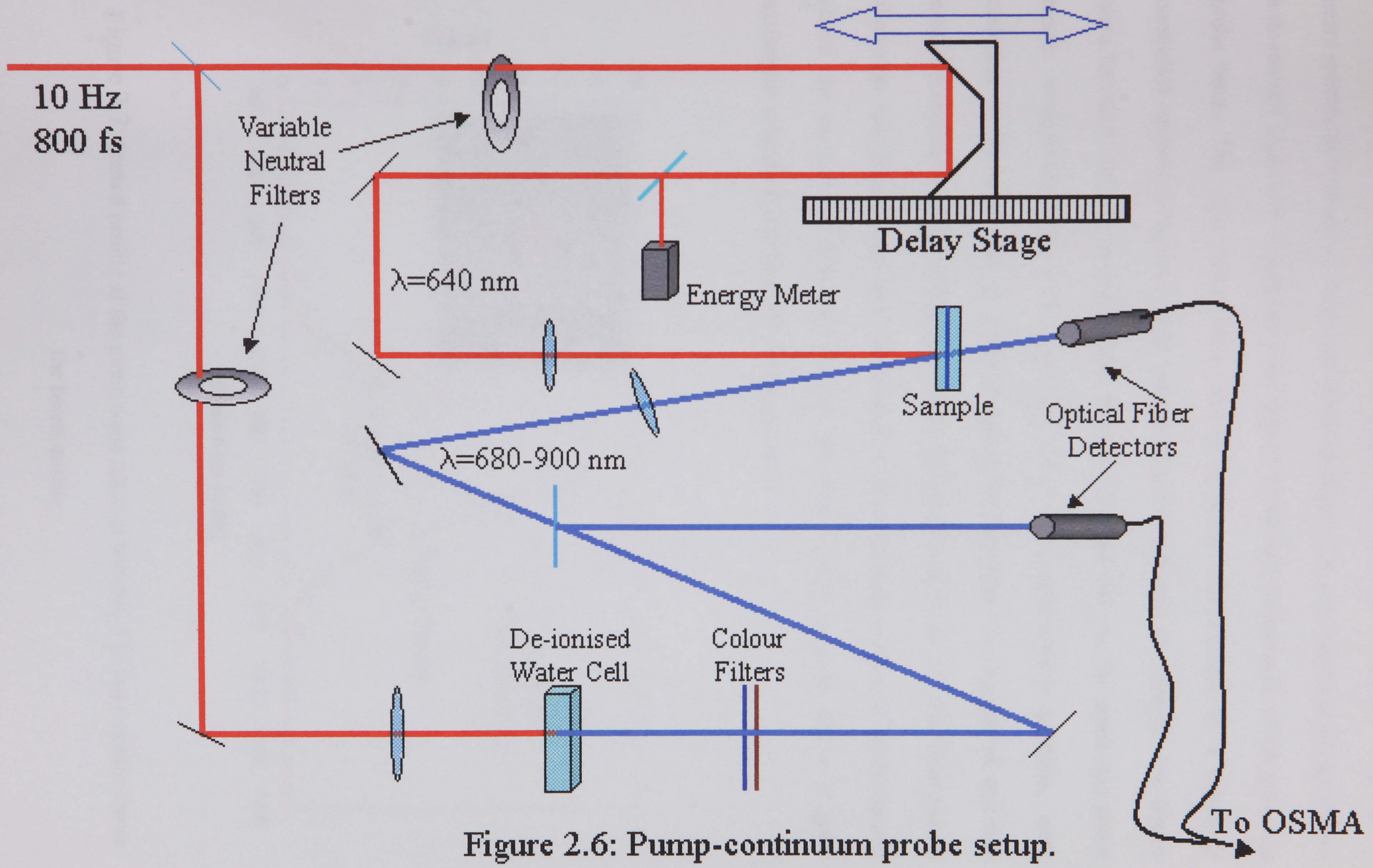

Figure 2.6: Pump-continuum probe setup.

The output from the laser system described above was split into two beams using a 50/50 beam splitter, as mentioned above and shown in Figure 2.6, one beam was focussed onto a de-ionised water cell to produce a low power white-light broad band, which gives the probe beam. The other beam, called the pump-beam, was reflected by a computer controlled time-delaying translation stage before arriving onto the sample. The beams were focussed onto the sample at spot sizes of 150 and 180 μm for probe and pump beams respectively. The spatial profiles, which are approximately gaussian, were measured by the translation of a pinhole across the laser spot. An example of spot size measurements taken using a 25 μm pinhole is given below in Figure 2.7. The inset picture shows the very good quality laser mode obtained from the laser system (PTA) mentioned above. As we can see from this picture, the spot is nearly circular and is in good agreement with the Gaussian fit to the beam profile.

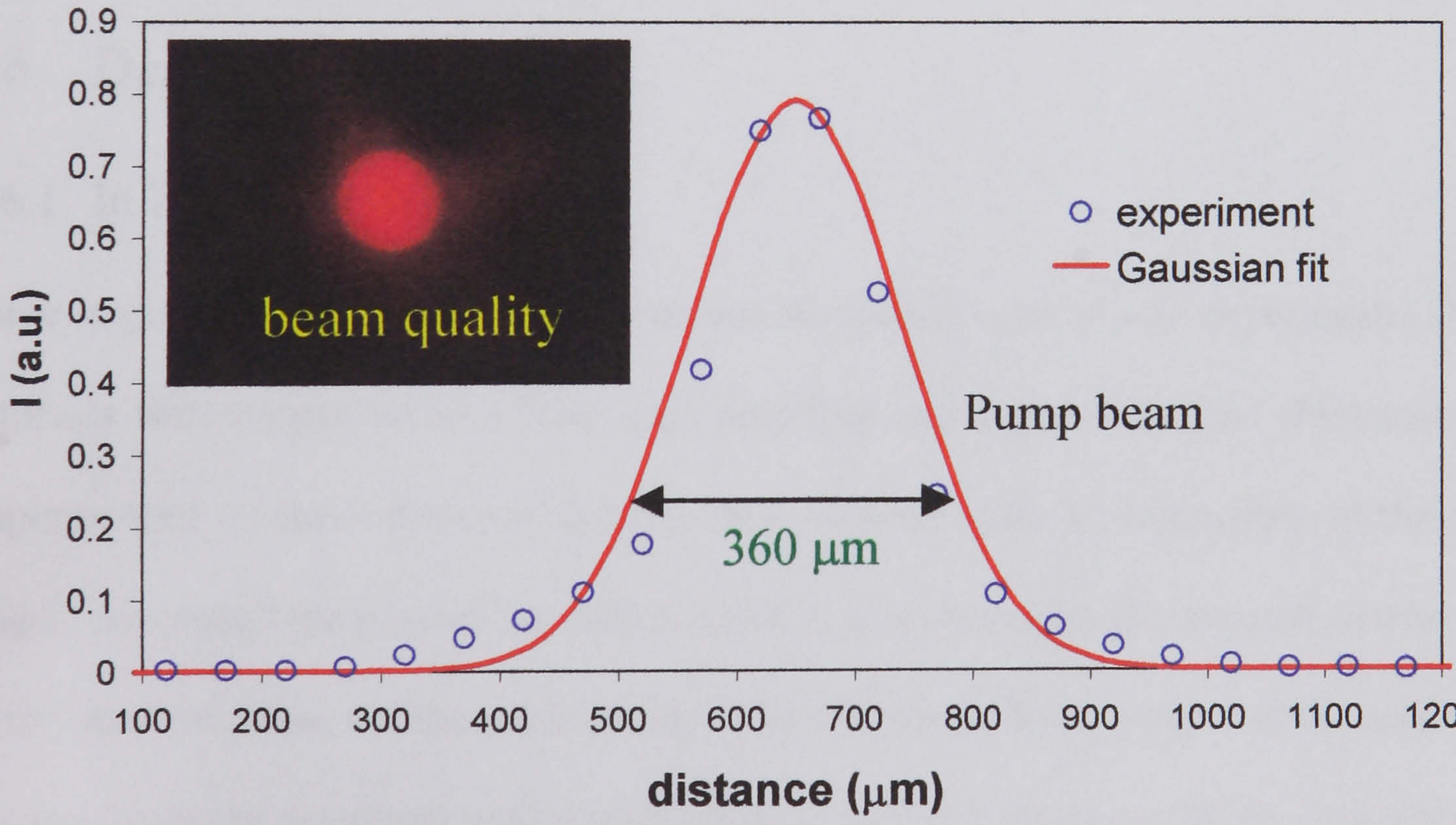

Figure 2.7: Spatial profile of the pump beam taken at 640 nm. The inset picture shows the beam quality.

The spatial overlapping of both beams was assured by imaging them onto a CCD camera (placed behind the etalon) and looking at the spots on the polymer film. This also allowed us to check that the spatial beam overlapping was kept as the time delaying process was performed. To find the time overlap various techniques can be used. In our case, taking advantage of the well studied nonlinear optical properties in ZnSe, we looked (using a CCD camera) at the self-diffracted beam spot produced when two non-collinear beams arrive simultaneously at the sample; this effect is based on an instantaneous index grating due to the Kerr effect [4], and is only present during coincidence of both beams. Once zero delay position was found, the reference sample was carefully replaced by the etalon ensuring it to be at the same place where the ZnSe sample was and in which the spatial overlapping was done. The incident and transmitted continuum beams were detected by a computer controlled dual-array multichannel analyser (OSMA) and each spectrum collected was an average of 35 pulses.

2.6 Detection system

2.6.1 In Z-scan experiments

Three large-area silicon photodiode detectors were used in all *z*-scan experiments. These detectors were connected to a fixed gain amplifier and a peak-and-hold (PH) unit. The response time of these detectors is very long (milliseconds) in comparison to the pulse length. As a result the peak of the output signal is proportional to the integration over time of the incident pulse, i.e. the pulse energy. The PH unit holds its output at the peak input voltage (from the detectors) until a reset signal is received (from the RGA). The output of the PH unit goes to the analogue inputs of the National Instruments AT-MIO16 A/D (analogue to digital) card, the reading of which by the computer is also triggered by the RGA pulse, resulting in a detected voltage proportional to the incident optical energy on the detector.

2.6.2 In pump-continuum probe experiments

In these experiments a photodiode silicon detector was used for measuring the incident pumping energy and an Optical Spectrometric Multi-channel Analyser (OSMA) for measuring the transmission spectra. The silicon photodiode detector had the same characteristics as that mentioned above and its main function was measuring the energy of the pump beam. The OSMA system consists of an Acton Research Corp. SP275 0.275m monochromator with a Princeton Instruments ST115 photodiode array. Interfacing to the respective controllers is achieved through a GPIB card. Triggering for the whole system is taken from the RGA.

2.7 Control software

The control software for the *z*-scan and pump-continuum probe experiments was written within an environment called *HPVee* from Hewlett Packard [5].

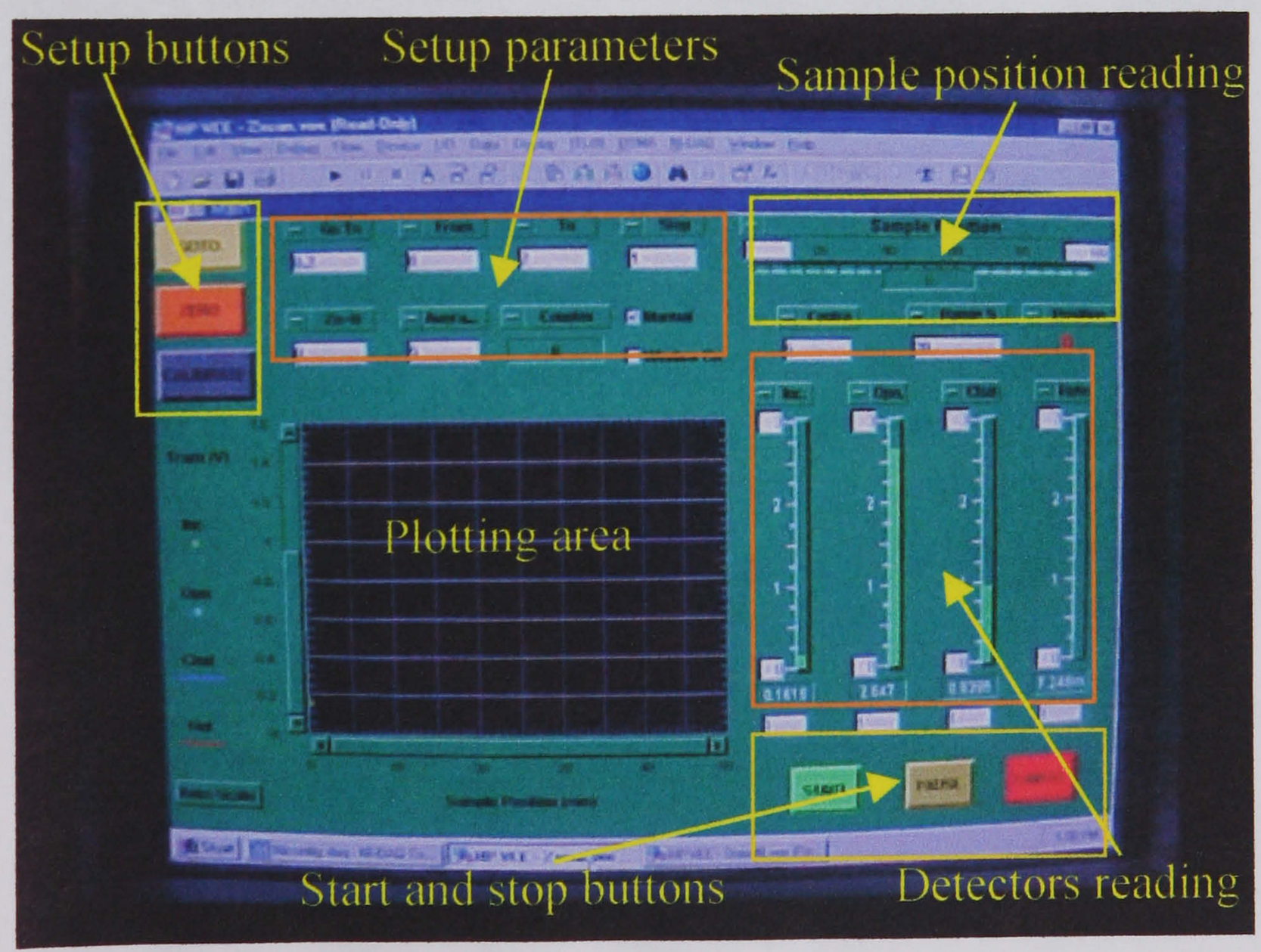

Figure 2.8: Control panel of the *z*-scan program.

HPVee provides a powerful suite of routines to aid in the implementations of hardware and user interfaces, data analysis and graphical representation. One program was written for each experimental technique and the software was designed to be able to perform specific functions. Figure 2.8 shows the control panel of the z-scan program.

Within the main features of the z-scan software were: obtaining the reading (energy) from the three silicon photodiodes, controlling the linear translation stage used for displacing the sample along the beam, plotting the reading of all detectors (energy vs. displacement) and getting the absolute incident and transmitted energy.

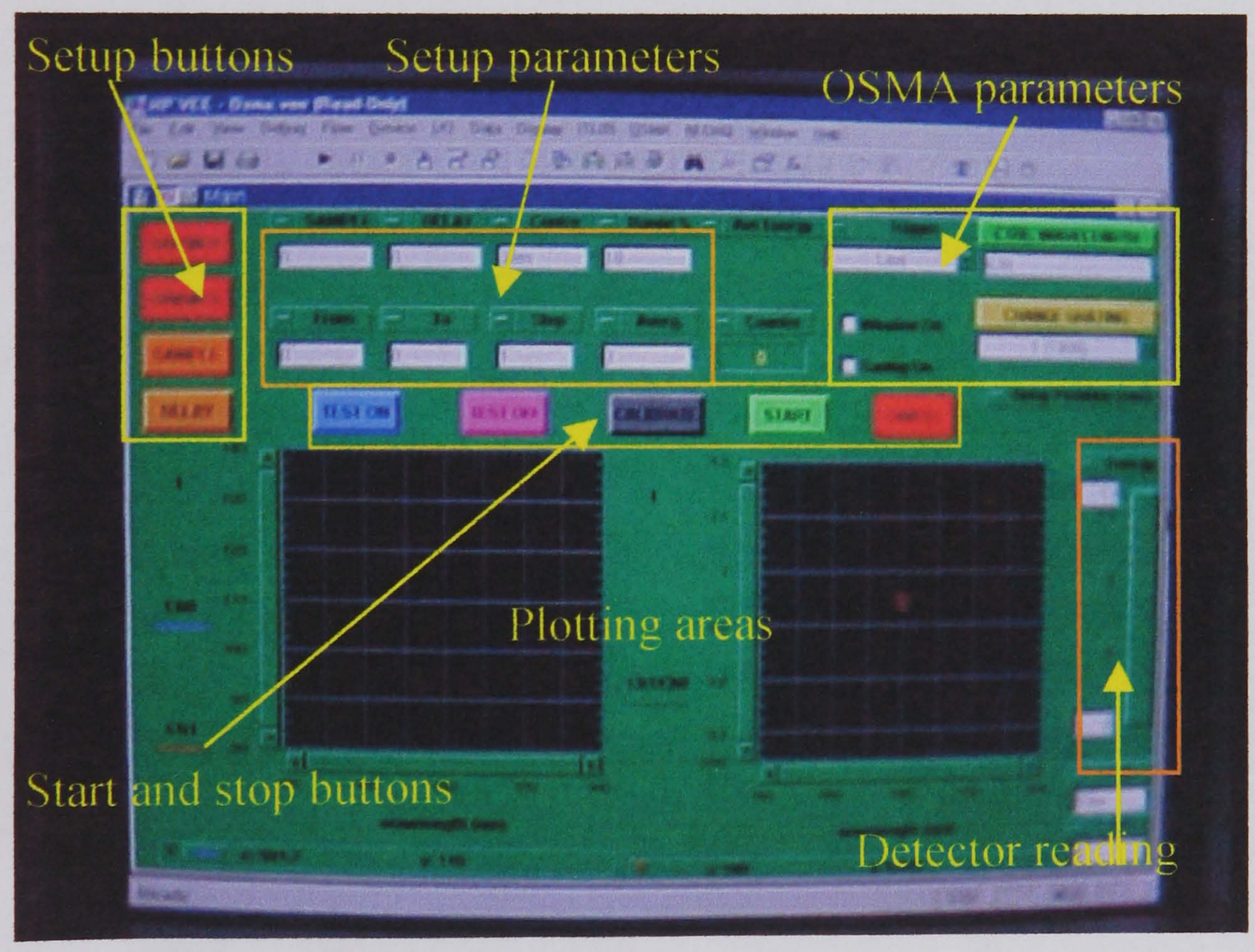

Figure 2.9: Control panel of the program used in the pump-continuum probe experiments.

With regard to the OSMA system, the software was able to control a linear translation stage (optical delay), obtaining and plotting the spectrum simultaneously from both channels and controlling some of the internal OSMA unit parameters. The control panel of this program is shown in Figure 2.9.

References

[1] J A Bolger, *Picosecond Nonlinear Optical Processes in Wide-gap Semiconductors and Polydiacetylenes*. PhD thesis, Heriot-Watt University, Edinburgh, 1992.

[2] M. Sheik-Bahae, A.A. Said, T.H. Wei, D.J. Hagan, and E.W. Van Stryland, *IEEE J. Quantum Electron*, **26**, 760, 1990.

[3] S. Molyneux *Third-Order Nonlinearities of Polydiacetylenes Studied by Subpicosecond Techniques*. PhD thesis, Heriot-Watt University, Edinburgh, 1995.

[4] T Schneider, D Wolffframm, R Mitzner and J. Reif, *Appl. Phys*. B, **68**, 749, 1999.

[5] Robert Helsel, "*Visual Programming with HP VEE*", 2nd ed, Hewlett-Packard Professional Books, Prentice Hall PRT, 1997.

Chapter 3

Polydiacetylene structures and sample preparation

3.1 Introduction

In the search for new nonlinear optical materials for photonic applications, organic materials have attracted considerable attention due to the enormous potential of molecular engineering. Polymers and polymer composites can be functionalised in order to possess electrical and/or optical properties. Organic materials, including polymers, have emerged as efficient nonlinear optical materials [1]. The combination of these three fast growing areas of Chemistry, Optics and Materials Sciences has led to the development of photorefractive polymers [2].

The development of highly efficient second-order and third-order nonlinear optical (NLO) polymeric materials has been energetically studied to achieve higher efficiency. Some polymeric materials have been reported to possess large optical nonlinearities and fast response times [3] [4]. It is possible to design their chemical structures and absorption wavelengths to achieve highly efficient functions for NLO device use. Therefore, they can be applied to many optical devices such as thin film waveguides and fibre waveguides. In particular, thin films, which exhibit large second-order and third-order optical nonlinearities, have many useful applications in integrated optics such as optical modulation, optical switching and optical data processing. Most of these materials reported so far have π-electron conjugated systems, which are the main origin of their

optical nonlinearities [5]. With a view to practical use, polymeric materials are expected to overcome the disadvantages of organic molecular crystals in terms of mechanical properties and processability. Various kinds of π-conjugated polymeric materials have been investigated as NLO materials [6]. They exhibit large electro-optical coefficients or efficient intensity-dependent refractive indices with very fast response times.

Another group of materials which are interesting within the nonlinear optics field, are the organic molecular crystals. In comparison with inorganic semiconductors, in which the excitons are based on the electron-hole pair in one-electron band states, excitons in molecular crystals are based on the vibronic excited states in the isolated free molecules. In such a molecular system a molecule or molecular pair at each site in a unit cell can already have various modes of vibrational excitation, which couple with the electronic excitation. The main intermolecular interaction between the molecules inside the molecular crystal is the Van der Waals interaction. The absorption spectra of molecular crystals are usually very complicated. The structure is mainly determined by the following five factors: 1) the exciton transition energy, 2) the excitonic bandwidth, 3) exciton-intramolecular vibration (exciton-phonon) interaction, 4) intramolecular vibrational energy, and 5) intramolecular vibrational frequency change between the ground state and the excited state.

Since conjugated polymers are composed of organic molecules with extremely large molecular weight, their electronic properties have common features with the molecular crystals.

The conjugation of the π-electron conjugated polymers is not limited three-dimensionally as in a small weight molecule. In polymers the π-electron conjugation is extended over a

much longer distance than the molecular size and is considered to be a one-dimensional system [7].

Conjugated polymers have been extensively investigated both experimentally and theoretically as model compounds of one-dimensional electronic systems. Among the many conjugated polymers, polydiacetylenes (PDAs) are the most intensively studied because of their well-defined, sharp excitonic absorption peaks, phase transitions with dramatic colour change and a wide variety of sample forms, *i.e.*, solutions, single crystals, and thin films. The work reported in this thesis was carried out on some metal-complexed PDA's (Chapter 5) and the PDA known as poly-DCHD (Chapter 6 and Chapter 8).

In order to understand the concepts developed in the next chapters, the following sections provide a very useful introduction to the science of macromolecules and some basic concepts on polymers. Also is presented a brief description of the chemical structure and preparation procedure of the samples studied in this thesis.

3.2 Molecule and orbital representation

Molecules may be represented in two dimensions by a structural diagram, for example the representation of the *ethylene* and *bromo-chloro-fluoro-iodo-methane* are shown below in Figure 3.1. While this representation allows for the derivation of the three dimensional structure of the left molecule (Figure 3.1(a)), the right molecule (Figure 3.1(b)) requires further description.

Figure 3.1: Molecular representation. a) *Ethylene* and b) *bromo-chloro-fluoro-iodo-methane.*

Molecules may be represented in three dimensions by a ball (atom) and stick (bond) configuration (Figure 3.2). This allows examination of the molecule's configuration, in this case an sp^3 hybridised (the combination of atomic orbitals on the same atom, i.e: sp^3, the mixing of one "*s*" orbital and three "*p*" orbitals) central carbon with four different atoms attached:

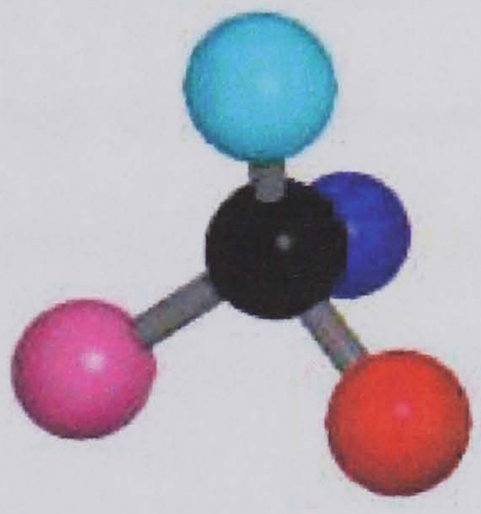

Figure 3.2: 3D-Molecule representation

Another method used to describe atoms and their bonding is through the location of the electrons in their outermost shell. The region in space where an electron is likely to be found is called an ***orbital***. There are different kinds of orbitals, which have different sizes and different shapes, and which are disposed about the nucleus in a specific way. The particular kind of orbital that an electron occupies depends upon the energy of the electron. It is convenient to picture an electron as being smeared out to form a cloud. We might think of this cloud as a sort of blurred photograph of the rapidly moving electron.

The shape of the cloud is the shape of the orbital. The cloud is not uniform, but is densest in those regions where the probability of finding the electron is highest, that is, in those regions where the average negative charge, or *electron density*, is greatest.

Let us see what the shapes of some of the atomic orbitals are. The orbital at the lowest energy is called the 1s orbital. It is a sphere with its centre at the nucleus of the atom, as represented in Figure 3.3(a). An orbital has no definite boundary since there is a probability, although a very small one, of finding the electron essentially separated from the atom, or even on some other atom. However the probability decreases very rapidly beyond a certain distance from the nucleus, so that the distribution of charge is fairly well represented by the electron cloud.

At the next higher energy level there is the 2*s* orbital. This, too, is a sphere with its centre at the atomic nucleus. It is naturally larger than the 1*s* orbital: the higher energy (lower stability) is due to the greater average distance between electron and nucleus, with the resulting decrease in electrostatic attraction. A few of these representations are presented here to illustrate this approach. The first three types of orbitals for individual atoms are shown below in Figure 3.3.

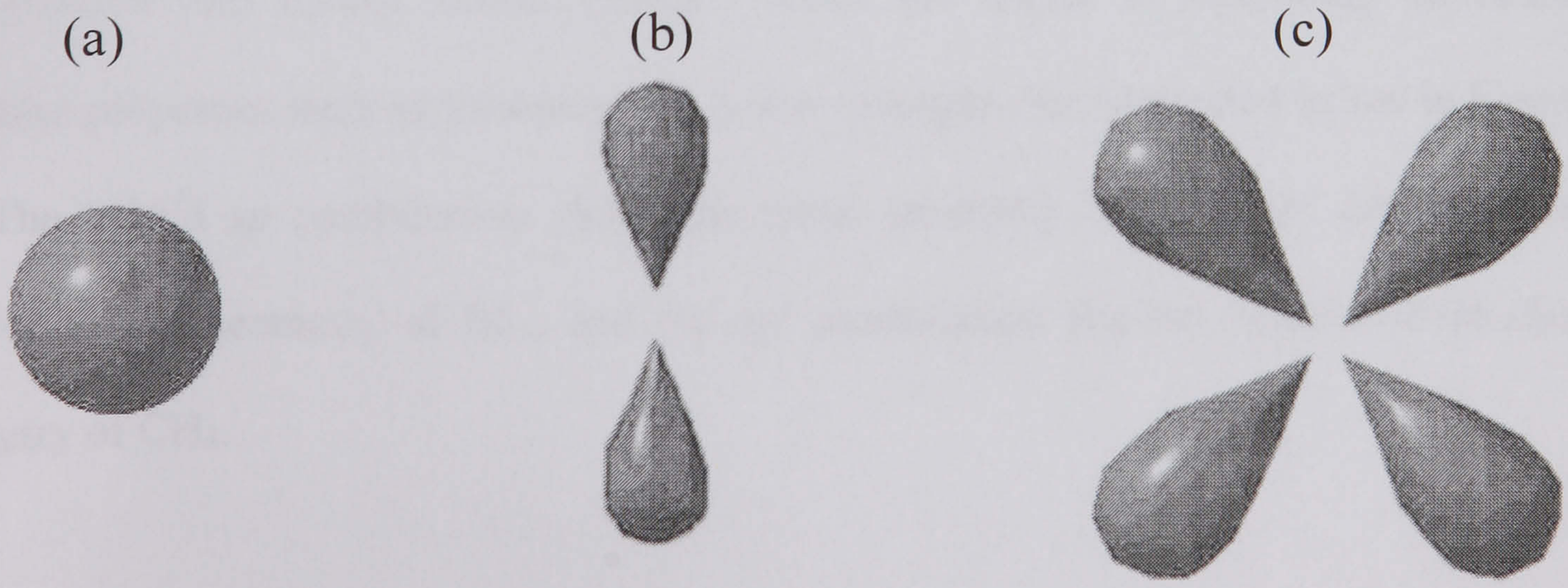

Figure 3.3: (a) Orbital *s*, (b) Orbital *p* and (c) Orbital *d*.

The *p* and *d* orbitals actually change according to how many electrons are in the outer shell. There are three orbitals of equal energy called 2*p* orbitals, shown in Figure 3.4. Each 2*p* orbital is dumbbell-shaped. It consists of two lobes with the atomic nucleus lying between them. The axis of each 2*p* orbital is perpendicular to the axes of the other two. They are differentiated by the names $2p_x$, $2p_y$, and $2p_z$ where the *x*, *y*, and *z* refer to the corresponding axes. A full *p* orbital is customarily indicated as shown below in Figure 3.4.

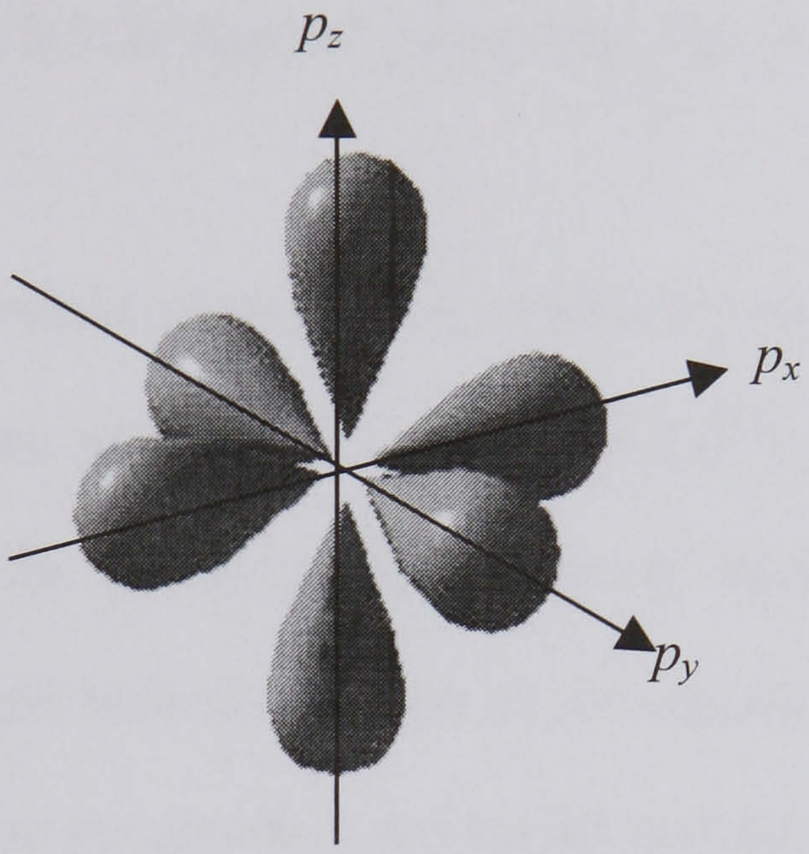

Figure 3.4: Full orbital *p* (p_x, p_y, p_z).

When two or more atoms are bound to form a molecule, the orbitals from each atom may be combined into hybrid atomic orbitals, which are useful in describing molecular structural properties such as geometry [8]. A few examples are illustrated below in Figure 3.5. The hybrid *sp* combination yields the linear geometry of CO_2; sp^2 describes the trigonal planar geometry of BF_3; and the sp^3 combination fits the familiar tetrahedral geometry of CH_4.

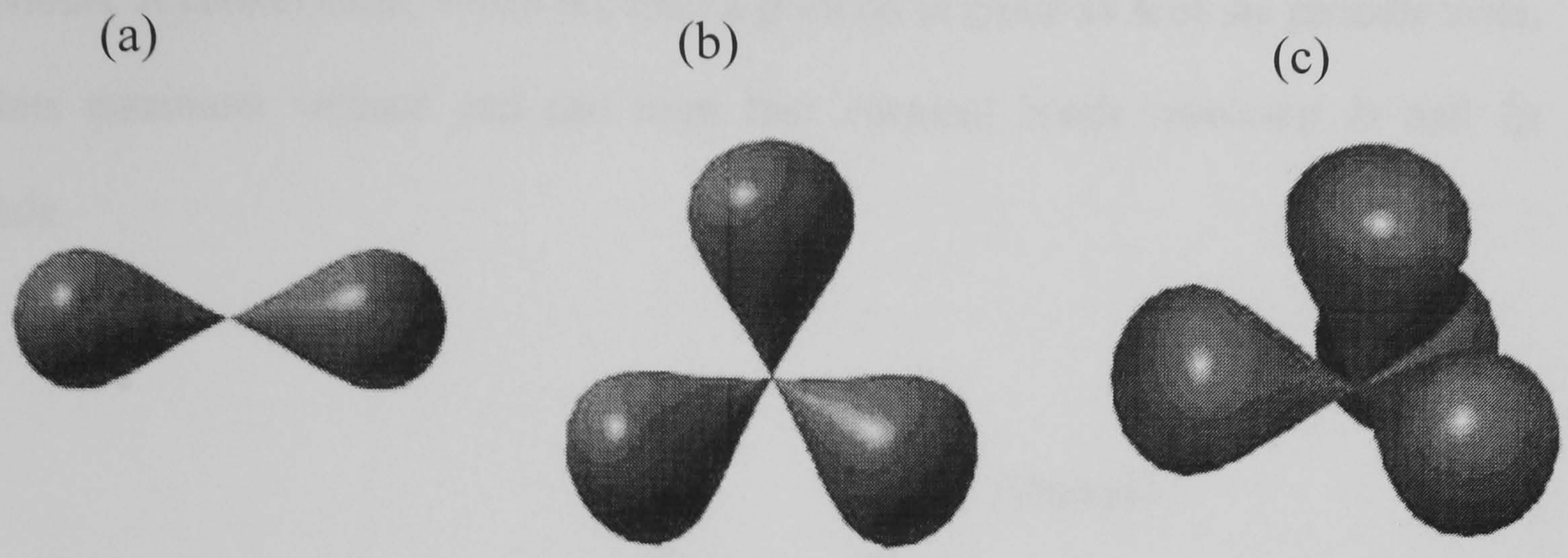

Figure 3.5: Hybrid orbitals. (a) *sp*, (b) sp^2, (c) sp^3.

Hybrid sp^2 orbitals (these hybrid orbitals are considered to arise from the mixing of one *s* orbital and two *p* orbitals) are also useful in describing double bond formation. They lie in a plane, which includes the carbon nucleus, and are directed to the corners of an equilateral triangle; the angle between any pair of sp^2 orbitals is thus 120°. This trigonal (three-cornered) arrangement permits the hybrid orbitals to be as far apart as possible. Just as mutual repulsion among orbitals gives four tetrahedral bonds, so it gives three trigonal bonds. For a more complete discussion of these topics see for example [9].

The next section illustrates the hybridisation for the case of *ethylene* (involves the overlap of two hybrid sp^2 orbitals in the double *carbon* = *carbon* bond, one sp^2 orbital per carbon), which will be used in the polymer synthesis section as an example of free radical formation in connection with addition polymerisation.

3.3 Elementary concepts on σ and π bonds

This section reviews some elementary concepts of σ and π bonds and their associated electrons. Many unique features exhibited by organic structures are easily understood by

invoking the conceptual separation of σ and π electrons and the differences in their behaviours. A carbon atom, which occupies a position in group **IVA** of the periodic table, exhibits maximum valence and can form four covalent bonds involving *2s* and *2p* orbitals.

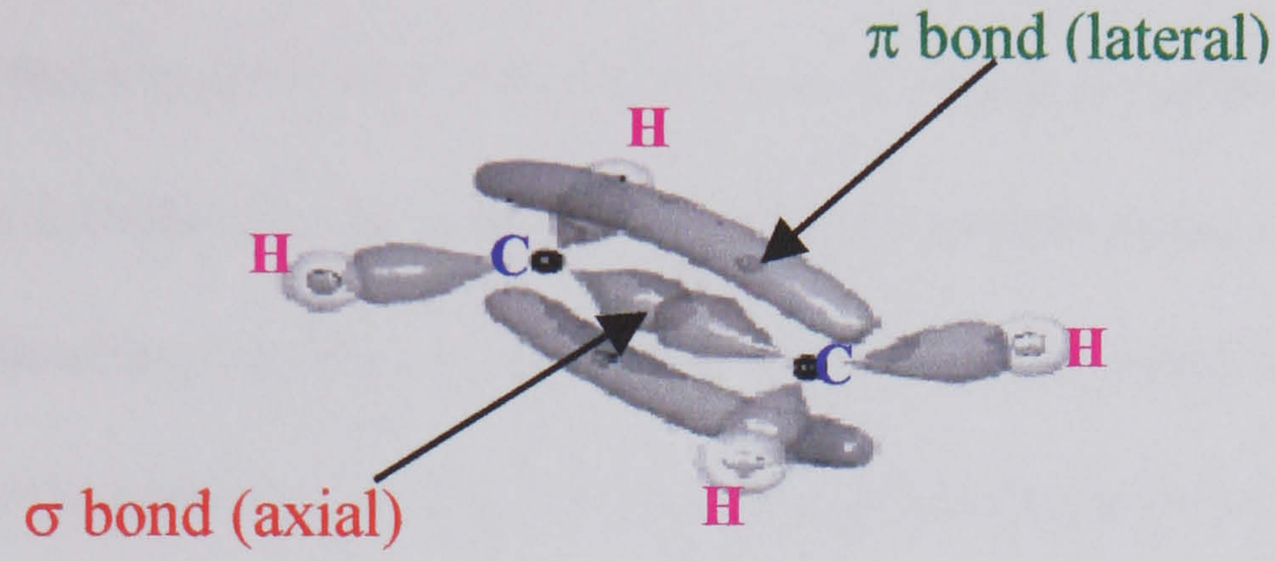

Figure 3.6: Representation of σ and π bonds in an *ethylene* molecule.

These orbitals when mixed as four sp^3 hybrid orbitals can form four single directed bonds in a tetrahedral geometry. Each bond involves the overlap of a sp^3 hybrid orbital of carbon and an orbital of the bonded atom (carbon or other) along the internuclear axis. Such bonds are called σ bonds by virtue of their axial symmetry and the electrons involved in the σ bonds are referred to as σ electrons. If a carbon atom forms four σ bonds involving all the four sp^3 hybridised orbitals, its valence is completely satisfied and it yields a saturated structure.

In order to give an example of these two types of bonds (π and σ bonds), consider specifically, a compound such as ethylene (Figure 3.6), which involves a double bond between two carbon atoms. In this case each carbon exhibits sp^2 hybridisation and yields three sp^2 hybridised orbitals which can form three σ bonds, two with hydrogen atoms and

one between the carbon atoms themselves. The orbitals involved in bonding overlap along the internuclear axis to give bonds with axial symmetry. However, the four valence requirements for each carbon atoms are not satisfied. There is one electron left in the *2p* orbitals of each of the carbon atom. Due to geometrical restrictions, the unhybridised *2p* orbitals on these two carbon atoms (usually designated as $2p_z$) cannot overlap along the internuclear axis, but can overlap laterally. This mode of overlap of orbitals leads to a π bond which has a mirror plane. The electrons in a π bond are called π electrons. The rule is that when a carbon forms a multiple bond with another atom, only one bond is of σ type. The remaining bond(s) is (are) of the π type. The π bonds are weaker, giving the carbon atom the tendency to form σ bonds through chemical reaction whenever possible. Compounds containing π bonds are called unsaturated [10].

3.4 Conjugated organic compounds

Organic compounds can be subdivided into saturated and unsaturated compounds. The latter are characterised by the fact that they contain at least one double or triple bond. Apart from their effect on the molecule chemical properties, these multiple bonds play a very important role in determining the spectroscopic properties of the molecule. If two double bonds containing π electrons are separated by a single bond, the two double bonds are called conjugated. Organic materials containing one or more of these conjugated double (or triple) bonds, are generically known as π-conjugated materials. Figure 3.7 shows such a conjugated system with the corresponding electron cloud representation.

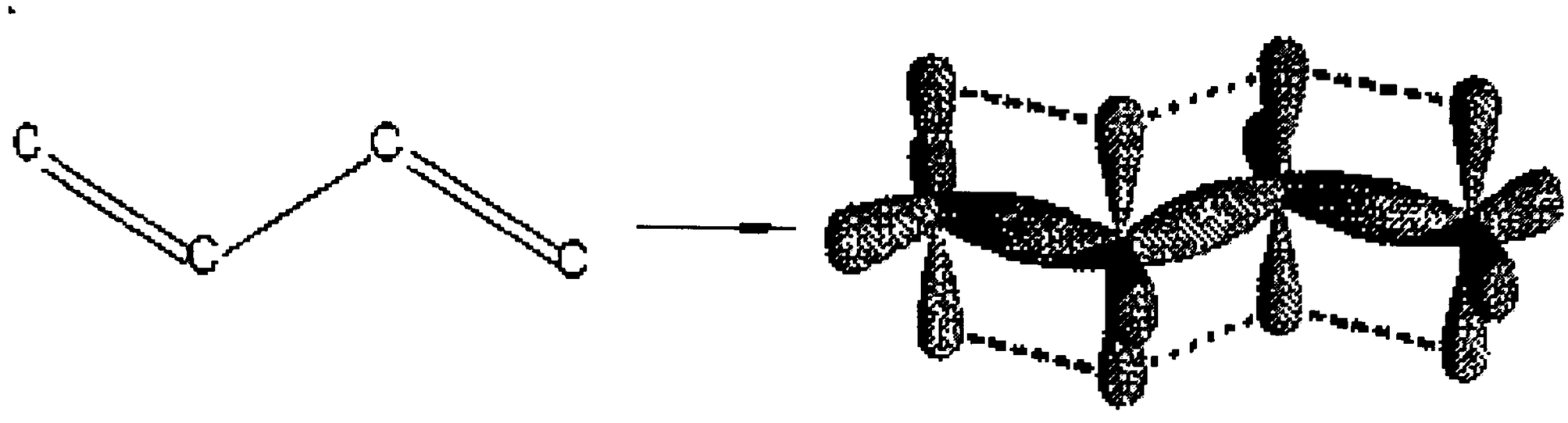

Figure 3.7: A conjugated bond system.

Although the standard representation shows the double bonds only interacting between the first and second atoms and the third and fourth atoms, there will also be a significant interaction between the *p* orbitals of the second and third atoms, hence making the whole system rigid and planar (i.e. there is, in this case, no rotation about the single bond allowed due to the interaction of the *p* orbitals of the neighbouring bonds). The π electrons are essentially delocalised over the whole conjugated chain, a striking example of which, commonly seen in organic molecules, is the benzene or aromatic ring. Here, the classical representation of the six-carbon ring is that of alternating single and double bonds.

Within a conjugated region the π electrons are delocalised over an extended region, blurring the distinction between single and double (or triple) bonds. The most direct physical indication of this is bond lengths. Double bonds are shorter than single bonds (triple bonds are shorter still) due to the different strengths of the interactions involved. How much a bond is *single* or *double* can thus be determined from the bond length, and from this the charge distribution within the molecule can be calculated. From this it is possible to make calculations of parameters such as the dipole moment, and of the energy level structure of the delocalised π electrons. A simple model of the energy level structure of the delocalised π-electrons, the free electron gas model [11], assumes that the

conjugated region is linear, and the potential energy profile is approximated to that of a simple square quantum well. This approximation is shown in Figure 3.8 for a simple conjugated molecule. If we take the conjugated chain length (the width of the quantum well) to be L, then the energy E_n of the n^{th} eigenstate of the π electron within this well can be shown to be;

$$E_n = \frac{\pi^2 n^2 \hbar^2}{2mL^2} \tag{3.1}$$

where m is the mass of an electron. If we further assume that, as in the diagram, the electrons are completely occupying the lower levels, then the lowest energy transition will be (taking N as the total number of electrons) between the $N/2$ and $N/2+1$ levels (assuming N is even) giving

$$E_{\frac{N}{2}+1} - E_{\frac{N}{2}} = \frac{\pi^2 \hbar^2}{2mL^2}(N+1) \tag{3.2}$$

It is important to note that L, the width of the quantum well represents the conjugation length which is not necessarily equal to the extent of the conjugated region. This is the case for many conjugated polymers, where the conjugation length does not equal the full polymer chain length, but some average value less than that [12]. However, in most smaller conjugated molecules, the two are approximately equal. This model is very much a simplification of the real picture. It does, nevertheless, give a useful picture of the nature of the energy level structure.

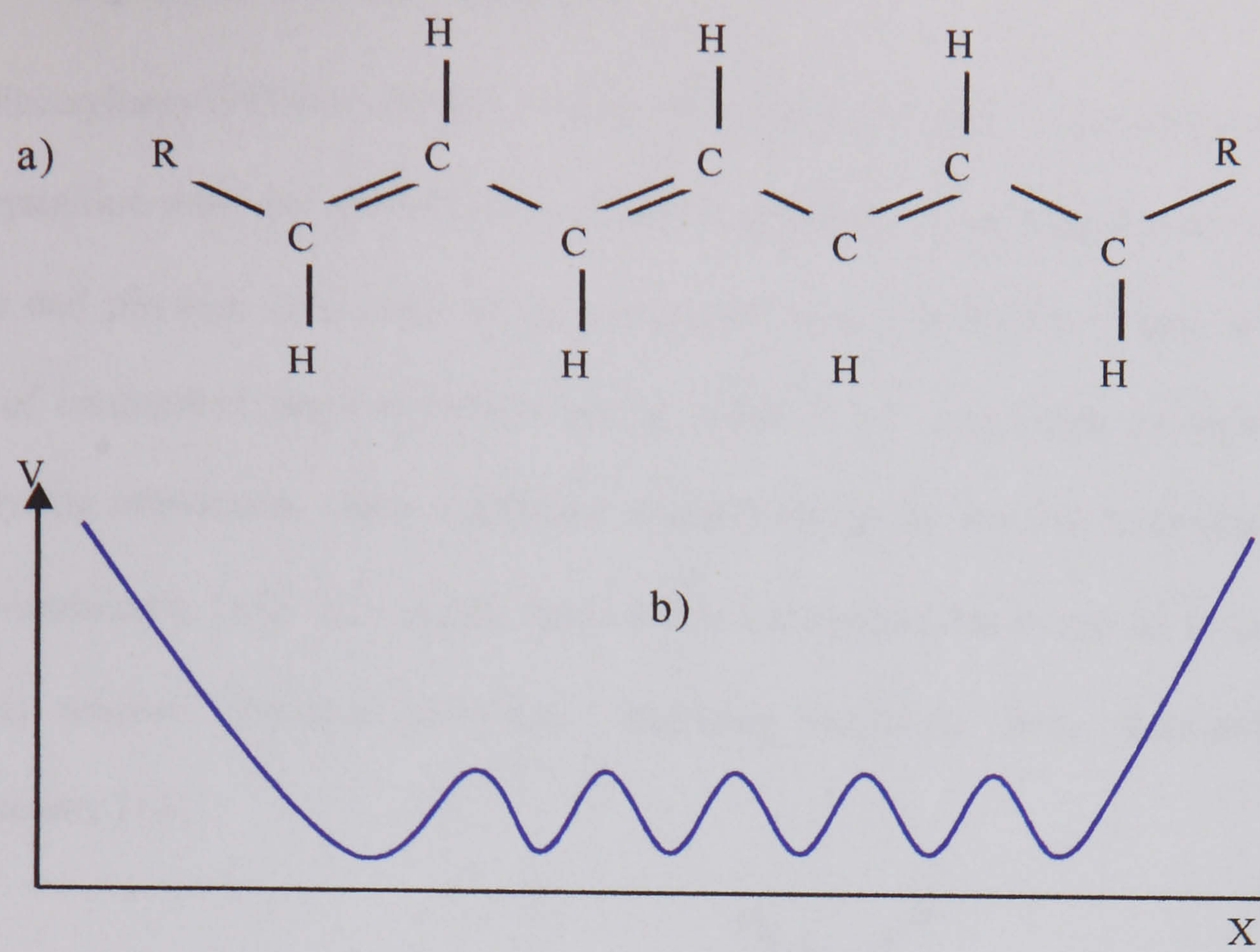

Figure 3.8: A simplified model of a π conjugated molecule; a) the structure of a generic conjugated molecule; b) the potential energy, V experienced by a π electron at position x within the molecule, c) an approximation of b) above using an infinite quantum well. Energy levels are shown with up and down arrows representing spin-up and spin-down electrons fully occupying the ground states. The ΔE shown is lowest excitation energy.

3.5 Polydiacetylenes structure

Polydiacetylenes (PDA's) exhibit (Figure 3.9) a fully conjugated and planar backbone in the crystalline state and are thus considered the prototype study object with regard to the nature and physical behaviour of polyconjugated macromolecules. These are a unique form of conjugated polymer which can be obtained as large single crystals [13] from diacetylene monomers, using solid-state polymerisation by thermal treatment or by UV and γ-irradiation [14]. The highly unsaturated conjugated backbone of these polymers imparts unusual physical properties, including relatively large third-order optical nonlinearity [13].

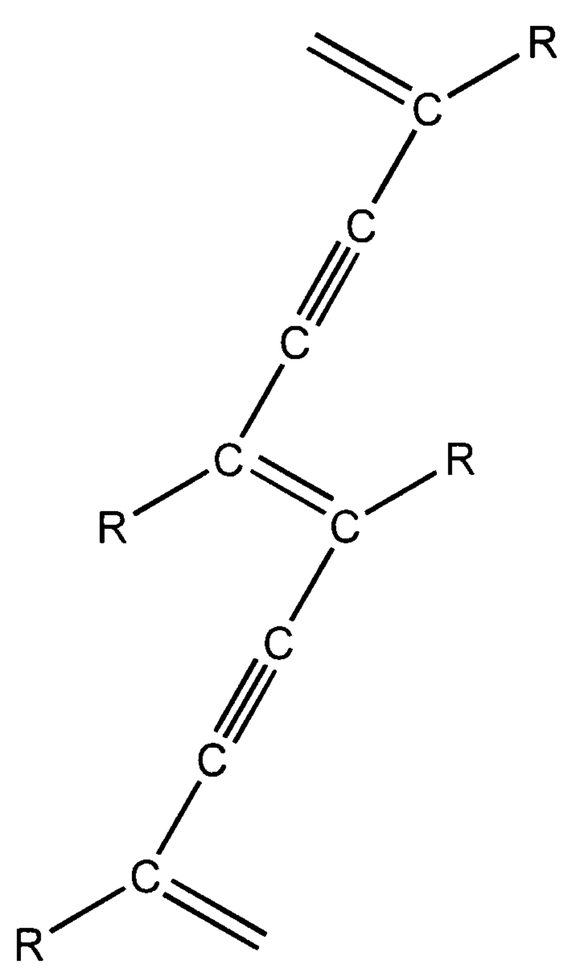

Figure 3.9: Polydiacetylene structure. *R* represents a side group.

A rather interesting facet of polydiacetylene research that has some impact on the development of nonlinear optical devices grew out of the successful attempt to polymerise molecules of *amphiphilic* character. Amphiphilic molecules consist of two parts that repel each other and/or are soluble in different solvents. The most widely studied of such systems are those composed of molecules called lipids with hydrophilic (water "liking") and hydrophobic (water "fearing") parts. The hydrophobic part consists

of one or two hydrocarbon chains containing 8 to 20 carbon atoms. The hydrophilic group generally has a charge or dipole moment [15].

As mentioned in section 3.4, the electronic structure of the polydiacetylenes leads to their description in terms of a wide-band one-dimensional semiconductor [16]. One-dimensional systems are characterised by highly anisotropic optical, dielectric, conducting and mechanical properties. This is because the valence electrons, responsible for these properties, are forced to move along linear chains of atoms or molecules with distances which are small enough to allow formation of energy states more or less delocalised in one direction; a similar delocalisation, on the other hand, in the other two directions is hindered by a surrounding sea of stable saturated bonds which keeps the chains well apart. This confers these systems with an insulator type behaviour in directions across the chains but a semiconducting or conducting behaviour along the chains.

The metallic state, on quite general grounds peculiar to the one-dimensional systems, is expected to be unstable in most cases. The complete delocalisation of the valence electrons along the chains is limited by different constraints like bond alternation and superalternation, heteroatomicity (atom alternation), chain coupling, electron repulsion, and the system is mostly forced to be in a semiconducting state. This is the case for almost all polymers, in particular, in polydiacetylenes every other pair of successive C-H bonds of a polyene chain is replaced by an additional carbon-carbon bond along the chain; further there is a change of hybridisation from sp^2 type to sp type on this pair of carbon atoms with corresponding stereochemical change of the chain. In the polydiacetylene chain shown above (Figure 3.9) appears an alternation of double and triple bonds separated by single bonds; this will be termed bond superalternation.

3.6 Generic linear optical properties of polydiacetylenes

The properties of the PDA group of materials have been found, to a first approximation, to be described by a one-dimensional semiconductor model [16]. The one-dimensionality of the PDA`s results from large interchain distances (typically around 1 nm) due to the bulky side groups, thereby making interchain coupling weak. This is one of the reasons PDA's are particularly interesting materials; the π-conjugated chains can be studied in effective isolation.

The 1-D semiconductor model proved useful in the explanation of early reflectivity experiments [17] however photoconductivity experiments failed to locate the expected photoconductivity edge. This result, combined with further studies of absorption spectra, led to the consideration of an excitonic transition as the lowest lying excited state, rather than an interband one. Modification of the semiconductor model to include Coulombic interactions did in fact predict the existence of an exciton [16]. Further theoretical work led to the prediction that the exciton has a significant charge-transfer character [18], whereby charge is re-distributed from the triple to the double bonds of the main chain upon excitation. This re-distribution was confirmed experimentally by electroreflectance and resonant Raman spectroscopy [19] [20].

The linear and nonlinear properties of polydiacetylenes (PDA's) are intricately linked through the influence of the material's electronic configuration on the polarisation that can be induced by an external field. In order to understand the nonlinear properties of PDA's, a review of the linear optical properties is presented.

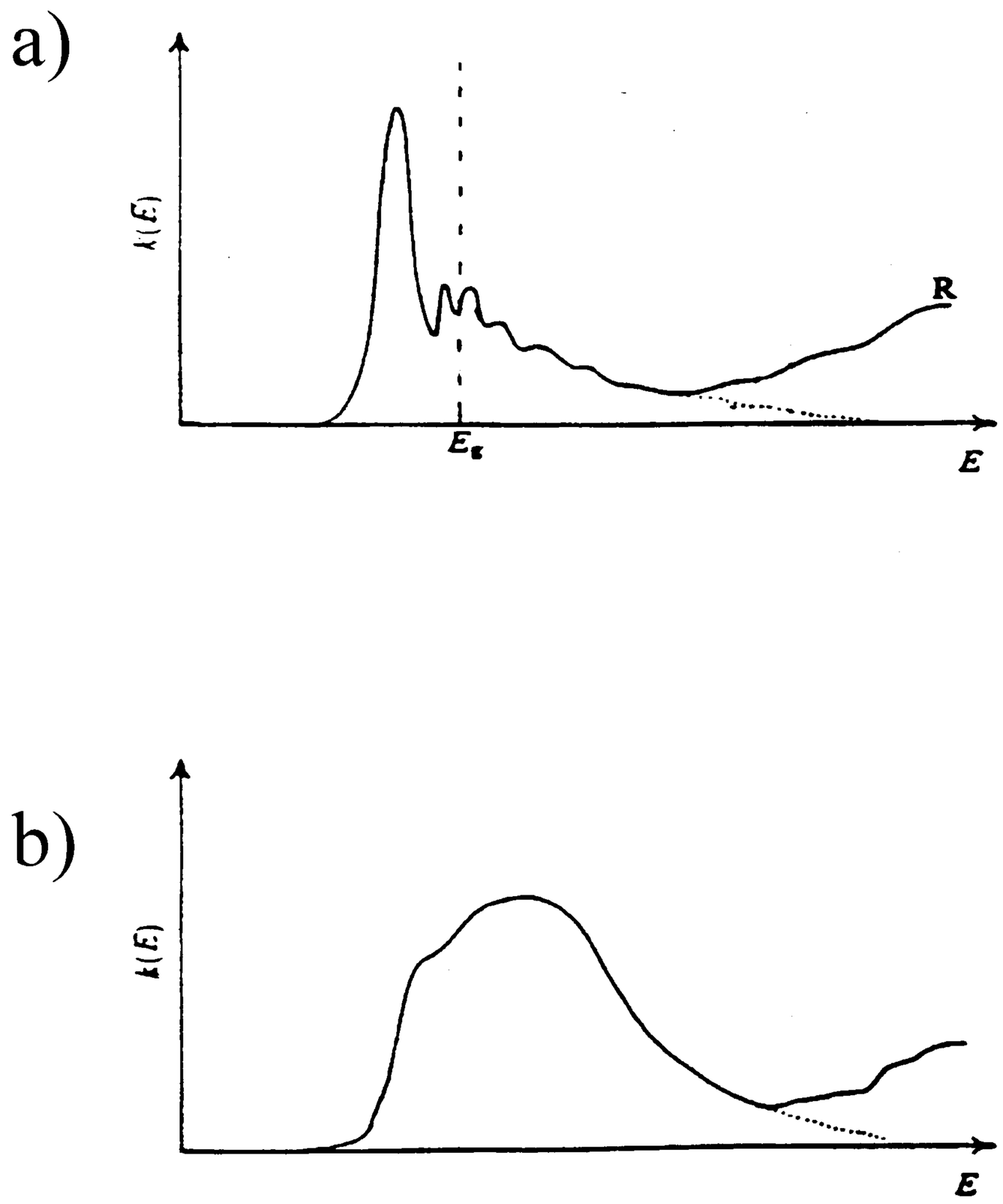

Figure 3.10: Optical spectrum of PDA. a) Obtained by calculation including Coulomb interaction, b) as in (a) above, but for an imperfect material. Taken from reference [16].

Linear absorption spectra of PDA single crystals were found to fit the "theoretical" spectrum well and many experimental results have been successfully interpreted using the excitonic approach e.g. electro-absorption [21] and optical spectroscopy [22]. Figure 3.10(a) shows the absorption spectra predicted by calculations including Coulomb interaction, and Figure 3.10(b) then illustrates the effect of disordering on the theoretical

spectrum. The excitonic peak, clearly visible in 3.10(a) is seen to broaden and shift to higher energies in 3.10(b).

In both crystals and films, there is generally no structure observed at energies below the absorption peak although the absorption often tails to longer wavelengths, usually associated with surface states or defects [21] [23]. The actual value of the exciton creation energy, defined here as E_0, has been found to be sensitive to the polymer chain conformation (geometrical arrangement in polymers arising from rotation about adjacent carbon-carbon single bonds), and as a consequence is dependent on the side-group substitutes and on the amount of disorder present in the material, which in turn is influenced by the molecular environment and processing techniques.

A variety of experimental techniques have been employed to study the electronic structure other than the fundamental exciton. Photoconductivity [24] and electroabsorption [21] spectra have placed the interband transition about 0.5 eV above the exciton level although the transition is a virtually indistinguishable feature in the absorption spectrum. Another state, lying between the exciton and the interband levels had also been reported as occurring in various PDA's [21] [25] [26]. The state is inactive in one-photon absorption, which correlates with the existence of a two-photon state that had been predicted by calculations [27]. A triplet excited state has also been observed in these materials [28] and the lowest triplet exciton energy was reported as 1.45eV (855 nm) in pTS [29] and 1.07eV (1160 nm) in DCH [30].

The available information on electronic structure was summarized by Bloor in order to construct a "generic" energy level scheme for PDA's [31], and a version of this is shown in Figure 3.11. As most of the aforementioned experimental studies were done on pTS,

the scheme best reflects the known levels for that material, however it does provide a starting point for the interpretation of various experimental results in all the PDA's.

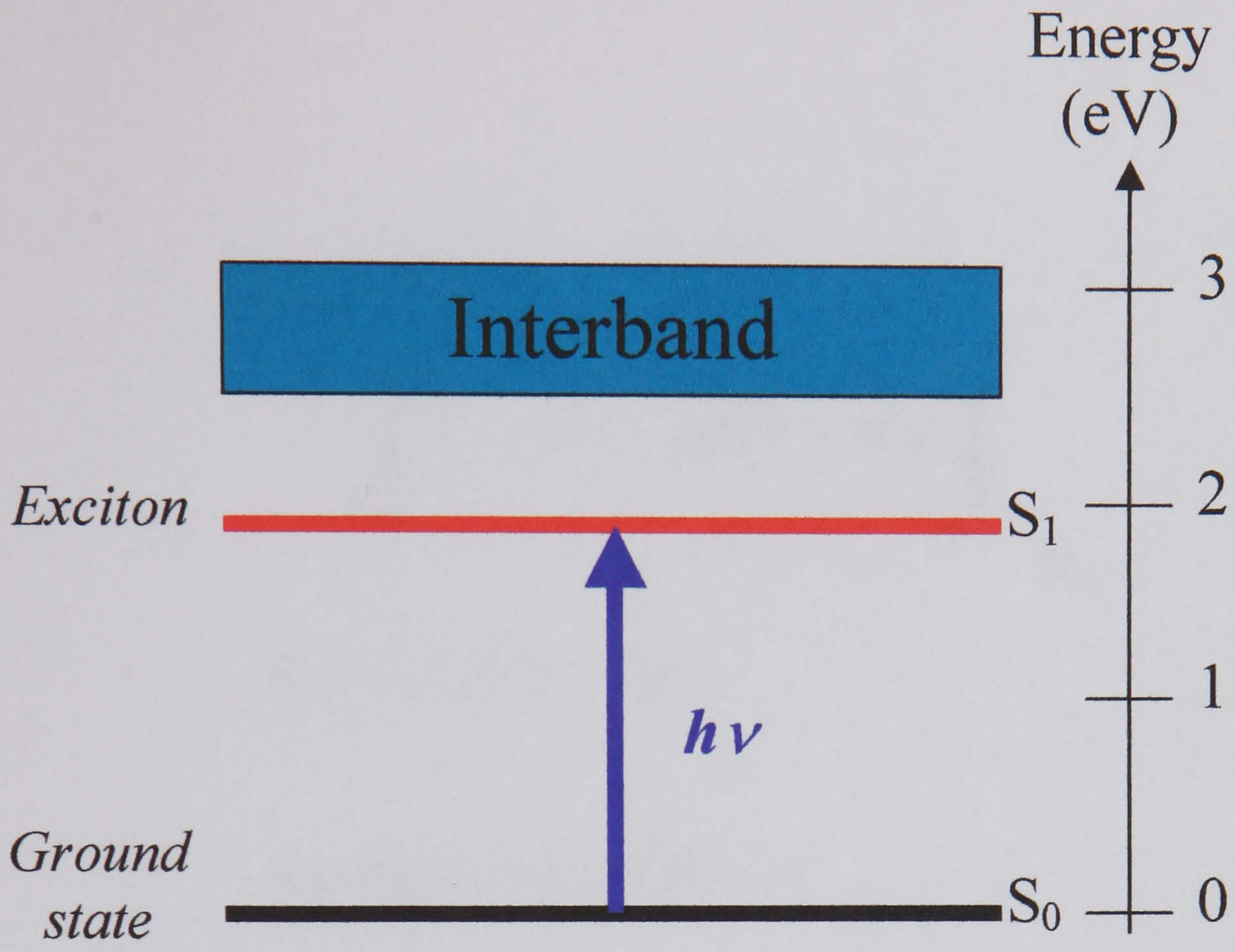

Figure 3.11: A simplified energy level diagram, representative of the basic electronic structure of polydiacetylenes, showing a singlet exciton as the first excited state (S_1) accessible by photons with energy $h\nu$. This scheme is based on that for pTS at 4K taken from reference [31].

3.7 Metal-complexed PDA's

In this section is given a brief description of the structure and preparation procedure of the set of PDA (Figure 3.12(a)) functionalised with tertiary amine groups (Figure 3.12(b)), into coordination complexes of nickel, copper, ruthenium and molybdenum. The optical (linear and nonlinear) studies, made on them are reported in Chapter 5.

The sample preparation and chemical characterisation was carried out by Dr. C. Murray, Dr. E. Lindsell and Dr. P. Preston in the Department of Chemistry of Heriot-Watt University and a complete description can be found elsewhere [32].

a) 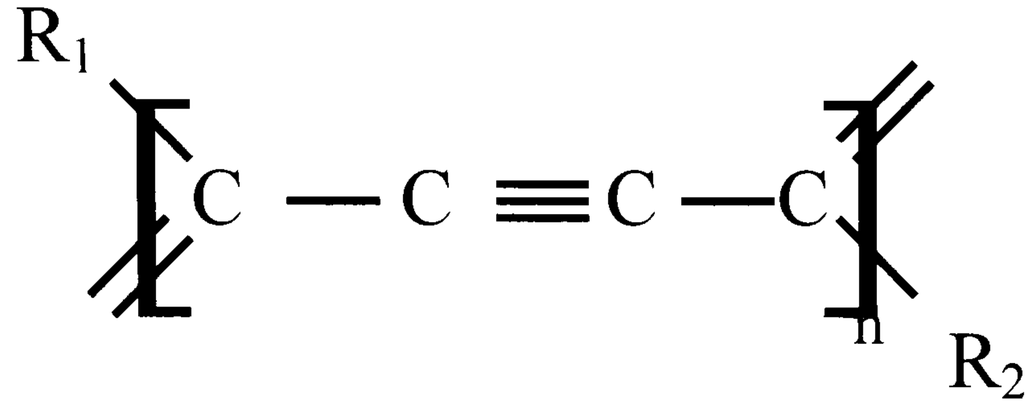

b) $R_1=R_2=(CH_2)_4NEt_2$

c) $R_1=R_2=(CH_2)_4NEt_2+Ni$

d) $R_1=R_2=(CH_2)_4NEt_2+Cu$

e) $R_1=R_2=(CH_2)_8CONH(bipy)Ru(bipy)_2^{2+}$

f) $R_1=R_2=(CH_2)_8CONH(bipy)Mo(CO)_4$

Figure 3.12: Metal-complexed PDA's structure. a) Polymerised form, b) amine side groups. Side groups structures containing-, c) nickel, d) copper e) ruthenium, and f) molybdenum.

The diethylamino-functionalised polydiacetylene (Figure 3.12(b)), which will be labelled as polymer *A,* was prepared by reaction of the tosylated polydiacetylene, with diethylamine, as reported in [33]. The molar concentration based on monomer unit was

1.58×10^{-2} M. The molar concentration *M* of a solution is defined as the number of moles of solute per liter of solution. The number of moles of solute is the amount of solute (in grams) divided by the molar mass. Molar mass is usually expressed in gmol or kgmol units. The gmol unit is recommended in polymer science.

Although polymer *A* is insoluble in water, stirring with aqueous solutions containing Ni^{2+} (from nickel chloride) or Cu^{2+} (from copper chloride), in varying molar ratios of metal-ion:diethylamino groups, produced completely soluble materials with molar concentrations of 1-2 x 10^{-2} M (based on monomer unit). Samples with molar ratios Ni^{2+}:NEt_2 of 1:1, Ni^{2+}:NEt_2 of 1:2, Cu^{2+}:NEt_2 of 1:1, Cu^{2+}:NEt_2 of 1:2 were prepared and here will be labelled *B*, *C*, *D* and *E*, respectively. Figures 3.12(c) and 3.12(d) show the corresponding side-group structures of the polymers mentioned above.

The other two samples also studied in this thesis (Chapter 5) and labelled as *F* and *G*, respectively, were PDA containing polymer-[-bipyRu$(bipy)_2]^{2+}$ terminal groups on the side-chains, with a molar ratio of ruthenium to polymer-bound bipyridyl groups of 1:1 and a molar concentration of 1.25 x 10^{-2} M; and PDA containing –{bipy} $Mo(Co)_4$ terminal groups on the side-chains, its molar concentration was 0.69 x 10^{-2}. A detailed explanation about their preparation procedure can be found in [32]. Figures 3.12(e) and 3.12(f) show their corresponding side-group structures.

3.8 Poly-DCHD microcrystals

The polymer material studied and reported in Chapter 6 and Chapter 8 was poly-[1,6-dicarbazolyl-2,4-hexadyne], better known as poly-DCHD. The DCHD is formed by solid-state polymerisation in the manner of 1,4-addition (this means that the side groups R_1 and

R_2 are attached to the carbons at the two ends of the conjugated system) as shown in Figure 3.13.

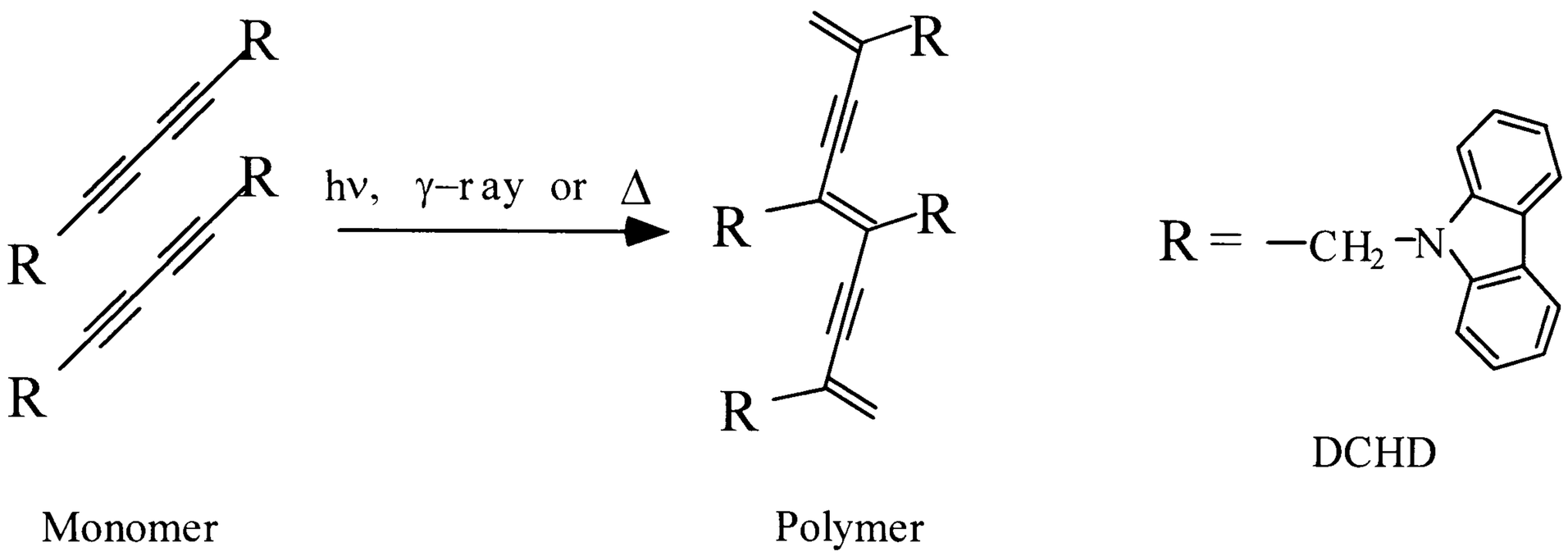

Figure 3.13: Solid-state polymerisation scheme of diacetylene and the chemical structure of the DCHD substituent.

Recently, Nakanishi and coworkers established a versatile and easy process to prepare aqueous dispersions of organic micro and nanoparticles by first preparing a finely divided dispersion of the target molecules in an appropriate solvent in water [34]. Amorphous spherical nano-micro particles of the target molecules are formed immediately after dispersion. Densification and crystallisation may subsequently follow, leading to the specific morphology and structure of the microparticle "single crystal". As mentioned above, polymer single crystal nanoparticles have been produced using solid-state polymerisation in single crystalline microparticles of a diacetylene monomer (DCHD).

A microcrystal dispersion of a diacetylene monomer (DCHD) in water was prepared. Polymerisation in the microcrystal-dispersed medium may be carried out at different times subsequent to dispersion by exposure to UV light. Immediately following dispersion, the morphology of the spherical amorphous particles is frozen by partial polymerisation by UV radiation. Complete polymerisation occurs and approximately

cubic poly-DCHD microparticles form, if the spherical amorphous monomer particles are allowed to stand in the dispersion; they first crystallise into DCHD monomer microparticle single crystals and subsequently lattice controlled photopolymerisation is carried out.

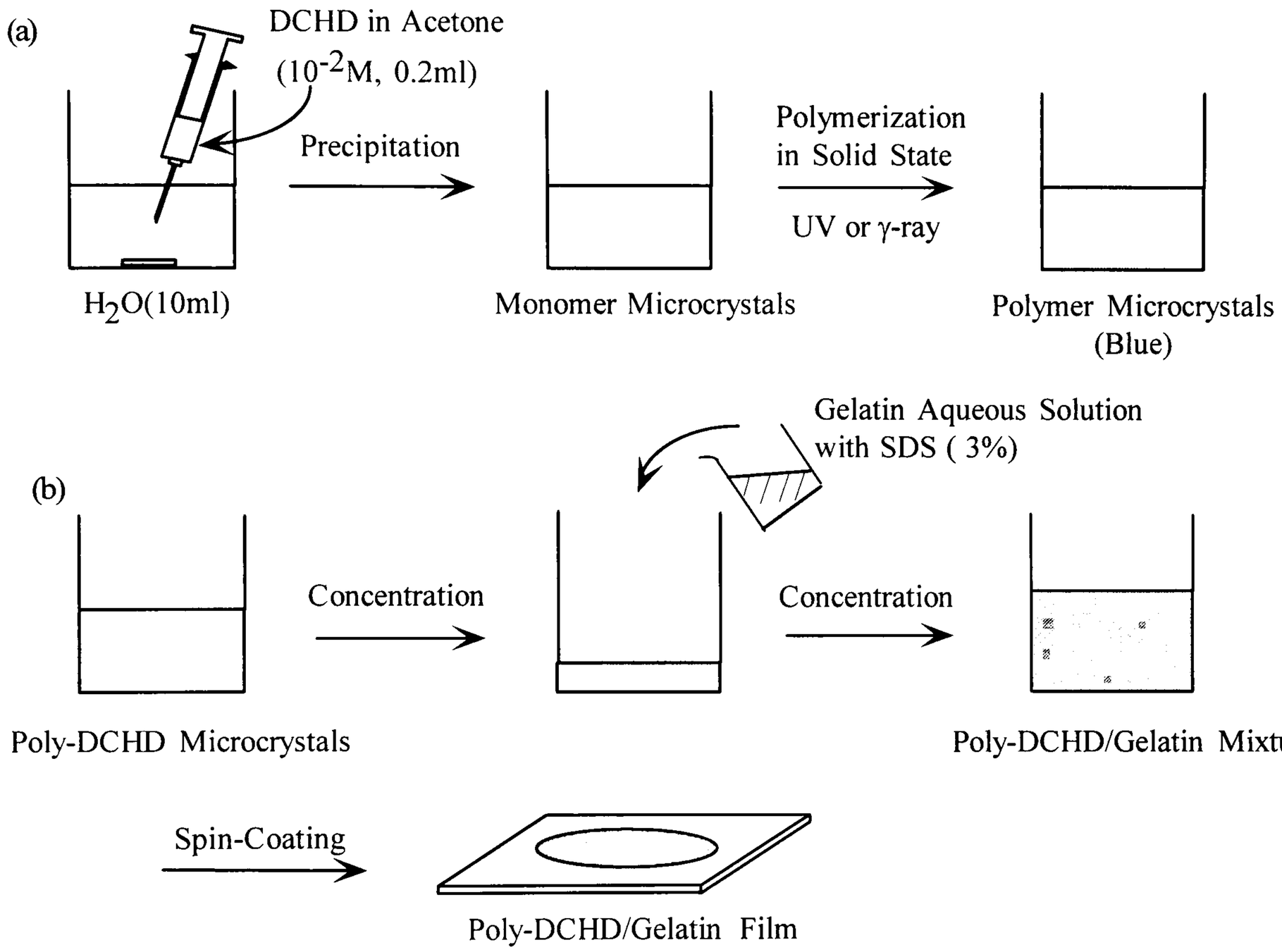

Figure 3.14: a) Preparation procedure of poly-DCHD microcrystals and b) thin-film preparation.

The typical procedure for preparation of poly-DCHD microcrystals preparation is schematically represented in Figure 3.14. A given amount (100 μl to 200 μl) of DCHD monomer-acetone solution (10^{-2} M) was injected, using a microsyringe into 10 ml of distilled water stirred vigorously. After about 20 min. of a retention time, UV-irradiation (254 nm) from a high-pressure mercury lamp was carried out to the obtained suspension

of DCHD microcrystals for the solid-state polymerisation [14]. During this process the colour of the dispersed DCHD in water changed from white to blue.

To fabricate the Fabry-Perot devices containing a thin film of poly-DCHD microcrystals and studied in Chapter 7, the suspension was concentrated at 3, 9 and 20wt%, and added a gelatine aqueous solution as a matrix polymer and a sodium dodecylsulphate (SDS) as a stabilizer [35]. The mixture was spin-coated onto one of the dielectric-coated mirrors (used to form the Fabry-Perot device). Then the second mirror was attached to complete the device. Figure 3.15 shows two pictures of one of these devices. The dark spot in the centre is the polymer thin-film (Figure 3.15). Films of a few microns thick were achieved and controlled by putting a polyester film between the two mirrors.

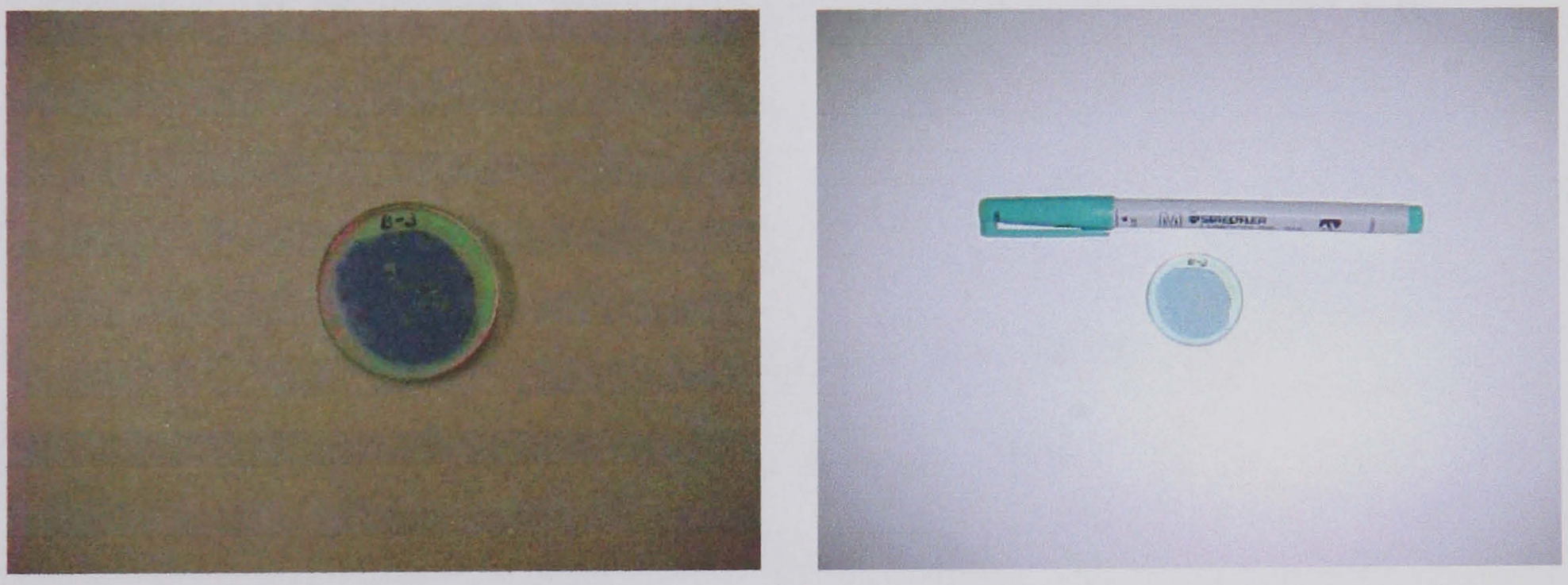

Figure 3.15: Fabry-Perot device containing a thin-film of poly-DCHD microcrystals.

In order to control the size of microcrystals, the concentration of the DCHD monomer acetone solution was also controlled. It may be possible to make smaller particles by controlling the size of the amorphous DCHD particles at the initial stage [14].

Microcrystals of different sizes such as 30, 50, and 100 nm, among others, have been obtained [14] [36]. In the present thesis only those of 100 nm were studied. Figure 3.16 shows the SEM micrograph of 100 nm poly-DCHD microcrystals.

Figure 3.16: SEM micrograph of poly-DCHD microcrystals of 100 nm size.

References

[1] D.M. Burland, R.D. Miller and C.A. Walsh, *Chem. Rev.*, **94**, 31, 1994

[2] W.E. Moerner and S.M. Silence, *Chem. Rev.*, **94**, 127, 1994

[3] A.J. Heeger and M. Sinclair, *Synth. Met.*, **15**, 95, 1986.

[4] G.M. Carter and Y.J. Chen, *Appl. Phys. Lett.*, **47**, 457, 1985

[5] C.S. Sauteret and R. Chance, *Phys. Rev. Lett.*, **36**, 956, 1976.

[6] S. Miyata, *Nonlinear Optics*, Proceedings of the fifth Toyota Conference on Nonlinear Optics, Elsevier Science Publishers, 1992.

[7] T. Kobayashi, *Polymers for Lightwave and Integrated Optics*, edited by L.A. Hornak, Inc., New York, 1992.

[8] J. McMurry, Organic Chemistry, Brooks/Cole Publishing Company, 1992.

[9] Seymour, Raymond B. and Charles E. Carraher., *Giant Molecules*, John Wiley & Sons, New York, 1990.

[10] Prasad P., *Introduction to nonlinear optical effects in molecules and polymers*, John Wiley & Sons, New York, 1991.

[11] H. Kuhn and D.L. Zechmeister, editor, *Progress in the Chemistry of Organic Natural Productos*, **16**, 17, Springer-Verlag Wiem, 1958.

[12] G.P. Agrawal, C. Cojan, and C. Flytzanis. *Phys. Rev. B*, **17**, 776, 1978.

[13] S. Molyneux, H. Matsuda, A.K. Kar, B.S. Wherrett, S. Okada, and H. Nakanishi, *Nonlinear Opt.*, **4**, 299-304, 1993.

[14] H. Katagi, H. Kasai, S. Okada, H. Oikawa, K. Komatsu, H. Matsuda, Z. Liu and H. Nakanishi, *Jpn. J. Appl. Phys.*, **35**, 1363-1366, 1996.

[15] P.M Chaikin, Principles of Condensed Matter Physics, Cambridge University Press, 1995.

[16] D. Bloor, *Phil. Trans. R. Soc. Lond. A*, **314**, 51-68, 1985.

[17] B. Reimer and H. Bassler, *Chem. Phys.*, **43**, 81, 1976.

[18] M Philpott, *Chem. Phys. Lett.*, **50**, 18 1977.

[19] L. Sebastian and G. Weiser, *Phys. Rev. Lett.*, **46**, 1156, 1981.

[20] D Batchelder and D Bloor, J. Phys. C: *Solid State Phys.*, **15**, 3005, 1982.

[21] L. Sebastian and G. Weiser, *Chem. Phys. Lett.*, **64**, 396, 1979.

[22] D. Bloor and F.H. Preston, *Phys. Stat. Sol.* A, **39**, 607, 1977.

[23] B. Reimer and H. Bassler, *Phys. Stat. Sol.* A, **32**, 435, 1975.

[24] H. Bassler, *Polydiacetylenes*, Eds. D. Bloor and R.R. Chance, p.135, 1985.

[25] Y. Tokura, T. Koda, A. Itsubo, M. Miyabayashi, K. Okuhara and A. Ueda, *J. Chem. Phys.*, **85**, 99, 1986.

[26] R.R. Chance, M.L. Shand, C. Hogg and R. Silbey, *Phys. Rev.* B., **22**, 3540, 1980.

[27] U. Dinur and M. Karplus, *Chem. Phys. Lett.*, **88**, 171, 1982.

[28] L. Robins, J. Orenstein and R. Superfine, *Phys. Rev. Lett.*, **56**, 1850, 1986.

[29] S. Molyneux, *Third-Order Nonlinear Optical of Polydiacetylenes Studied by Sub-Picosecond Techniques*, PhD thesis, Heriot-Watt University, Edinburgh, 1995.

[30] C. Jundt, G. Klein and J. LeMoigne, *Chem. Phys. Lett.*, **203**, 307, 1993.

[31] D Bloor, D Ando, P Norman, J Ohibi, P Kolinsky and B Movaghar, *Physica Scripta*, **T19**, 226, 1987.

[32] M.A. Camacho, A.K. Kar, W.E. Lindsell, C. Murray, P.N. Preston and B.S. Wherrett, *J. Mater. Chem.*, **9**, 1251, 1999.

[33] R.R. Chance, *Macromolecules*, **13**, 396, 1980.

[34] H. Nakanishi *et.al*, *Jpn. J. Appl. Phys.*, **31**, L1132, 1992

[35] H. Katagi, H. Kasai, S. Okada, H. Oikawa, E.V. Keuren, E.C. Smith, H. Matsuda, H. Oshikiri, H. Nakanishi, A.K. Kar and B.S. Wherrett, *SPIE,* **2998**, 241, 1997.

[36] S. Tripathy, H. Katagi, H. Kasai, S. Balasubramanian, S. Okada, H. Oikawa, K. Komatsu, J. Kumar, H. Matsuda, H. Oshikiri, and H. Nakanishi, *Jpn. J. Appl. Phys.*, **37**, 343, 1996.

Chapter 4

Theoretical description of the third-order processes and z-scan technique.

4.1 Introduction

The term nonlinear optics refers to phenomena affecting the propagation of light, which are dependent on other than the first power of the electric field strength. The advent of lasers with their very intense monochromatic beams has made possible the observation of a wide range of nonlinear optical phenomena. These phenomena are of particular importance because through their use one would hope to be able to modulate, to control the phase, amplitude and direction of light, as well as amplify and mix beams of light.

The first use of lasers to observe new nonlinear optical effects was the work of Franken *el al*. [1] at the University of Michigan when they observed optical second harmonic generation (SHG). Since then the work in the field has been expanding rapidly.

The third-order nonlinear susceptibility $\chi^{(3)}$ is associated with the optical Kerr effect [2]. Optical Kerr effect is very useful in nonlinear optical devices (i.e., all-optical switches, optical power limiters, optical computers, etc.). The intensity dependence of the refractive index provides a basis for all-optical processing of information, which could result in tremendous gain in speed. In addition to this important technological thrust, the irradiance-dependent refractive index also gives rise to a large number of phenomena such as self-focusing or defocusing, four-wave mixing, optical bistability, and the optical

Kerr gate effect [2]. Furthermore, the third-order nonlinear response coupled with electronic and vibrational resonances yields phenomena such as two-photon absorption and coherent Raman effects [3].

Several techniques have been developed in the past to measure the nonlinear refractive index n_2, or, equivalently, the real part of the third-order susceptibility $\chi^{(3)}$. These include nonlinear interferometry [4], wave mixing [5] [6], and the z-scan technique [7] [8]. Interferometry and wave mixing are potentially sensitive techniques, but require relatively complex experimental arrangements.

The Z-scan technique translates changes in beam curvature induced by the nonlinear response of the sample under study into transmittance changes measured by a detector placed behind an aperture in the far field. Another, unapertured detector is also placed in the far field to detect possible transmittance changes that are due only to nonlinear absorption processes.

In this chapter we present the theoretical description of the third-order processes [9]. We also discuss some of the third-order nonlinear processes such as irradiance-dependent refractive index, two-photon absorption (TPA), and absorption saturation. The z-scan technique used in measuring the nonlinear coefficients (absorption and refraction) of the samples studied in Chapter 5 and Chapter 6, is also described.

4.2 Linear optical media

4.2.1 Interaction of light with a linear medium

A molecular medium, such as an organic crystalline or polymeric solid, is generally nonconducting and nonmagnetic and the electrons are regarded as being tightly bound to

the nucleus. For such media the interaction with light can generally be regarded within the framework of a dielectric subjected to an electric field. This approach is sometimes referred to as the dipole approximation since the charge distribution induced in the molecule by the field is readily approximated by the induced dipole. The applied field polarises the molecules in the medium, displacing their charges from their equilibrium positions and induces a dipole moment μ given by

$$\mu = -er \tag{4.1}$$

where e is the electronic charge and r is the field induced displacement. The bulk polarisation **P** resulting from this induced dipole is given by

$$\mathbf{P} = -N e \mathbf{r} \tag{4.2}$$

where N is the density of dipoles in the medium.

The electric field inside the material is lowered by the polarisation that opposes the externally applied field. The reduction in field intensity in the volume element containing the molecule of interest is by the factor $1+\varepsilon$, where ε is defined as the dielectric constant of the medium [10]. If the field strength is relatively low, the polarisation of the medium is linear in the applied field. The linear polarisation is often expressed (in the *esu* system of units [11]) in terms of a susceptibility $\chi^{(1)}$ as

$$\mathbf{P} = \chi^{(1)}\mathbf{E} \tag{4.3}$$

where the proportionality constant is related to the dielectric constant by

$$\varepsilon = 1 + 4\pi\chi^{(1)} \tag{4.4}$$

in the esu system of units **P** and **E** are given in statvolt·cm^{-1} (1 statvolt·cm^{-1}=3x10^4 Vm^{-1}). The susceptibility $\chi^{(1)}$ is dimensionless in both SI and the esu systems.

The susceptibility is a second-rank tensor because it relates all of the components of the polarisation vector to all the components of the electric field vector. It contains all of the information about the medium needed to relate the polarisation in a particular direction to the various Cartesian components of an electric field vector in an arbitrary direction.

Another quantity that is related to the polarisation is the dielectric displacement **D**, defined as

$$\mathbf{D} = \mathbf{E} + 4\pi\mathbf{P} \tag{4.5}$$

The first term on the right side, **E**, gives the contribution to the electric flux density emanating from a distribution of charges, if those charges were in free space. The effect of a medium is usually to reduce the forces between charges by an amount proportional to the polarisation of the medium. In a vacuum, **D** and **E** are equal. In an isotropic medium, **D** and **E** are parallel vectors and the polarization response is equal in all directions [10]. From a comparison of equations 4.3-4.5, it is clear that the dielectric constant ε is equal to $\frac{|\mathbf{D}|}{|\mathbf{E}|}$. In anisotropic media, the vectors **D** and **E** are no longer parallel and ε is therefore a second-rank tensor with properties similar to the susceptibility tensor.

The wavelike properties of light are described by an oscillating electromagnetic field. The oscillating nature of the electric component can be described in the time domain as a

propagating electric field $\mathbf{E}(\boldsymbol{r},t)$ which is varying in space $\boldsymbol{r}$ and time t. Consequently, the material response $\mathbf{P}$ and its linear susceptibility are also time and space-varying quantities. Therefore, equation 4.3 is modified by time and space convolutions of $\chi^{(1)}$ and $\mathbf{E}$, as described by Shen in [12]. Alternatively, one can use the frequency-domain representation where the electric field $\mathbf{E}(\omega,\boldsymbol{k})$ is described by its oscillation frequency ω and its propagation vector $\boldsymbol{k}$. Both of these representations are convenient for understanding various aspects of optical behaviour. It is important to note that the principal physical phenomena are manifested in either representation and therefore both representations are equivalent.

The dielectric constant $\varepsilon(\omega)$ for a linear optical medium at optical frequencies is related to the linear optical susceptibility $\chi^{(1)}$ by an equation analogous to equation 4.4, except that $\chi^{(1)}$, specified to be the value appropriate for the optical frequency $\chi^{(1)}(\omega)$, and hence $\varepsilon(\omega)$, describes the linear optical response of the media. Such phenomena as absorption and refraction are accounted for by this relationship. The optical response of a medium is represented equivalently by its refraction index. For an isotropic medium

$$n_c^2(\omega) = \varepsilon(\omega) = 1 + 4\pi\chi^{(1)}(\omega) \tag{4.6}$$

Because of resonances in molecules and solids associated with electronic and nuclear motions, the refractive index and, hence, the dielectric constant are complex quantities. The propagation constants can be expressed in terms of a complex refractive index n_c, which is written in terms of a real refractive index, n and a real loss factor, κ

$$n_c = n + i\kappa \tag{4.7}$$

Essentially, the real part of $\varepsilon(\omega)$ and, hence, n accounts for refraction while the imaginary part (κ) describes the absorption of light in the dielectric medium. For a linear optical medium, the refractive index is independent of the electric field strength.

4.2.2 Light propagation through an optical linear medium

The propagation characteristics of light need to be described to fully understand the interaction of light with the medium. While this is fully described by the Maxwell's equations, a detailed discussion is outside the scope of this thesis. Here the wave equation, which follows from the Maxwell's equations under the assumptions that the medium is insulating and nonmagnetic and that the interaction with the medium is electric dipolar, is simply stated and used to describe the propagation characteristics of light. The latter assumption is valid for molecular entities where the wavelength of light is large compared to the dimensions of the unit being polarised. The wave equation describing the propagation of an electromagnetic wave is given by [13]

$$\nabla^2 \mathbf{E} = -\frac{\varepsilon}{c^2}\left(\frac{\partial^2 \mathbf{E}}{\partial t^2}\right) \tag{4.8}$$

where c is the speed of light and ∇ is the Laplace operator and in Cartesian coordinates is defined as

$$\nabla^2 = \left(\frac{\partial^2}{\partial x^2} + \frac{\partial^2}{\partial y^2} + \frac{\partial^2}{\partial z^2}\right) \tag{4.9}$$

The above equation relates the time and space variation of the electric field of light through the materials response, specified by the dielectric constant ε and is therefore of

fundamental importance in understanding the interaction of the field with the medium. If we assume for example the case in which the light is propagating as a plane wave in the z direction, in such a case the equation 4.8 simplifies to

$$\frac{\partial^2 \mathbf{E}}{\partial z^2} = -\frac{\varepsilon}{c^2}\left(\frac{\partial^2 \mathbf{E}}{\partial t^2}\right) \tag{4.10}$$

One solution for the above equation is a travelling wave in the z direction with the electric field $\mathbf{E}(z,t)$ given in the complex representation with an arbitrary phase factor as

$$\mathbf{E}(z,t) = \frac{1}{2}(\mathbf{E}_0 e^{-i(kz-\omega t)} + c.c.) \tag{4.11}$$

or, equivalently, as a cosinusoidal oscillation

$$\mathbf{E}(z,t) = \mathbf{E}_0 \cos(\omega t - kz) \tag{4.12}$$

with

$$k^2 = \frac{\varepsilon \omega^2}{c^2} \tag{4.13}$$

and with $\mathbf{E}_0$ defining the amplitude of the field. The term k is the propagation constant in the material and is equal to 2π times the number of waves per unit length, that is,

$$k = \frac{2\pi}{\lambda} \tag{4.14}$$

It characterises the phase of the optical wave with respect to a reference point ($z=0$, for instance) and kz describes the relative phase of the wave. The phase velocity v of a wave in a medium is given by ω/k, then using the relation $\varepsilon=n^2$ in equation 4.14 leads to

$$k = \frac{n\omega}{c} \tag{4.15}$$

and

$$v = \frac{c}{n} \tag{4.16}$$

Therefore, the propagation of an optical wave through a medium is slower than that in vacuum. The reduction factor is the refractive index n of the medium. The refractive index n of an optically linear medium is independent of the field strength **E**. Consequently from the last two equations, it is apparent that the propagation constant k, the relative phase kz, and the light velocity v are all independent of the electric field strength **E**.

4.3 Nonlinear optical media

When a medium is subject to an intense electric field such as that produced by an intense laser pulse, the polarisation response of the material is not adequately described by equation 4.3. Assuming that the polarisation of the medium is still weak compared to the binding forces between the electrons and nucleus, one can express the polarisation components in a power of series of the electric field components $\mathbf{E}(\omega,\boldsymbol{k})$ as [3]

$$\mathbf{P}(\omega,\mathbf{k}) = \mathbf{P}^{(1)}(\omega,\mathbf{k}) + \mathbf{P}^{(2)}(\omega,\mathbf{k}) + \mathbf{P}^{(3)}(\omega,\mathbf{k}) + \cdots \tag{4.17}$$

where

$$\mathbf{P}^{(1)}(\omega,\mathbf{k}) = \chi^{(1)}(\omega,k)\cdot\mathbf{E}(\omega,k)$$
$$\mathbf{P}^{(2)}(\omega,\mathbf{k}) = \chi^{(2)}(\omega=\omega_i+\omega_j, k=k_i+k_j):\mathbf{E}(\omega_i,k_i)\mathbf{E}(\omega_j,k_j) \quad (4.18)$$
$$\mathbf{P}^{(3)}(\omega,\mathbf{k}) = \chi^{(3)}(\omega=\omega_i+\omega_j+\omega_l, k=k_i+k_j+k_l)\vdots\mathbf{E}(\omega_i,k_i)\mathbf{E}(\omega_j,k_j)\mathbf{E}(\omega_l,k_l)$$

In the equations 4.18 the term that is quadratic in the electric field describes the first nonlinear effect. The coefficient $\chi^{(2)}$ relating the polarisation to the square of the electric field **E** is called the second-order nonlinear susceptibility of the medium and is a third-rank tensor. Its magnitude describes the strength of second order processes. The $\chi^{(3)}$ term is referred to as the second nonlinear susceptibility describing third-order processes, and is a fourth-rank tensor. Similarly, higher-order terms describe the higher-order processes. For most materials, the higher-order effects are extremely difficult to observe. We can rewrite equation 4.17 as

$$\mathbf{P}(\omega,\mathbf{k}) = \chi_{eff}\mathbf{E}(\omega,\mathbf{k}) \quad (4.19)$$

where essentially:

$$\chi_{eff} = \chi^{(1)} + \chi^{(2)}\mathbf{E}(\omega,\mathbf{k}) + \chi^{(3)}\mathbf{E}^2(\omega,\mathbf{k}) + \ldots \quad (4.20)$$

This analogous to equation 4.3 except that χ_{eff} is now dependent on the electric field. For optical waves this has important consequences. An inspection of equation 4.6, 4.14 and 4.15 reveals that with $\chi^{(1)}$ replaced by χ_{eff} the refractive index n, the phase of the wave kz, and the velocity v of the optical wave are now all dependent on **E**.

The manifestation of nonlinear optical behaviour can be clearly seen by substituting a cosinusoidal field equation (4.11) into the polarisation expansion equation (4.17) and ignoring imaginary χ terms. After using some trigonometric identities, we obtain the following equation

$$\mathbf{P} = \chi^{(1)}\mathbf{E}_0\cos(kz-\omega t) + \frac{1}{2}\chi^{(2)}\mathbf{E}_0^2\left[1+\cos(2kz-2\omega t)\right]$$
$$+\chi^{(3)}\mathbf{E}_0^3\left[\frac{3}{4}\cos(kz-\omega t)+\frac{1}{4}\cos(3kz-3\omega t)\right] \qquad (4.21)$$

The above equation clearly shows the presence of new frequency components due to the nonlinear polarisation. The second-order term gives a frequency independent contribution leading a process called optical rectification and one at 2ω giving rise to second harmonic generation (*SHG*) [3]. The third term indicates a frequency response at the same frequency ω of the electric field **E**, and one at the frequency 3ω. The latter gives rise to third-harmonic generation (*THG*). The even-order and odd-order terms in the expansion therefore lead to fundamentally different types of nonlinear responses.

In a nonlinear medium, the wave equation 4.8 must be modified to include the impact of the medium on the time and space variations of the electric field. The equation now becomes

$$\nabla^2\mathbf{E}(\omega) = -\frac{\varepsilon}{c^2}\frac{\partial\mathbf{E}^2(\omega)}{\partial t^2} - \frac{4\pi}{c^2}\frac{\partial^2\mathbf{P}}{\partial t^2} \qquad (4.22)$$

In which **P** is the nonlinear polarisation given as

$$\mathbf{P} = \chi^{(2)}(\omega;\omega_1,\omega_2)\mathbf{E}(\omega_1)\mathbf{E}(\omega_2) + \chi^{(3)}(\omega;\omega_1,\omega_2,\omega_3)\mathbf{E}(\omega_1)\mathbf{E}(\omega_2)\mathbf{E}(\omega_3) + \ldots \quad (4.23)$$

The linear part of **P** of the medium is included in ε. In general the processes are described by the interaction of waves at frequencies ω_i to produce a new frequency ω_j, (i,j=1,2,…).The polarisation term on the right side of the equation 4.23 can act as the source of new components of the electromagnetic field. In other words, this equation expresses the fact that, whenever the second term on the right side of equation 4.22 is nonzero, charges are being accelerated, and according to Larmor's theorem from electromagnetism [14], accelerated charges generate electromagnetic radiation.

4.4 Nonlinear optical processes

Third-order nonlinear optical interactions yield a rich variety of phenomena that can provide useful fundamental information on the structure and dynamics of molecules and polymers and can be utilised for device concepts. There are numerous third-order processes that can be distinguished on the basis of frequencies of the output and input waves, as well as by the nature of any material resonance encountered. Consequently, different $\chi^{(3)}$ terms are used to describe the various processes.

4.4.1 Irradiance-dependent refractive index

The refractive index of many materials depends upon the irradiance of the light propagating through the material and can be described in terms of the nonlinear polarisation. The part of the nonlinear polarisation for the general case (where $\chi^{(3)}$ may be a complex quantity), that influences the propagation of a beam of frequency ω is given by the relation [10]

$$P(\omega) = \frac{3}{4}\mathrm{Re}\left[\chi^{(3)}(-\omega;\omega,-\omega,\omega)\right]E(\omega)\left|E(\omega)\right|^2 \tag{4.24}$$

For simplicity we are assuming here that the light is linearly polarised and are suppressing the tensor indices of $\chi^{(3)}$. The total polarisation of the material system is then described by

$$P(\omega) = \chi^{(1)}E(\omega) + \frac{3}{4}\mathrm{Re}\,\chi^{(3)}\left|E(\omega)\right|^2 E(\omega) = \chi_{eff}(\omega)E(\omega) \tag{4.25}$$

With the effective susceptibility defined as

$$\chi_{eff} = \chi^{(1)} + \frac{3}{4}\mathrm{Re}\,\chi^{(3)}\left|E(\omega)\right|^2 \tag{4.26}$$

Then, by analogy to equation 4.6 we can write the expression which relates the refractive index to the effective susceptibility as

$$n^2 = 1 + 4\pi\chi_{eff} \tag{4.27}$$

An alternative way of defining the irradiance-dependent refractive index n, is by means of the relation

$$n = n_0 + n_2 I \tag{4.28}$$

where n_2 is known as the nonlinear refractive index and I is the irradiance. Finally, by using equations 4.27 and 4.28, and correcting to terms of order $|E(\omega)|^2$, the nonlinear refractive index n_2, will be given by the next expression

$$n_2 = \frac{12\pi^2}{cn_0^2}\mathrm{Re}\chi^{(3)} \tag{4.29}$$

where *Re* represents the real part of $\chi^{(3)}$.

The pulse irradiance *I* is given by

$$I = \frac{n_0 c}{2\pi}\left|E(\omega)\right|^2 \tag{4.30}$$

In this thesis the irradiance (*I*) will be measured in units of $GWcm^{-2}$, and n_2 will be measured in units of cm^2W^{-1}. The third-order nonlinear susceptibility $\chi^{(3)}$ is usually expressed in units of esu (electrostatic units), then, in order to be able to make a transformation of these units, the next relation will be very useful [3]

$$n_2\left(\frac{cm^2}{W}\right) = \left(\frac{0.0395}{n_0^2}\right)\chi^{(3)}(esu) \tag{4.31}$$

4.4.2 Self-focusing and self-defocusing

Self-focusing is a dramatic consequence of the nonlinear refractive index. This occurs as a combined result of a positive n_2 (defined above in equation 4.28) and a spatial variation of the laser intensity in which the beam is more intense in the centre than at the edges. The result is that the refractive index of the nonlinear medium in the centre of the beam is larger than that at the edges and the medium acts as a positive lens focusing the beam, as is shown in Figure 4.1

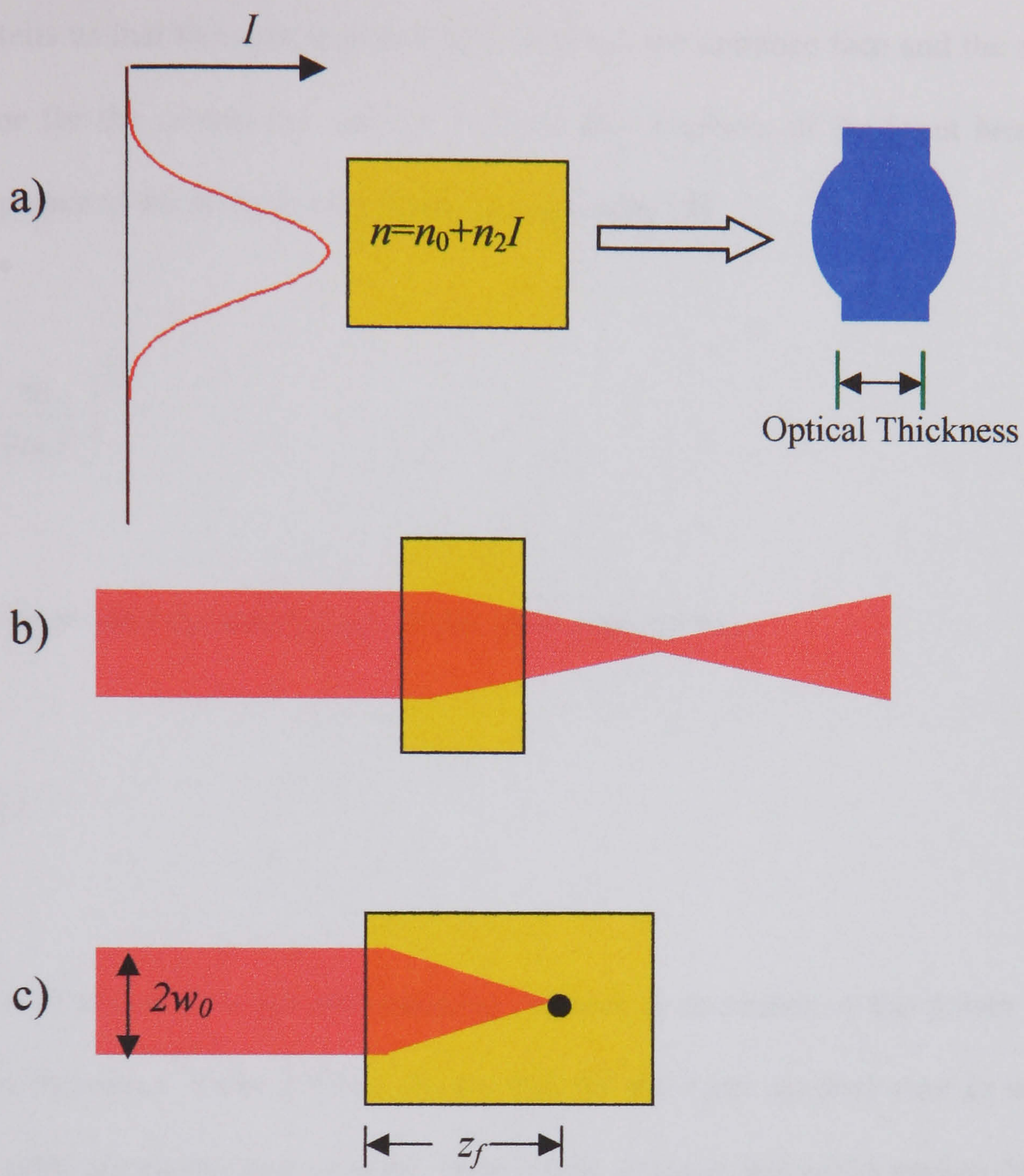

Figure 4.1: Self-focusing of light in a nonlinear medium.

The incident laser beam will tend to be brought to a focus by the action of this lens. If the medium is short enough, this focus will occur outside of the medium (Figure 4.1(b)). However, as we can see in Figure 4.1(c) if the medium is sufficiently long or the irradiance is sufficiently large, the focus will occur within the medium and a high risk of damaging the material will be present. Self-focusing can occur only if the power P of the laser beam is sufficiently large. Assuming that the laser beam has a gaussian transverse intensity distribution, and that the beam waist w_0 is located at the entrance face of the

nonlinear optical medium, by using Fermat's principle [15] we can estimate the distance z_f from the input face to the position of the focus created by self-focusing. Fermat's principle tells us that the optical path length between the entrance face and the self-focus is the same for the central ray and for a ray at the periphery of the input beam. Then, when the power of the beam is very large, z_f is given by [3]

$$z_f = w_0^2 \left(\frac{\pi n_0}{2 n_2 P} \right)^{1/2} \tag{4.32}$$

where we have taken the total power of the input beam to be

$$P = \frac{1}{2} \pi w_0^2 I \tag{4.33}$$

Equation 4.32 shows how the self-focusing distance z_f decreases as the power P of the laser beam increases. Yariv [2] has shown that for the more general case in which the beam has arbitrary power and arbitrary beam waist position, the self-focusing distance is given by

$$z_f = \frac{\frac{1}{2} k w^2}{\sqrt{\left(\frac{P}{P_{cr}} - 1 \right)} + 2 z_{\min} / k w_0^2} \tag{4.34}$$

Where the beam radius w and z_{min} parameters are defined in Figure 4.2. P_{cr} is called critical power and is defined as

$P_{cr} = (0.146) \frac{\lambda^2}{n_0 n_2}$, λ is the wavelength of the laser beam. (4.35)

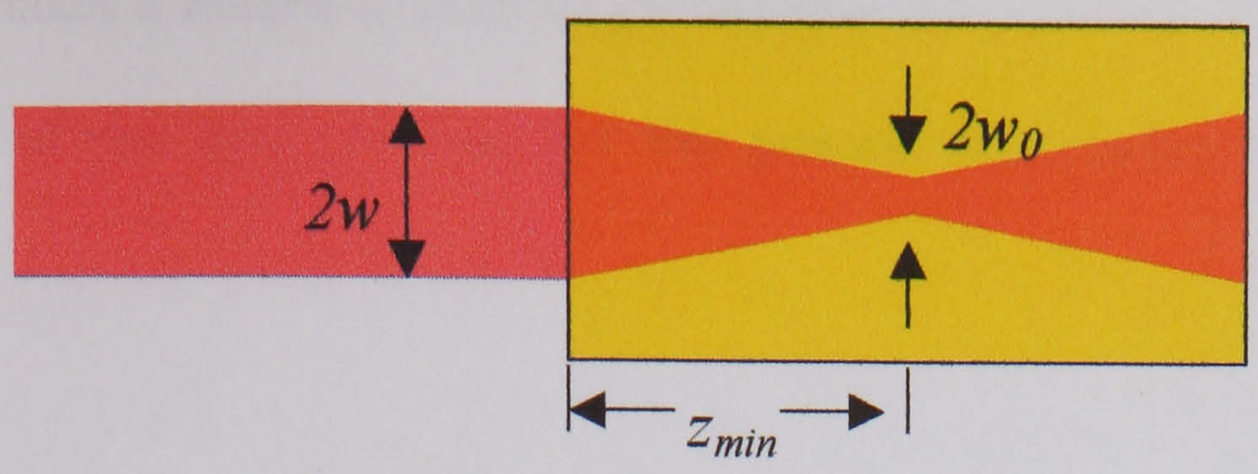

Figure 4.2: Definition of the parameters w, w_0, and z_{min}.

On the other hand, self-defocusing occurs when the nonlinear refractive index n_2 of the medium is negative. In this case the spatial variation of the laser intensity creates a negative lens resulting in defocusing of the beam. As we shall see in section 4.5, the z-scan technique is based on self-focusing (or self-defocusing) to measure the sign as well as the magnitude of n_2 (or $\mathrm{Re}\chi^{(3)}$).

4.4.3 Two photon absorption

This process illustrated in Figure 4.3, occurs when a material has an electronic excited level at twice the frequency ω of the laser beam.

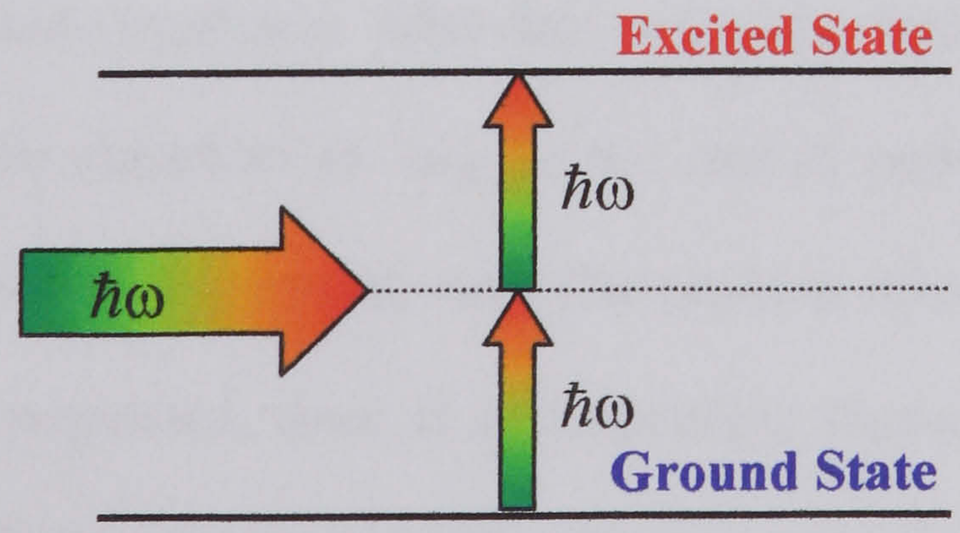

Figure 4.3: Two-photon absorption diagram.

An atom makes a transition from its ground state to an excited state by the simultaneous absorption of two laser photons. For this process the resulting polarisation is given by [16]

$$P(\omega) = i\frac{3}{4}\mathrm{Im}\left[\chi^{(3)}(-\omega;\omega,\omega,-\omega)\right]E(\omega)\left|E(\omega)\right|^2 \tag{4.36}$$

Comparing equations 4.25 and 4.36 One can see that the self-refraction (self-focusing or self-defocusing) involves the real part of $\chi^{(3)}$, while the two-photon absorption involves the imaginary part of $\chi^{(3)}$. A process involving the imaginary part of the susceptibility implies damping of the wave in the medium resulting from the exchange of energy between the optical field and the medium. In contrast, the self-refraction effect requires no net exchange of energy between the optical field and the nonlinear medium. These processes may be resonantly enhanced if the input and (or) output frequencies are near an electronic or vibrational resonance [11].

4.4.4 Saturable absorption

Many material systems have the property that their absorption coefficient decreases when measured using high laser irradiance. Materials possessing strong electronic absorption can behave as saturable absorbers as long as the rate of populating the excited state exceeds the rate of return to the ground state. The physical origin lies in the fact that as the excited states are populated, there is corresponding depletion of the ground state population, which leads to a decrease in the absorption involving transitions from the ground state. Consequently, the absorption saturates at higher intensities and the medium can almost bleach (the material becomes transparent) at sufficiently high irradiances. Often the dependence of the measured absorption coefficient α on the irradiance I of the incident laser beam is given by the expression [3]

$$\alpha = \frac{\alpha_0}{1 + I/I_s} \tag{4.37}$$

where α_0 is the linear absorption coefficient, and I_s is a parameter known as the saturation irradiance.

4.5 Theoretical description of the z-scan technique

As explained in Chapter 2, the z-scan technique is a single beam technique for measuring the sign and magnitude of refractive nonlinearities, as well as the absorptive ones. This technique is relatively simple to implement and has a high sensitivity. It is based on the transformation of phase distortion to amplitude distortion during beam propagation (refractive part), and the transmission change due to the nonlinear absorption (or saturation absorption) of the sample [17].

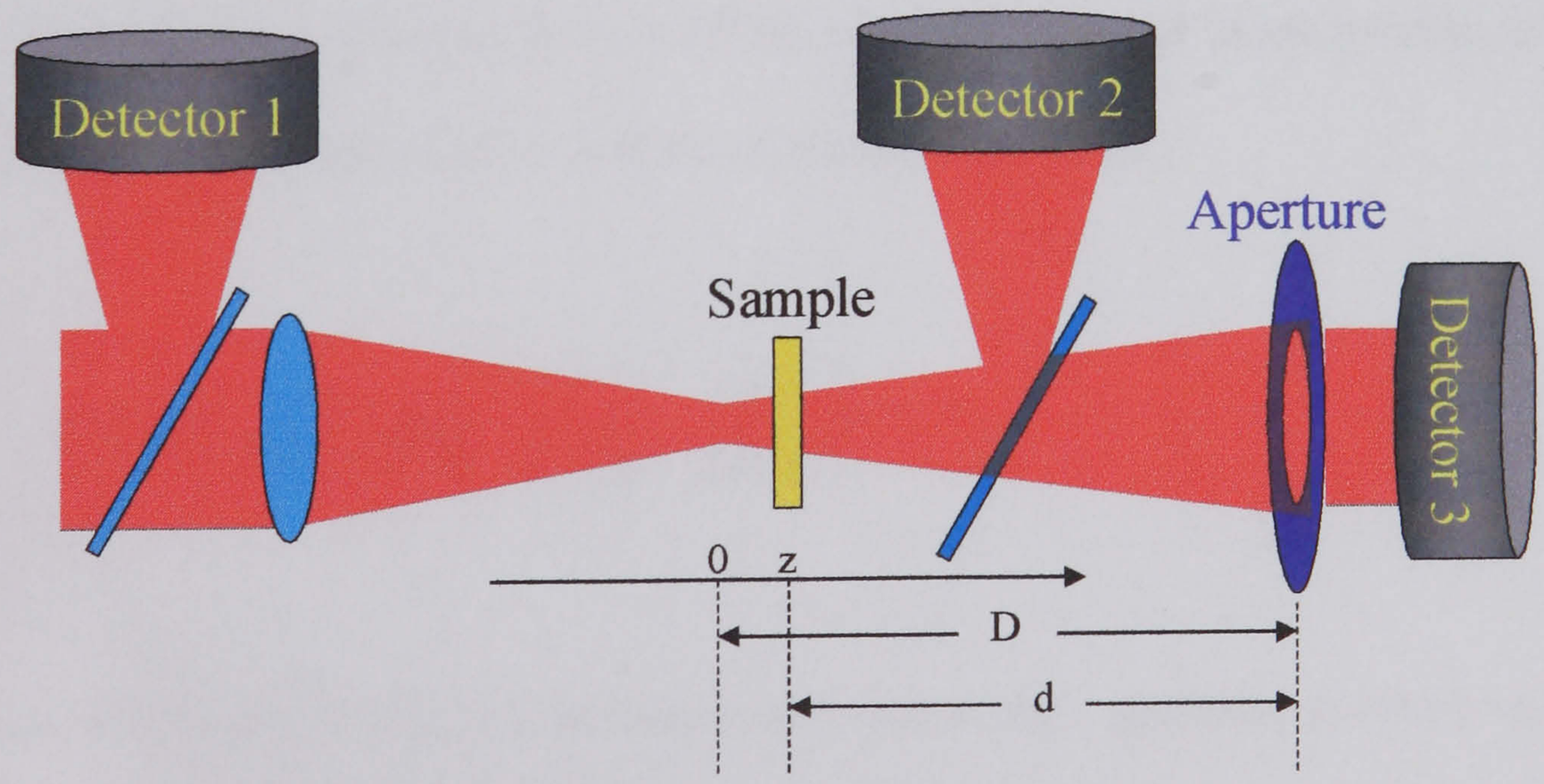

Figure 4.4: Z-scan setup showing some of the parameters involved in this technique.

A single Gaussian beam is tightly focused onto the sample under investigation (Figure 4.4), and the transmitted light irradiance is detected using apertured and unapertured detectors placed in the far field, allowing one to obtain at the same time the refractive and absorptive nonlinearities.

4.5.1 Z-scan in the case of a purely refractive nonlinearity

Considering firstly the problem of the propagation of an intense laser beam inside a nonlinear material, which will be considered to have an irradiance-dependent refractive index $n(I)$, that in the most general case takes the form:

$$n(I) = n_0 + \Delta n(I) \tag{4.38}$$

where n_0 is the linear refractive index, and I is the laser beam irradiance. For third-order processes $\Delta n(I)=n_2 I$ with n_2 given by equation 4.29.

If the laser beam is assumed to be a TEM_{00} Gaussian beam of beam waist w_0 propagating in the $+z$ direction, the electric field $E(z,r,t)$ will be given by:

$$E(z,r,t) = E_0(t)\frac{w_0}{w(z)}\exp\left[-\frac{r^2}{w^2(z)} - \frac{ikr^2}{2R(z)}\right]e^{-i\varphi(z,t)} \tag{4.39}$$

Where $w^2(z)=w_0^2(1+z^2/z_0^2)$ is the beam spot-size at the z position, $R(z)=z(1+z_0^2/z^2)$ is the radius of curvature of the wavefront at z, $z_0=\pi w_0^2/\lambda$ is the Rayleigh range of the beam and λ is the light wavelength in vacuum. The $e^{-i\varphi(z,t)}$ term contains all the radially uniform phase variations.

The evolution of the beam inside the sample is calculated by solving the wave equation 4.22 for the electric field envelope $E(z,r,t)$ with the appropriate polarisation source term. Only cases when the nonlinear response is very fast compared to the pulse length will be considered (the adiabatic limit). The effect of nonlinear refraction is made explicit by factorising the envelope function $E(z,r,t)$ in terms of an amplitude A and a phase ϕ, $E(z,r,t)=A(z,r,t)e^{i\phi(z,r,t)}$. For samples that are thin enough, changes in the beam diameter within the sample due to either diffraction or nonlinear refraction can be neglected. In this thesis, only this case, where the self-refraction can be considered as 'external self-action' [18] will be considered. For linear diffraction this implies that the sample thickness L should be such that $L<<z_0$, while for nonlinear refraction $L<<z_0/\Delta\phi(0)$ [9] [12], where $\Delta\phi(0)$ is the induced phase change on axis. In most z-scan experiments the second condition is met, since $\Delta\phi$ is usually small. Moreover Sheik-Bahae *et al* [17] have found that the linear diffraction condition can be relaxed to $L<z_0$ without losing accuracy. Under the 'external self-action' approximation, the wave equation 4.22 for E can be factorised into two independent equations for the evolution of the irradiance (proportional to A^2) and the nonlinear phase change $\Delta\phi$. Under these conditions, these equations can be written as [19]:

$$\frac{dI}{dz'} = -\alpha(I)I\,, \tag{4.40}$$

and

$$\frac{d\Delta\phi}{dz'} = \frac{2\pi}{\lambda}\Delta n \tag{4.41}$$

where z` is the propagation depth inside the sample and $\alpha(I)$ can include nonlinear absorption terms. It is important to notice that the coordinate z is reserved to note the sample position relative to the focal plane and z' is used to calculate the field propagation inside the sample. Only linear absorption, characterised by α_0, the linear absorption coefficient, will be considered in this section. The case where nonlinear absorption is present will be treated in the next section. With this assumption, the solution to equation 4.40 is given by

$$I(z') = (1-R)I(z,r,t)e^{-\alpha_0 z'} \tag{4.42}$$

where R is the air-sample interface reflectivity. For the case of a third-order nonlinearity, where $\Delta n = n_2 I$, the nonlinear phase change, calculated by integrating equation 4.41 and 4.42 will be

$$\Delta\phi_{out}(z,r,t) = (1-R)I_0(t)\gamma_2 L_{eff}\frac{w_0^2}{w^2(z)}\exp\left[-\frac{2r^2}{w^2(z)}\right] \tag{4.43}$$

where $L_{eff}=[1-exp(-\alpha_0 L)]/\alpha_0$, $\gamma_2=2\pi n_2/\lambda$, $I_0(t)$ is the on-axis irradiance at focus, and the Gaussian nature of the input irradiance has been made explicit. The electric field exiting the sample E_{out} will be

$$E_{out}(z,r,t) = (1-R)E(z,r,t)e^{-\alpha_0 L/2}e^{i\Delta\phi_{out}(z,r,t)} \tag{4.44}$$

i.e. E_{out} will be a Gaussian beam with a phase distortion given by $\Delta\phi_{out}$. The far field pattern of the beam can be obtained using the Huygens-Fresnel formalism, the electric

field at the apertured detector plane, situated at a distance D from the focal plane, $E_{ap}(z+d,r,t)$, with $d=D-z$, will be given by [12]

$$E_{ap}(z+d,r,t)=\frac{2\pi}{\lambda}\exp\left(\frac{i\pi r^2}{\lambda d}\right)\int_0^\infty\left[E_{out}(z,r',t)\exp\left(-\frac{i\pi r'^2}{\lambda d}\right)J_0\left(\frac{2\pi rr'}{\lambda d}\right)\right]r'dr' \qquad (4.45)$$

where J_0 is the zeroth-order Bessel function. Such integration has to be carried out numerically. Because of this, another method has been proposed for calculating the field propagation [17], that involves using a technique known as 'Gaussian decomposition' [20]. This consists of expressing the phase distortion term as a series of variable spot size Gaussian terms and propagating each component separately. The problem with that technique is that the series only converges for small values of the phase change $\Delta\phi$, and it cannot be easily adapted to nonlinearities other than third-order ones. The transmitted power through the aperture is obtained by spatially integrating $E_{ap}(r,t)$ up to the aperture radius r_a. Finally, the normalised aperture transmittance $T(z)$ will be given by temporal integration over the pulse shape:

$$T(z)=c\varepsilon_0 n_0\frac{\int_{-\infty}^{\infty}\int_0^{r_a}\left|E_{ap}(r,t)\right|^2 rdrdt}{S\int_{-\infty}^{\infty}P_{in}(t)dt} \qquad (4.46)$$

where $P_{in}(t)=\pi w_0^2 I_o(t)/2$ is the instantaneous input power and $S=1-exp(-2r_a^2/w_a^2)$ is the aperture linear transmittance.

4.5.2 Z-scan in the presence of nonlinear absorption

When an absorptive nonlinearity is present, it has a strong effect on the measurement of the nonlinear refraction using the z-scan technique. Its effect on the z-scan trace

(transmitted signal) can be described, in the case of absorption saturation, as a reduction or elimination of the transmittance minimum and an enhancement of the maximum, and the opposite happens for two-photon absorption or other induced absorption processes. In a z-scan experiment conducted with an 'open' aperture (S=1), the effect of nonlinear refraction is eliminated and the result is only sensitive to the nonlinear absorption present in the sample. The relevant coefficients characterising the absorption can then be extracted from such an open z-scan experiment and then used to interpret the 'closed' (S<1) z-scan results.

In the case when two-photon absorption is present, its effect on the pulse propagation can be accounted for by modifying equation 4.40 to

$$\frac{dI}{dz'} = -\alpha_0 I - \beta I^2 \tag{4.47}$$

Where

$$\beta = \frac{4\pi}{c\varepsilon_0 {n_0}^2 \lambda} \operatorname{Im} \chi^{(3)} \tag{4.48}$$

is the two-photon absorption coefficient. The solution to equation 4.47 is straightforward

$$I(z', r, t) = (1 - R)\frac{I(0, r, t)e^{-\alpha_0 z'}}{1 + q(z', r, t)} \tag{4.49}$$

Where

$$q(z',r,t) = \frac{\beta(1-R)I(0,r,t)}{\alpha_0}(1-e^{-\alpha_0 z'}) \tag{4.50}$$

To calculate the open aperture z-scan trace only the integral of $I_{out}(z,r,t)$ over radius and time needs to be calculated. The normalised transmittance $T(z,S=1)$ will be given by

$$T(z,S=1) = \frac{\int_{-\infty}^{\infty}\int_{0}^{\infty} I_{out}(L,z,r,t)rdrdt}{\int_{-\infty}^{\infty}\int_{0}^{\infty} I(z,r,t)rdrdt} \tag{4.51}$$

The result of this integration is

$$T(z,S=1) = \frac{(1-R)^2 e^{-\alpha_0 L}}{\sqrt{2}q_0(z,t=0)}\int_{-\infty}^{\infty}\ln\left[1+q_0(z,0)f(t)\right]dt \tag{4.52}$$

where $q_0(z,t)=\beta(1\text{-}R)I_0(t)L_{eff}$ and $f(t)$ is the pulse shape in time, normalised such that its time integral is equal to 1.

$I(z',r,t)$ can now be used to calculate the nonlinear phase change, by integrating 4.41 and using 4.49 to give

$$\Delta\phi(z,r,t) = \frac{\gamma_2}{\beta}\ln\left[1+q(z,r,t)\right] \tag{4.53}$$

with $q(z,r,t)=\beta I(z,r,t)(1\text{-}R)L_{eff}$. The phase distortion suffered by the beam is

$$e^{i\Delta\phi(z,r,t)} = \left[1+q(z,r,t)\right]^{i\gamma_2/\beta} \tag{4.54}$$

The electric field exiting the sample $E_{out}(z,r,t)$ will be proportional to

$$\sqrt{I(L,z,r,t)}\exp[i\Delta\phi(z,r,t)] \tag{4.55}$$

then

$$E_{out}(z,r,t) = (1-R)E(z,r,t)e^{\alpha_0 L/2}\left[1+q(z,r,t)\right]^{[i\gamma_2/(\beta-1/2)]} \tag{4.56}$$

The closed aperture z-scan trace is then calculated by propagating the field $E_{out}(z,r,t)$ to the detector plane. When $q(z,r,t)<1$ the Gaussian decomposition technique can be used to do this, otherwise, the Huyens-Fresnel propagation expression previously shown has to be used.

In an experiment, the open and closed aperture z-scan traces will be recorded simultaneously. Using the formalism described above, a program has been written and used in previous works to analyse the z-scan experiment data [21]. In this thesis it will be used to analyse the experimental results of Chapter 5 and Chapter 6. The analysis consists of fitting the open and closed aperture traces (experimental data), and then obtaining the two-photon absorption coefficient β as well as the nonlinear refractive index n_2.

4.5.3 Nonlinearity time dependence in z-scan measurements

In modelling the z-scan properties, the sample nonlinear response and decay times have been assumed to be very fast compared to the pulse length of the laser used. In general, for an arbitrary response time, the quantity measured in the z-scan will be the time averaged index change $\langle \Delta n_0(t) \rangle$, where

$$\langle \Delta n_0(t) \rangle = \frac{\int_{-\infty}^{\infty} \Delta n_0(t) I_0(t) dt}{\int_{-\infty}^{\infty} I_0(t) dt} \tag{4.57}$$

For a nonlinearity that has a response time much shorter than the pulse length and for a temporally Gaussian pulse $\langle \Delta n_0(t) \rangle = \Delta n_0/2$. For materials and laser systems where the pulse length and the response time are on a similar time scale a detailed model for $\Delta n_0(t)$ is needed to calculate the average 4.57.

References

[1] J.F. Ward and G.H.C. New, *Phys. Rev.* **185**, 57, 1969.

[2] A. Yariv, *Quantum Electronics*, John Wiley, 3rd ed., 1988.

[3] R.W. Boyd, *Nonlinear Optics*, Academic Press, 1992.

[4] M.J. Weber, D. Milan, and W.L. Smith, *Opt. Eng.*, **17**, 463, 1978.

[5] S.R. Frigberg and P.W. Smith, *IEEE J. Quantum Electron.*, **QE-23**, 2089, 1987.

[6] R. Adair, L.L. Chase, and S.A. Payne, *J. Opt. Soc. Am. B*, **4**, 875, 1987.

[7] W.E. Williams, M.J. Soileau, and E.W. Van Stryland, *Opt. Comm.*, **50**, 256, 1984.

[8] W.E. Williams, M.J. Soileau, and E.W. Van Stryland, *Proc. Annual Symp. On Optical Materials for High Power Lasers,* Boulder, Co 1983.

[9] M. Sheik-Bahae, A.A. Said, T.H. Wei, D.J. Hagan, and E.W. Van Stryland, *IEEE J. Quantum Electron*, **26**, 760, 1990.

[10] P.N. Prasad and D.J. Williams, *Introduction to Nonlinear Optical Effects in Molecules and Polymers*, John Wiley, 1991.

[11] P.N. Butcher and D. Cotter, *The Elements of Nonlinear Optics*, Cambridge University Press, 1990.

[12] Y.R. Shen, *The principles of Nonlinear Optics*, John Wiley, 1984.

[13] R.P. Clyton and A.N. Syed, *Introduction to Electromagnetic Fields*, McGraw-Hill, 2nd ed., 1987.

[14] see for example: J.D. Jackson, *Classical Electrodynamics*, 3rd ed., John Wiley, 1999.

[15] E. Hetch and A. Zajac, *Optics*, Addison Wesley Publishing Company, 7th ed., 1982.

[16] J.F. Reintjes, *Nonlinear Optical Parametric Process in Liquids and Gases*, Academic Press, 1984.

[17] M. Sheik-Bahae, A.A. Said and E.W. Van Stryland, *Opt. Lett.* **14**, 955, 1989.

[18] R. Rangel-Rojo. *Picosecond Third-Order Nonlinearities in Organic Materials and Chalcogenide Glasses*. PhD thesis, Heriot-Watt University, Edinburgh, 1994.

[19] E.W. Van Stryland, H. Vanherzeele, M.A. Woodall, M.J. Soileau, A.L. Smirl, S. Guha and T.F. Boggess, *Opt. Engineering* **24**, 613, 1985.

[20] D. Weaire, B.S. Wherrett, D.A.B. Miller and S.D. Smith, *Opt. Lett.* **4**, 331, 1974.

[21] J.M. Burzler, J.M. Hughes, B.S. Wherrett, *Applied Physics B-Lasers and Optics*, **62**, 389, 1996.

Chapter 5

Third-order optical nonlinearities of metal-complexed PDA's

5.1 Introduction

There has been considerable interest in the molecular origin of large nonlinear optical susceptibilities in organic materials. Calculations for octatretaene, a prototype delocalised π system, imply that virtual transitions between states that produce a large charge separation make the predominant contributions to the molecular third-order susceptibility [1]. This raises the possibility that introducing charge transfer states into a conjugate molecule and thereby increasing the number of states with a large charge separation might enhance the nonlinear susceptibility.

The phthalocyanines are a class of compounds with an extensively delocalised π system. In addition, they form well-characterized complexes with a variety of metals. Metal substitution introduces metal-to-ligand and ligand-to-metal charge transfer states into the electronic manifold, many of which are low in energy [2].

J S Shirk *et. al.* [3], have studied the influence of metal substitution in phthalocyanines on their nonlinear optical susceptibility. Specifically, the $\chi^{(3)}$ at 1.064 μm (far from resonance with the π-π^* transition) of metal free tetrakis (cumylphenoxy) phthalocyanine (Pc) was compared with that of a transition metal (Pt) and a main group metal (Pb) complex. It was clear that the third-order susceptibility of these phthalocyanines is greatly

enhanced by metal substitution. The $\chi^{(3)}$ (2 x 10^{-10} esu) for PtPc was about 45 times that for the metal-free form and about an order of magnitude larger than PbPc. PtPc and PbPc have a number of low-lying charge transfer states not present in the metal-free compound. The enhancement of the third-order susceptibility of these phthalocyanines has been related to the increase in the number of low-lying charge transfer states in the molecule [4].

PDA's are highly coloured materials, often red, blue or black and usually insoluble but some, including those with urethane [5], sulphonate [6] and ester [7] side-chains, are soluble in common organic solvents. The highly unsaturated conjugated backbone of PDAs imparts unusual physical properties, including relatively large third-order optical nonlinearity [8]. Another interesting feature is their property of chromism [9], which can be induced thermally and photochemically, or in solution by variation of the solvent to non-solvent ratio (solvato-chromism) [10]. An intriguing feature of PDAs containing carboxylic acid groups is the effect of pH on the absorption spectra; such materials are yellow in alkaline solution but red in acid [11]. Polydiacetylenes with pyridyl-ester substituents have also been reported and show similar colour changes on protonation or complexation with some transition metals [12]. This type of dichroic behaviour is attributed to a change of effective conjugation length of the polymer backbone, accompanied in some cases by aggregation effects [13].

In this chapter I present a picosecond study of the third-order nonlinear properties of new PDAs in which the side-chains (R) contain a ligating bipyridyl substituent, and a related PDA functionalised with tertiary amine groups, into coordination complexes of copper (II), nickel (II), ruthenium (II) and molybdenum. The z-scan technique described in

Chapter 3 is used to measure their nonlinear absorption coefficient β (related to $\mathrm{Im}\chi^{(3)}$), and nonlinear refractive index n_2 (related to $\mathrm{Re}\chi^{(3)}$).

5.2 Experimental details and linear optical properties

The samples studied in this chapter and described in detail in Chapter 3 were a set of seven different suspensions (metal-complexed PDA's) each one contained in a 1mm thick quartz cell. All the z-scan experiments reported in the present chapter were performed at λ=532 nm by using the laser system described in Chapter 2. Since the Rayleigh range ($z_0=\pi w_0^2/\lambda$) was 8.3 mm, which is larger than the sample thickness of 1 mm, the desirable condition (sample thickness < z_0) for the z-scan technique is readily fulfilled [14]. All the nonlinear measurements were made at irradiance levels of around 5 $\mathrm{GWcm^{-2}}$, and care was taken to avoid damaging (burning the polymer solutions) the samples, as well as producing thermal effects. The z-scan system was previously calibrated and tested by scanning a reference sample for which the nonlinear coefficients (absorption and refraction) are already reported. Some people use CS_2 to calibrate their systems [15], but apart from all the special equipment required, due to its harmful effects (high toxicity), extra-care in handling this should be taken. In this work, a ZnSe sample was used as reference, its nonlinear coefficients have been measured at several wavelengths (including 532 nm) [14].

The structural characteristics of the metal-complexed PDAs samples studied here have been described in section 3.7. Figure 5.1 shows the linear absorption spectra of samples labelled as *A, B, C, D* and *E*. As described in section 3.7, these samples correspond to the uncomplexed diethylamino-functionalised PDA (sample *A*), Cu[1:1]-complex (sample *B*), Cu[1:2]-complex (sample *C*), Ni[1:1]-complex (sample *D*) and Ni[1:2]-complex (sample *E*).

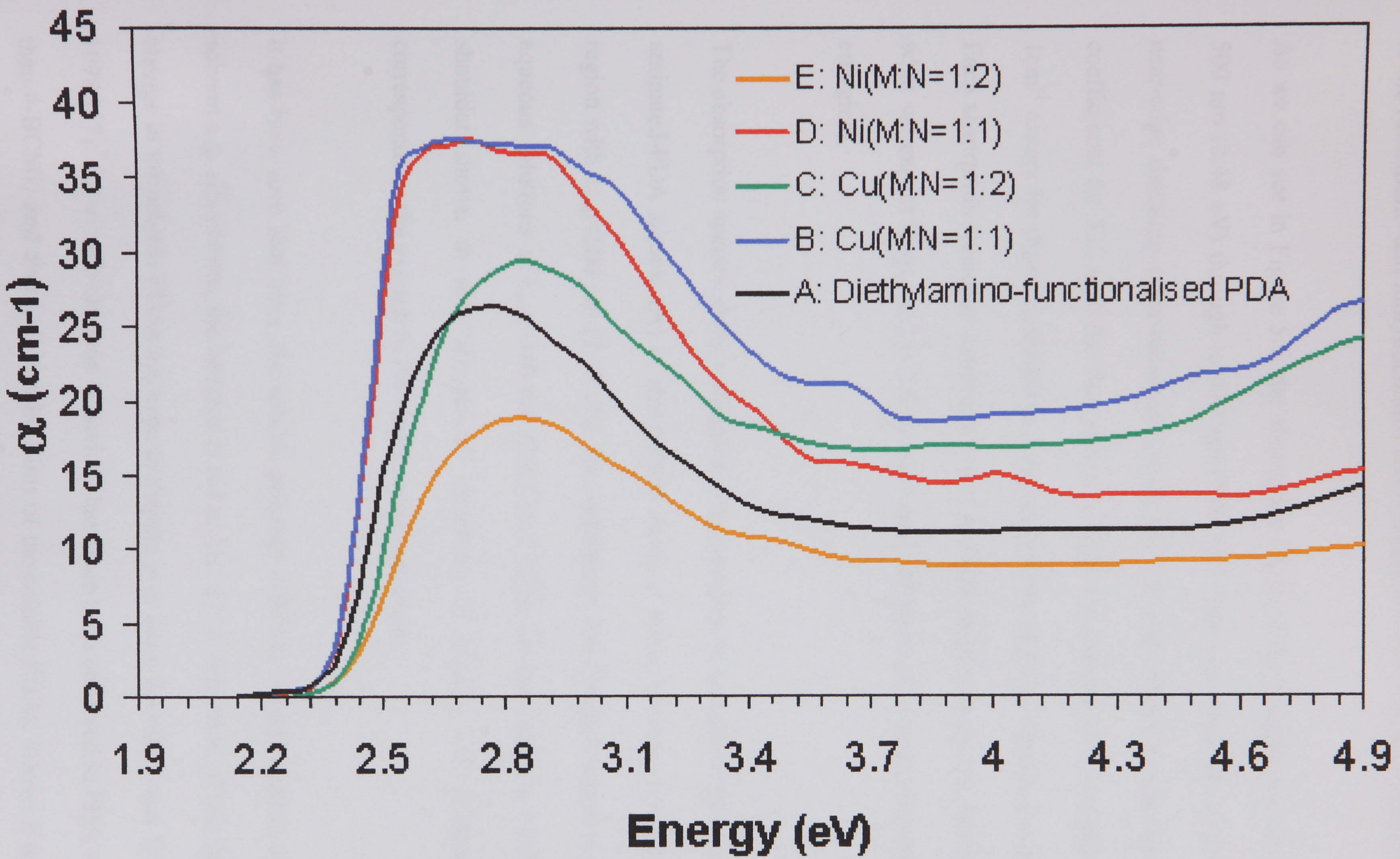

Figure 5.1: Absorption spectra of the diethylamino-functionalised PDA (sample *A*) and its complexes with Cu and Ni (samples *B-E*).

Figure 5.2 shows the linear absorption spectra of the samples *F* and *G*, which correspond to the ruthenium- and molybdenum-PDAs complexes with bipyridyl ligands, respectively.

As we can see in Figure 5.1, the absorption edges of the samples varied from less than 500 nm (2.48 eV) through to 530 nm (2.34 eV). We were therefore probing a range of near-edge detuning (near-resonance) with the 532 nm radiation. The linear absorption coefficients (at 532 nm) for the typically 0.015 M concentration samples were around $1cm^{-1}$ except for those metal-PDAs complexes with bipyridyl ligands (samples *F* and *G*). Each absorption spectrum exhibits a broad and featureless absorption, however this is not what we expect from section 3.6 (a wide peak followed by a broad absorption to higher energies).

The absorption spectra show a variation in the position of maximum absorption, λ_{max}. The aminated-PDA sample (A) in chloroform shows a strong absorption band in the visible region with λ_{max}<500 nm (2.48 eV). On metallation this strong absorption is observed in aqueous solutions at λ_{max}~440 nm (2.82 eV). None of these spectra exhibit the typical shoulder shown in the "theoretical" spectrum of Figure 3.10 (Chapter 3), which corresponds to the exciton in the single crystal spectrum.

It has been seen that when the soluble polymer 4-BCMU is dissolved in a good organic solvent e.g. chloroform, the solution is red or blue [16]. The cause of this dramatic colour change in the soluble PDAs has been in dispute ever since the effect was first observed in 1978 [17]; the solvato-chromic behaviour has since been observed in PDA solutions other than 4-BCMU and also in thin solid films of the soluble PDAs. Whilst it is clear that the changes are a direct manifestation of the amount of disorder in the polymer, the precise nature of the polymer conformation is disputed.

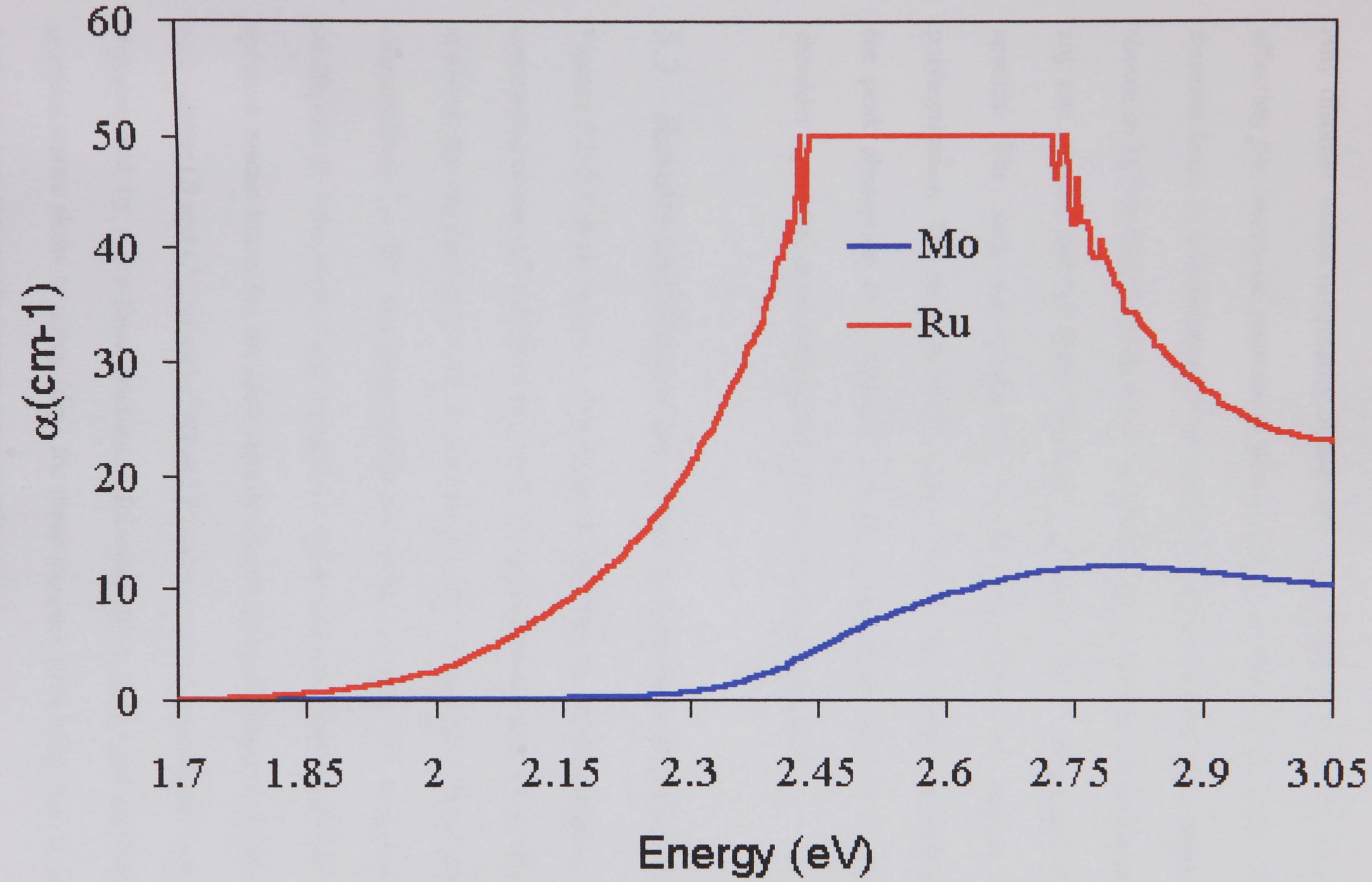

Figure 5.2: Absorption spectra of the bypiridyl-Ru and -Mo complexes (samples *F* and *G*). The flat section of the top spectrum is caused by the spectrometer saturation.

The explanation that currently carries favour is that the disorder results from distortion imposed on the polymer backbone by side-groups and possibly inter-chain interactions [18].

Any disorder would necessarily disrupt the π-conjugation along the main chain thereby affecting the electronic resonances and optical absorption of the chain. The presence of disorder leads to a broadening of the exciton lineshape as well as a spectral shift. It was shown in TCDA films [19] that it is possible to have a mixture of polymerised species in any one sample, and the linear absorption spectrum can be interpreted in terms of three species. The long wavelength tail could be polymer in regions of incomplete polymerisation. The shoulder could correspond to intermediate polymerised species and the peak absorption to a disordered, fully polymerised form. It seems then that the shoulder represents the lowest-lying excitonic transition, λ_{ex} [20].

5.3 Results and discussion of the z-scan measurements

Figures 5.3-5.7 show typical z-scan experimental data for all the samples. The solid lines correspond to the theoretical fits made to the experimental data. These fits were made by applying the method described in section 4.5, and assuming a third-order nonlinearity characterised by the nonlinear refractive index n_2 and the two-photon absorption coefficient β. Values of β and n_2 used for these fits are listed in Table 5.1. The closed aperture z-scan traces for the diethylamino-functionalised polymer (*A*) and its complexes with copper (*B* and *C*) and nickel (*D* and *E*) show a negative nonlinear refractive index n_2, characterised by a pre-focal maximum followed by a post-focal minimum. The open-aperture traces show a valley (dip) for these samples indicating that at this wavelength (532 nm), a nonlinear absorption process takes place.

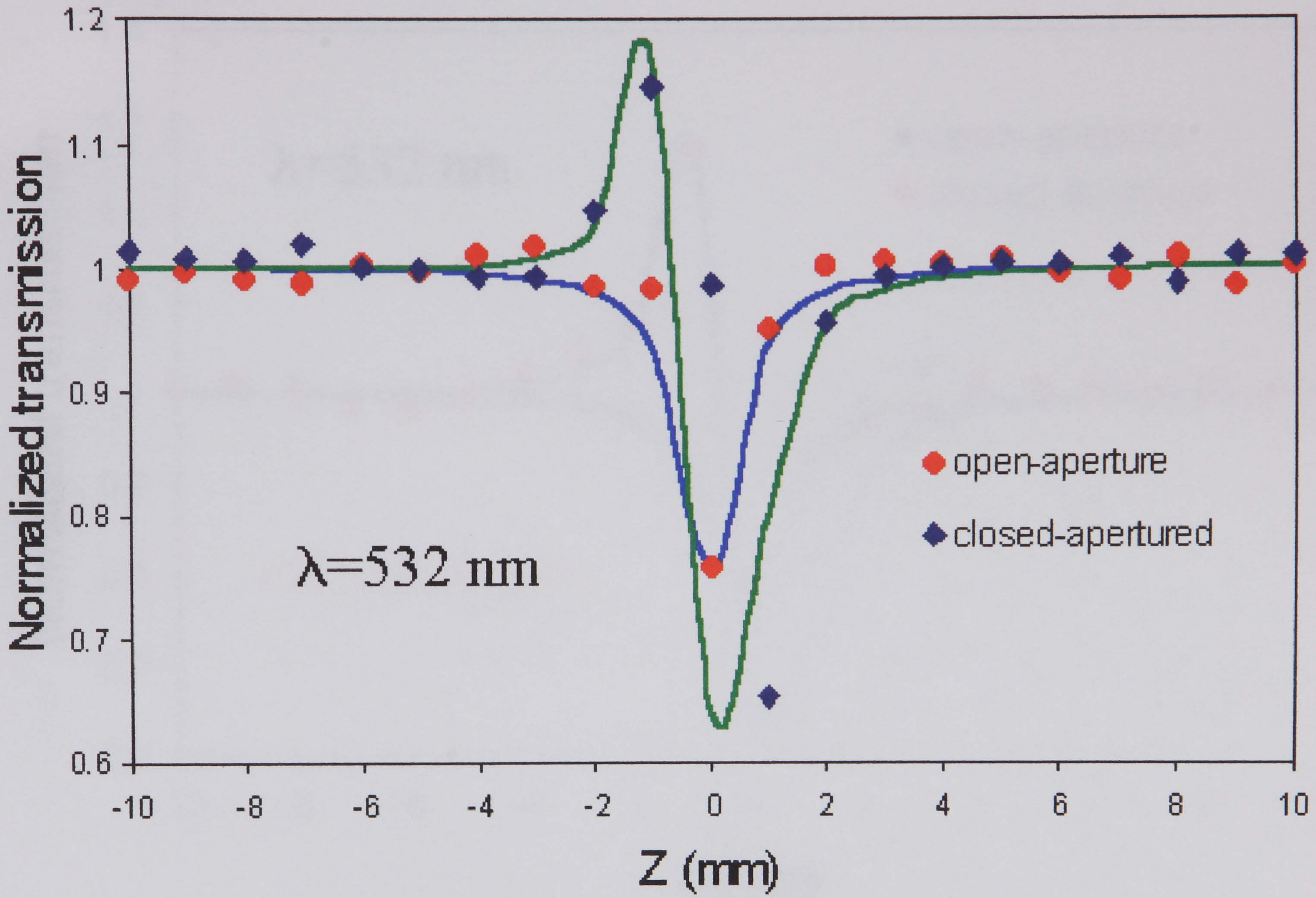

Figure 5.3: Z-scan results at 532 nm for sample *A* (diethylamino-functionalised). Solid lines represent the fits made to the data.

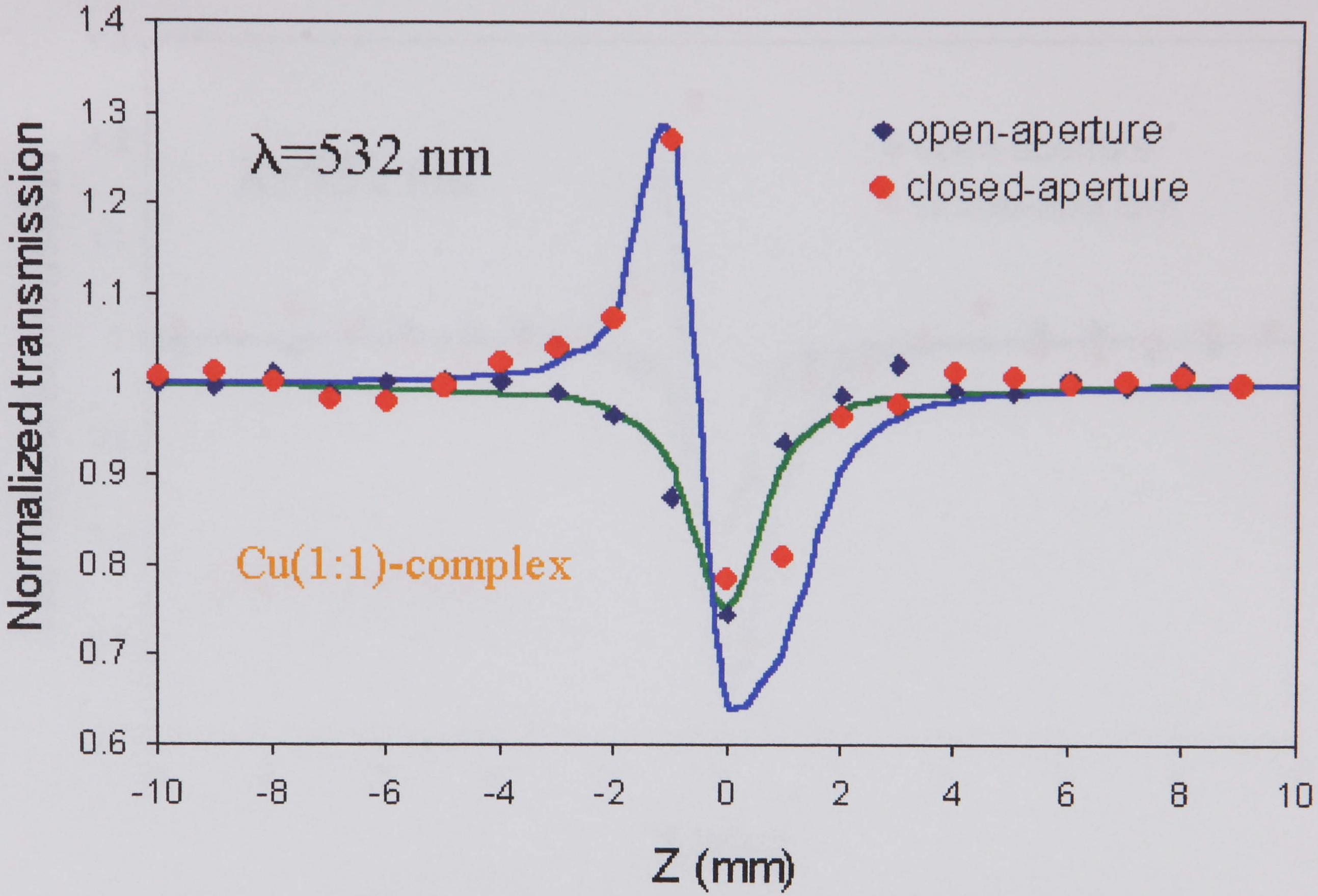

Figure 5.4: Z-scan results at 532 nm for sample *B* (Cu[1:1]-complex). Solid lines represent the fits made to the data.

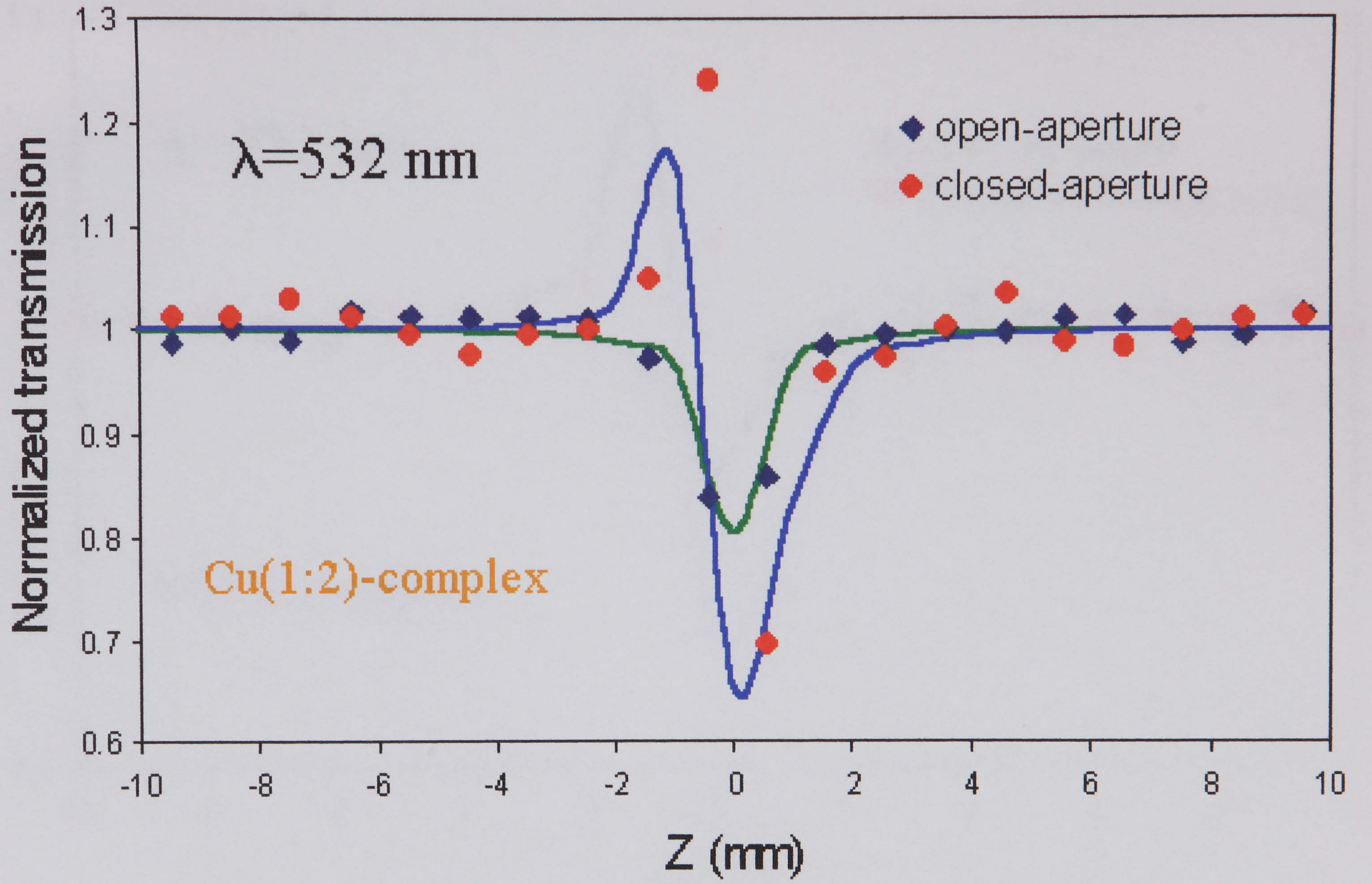

Figure 5.5: Z-scan results at 532 nm for sample *C* (Cu[1:2]-complex). Solid lines represent the fits made to the data.

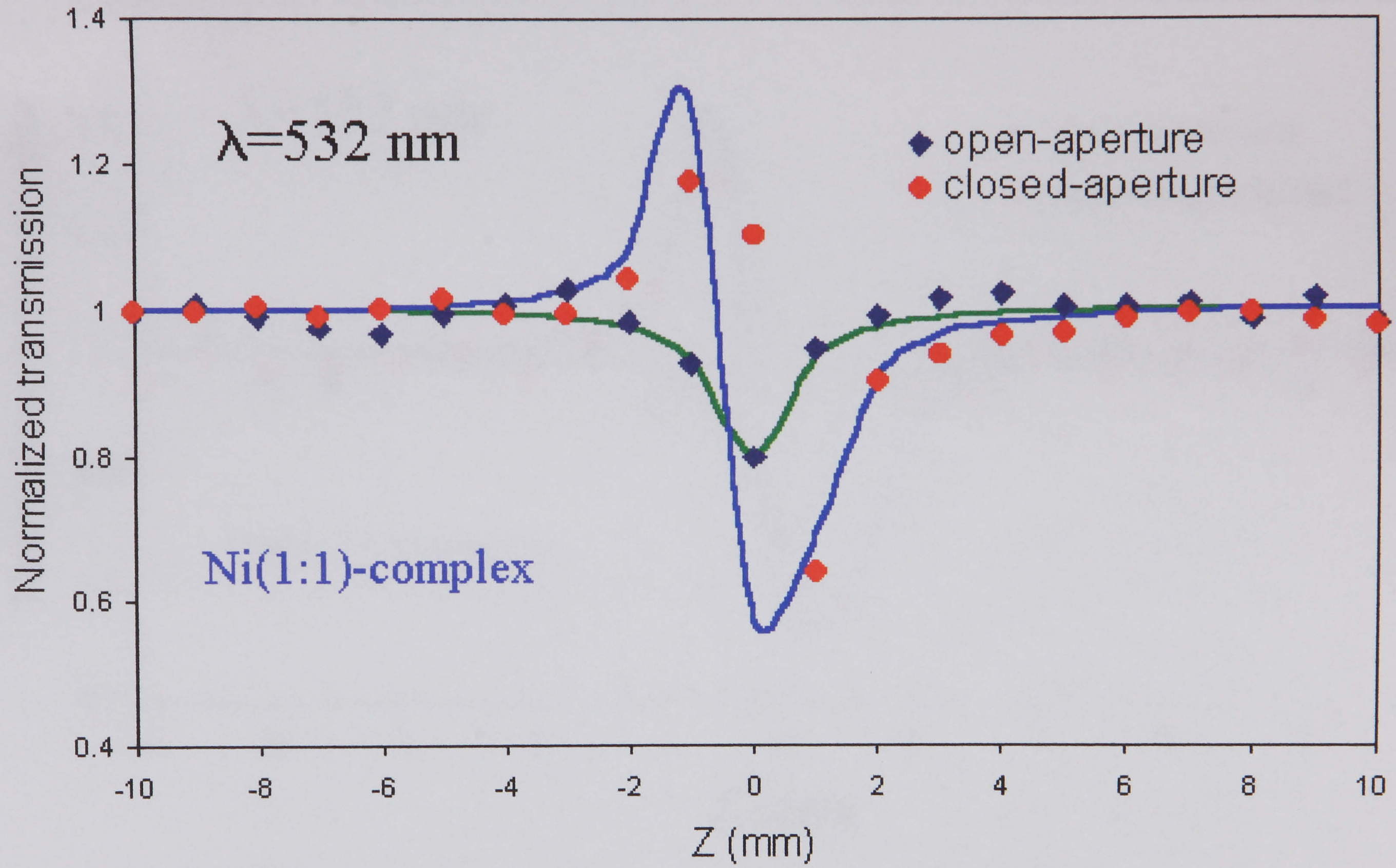

Figure 5.6: Z-scan results at 532 nm for sample *D* (Ni[1:1]-complex). Solid lines represent the fits made to the data.

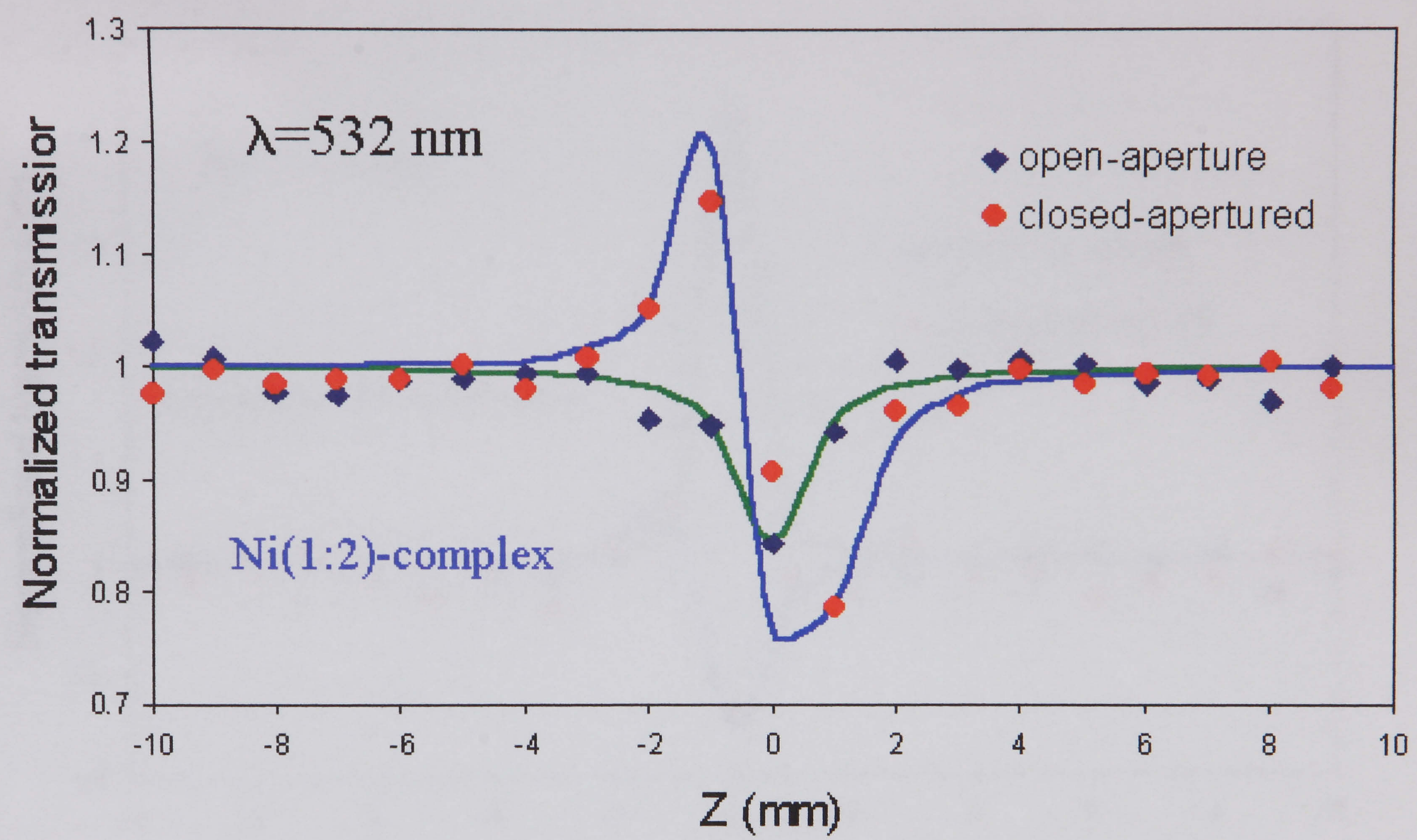

Figure 5.7: Z-scan results at 532 nm for sample *E* (Ni[1:2]-complex).
Solid lines represent the fits made to the data.

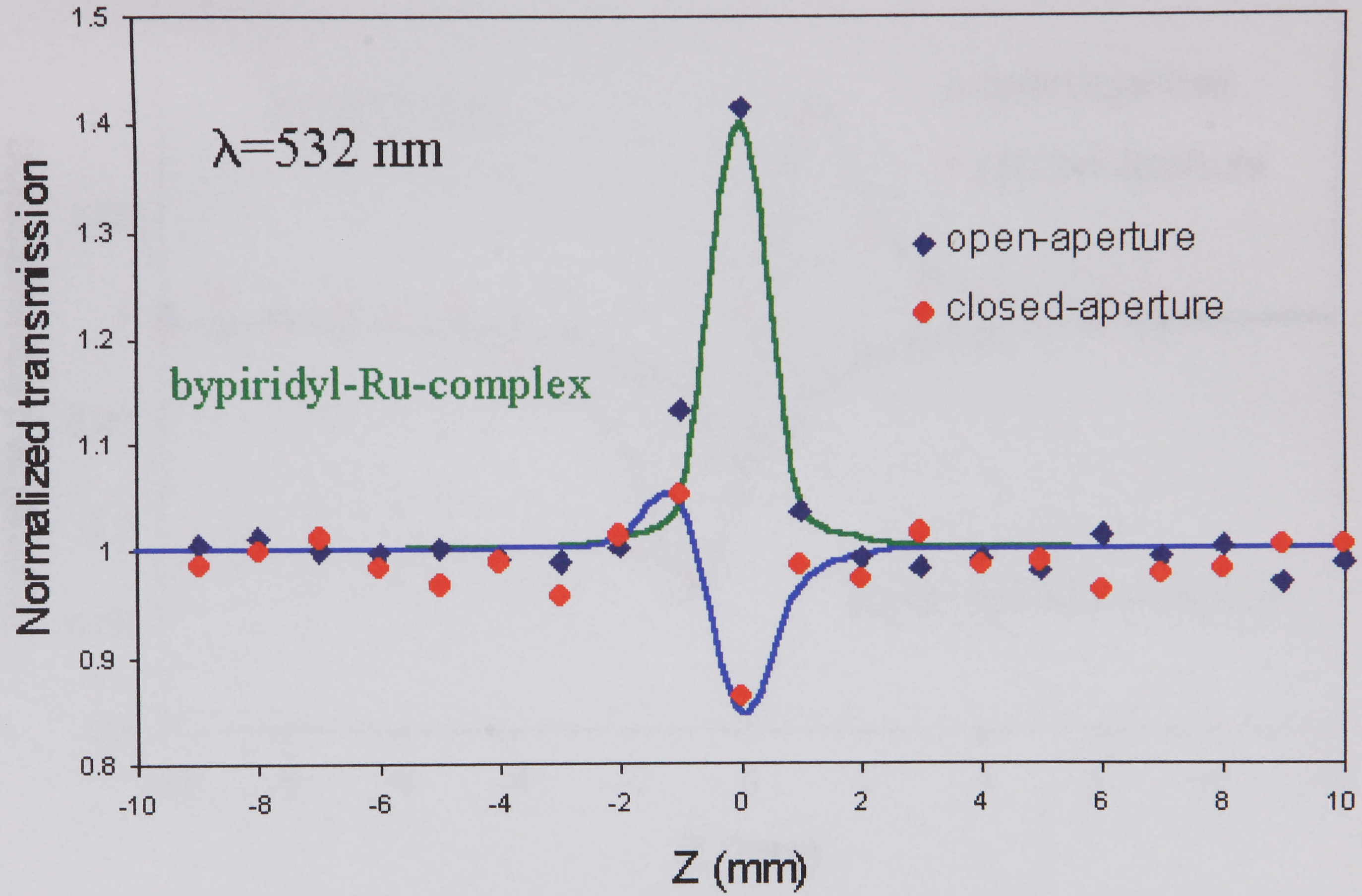

Figure 5.8: Z-scan results at 532 nm for sample *F* (bypiridyl-Ru complex). Solid lines represent the fits made to the data.

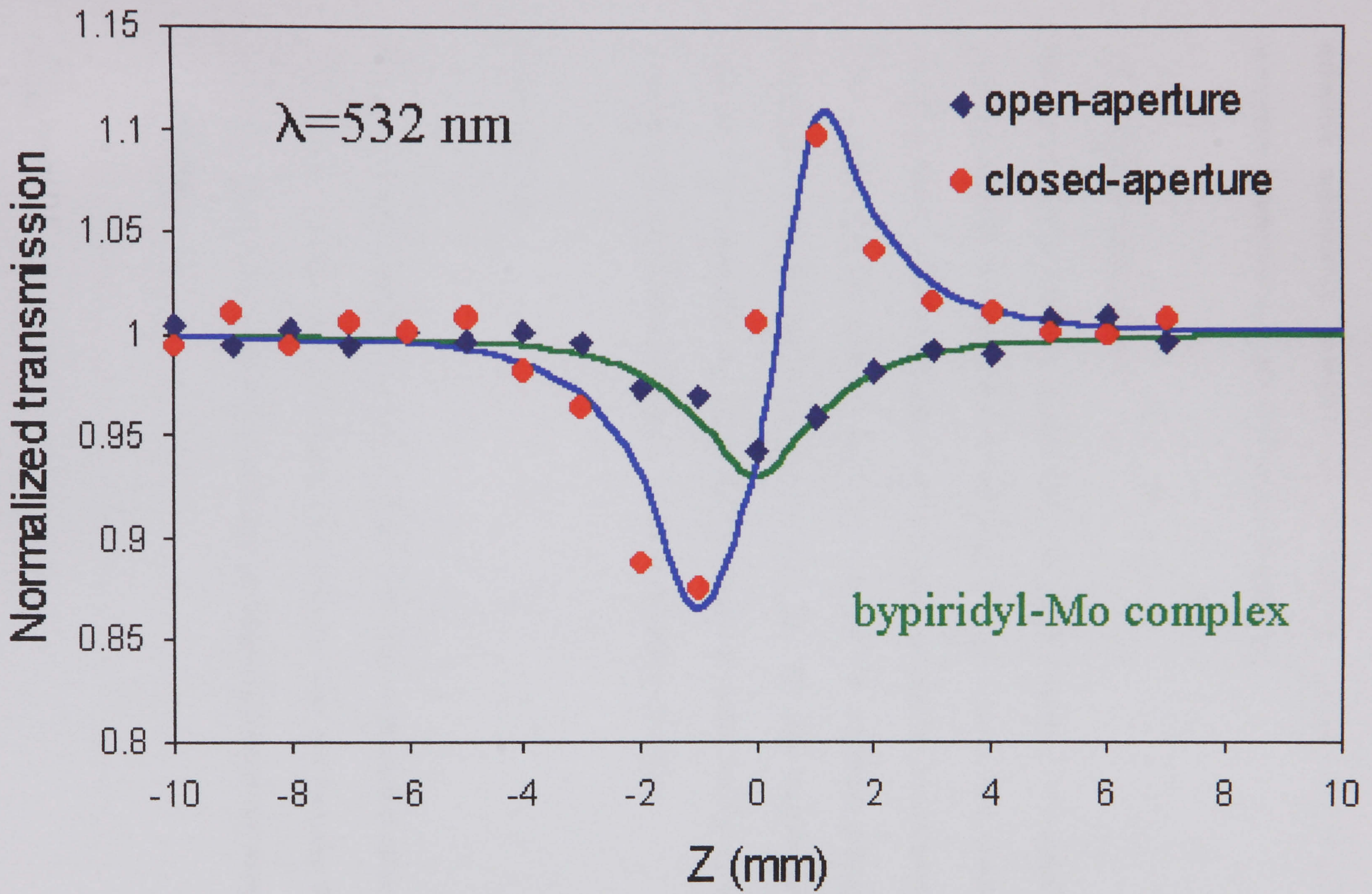

Figure 5.9: Z-scan results at 532 nm for sample *G* (bypiridyl-Mo complex). Solid lines represent the fits made to the data.

For the PDA functionalised with bipyridyl-Ru complex (sample *F*), for which the excitation wavelength is on or close to the absorption peak, saturated absorption dominates, as was seen in solid PDA films [21], this saturation leads to a negative refractive nonlinearity. However, its Mo-complex (sample *G*) shows an induced absorption feature and a positive refractive nonlinearity.

5.3.1 Induced absorption

Induced absorption typically occurs when the photon energy is too small to produce a transition directly but when the lowest-lying excited state can be reached by a two-photon-absorption (TPA) process. Another important process (excited-state absorption) often occurs when the photon energy is larger than the resonance energy, and further absorption to higher-lying states becomes possible. We can describe generic induced absorption by considering the irradiance-dependent absorption coefficient $\alpha(I)$, which for the case of TPA is written in terms of the TPA coefficient β [22] as

$$\alpha(I) = \alpha_0 + \beta I \tag{5.1}$$

Where α_0 is the linear absorption coefficient. The TPA coefficient is related to $\mathrm{Im}\chi^{(3)}$ by $\mathrm{Im}\chi^{(3)} = \lambda\varepsilon_0 n_0^2 c\beta/4\pi$, where S.I. units are employed. One can then use this irradiance-dependent absorption coefficient to calculate propagation through the sample the sample by integrating

$$dI/dz' = -\alpha(I)I \tag{5.2}$$

Over the sample thickness L, integration of equation 5.2 by use of equation 5.1 is straightforward and results in the well-known expression for the transmittance T for TPA:

$$T = \frac{\exp(-\alpha_0 L)}{1 + \beta I_0 L_{eff}} \tag{5.3}$$

with $L_{\text{eff}} = [1\text{-}\exp(\alpha_o L)]/\ \alpha_o$. The open aperture z-scan is fitted from equation 5.3 with the dependence of the input irradiance I_o of the Gaussian beam considered as a function of the sample position z.

If the input irradiance is sufficiently high, a significant population can be generated in the excited state, from where the absorption into higher-lying states is possible. In such a case equation 5.1 needs to be modified to account for this one- or two-photon-generated excited-state absorption through a fluence-dependent term coupled to the appropriate population evolution equation.

5.3.2 Saturable absorption

Saturable absorption usually results from the decrease in absorption produced by direct excitation of an electronic transition, whereas induced absorption can be the result of any of several physical processes, such as two-photon excitation or an electronic transition, excited-state absorption, and free-carrier absorption. Induced absorption is also known as reverse saturable absorption RSA [23]. In both cases the presence of nonlinear absorption will distort the closed-aperture trace, and its effects need to be taken into account.

The simplest model for saturable absorption consists of a two-level system that is resonantly excited by the laser field. In this case the open-aperture z-scan results can be

modelled under the assumption that the nonlinear absorption coefficient $\alpha(I)$ for such a two-level system has the form [22]

$$\alpha(I) = \frac{\alpha_0}{1 + I/I_s} \tag{5.4}$$

Where I_s is the saturation irradiance. Again, to calculate the transmittance of the sample we insert the model absorption equation 5.4 into the irradiance propagation equation 5.2.

The result is now an implicit equation for the exit irradiance [22]:

$$\ln\frac{I(L)}{I_0} = -\alpha_0 L - \frac{I(L) - I_0}{I_s} \tag{5.5}$$

The transmittance of the sample is calculated by solution of equation 5.5 numerically for $I(L)$.

A saturable nonlinearity is not strictly a third-order nonlinear process; in fact, it can be seen as containing contributions to many orders:

$$\alpha(I) = \frac{\alpha_0}{1 + I/I_s} \approx \alpha_0\left[1 - \frac{I}{I_s} + \left(\frac{I}{I_s}\right)^2 - \left(\frac{I}{I_s}\right)^3 + \cdots\right] \tag{5.6}$$

However, for low excitation irradiances one can calculate an effective negative $\mathrm{Im}\chi^{(3)}$ by considering the $I/I_s \ll 1$ limit to equation 5.4, $\alpha(I) \approx \alpha_o - (\alpha_o/I_s)I$, and by comparison with

equation 5.1, $\beta > -\alpha_o/I_s$; therefore an effective $\mathrm{Im}\chi^{(3)}$ can be calculated; $\mathrm{Im}\chi^{(3)} = -\lambda\varepsilon_0 n_o^2 c\alpha_o/4\pi I_s$.

5.3.3 Nonlinear refraction

In all cases, the refractive part of the nonlinearity was assumed to be a purely third-order process, characterized by the irradiance-dependent refractive index coefficient $n(I)$, given by [23]

$$n(I) = n_0 + n_2(I) \tag{5.7}$$

where n_2 is the usual nonlinear refractive index ($\mathrm{Re}\chi^{(3)} = \varepsilon_o n_o^2 c n_2$). Although for saturable absorption equation 5.7 is not exact, it is nevertheless a good approximation for low irradiances.

The nonlinear phase propagation through the sample, $\Delta\phi_{NL}$, is calculated from

$$\frac{d\Delta\phi_{NL}}{dz'} = \frac{2\pi}{\lambda} n_2 I(z') \tag{5.8}$$

Because the irradiance is a function of the position inside the sample, z', an adequate function has to be used in each case, i.e., equation 5.3 (evaluated at z' instead of at L) for induced absorption or equation 5.5 for saturable absorption. As was mention above, in the case of induced absorption, excited-state absorption can contribute an extra fluence-dependent term, which can also introduce a refractive component, as has been discussed for semiconductors [24]. As was described in detail in section 4.5 (Chapter 4), one uses the Huygens-Fresnel formalism to propagate the resultant field from the sample exit face

to the detector plane and performs an integration over the aperture radius to calculate the closed-aperture z-scan transmittance.

The solid lines shown in figures 5.3-5.9 correspond to the fits to the data through the procedure described in this section. Table 5.1 contains the nonlinear parameters (nonlinear absorption coefficient β and nonlinear refractive index n_2 values) extracted from the fits to the experimental data. From the results listed in Table 5.1, we can see that the induced absorption (β) and the nonlinear refractive index (n_2) are essentially constants.

Table 5.1: Two-photon absorption and nonlinear refraction coefficient of metal-complexed PDA's.

Sample	α_0 (cm^{-1})	**Concentration** Molar (M)	β (cm/GW)	n_2 (x 10^{-14} cm^2W^{-1})
E	0.7	0.0148	1.1 ± 10%	-5.0 ± 10%
C	0.8	0.0105	1.2 ± 10%	-5.3 ± 10%
G	1.1	0.0069	0.47 ± 10%	2.8 ± 10%
D	1.8	0.0165	1.6 ± 10%	-8.0 ± 10%
A	2	0.0158	1.7 ± 10%	-6.2 ± 10%
B	2.3	0.0192	1.8 ± 10%	-6.3 ± 10%
F	25.8	0.0125	-6.5 ± 10%	-5.9 ± 10%

Studies on metal (Cu, Ni, Co, Pb, and Pt) tetrakis(cumylphenoxy)phthalocyanines conducted at 1.064 μm (far from the main absorption band) [3] [25], have given evidence that metal substitution can significantly enhance the third-order susceptibility of these phthalocyanines. The largest nonlinearity was found in the Co ($\chi^{(3)} = 8 \times 10^{-11}$ esu), Ni ($\chi^{(3)} = 6 \times 10^{-11}$ esu), and Pt ($\chi^{(3)} = 2 \times 10^{-10}$ esu) complexes. The nonlinear susceptibility $\chi^{(3)}$ of the Pt phthalocyanine was about a factor of 10 larger that that of the Pb ($\chi^{(3)} = 2 \times 10^{-11}$ esu) phthalocyanine and a factor of 45 larger than the metal free compound ($\chi^{(3)} = 4$

x 10^{-12} esu). This enhancement of $\chi^{(3)}$ in these phthalocyanines has been attributed to the contributions of the new electronic states introduced by metal substitution.

We have not observed this kind of enhancement in our metal-complexed PDAs, however the values for the nonlinear susceptibility $\chi^{(3)}$ in the Cu and Ni complexes (PDAs) at 532 nm are of the same order of those Co and Ni phthalocyanines at 1.064 μm.

Table 5.2, presents the metal:nitrogen ratio dependence of the nonlinear susceptibility $\chi^{(3)}$ (normalised by the corresponding sample concentration). From the values of $\chi^{(3)}$ listed there we observe that in the Cu complex, the [1:2] ratio gives the largest value of $\chi^{(3)}$. However in the Ni complex, the [1:1] ratio gives the largest value of $\chi^{(3)}$. That is, the metal:nitrogen ratio seems to behave in different way for these Cu and Ni complexes. This metal:nitrogen ratio may be the responsible for this sligh variation in the value of the nonlinear susceptibility, but this requires further clarification.

Table 5.2: Metal:nitrogen dependent third-order nonlinear susceptibility of metal-complexed PDA's.

Sample	**Metal**	**Metal:nitrogen ratio**	$\lvert\chi^{(3)}\rvert$**/Conc.** (x 10^{-11} esu/M)
A	Metal free		74 ± 10%
B	Cu	[1:1]	62 ± 10%
C		[1:2]	96 ± 10%
D	Ni	[1:1]	92 ± 10%
E		[1:2]	64 ± 10%
F	Ru	[1:1]	90 ± 10%
G	Mo	[1:1]	77 ± 10%

5.4 Figures of merit (FOM)

There are a number of criteria to be met before a material is suitable for optical switching applications, depending on the specific application in mind. There are two types of all-optical switching geometries which will be considered, the nonlinear Fabry-Perot cavity and the nonlinear directional coupler [26]. Here only the first type will be treated and its figures of merit W, and T, are determined.

For switching to occur, it must be possible for a sufficient nonlinear phase change to be induced in an incident beam. It is of course possible to extend the optical path through the material to take advantage of a small index change, however the maximum practical optical path length will be limited by absorption. The figure of merit that characterises a material's potential switching capability W is expressed as the ratio of the induced phase change per unit length ($\Delta n/\lambda$) to the material's linear absorption, and is given by

$$W = \frac{\Delta n_{\max}}{\lambda \alpha_0} \tag{5.9}$$

Where Δn_{max} is the maximum possible induced index change and α_0 is the material's linear absorption coefficient. As mentioned in [26], nonlinear Fabry-Perot devices require $W > \sqrt{3}/2\pi$ [26]. In general $\Delta n_{max}=n_2 I_{max}$ where I_{max} is the maximum irradiance employable without damaging the sample.

The effect of two-photon absorption in preventing switching will depend on the relative strength of the irradiance-dependent refractive index n_2, and the two-photon absorption coefficient β, which is also an irradiance-dependent term. A figure of merit T is defined as;

$$T = \frac{\beta\lambda}{|n_2|} \tag{5.10}$$

which represents the absorption increase per unit of induce phase change. The higher this value the more likely it is that TPA will prevent switching. Fabry-Perot devices require $T < 2\pi/\sqrt{3}$ and T<0.5 for a nonlinear directional-coupler.

It should be noted that it is normally one or other of these figures of merit that prevents switching. In the resonant regime the linear absorption coefficient is large, limiting W, but the absorptive nonlinearity is often dominated by a bleaching effect and hence T is not relevant. Off-resonant, in the transparency regime, linear absorption is low resulting in large values of W. However it is in this regime that two-photon absorption is often dominant. If these figures of merit are met, then optical switching will be possible.

Table 5.3: Figures of merit (FOM) T and W.

Sample	T	W
A	1.5	3
B	1.5	2.6
C	1.2	6.4
D	1.1	3.8
E	1.2	6.2
F	---	0.08
G	0.9	2.4

The T-criteria are not relevant for cases of saturating absorption (bleaching). Table 5.3 shows the values of W and T for the PDA's solutions; a value of I_{max}=5 GWcm^{-2} was used in the evaluation of W. The values of W meet the criterion W >1, except for sample F, for which the high linear absorption prevents switching, and indeed for which heating

occurred at peak irradiances exceeding 2 $GWcm^{-2}$. The T values are sufficient for Fabry-Perot switching, but not for directional-coupler application. Figures of merit W and T for other materials have been reported, for example values of W=17 (at 595 nm) for C_{10}, W=1.7, T=0.14 (at 642 nm) and W=160, T=13 (at 1064 nm) for poly-9BCMU; and T=0.64 (at 690 nm) for pTS have been reported [27]. The figures of merit for C_{10} show it to be a suitable material for all-optical switching. It is a material with a low linear absorption and negligible nonlinear absorption at the tested wavelength (595 nm). Although 9BCMU has been shown to be a material suitable for all-optical switching, it has yet to be realised into a practical device. The figures of merit W and T of the metal-complexed PDAs studied in this chapter compare favourably with these materials.

5.5 The time response

Z-scan experiments do not provide information about the dynamic response of the observed nonlinearity. For many polydiacetylenes, the excited state lifetime is in the range between 1 and 10 ps [28]. However, depending on the input irradiance, a finite proportion of the ground-state population will be promoted by either linear or nonlinear absorption, to an excited state, from which it will decay to the ground state at a rate given by the inverse of the excited state lifetime τ. Absorption from the population in the excited state to higher lying levels (excited-state absorption) will contribute to the nonlinearity and become the limiting factor in the response time of the sample.

Conclusions

We have studied the third-order nonlinear optical coefficients of a set of metal-complexed PDA's using picosecond pulses at 532 nm (near-resonance). These polydiacetylenes have been shown to have large nonlinearities, where the linear absorption is very low. No enhancement has been observed in the nonlinear susceptibility of the metal-complexed

PDAs, with respect to that measured in the metal free sample. However, a metal:nitrogen ratio dependence of the nonlinear susceptibility of the copper and nickel complexes has been observed. The measured values for the nonlinear susceptibility $\chi^{(3)}$ range from 0.53 to 1.52 x 10^{-11} esu. These values were of the same order of those measured in metal-complexed tetrakis(cumylphenoxy)phthalocyanines.

Also, their figures of merit T and W have been evaluated and their corresponding values have been given. The combination of a large nonlinear refractive index and very low absorption coefficient, such as those observed in these samples studied here, make them suitable candidates to be employed into the all-optical switching field. Their figures of merit confirm the latter [29].

References

[1] J R Heflin, *et. al.*, *Phys. Rev. B*, **38**, 1573, 1988.

[2] A M Schaffer and E R Davidson, *Theor. Chem.*, **30**, 9, 1973.

[3] J S Shirk *et. al.*, *Appl. Phys. Lett.*, **55**, 1287, 1989.

[4] A B Lever *et. al.*, *J. Am. Chem. Soc.*, **103**, 6800, 1981.

[5] G N Patel, R R Chance and J D Witt, *J. Polym. Sci. Polym. Lett. Ed.*, **16**, 607, 1978.

[6] G Wenz, M A Muller, M. Schmit and G. Wegner, *Macromolecules*, **17**, 837, 1984.

[7] C Plachetta, N.O. Rau and R.C. Schulz, *Mol. Cryst. Liq. Cryst.*, **96**, 141, 1983.

[8] P N Prasad and D.R. Ulrich, *Nonlinear Optical and Electroactive Polymers, Plenum Press, NY*, 1988.

[9] R Chance, *Macromolecules*, **13**, 396, 1980.

[10] M C. Gupta, *Hanbook of Photonics*, *CRC Press*, Boca Raton NY, p.p., 171, 1997.

[11] G N Patel, *et. al.*, *J. Polym. Sci., Polym. Symp.*, **71**, 247, 1984.

[12] B Tieke, *Makromol. Chem.*, **185**, 1455, 1984.

[13] G N Patel and G G Miller, *J. Macromol. Sci. Phys.*, **20**, 111, 1981.

[14] M Sheik-Bahae, A A Said, T H Wei, D J Hagan and E W Van Stryland, *IEEE J. Quantum Electron.*, **26**, 760, 1990.

[15] J Wang, M Sheik-Bahae, A A Said, D J Hagan, and E W Van Stryland, *J. Opt. Soc. Am. B*, **11**, 1009, 1994.

[16] S. Molyneux, *Third-Order Nonlinear Optical of Polydiacetylenes Studied by Sub-Picosecond Techniques*, PhD thesis, Heriot-Watt University, Edinburgh, 1995.

[17] G N Patel, *Polym. Pre. Am. Chem. Soc. Div. Polym. Chem.*, **19**, 154, 1978.

[18] D Bloor, *Synthetic Metals*, **21**, 71, 1987.

[19] B Tieke and D. Bloor, *Makromol. Chem.*, **180**, 2275, 1979.

[20] T Hattori and T Kobayashi, *Chem Phys. Lett.*, **133**, 230, 1987.

[21] S Molyneux, A K Kar, B S Wherrett, T L Axon and D Bloor, *Opt. Lett.*, **18**, 2093, 1993.

[22] R.W. Boyd, *Nonlinear Optics*, Academic Press, 1992.

[23] C Giuliano and L Hess, *J. Quant. Electron.*, **QE-3**, 358, 1967.

[24] X J Zhang, W Ji and S H Tang, *J. Opt. Soc. Am. B*, **14**, 1951, 1997.

[25] D R Prasad and G Ferraudi, *Inorg. Chem*, **21**, 2967, 1982.

[26] See for example: *Optical Bistability in Nonlinear Optics in Signal Processing*, B S Wherrett and D C Hutchings, ed. R W Eason and A Miller, *Chapman and Hall*, London, p.143, 1993.

[27] A Kar, *Polym. Adv. Technol.*, **11**, 553, 2000.

[28] S Koshihara, T Kobayashi, H Uchiku, T Kotaka and H Ohnuma, *Chem. Phys. Lett.*, **114**, 446, 1985.

[29] M A Camacho, A K Kar, W E Lindsell, C Murray, P N Preston and B S Wherrett, *J. Mater. Chem.*, **9**, 1251, 1999.

Chapter 6

Third-order optical nonlinearities of poly-DCHD microcrystals.

6.1 Introduction

The growing interest in all-optical switching and high-speed optoelectronics has promoted the search for new materials with large nonlinear optical susceptibilities and fast time response [1]. Polymers with long conjugated chains are natural candidates and their electrical and optical properties are gaining considerable interest. Such materials can be suitable for the fabrication of waveguides, couplers, switches, modulators, etc. The optical properties required for these new materials can be classified in two categories, namely: intrinsic optical properties and bulk mechanical and optical properties [2]. The first category includes a large (>10^{-9} esu) and fast (10^{-12} -10^{-15} s) nonlinear optical response, a low energy dissipation and low optical losses in the infrared; the second category includes a good and long lived chemical stability, easy processability for the fabrication of thin film and finally a remarkable mechanical strength.

Recently, Nakanishi and coworkers established a versatile and easy process to prepare aqueous dispersions of organic micro and nanoparticles by first preparing a finely divided dispersion of the target molecules in an appropriate solvent in water [3]-[6]. Densification and crystallisation may subsequently follow, leading to the specific morphology and structure of the microparticle 'single crystal' [5] [7]. As was already mentioned in Chapter 2, polymer single particles have been produced using solid-state topochemical

polymerisation in single crystalline microparticles of a diacetylene monomer (DCHD) [3]. Poly-DCHD nanocrystals have been obtained in two different sizes: 30 and 100 nm.

During studies of the third-order nonlinearity of PDA pTS (polytoluene sulphonate) [8], the absorptive part of the nonlinear susceptibility $\chi^{(3)}$ was found to change sign between measurements taken on resonance and near resonance [9]. On resonance, a bleaching effect was observed, whereas in the near-resonance regime an induced absorption effect dominated. These results implied the existence of a photon energy at which the nonlinear absorption was zero (Im $\chi^{(3)} = 0$). The results in pTS led to the development of a semiquantitative three-level model [9] that described the behaviour and predicted the photon energy at which the nonlinearity changed from induced transparency to induced absorption. Experimental verification of an Im $\chi^{(3)} = 0$ position was important to the understanding of the nonlinear processes in PDAs and has implication for optical processing.

Molyneux et. al. [10], studied the third-order nonlinear properties of the PDA called red-phase 9-BCMU, in the form of a thin-film. They analysed the spectral dependence of the third-order nonlinear susceptibility $\chi^{(3)}$ and found that the imaginary component Im $\chi^{(3)}$ (absorptive part) changed sign in the exciton absorption tail. The three-level model mentioned above, was also applied to that sample, and a crossover point (Im $\chi^{(3)} = 0$) in the region of 1.94 eV was predicted for this PDA, which had an absorption peak at 2.29 eV.

In this chapter, I present the z-scan studies made in poly-DCHD microcrystals with average particle sizes of 100 nm with the picosecond laser system described before in Chapter 2. Their third-order nonlinear optical properties near and on resonance are

studied, and the values of the nonlinear refractive and absorptive coefficients are measured at different wavelengths. Here is also presented a simple three-level model for the nonlinear response, developed by R. Rangel *et.al* [11], which contains additional consideration with respect to that used by Bolger *et. al*. in [9]. This "modified" model is used to fit the experimental data. From this model a crossover point is predicted to occur near 710 nm (1.75 eV).

6.2 Experimental details and linear properties of poly-DCHD

The z-scan technique has been well explained in detail in Chapter 2. In these experiments the sample employed was a poly-DCHD suspension loaded into a 1mm thick quartz cell. By sealing the cell, the suspension can be kept in good condition for a long time, which allows it to be used in many experiments. A spatial filtering system was used to produce a gaussian beam with typical pulse energies around 1μJ. The laser beam was focused on the sample at a spot size of 30 μm (radius).

The low repetition rate (10 Hz) of the laser ensures that no pulse-to-pulse buildup effects are present. The low pulse energies employed, as low as 1 nJ in some cases, also minimize the influence of thermal effects. A computer-controlled translation stage scans the sample position, and the detected signals are acquired and stored by the computer. Each experimental point is the average from 25 pulses, each within 10% of the nominal pulse energy.

Figure 6.1 shows the absorption spectrum of the poly-DCHD microcrystal water solution. The linear absorption spectrum of this sample exhibits a wide peak followed by a broad absorption to higher energies, as expected from section 3.6.

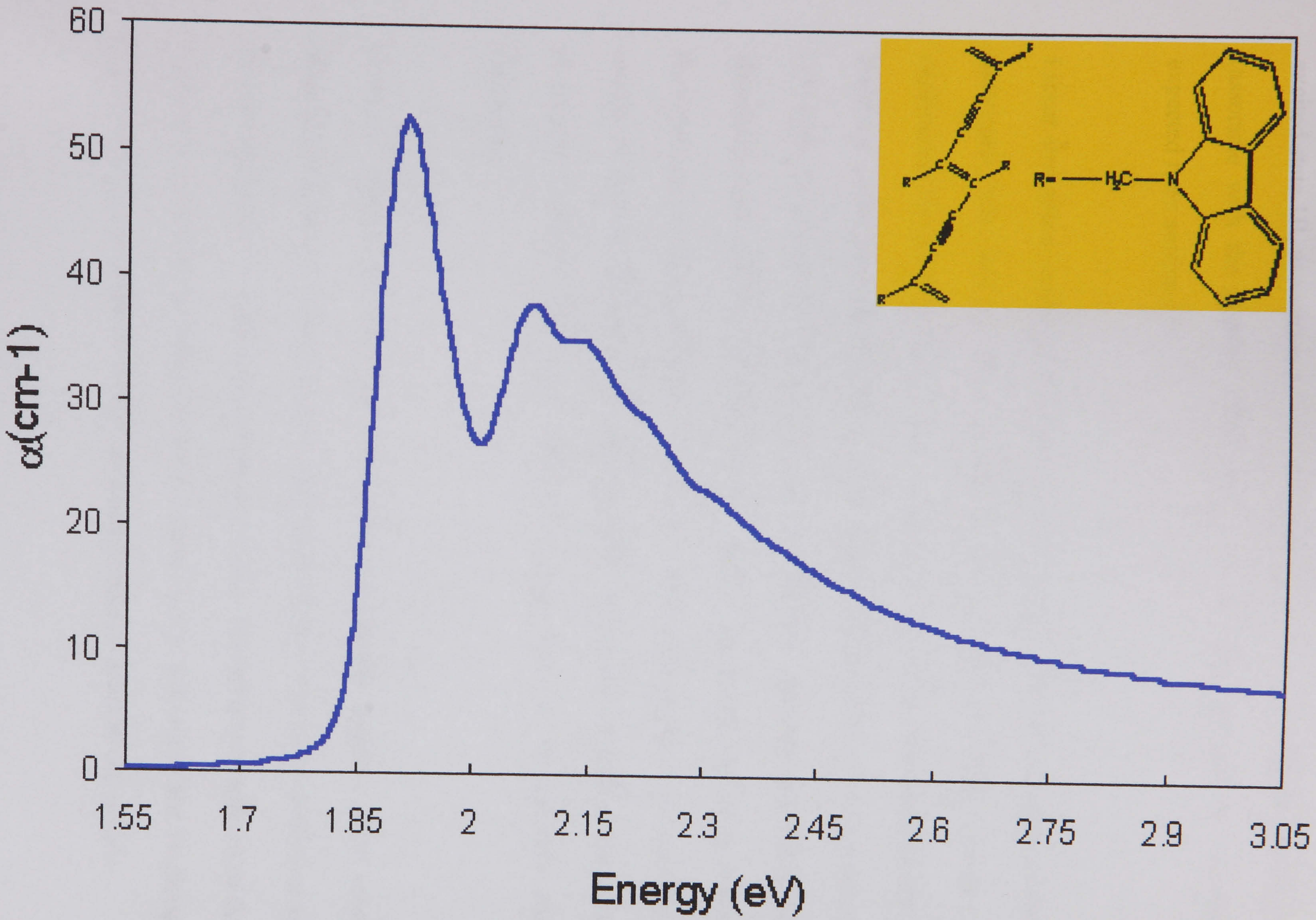

Figure 6.1: Absorption spectrum of poly-DCHD microcrystals in water suspension.

The spectrum exhibits a strong and very sharp excitonic peak (associated with the first excited state $1B_u$ exciton) at 1.9eV (650 nm) followed by a well-resolved vibronic replica (associate with the phonon side-band) at 2.1eV (580 nm) and an extended tail, as expected from section 3.6.

Linear absorption studies have shown that as the size of the microcrystals is decreased, a systematic blue-shift in the excitonic peaks is produced [12]. Another possible explanation for this behaviour is that, in the smaller crystals, deformation of the polymer backbone could occur and therefore exciton delocalisation would be decreased [13] [14] [15] [16]. D. Bloor [17] has pointed out that disorder broadens and shifts the exciton absorption band of PDAs and produces an extended tail of localised states extending into the band gap as shown in figure 3.12(b). He also explains that there are two possible origins of spectral shifts; changes in conjugation length and changes in the environment of extended chains. The latter effects are large because the polymer chains are deformable.

Figure 6.2 shows the linear refractive index n_0 for this sample. These values were obtained by Kramers-Kronig analysis [18] of the linear absorption coefficient (α_0) data from a Shimadzu UV-3100 spectrophotometer [19]. The refractive index n_0 of this water suspension is close to the refractive index of pure water; this means that by changing the host medium, it is possible to modify the linear refractive index of the sample.

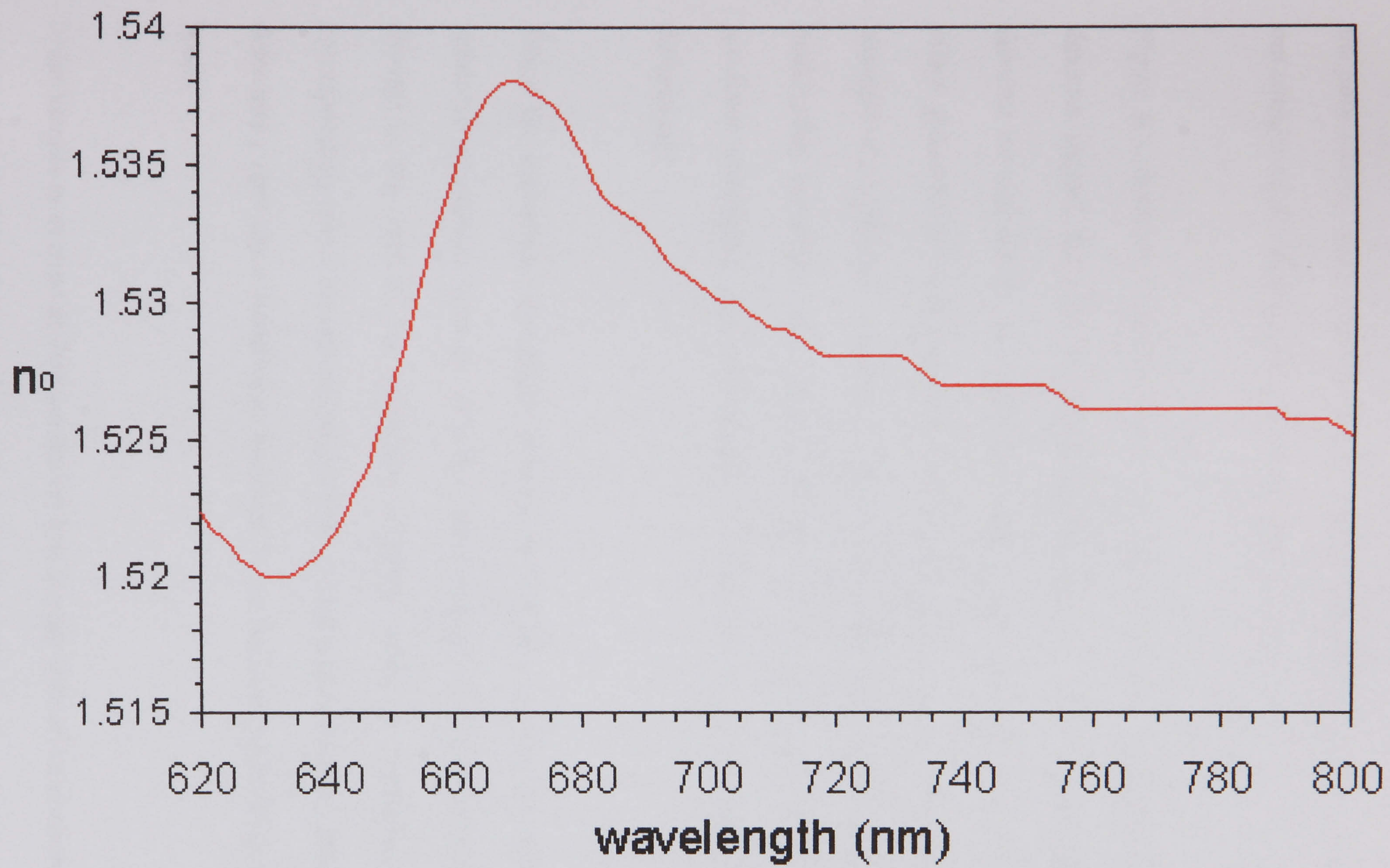

Figure 6.2: Linear refractive index n_0 of poly-DCHD, obtained by the Kramers-Kronig analysis.

6.3 Results and discussion of the z-scan measurements

In order to obtain the nonlinear absorption (β) and nonlinear refraction (n_2) coefficients of the poly-DCHD water solution, z-scan measurements at several wavelengths were carried out using a 1 mm thick quartz cell containing the sample.

Figure 6.3 shows the typical z-scan traces resulting from the open- and closed-aperture detector signals, here the pumping wavelength was tuned to 610 nm. From the open detector we can see the characteristic peak feature indicating that a saturable absorption effect (bleaching) took place, or in other words, at this wavelength the nonlinear absorption coefficient is negative. On the other hand, the closed aperture trace shows a peak-valley behaviour and, which is produced by a negative nonlinear refractive index, a pre-focal maximum (beam-focusing) is followed by a post-focal minimum (beam-defocusing).

When the excitation wavelength is tuned to 630 nm, we can see in Figure 6.4 that the saturable absorption remains, with the same strength as before (at 610 nm), however a change in the sign of the nonlinear refractive index is produced, that is, now the corresponding trace (closed-aperture) shows a valley-peak feature. This is produced by a defocusing (pre-focal minimum) followed by a focusing (post-focal maximum) of the beam.

If the sample is excited at 760 nm on the low energy side of its exciton peak (650 nm), a clear induced absorption is observed from the open-aperture trace, as it is showed in Figure 6.5. In this case the nonlinear absorption coefficient has turned positive.

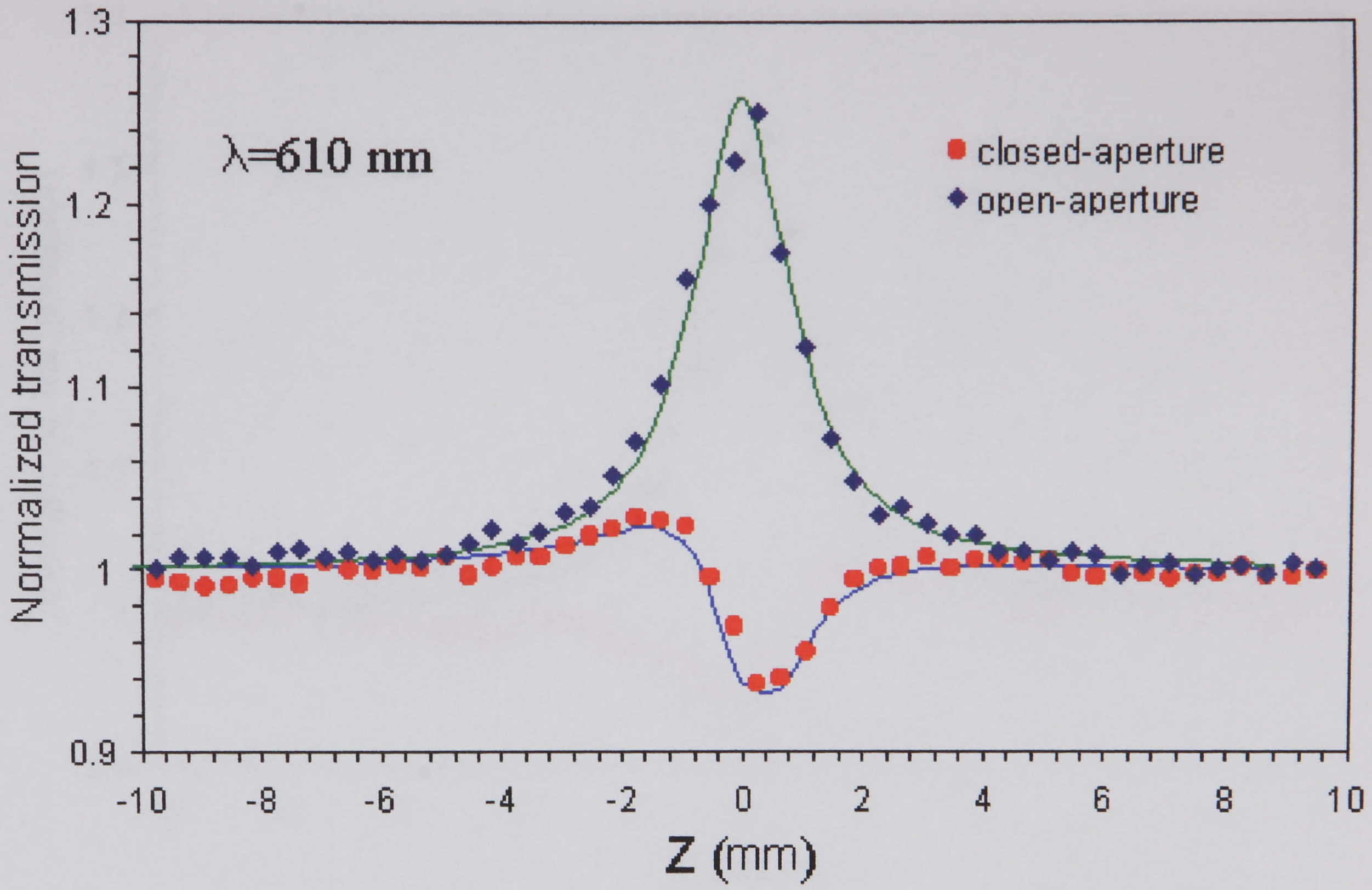

Figure 6.3: Z-scan results at 610 nm on poly-DCHD. Solid lines are the theoretical fits to the data made through the procedure described in section 5.3 (Chapter 5).

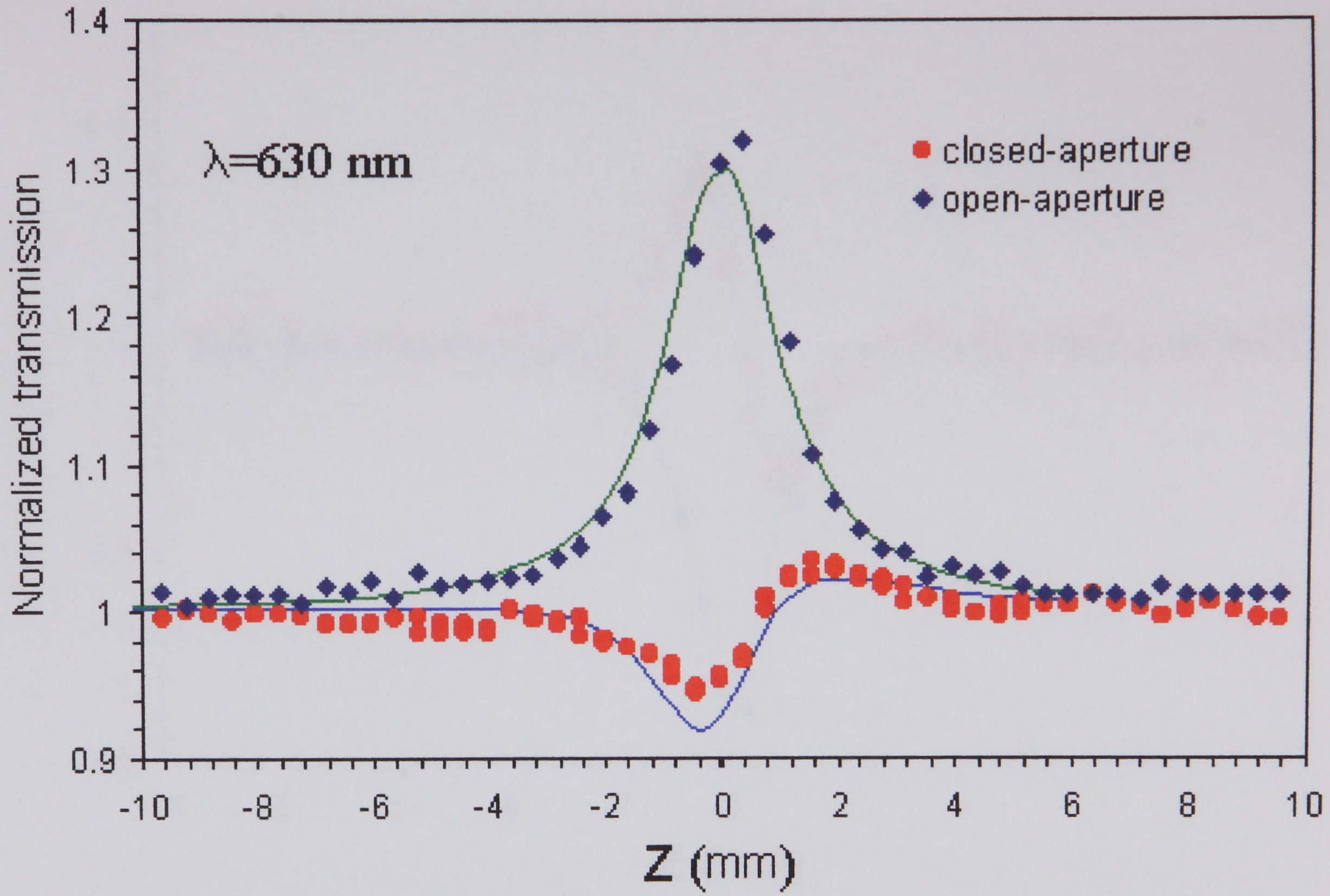

Figure 6.4: Z-scan results at 630 nm on poly-DCHD. Solid lines are the theoretical fits to the data made through the procedure described in section 5.3 (Chapter 5).

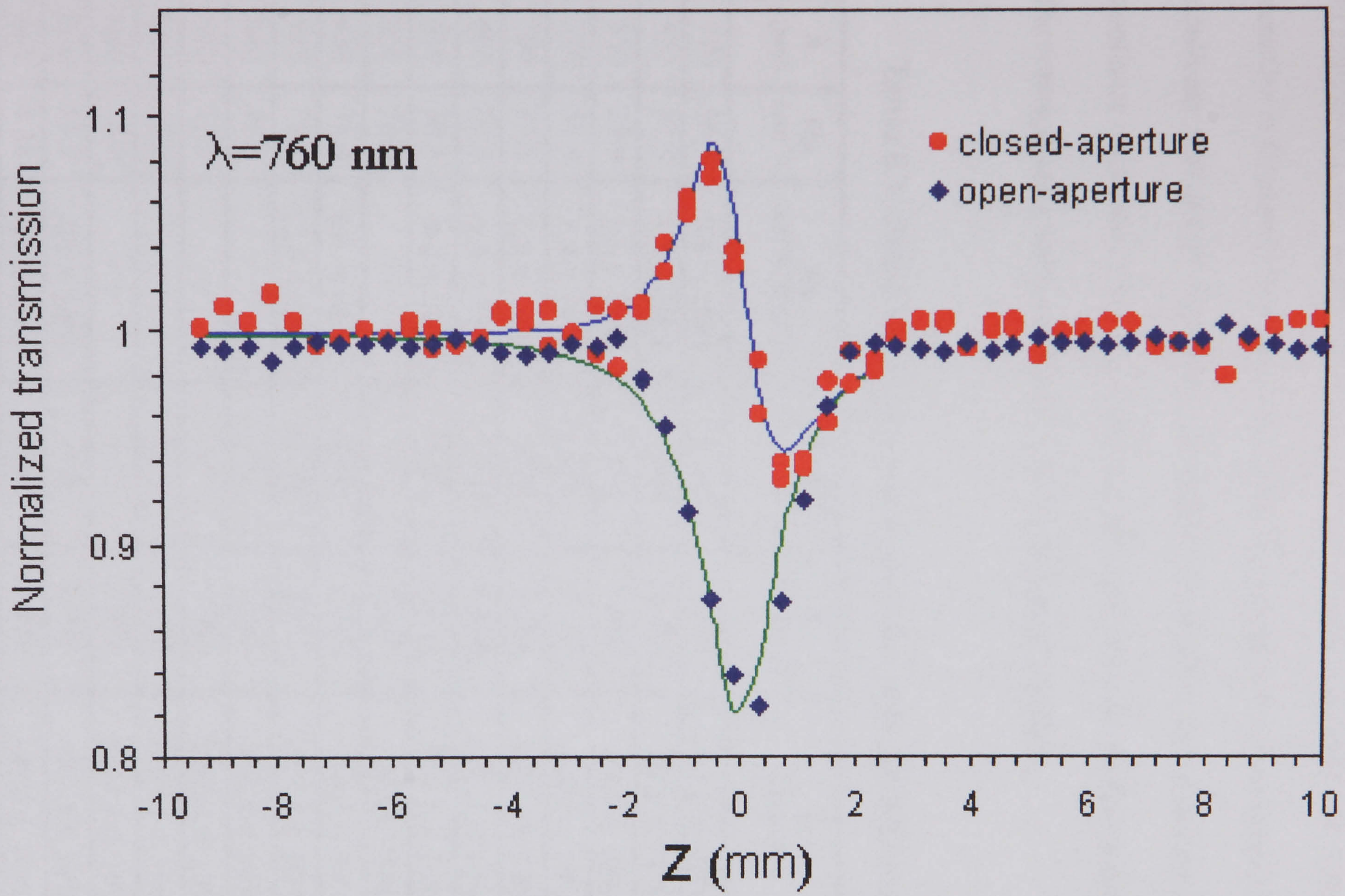

Figure 6.5: Z-scan results at 760 nm on poly-DCHD. Solid lines are the theoretical fits to the data made through the procedure described in section 5.3 (Chapter 5).

From the close-aperture trace we can see that the peak-valley feature has appeared again. Now the peak is stronger than in the first case, when the sample was excited at 610 nm. In the same way as before, the nonlinear refractive index is negative. The solid lines shown in Figures 6.3, 6.4, and 6.5 correspond to the theoretical fits made through the procedure describe in Chapter 5 (section 5.3). Table 6.1 contains the wavelength dependence of the nonlinear parameters (nonlinear absorption coefficient β, saturation irradiance I_s, and nonlinear refractive index n_2 values) extracted from the fits to the experimental data. Also the corresponding values of Im $\chi^{(3)}$ and Re $\chi^{(3)}$ are given there.

Table 6.1: Fitted nonlinear parameters for poly-DCHD microcrystals

λ (nm)	α_0 (cm^{-1})	n_2 ($cm^2/GW \times 10^{-4}$)	Re $\chi^{(3)}$ (esu $\times 10^{-11}$)	I_s (GW/cm^2)	β (cm/GW)	Im $\chi^{(3)}$ (esu $\times 10^{-11}$)
510	16.9	0.4 ± 10%	0.124	1.534	-15.1 ± 10%	-0.150
532	21.5	1.5 ± 10%	0.490	0.585	-51.8 ± 10%	-0.523
550	25.9	2.6 ± 10%	0.882	0.486	-68.9 ± 10%	-0.784
570	31.9	1.9 ± 10%	0.626	0.317	-140.7 ± 10%	-1.536
590	35.5	0.3 ± 10%	0.086	0.264	-187.3 ± 10%	-2.124
600	37.3	-2.0 ± 10%	-0.610	0.166	-337.4 ± 10%	-3.595
610	30.1	-8.5 ± 10%	-2.84	0.181	-227.2 ± 10%	-2.712
620	26.9	------	------	1.871	-19.6 ± 10%	-0.238
630	34.4	8.6 ± 10%	2.908	0.219	-213.5 ± 10%	-2.647
635	39.7	12.6 ± 10%	4.248	0.147	-334.4 ± 10%	-4.575
640	45.6	------	------	0.095	-592.5 ± 10%	-8.17
650	52.2	------	------	0.066	-1076.4 ± 10%	-13.73
655	47.9	------	------	0.055	-1195.1 ± 10%	-15.36
660	38.4	------	------	0.051	-1034.6 ± 10%	-13.4
670	15.2	-29 ± 10%	-9.8	0.046	-447.4 ± 10%	-5.882
680	4.38	-17 ± 10%	-5.56	0.076	-80.8 ± 10%	-1.046
740	0.45	-0.2 ± 10%	-0.055	------	1.3 ± 10%	0.0265
760	0.31	-0.2 ± 10%	-0.082	------	1.6 ± 10%	0.0327
800	0.19	-0.1 ± 10%	-0.046	------	1.2 ± 10%	0.0255

From the experimental results we can see that both the refractive and the absorptive contributions of the nonlinearity are dominated by the excitonic resonance. We can see also that Im $\chi^{(3)}$ is positive (induced absorption) at long wavelengths, but it changes to negative (saturable absorption) on and near resonance. This induced absorption observed at long wavelengths could be due to either, excited-state absorption or two-photon absorption (TPA) [20] [21].

A three-level model (discussed in next section) for the nonlinearity has been used to describe these effects [11]. From this model it has been shown that the absorption observed can be attributed to one-photon resonant interaction only. The same model has been used to understand the experimental dispersion of Re $\chi^{(3)}$.

Figures of merit W and T defined in Chapter 5 have been evaluated at all the wavelengths (except for those wavelengths at which the nonlinear refractive index n_2 is unknown) using the values contained Table 6.1. Table 6.2 contains the calculated values of W and T at the corresponding wavelengths.

The switching parameter W calculated at 680 nm (near to the crossover point, 710 nm) is well within the requirements for both Fabry-Perot ($W > \sqrt{3}/2\pi$) and nonlinear directional-coupler ($W > 1$) switch operation. Note that at this wavelength the absorptive nonlinearity is dominated by a bleaching (saturable absorption) and hence the parameter T is not relevant for both Fabry-Perot and nonlinear directional-coupler geometries. With minimal nonlinear absorption, such as that for longer wavelengths (beyond 680 nm), the linear absorption becomes the limiting factor.

Table 6.2: Figures of Merit W and T for poly-DCHD microcrystals.

λ (nm)	$\|\mathbf{W}\|$ $\left(W > \sqrt{3}/2\pi\right)$	$\|\mathbf{T}\|$ $\left(T < 2\pi/\sqrt{3}\right)$
510	18.80	20.73
532	35.46	18.36
550	59.50	14.57
570	33.70	42.19
590	4.13	425.11
600	20.64	101.20
610	75.47	16.40
620	------	------
630	102.84	15.63
635	115.80	16.85
640	------	------
650	------	------
655	------	------
660	------	------
670	10.22	30.58
680	2.72	9.88
740	------	17.08
760	------	14.83
800	------	20.69

In the resonant regime the absorption coefficient is large, limiting W, but the absorptive nonlinearity is often dominated by a bleaching effect and hence T is not relevant. Off-resonance, in the transparency regime, absorption is low resulting in large values of W.

6.4 Three-level model

Theoretical models of various degrees of complexity have been used to model and predict the nonlinear behaviour of PDA's. In particular, a simple three-level model was used by Bolger *et. al.* [9] to explain the dispersion of the nonlinearity of pTS (poly toluene sulphonate) for wavelengths on the low-photon-energy side of the excitonic resonance of the material. The three levels involved in the model were the ground state $1A_g$, the excitonic state $1B_u$, and a conduction-bandlike state [21]. Because of the limited spectral

range explored in those experiments, only one-photon transitions from the ground state to the excitonic state, and from the excitonic state to the conduction band, were taken into account, but the direct excitation from the ground state to the conduction band was not accounted for.

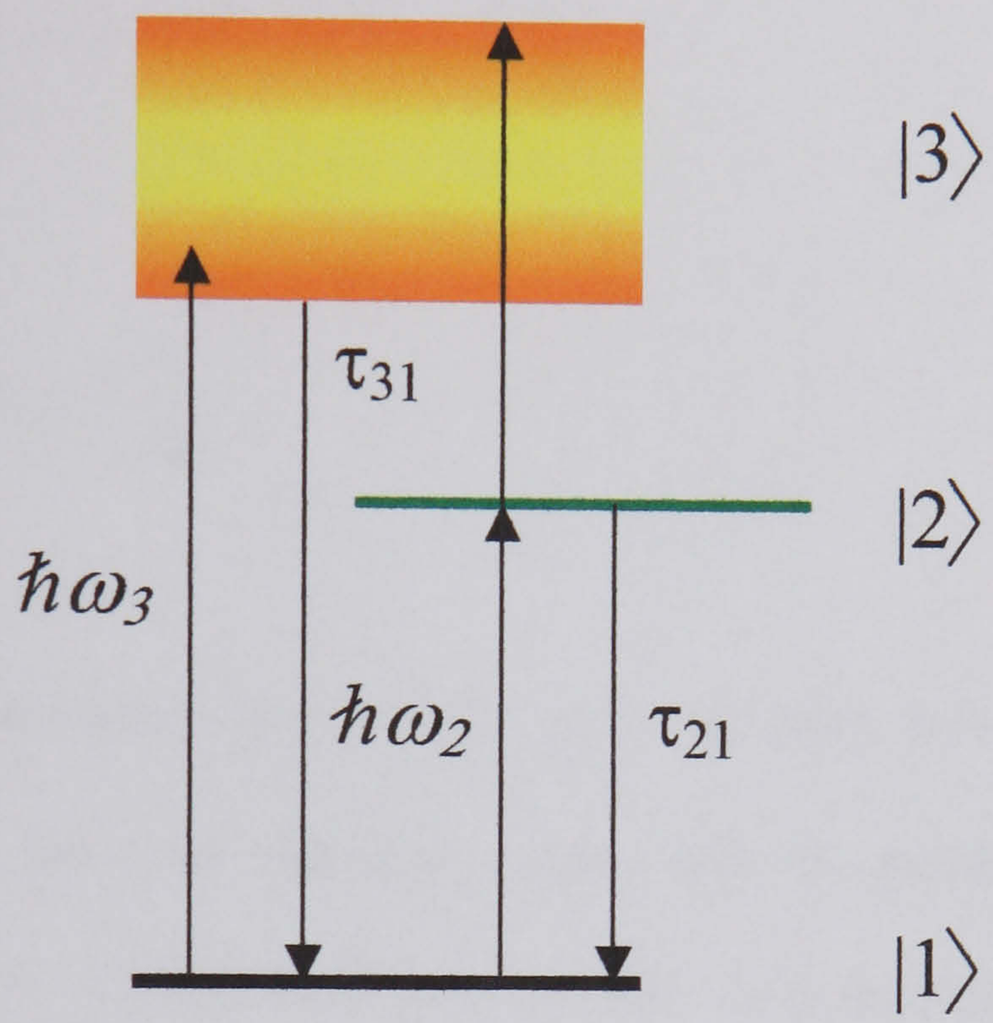

Figure 6.6: Energy-level diagram for the three-level model, showing the possible absorption and decay processes. Level $|1\rangle$ represents the ground state $1A_g$, level $|2\rangle$ the exciton state $1B_u$, and level $|3\rangle$ the conduction band.

This omission of course becomes important for photon energies above the exciton resonance energy. To consider the nonlinear response over a wider spectral range, R. Rangel *et. al* [11] developed an extension to the model described above. In their model they permit direct transitions from the ground state to the conduction band as well, as shown in Figure 6.6. Because a definite parity cannot be assigned to the conduction band, direct one-photon excitation from the ground state does occur. Linear absorption spectra and photoconduction studies confirm that direct one-photon excitation to the conduction

band is indeed allowed, with an oscillator strength comparable with that of the exciton absorption. The time evolution of the population densities N_i of states $1A_g$ (level $|1\rangle$) and $1B_u$ (level $|2\rangle$) and the conduction band (level $|3\rangle$) is given by the following set of rate equations:

$$\frac{dN_3}{dt} = (N_2 - N_3)\sigma_{23}p + (N_1 - N_3)\sigma_{13}p - \frac{N_3}{\tau_{31}} \tag{6.1}$$

$$\frac{dN_2}{dt} = (N_1 - N_2)\sigma_{12}p - \frac{N_2}{\tau_{21}} \tag{6.2}$$

Where $p=I/\hbar\omega$ is the photon flux density, σ_{ij} are the absorption cross sections for the $i \rightarrow j$ transitions, τ_{ij} are the $i \rightarrow j$ relaxation times, and the populations are subject to the constraint that $N_1+N_2+N_3=N_0$ at all times, where No is the number density. One can then use the steady-state solution ($dN_i/dt=0$) to the system of equations 6.1 and 6.2 to calculate an effective susceptibility for the system:

$$\mathrm{Im}\,\chi_{eff} = \frac{n_0 c}{\omega}\left[(N_1 - N_2)\sigma_{12} + (N_2 - N_3)\sigma_{23} + (N_1 - N_3)\sigma_{13}\right]p \tag{6.3}$$

Solving for the steady state and substituting the result into equation 6.3 yields [11]

$$\mathrm{Im}\,\chi_{eff} = \frac{n_0 c}{\omega} N_0 \left\{ \frac{p\sigma_{12}\left[W_{21}(\sigma_{23}+\sigma_{13}) + W_{31}(\sigma_{23}+\sigma_{13})\right] + W_{31}W_{21}(\sigma_{12}+\sigma_{13})}{3p^2\sigma_{12}(\sigma_{23}+\sigma_{13}) + p\left[W_{21}(\sigma_{23}+2\sigma_{13}) + 2W_{31}\sigma_{12}\right] + W_{31}W_{21}} \right\} \tag{6.4}$$

Where $W_{ij}=1/\tau_{ij}$ are the decay rates for the $i \rightarrow j$ transitions. Expanding in powers of the photon flux density and writing this explicitly in terms of the light intensity, one arrives at

$$\mathrm{Im}\,\chi_{eff} = \frac{n_0 c}{\omega} N_0 \left\{ (\sigma_{12} + \sigma_{13}) + \frac{I}{\hbar\omega} \left[\begin{array}{l} -\dfrac{2\sigma_{12}^2}{W_{21}} - \dfrac{2\sigma_{13}^2}{W_{31}} + \dfrac{(\sigma_{12}\sigma_{23} - \sigma_{12}\sigma_{13})}{W_{21}} \\ -\dfrac{(\sigma_{12}\sigma_{13} + \sigma_{23}\sigma_{13})}{W_{31}} \end{array} \right] \right\} \tag{6.5}$$

We can rewrite this result by noting that

$$\chi_{eff} = \chi^{(1)} + \chi^{(3)} \left| E \right|^2 = \chi^{(1)} + \chi^{(3)} \frac{2I}{c\varepsilon_0 n_0} \tag{6.6}$$

And therefore that

$$\mathrm{Im}\,\chi^{(3)} = \frac{\varepsilon_0 n_0^2 c^2 N_0}{2\hbar\omega^2} \left[-\frac{2\sigma_{12}^2}{W_{21}} - \frac{2\sigma_{13}^2}{W_{31}} + \frac{(\sigma_{12}\sigma_{23} - \sigma_{12}\sigma_{13})}{W_{21}} - \frac{(\sigma_{12}\sigma_{13} + \sigma_{23}\sigma_{13})}{W_{31}} \right] \tag{6.7}$$

The frequency dependence of $\mathrm{Im}\chi^{(3)}$ given by equation 6.7 is implicit in the frequency dependence of the absorption cross-section σ_{ij}. One can make this dependence explicit by putting σ_{ij} in terms of the absorption line shape $g_{ji}(\omega)$:

$$\sigma_{ij} = \frac{2\pi^2 \mu_{ij}^2}{\lambda \varepsilon_0 \hbar} g_{ji}(\omega) \tag{6.8}$$

where the line shape is assumed to be well described by a Lorentzian:

$$g_{ji}(\omega) = \frac{\Gamma_{ij}}{2\pi} \frac{1}{(\omega_{ij} - \omega)^2 + (\Gamma_{ij}/2)^2} \tag{6.9}$$

$\mu_{ij}=\langle j \mid er \mid i \rangle$ are the transition dipole moments, Γ_{ij} is the inverse of the dephasing time T_j, and $\omega_{ij}=(E_j-E_i)/\hbar\omega$ are the resonant frequencies. This assumption is justified by the fact that a homogeneously broadened profile permits a reasonably good fit to the linear and the nonlinear absorption frequency dependence, as is discussed below. If the overlap of the absorption line shapes for transitions $1 \rightarrow 2$ and $1 \rightarrow 3$ is small, the terms $\sigma_{12}\sigma_{13}/W_{21}$ and $\sigma_{12}\sigma_{13}/W_{31}$ in equation 6.7 can be neglected. Similarly, the overlap of the $1 \rightarrow 3$ and $2 \rightarrow 3$ transitions will be small, and the term $\sigma_{23}\sigma_{13}/W_{31}$ can also be neglected. With these approximations one can rewrite

$$\mathrm{Im}\,\chi^{(3)} = \frac{\pi^2 N_0 \mu_{21}^4 \tau_{21}}{2\varepsilon_0 \hbar^3}\left[\frac{\mu^2{}_{32}}{\mu_{21}^2} g_{21}(\omega) g_{32}(\omega) - 2g_{21}^2(\omega) - 2\frac{\tau_{31}\mu_{31}^4}{\tau_{21}\mu_{21}^4} g_{31}^2(\omega)\right] \tag{6.10}$$

Following an analogous procedure for the real part of the susceptibility, one arrives at

$$\mathrm{Re}\,\chi^{(3)} = \frac{\pi^2 N_0 \mu_{21}^4 \tau_{21} T_2}{2\varepsilon_0 \hbar^3}\left\{\begin{array}{l}(\omega_2-\omega)\left[\dfrac{T_3\mu^2{}_{32}}{T_2\mu_{21}^2} g_{21}(\omega) g_{32}(\omega) - 2g_{21}^2(\omega)\right] \\ -2(\omega_3-\omega)\dfrac{T_3\tau_{31}\mu_{31}^4}{T_2\tau_{21}\mu_{21}^4} g_{31}^2(\omega)\end{array}\right\} \tag{6.11}$$

Where for simplicity one calls ω_2 the resonant frequency for the $1 \rightarrow 2$ transition, i.e., $\omega_2=\omega_{21}$, and similarly $\omega_3=\omega_{31}$. The line shape $g_{32}(\omega)$ is centred about $\omega_{32}=\omega_3-\omega_2$, and therefore will have a slow variation across the spectral region considered here. These expressions for $\mathrm{Re}\chi^{(3)}$ and $\mathrm{Im}\chi^{(3)}$ can then be used to fit the corresponding experimental data for the poly-DCHD sample as shown in Figures 6.7 and 6.8 (solid lines).

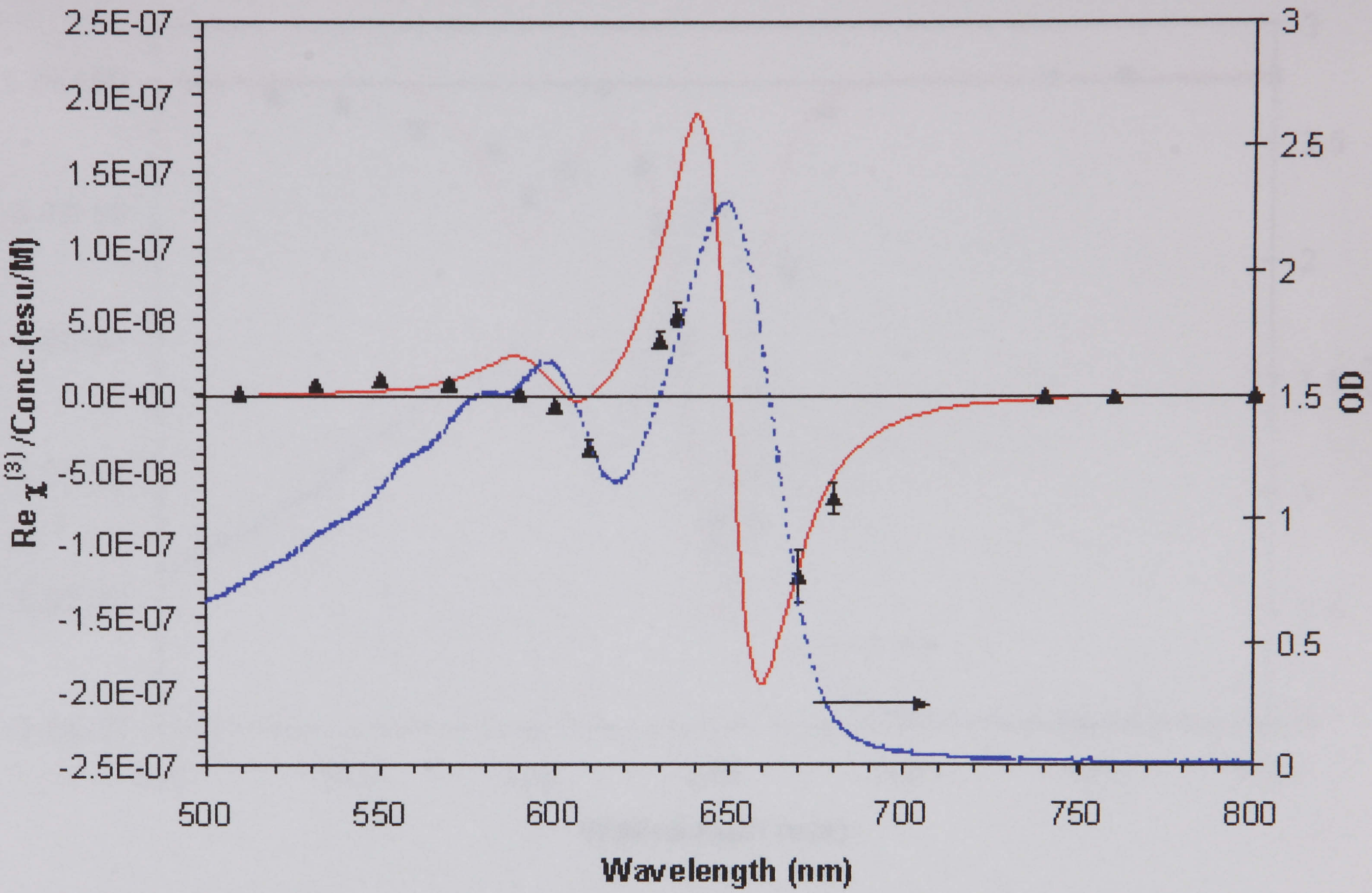

Figure 6.7: Calculated Re $\chi^{(3)}$ as function of wavelength for poly-DCHD microcrystals. Solid and dotted lines are the theoretical fit obtained with the three-level model, and the linear absorption spectrum, respectively.

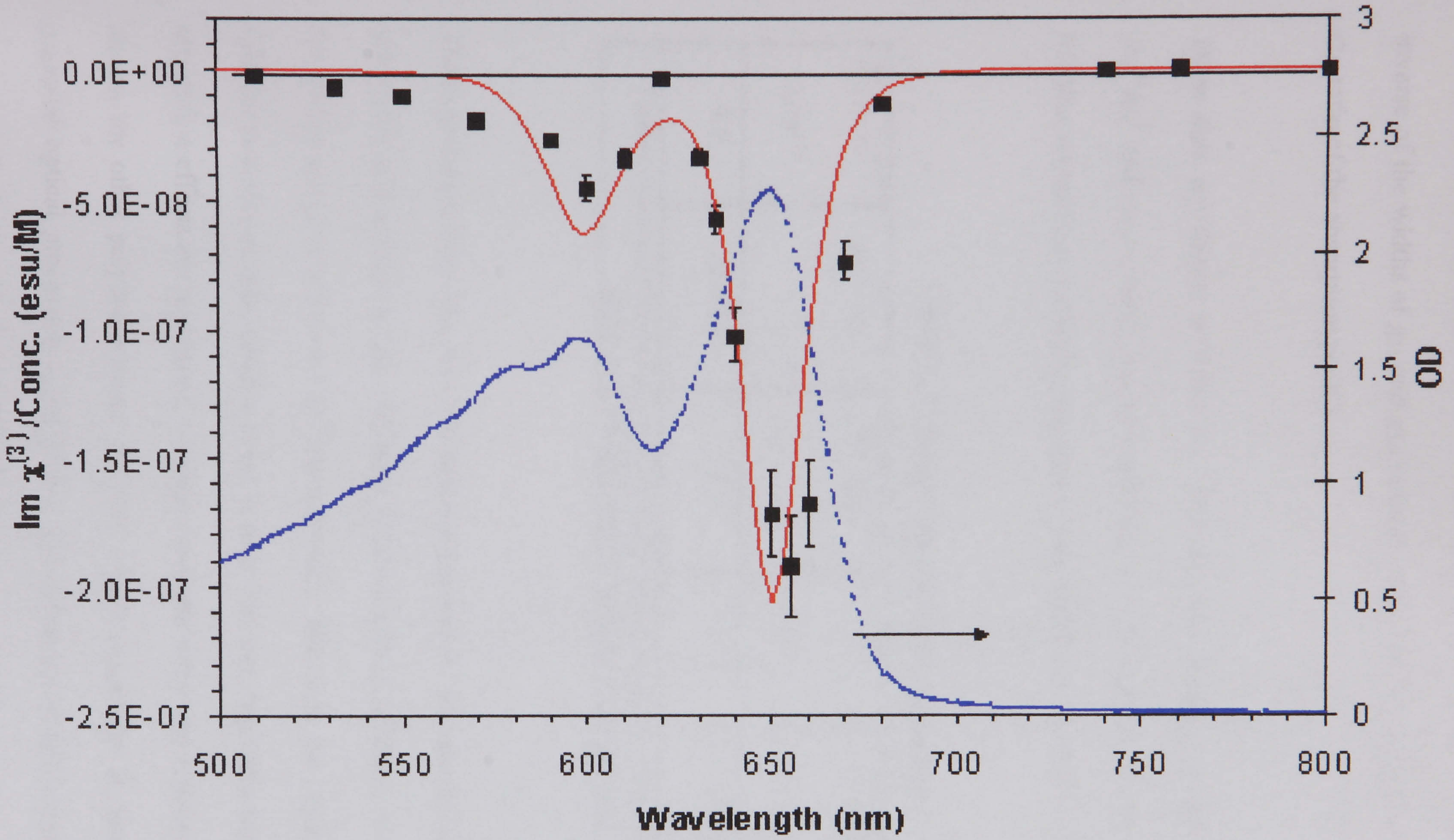

Figure 6.8: Calculated Im $\chi^{(3)}$ as function of wavelength for poly-DCHD microcrystals. Solid and dotted lines are the theoretical fit obtained with the three-level model, and the linear absorption spectrum, respectively.

To perform the fits one uses the linear absorption spectrum data to determine the values of the resonant frequencies ω_{12} and ω_{13}, the dephasing times T_2 and T_3 (given by the inverse of the widths of g_{21} and g_{31}, respectively), and the μ_{31}^2/μ_{21}^2 ratio (proportional to the ratio of the absorption peaks).

These data are shown in Table 6.3. The only free fitting parameters are therefore the μ_{32}^2/μ_{21}^2 and τ_{31}/τ_{21} ratios, together with the overall scale factor $\pi^2 N_0 \mu_{21}^4 \tau_{21}/2\varepsilon_0\hbar^3$. Table 6.3 also summarises the fitting parameters obtained for the sample studied.

Table 6.3: Three-level model parameters.

N_0 x 10^{-17} (cm^{-2})	μ_{31}^2/μ_{21}^2	μ_{32}^2/μ_{21}^2*	T_2 (fs)	T_3/T_2*	τ_{31}/τ_{21}*
4.8	0.943	11.5	7.1	0.65	0.55

Parameters marked * were obtained by fitting the spectral dependence of Re$\chi^{(3)}$ and Im$\chi^{(3)}$; all the others were obtained from the linear absorption spectra.

The model reproduces the observed spectral features for the sample. Moreover, the model also predicts a change of the nonlinear absorption from saturable to induced absorption for photon energies below the exciton resonance. The fit to the experimental data shows that the position of this crossing point is near 710 nm. Near this wavelength, nonlinear absorption effects are negligible, whereas nonlinear refraction remains finite, as has been shown for other polydiacetylenes [9] [10], which constitutes an interesting regime for potential optical processing applications. The existence of this crossing point was also accounted for in the simpler model of Bolger *et. al.*, for poly(toluene sulphonate) [9]. For a given material its actual value will be similar in the two models. However, Rangel's model describes nonlinear absorption and refraction over a broader spectral range.

Conclusions

The nonlinear coefficients β and n_2 at several wavelengths of poly-DCHD microcrystals (average size of 100 nm) in aqueous solution have been measured by using the z-scan technique within the spectral range 510–800 nm. The real and imaginary part of the nonlinear susceptibility $\chi^{(3)}$, as well as their signs have been obtained also. Results obtained from the z-scan experiments performed in this sample showed that the absorptive part of the nonlinear susceptibility ($\mathrm{Im}\chi^{(3)}$) was found to change sign between measurements taken on resonance and near resonance.

The nonlinear refractivity measured in this sample was three times larger than that measured the sample (poly-DCHD microcrystals) with average particle size of 30 nm [11]. One possible explanation is that smaller microcrystal sizes imply a higher degree of topological disorder of the polymer backbone, which would reduce exciton delocalisation and hence the exciton oscillator strength.

It was found that the dominant nonlinearity arises from the excitonic absorption peak. A strong nonlinear absorption was measured around the exciton peak; such absorption is a limiting factor for its application in the all-optical switching field.

A simple three-level model was used for the observed nonlinearity that reproduces the observed behaviour in the spectral range studied. This model predicted a crossover point (where $\mathrm{Im}\,\chi^{(3)} = 0$) to occur near 710 nm. Similar studies in polytoluene sulphonate (pTS) and red-phase 9BCMU thin-films have shown the existence of this crossover point.

Figures of merit W and T were estimated through the spectral range studied, near the crossover point (at 680 nm), W met the required value for Fabry-Perot and nonlinear

directional-coupler geometries. Since the absorptive nonlinearity at this wavelength (680nm) was dominated by a bleaching effect, the corresponding figure of merit T becomes irrelevant, and hence it does not represent a limiting factor for its application in all-optical switching. This constitutes an interesting regime for potential optical processing applications.

References

[1] T Koyashy, *Nonlinear optics of organics and semiconductors*, Springer-Verlag, Berlin 1989.

[2] A Cybo-Ottone, et. al., *Frontiers in nonlinear optics*, IOP publishing, London 1993.

[3] Hiro Matsuda, Shinji Yamada, Edward Van Keuren, *et al.*, *SPIE Proceedings*, **2998**, 241 1997.

[4] S Okada, H Matsuda, H Nakanishi, *et al.*, *Jpn. J. Appl. Phys.*, 31, L1132, 1992.

[5] K Yase, H Nakanishi, *et al.*, *Mol. Cryst. And Liq. Cryst.*, **294**, 71, 1996.

[6] H Katagi, H Matsuda, H Nakanishi, et al., *Jpn. J. Appl. Phys.*, **35**, L1364, 1996.

[7] Nanostructured Materials, *Chem. Mater.* **8**, 1569, 1996.

[8] C Saurrent, et. al., *Phys. Rev. Lett.* **36**, 956, 1976.

[9] J Bolger, et. al., *J. Opt. Soc. Am.* B **9**,1552, 1992.

[10] S Molyneux et. al., *Opt. Lett.* **18**, 2093, 1993.

[11] R Rangel-Rojo, S Yamada, H Matsuda, H Kasai, H Nakanishi, A K Kar and B S Wherrett, *J. Opt. Soc. Am.* B, **15**, 2937, 1998.

[12] H Bassler, *Polydiacetylenes*, Eds. D. Bloor and R.R. Chance, p.135, 1985.

[13] L Sebastian and G Weiser, *Chem. Phys. Lett.*, **64**, 396, 1979.

[14] B Reimer and H Bassler, *Phys. Stat. Sol.* A, **32**, 435, 1975.

[15] Y Tokura, T Koda, A Itsubo, M Miyabayashi, K Okuhara and A Ueda, *J. Chem. Phys.*, **85**, 99, 1986.

[16] R R Chance, M L Shand, C Hogg and R Silbey, *Phys. Rev.* B., **22**, 3540, 1980.

[17] D Bloor, Phil. Trans. R. Soc. Lond. A., **314**, 51 1985.

[18] See for example: *Introduction to Nonlinear Optical Effects in Molecules and Polymers*, ed. P N Prasad and D.J. Williams, John Wiley, New York, p.189, 1991.

[19] S Molyneux, *Third-Order Nonlinear Optical of Polydiacetylenes Studied by Sub-Picosecond Techniques*, PhD thesis, Heriot-Watt University, Edinburgh, 1995.

[20] U Dinur and M Karplus, *Chem. Phys. Lett.*, **88**, 171, 1982.

[21] L Robins, J Orenstein and R. Superfine, *Phys. Rev. Lett.*, **56**, 1850, 1986.

Chapter 7

Ultrafast optical switching in integrated Fabry-Perot devices containing poly-DCHD.

7.1 Introduction

The prospect of using the third-order optical nonlinearity described by the nonlinear refractive index, n_2 (related to the third-order nonlinear optical susceptibility $\chi^{(3)}$) for all-optical switching in waveguides has been of considerable interest during the past two decades. Many waveguide structures capable of switching have been suggested, but generally each places similar demands on the linear and nonlinear properties of the material when the practical issues such as small size, high speed and low energy consumption per switching event are taken into account.

During the 1980s excitement was generated by the discovery of large and fast nonresonant third-order nonlinear responses in organic materials, especially those possessing extended π-electron conjugation such as π-conjugated polymers. Efforts to characterize the nonlinear properties of such materials have often lacked the proper scope, largely due to the scarcity of appropriate laser equipment to perform such characterization, particularly in chemistry laboratories where most of the synthesis has been performed. Experimental data has often been misleading due to influence of thermal effects, the creation of excited states during measurement, or the failure to identify both absorptive and refractive components of the nonlinearity. In addition few measurements

have been performed at anything but a single wavelength and often the measured component of the nonlinear susceptibility relates only indirectly to that needed for all-optical switching.

It has taken some time to become accepted that various figures of merit (W and T) determine the applicability of any material to standard switching devices [1]. Simply observing a high value of nonlinearity is insufficient. The nonlinearity must generally be fast (<ps) [2] [3]: the optical losses (linear and nonlinear) suitably low; the material dispersion should not lead to pulse break-up in the device; and the performance must be stable at the operating peak and average powers otherwise degradation due to optical damage or thermal effects could occur. These figures of merit W and T are now gaining attention in the literature and direct the effort to demonstrate that the organic third-order nonlinear materials can be used to make waveguide based switching devices. So far, however, only a few organic materials have been shown to possess suitable figures of merit.

Polydiacetylenes were among the first conjugated polymers considered for all-optical switching [4]. Recent work has concentrated on polytoluene sulphonate, commonly abbreviated to pTS [5] [6], which has been found to possess reasonably good values of the T parameter in the infrared region. The difficulty in working with pTS is, however, that the material has to be prepared as a single crystal of the monomer, which is then polymerised (thermally or by UV irradiation) to the polymeric form. This makes it difficult to prepare waveguide devices in comparison with noncrystalline materials where waveguiding films can often be prepared simply by spin-coating.

Soluble polydiacetylenes, such as those referred to by the nBCMU abbreviation (BCMU=(butoxycarbonyl)methylurethanyl), have also been investigated [7] [8]. Thin

film waveguides can be obtained from BCMU polymers such as 9BCMU polydiacetylene [9]. Poly-9BCMU has been shown to be a material suitable for optical switching [10]. It has yet to be realized into a practical device, and the main reason for this is the difficulty in fabricating a device.

For telecommunications systems to take full advantage of the optical fibre bandwidth it will be necessary to have components responding at picosecond speeds. The only way currently known to achieve these speeds is using all-optical switching [11]. One promising type of all-optical switching device for use in future telecommunication systems is the Fabry-Perot (*F-P*) device.

Nonlinear optical measurements off-resonance (1.06 μm) have been made in a Fabry-Perot cavity containing a pTS single crystal [12]. In this work the cavity length was controlled to select specific bias points on the *F-P* fringe and the measurements were made by a pump-probe technique using 90 ps pulses. The changes in transmission at selected bias points were measured as a function of time delay between the pump and the probe. The measured response time was found to be pulse-width limited and the maximum changes in transmission were as large as 50% at low optical irradiances (~10 $MWcm^{-2}$). The sign of n_2 was determined from the direction of the fringe shift and was found to be negative.

In this chapter I present a systematic study (pump-probe experiments) of four symmetric (partially reflective mirrors with the same characteristics) Fabry-Perot devices (etalons) containing poly-DCHD microcrystal thin-films of different concentrations, using a picosecond broad band white-light probe [13] [14]. The mirrors were > 95% reflective between 700 and 800 nm and nearly transparent at the pump wavelength of 640 nm. A theoretical model used to describe the Fabry-Perot linear transmission was developed and

is presented here. This model was used to fit the experimental data and it was found to give a good description of the linear transmission in all the samples. The time-resolved nonlinearity of the thin film was studied by the pump-probe technique (described in Chapter 2) using resonant pump pulses and broadband (white light) probe pulses (600-850 nm). The use of a spectrally broad probe beam allowed us to investigate the nonlinear response of poly-DCHD at wavelengths away from resonance as a result of excitation at near-resonant wavelengths. A blue-shift of the Fabry-Perot peaks, which is induced by the pump pulse (excitation), with a duration of 800 fsec, was clearly observed in all the etalons studied. From the blue-shift of the *F-P* peaks we estimate the maximum refractive index change Δn_{max}. From this maximum fringe shift we have calculated the refractive cross-section (change in refractive index per generated excitation per unit volume). The dynamics of the refractive-index change (or fringe-shift) were investigated and the peak-shift recovering lifetime was estimated. Figures of merit W and T, as well as the switching energy $\mathcal{E}_s$ for this Fabry-Perot geometry, were also calculated at the *F-P* peak wavelengths.

7.2 Experimental details

The technique used in these experiments is well known as excite-continuum probe and has been described in section 2.3. The laser system used in this work was a Nd:YAG laser, modelocked at 76 MHz, pumping a dual-jet dye laser. The dye-laser output was amplified via a Nd:YAG regenerative amplifier and three-stage dye amplifier, to produce tuneable pulses of approximately 800 fs duration at 10 Hz with greater than 0.3 mJ/pulse.

A broadband subpicosecond white-light continuum (probe) pulse was generated in a 1 cm long cuvette of distilled water. A small fraction of the continuum pulse was extracted through a beam splitter to give the reference signal. The sample's transmission spectrum

was determined by simultaneously monitoring the reference and transmitted continuum spectra with a Princeton Instrument dual-array optical multi-channel analyser (*OSMA*). Each spectrum collected was an average of 35 pulses. The excitation and continuum probe (centred at the excite-beam centre) beams were focused to a 1/*e* irradiance radius of 180 and 150 μm, respectively. A variable time delay on the continuum probe allowed us to time resolve the dynamics of the transmission spectrum following the excitation pulse.

The samples were four Fabry-Perot etalons formed by two high reflecting dielectric coated mirrors containing a poly-DCHD thin-film sandwiched between them, as shown in Figure 7.1. In order to fabricate uniform through plane devices we have prepared thin films containing nanometer size microcrystals of poly-1,6-dicarbazoly1-2,4-hexadiyne (DCHD). The thin film was deposited on a reflecting dielectric-coated substrate and a second mirror was attached with clamps to complete the device.

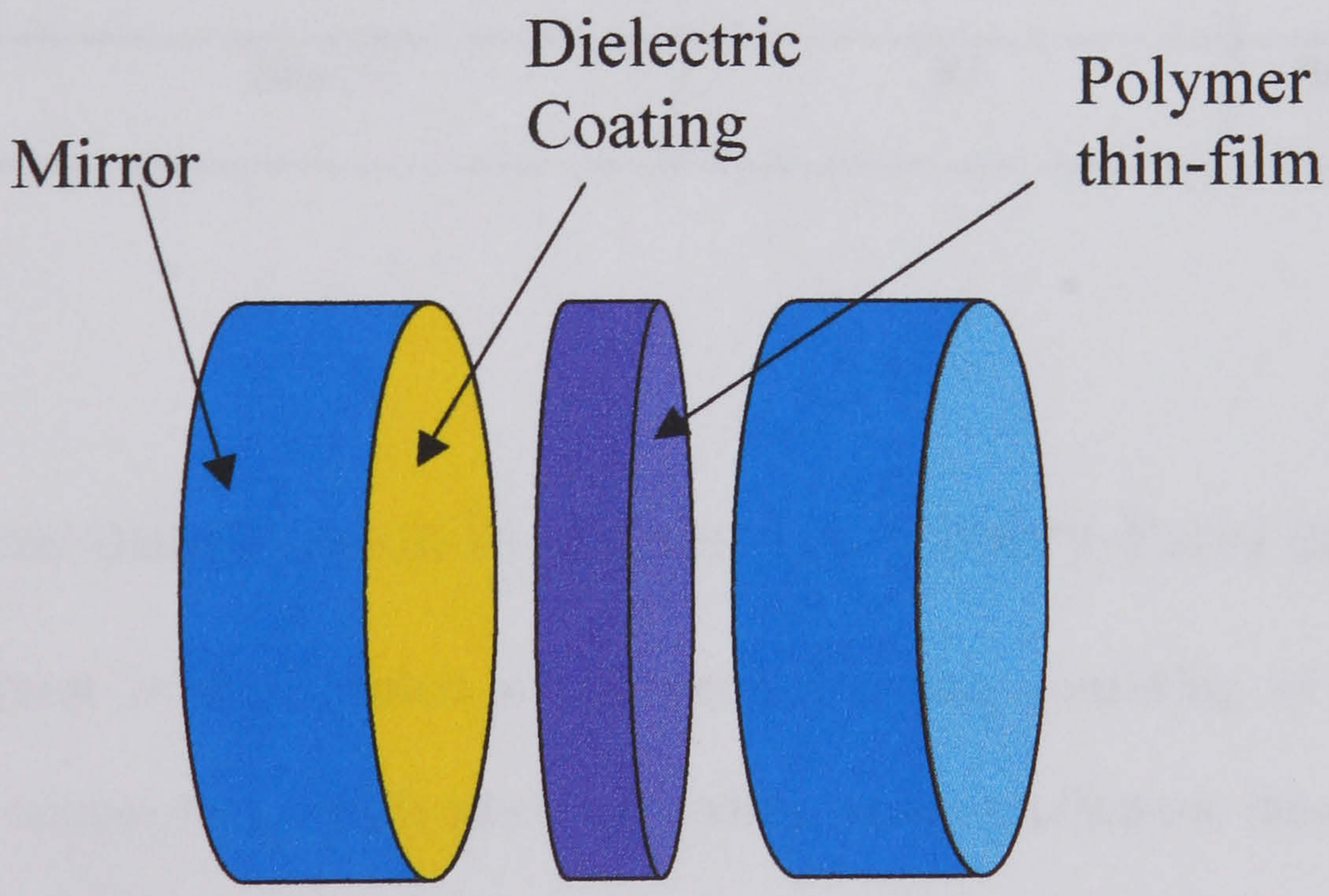

Figure 7.1: Diagram of a Fabry-Perot device containing a polymer thin-film.

In Table 7.1 the parameters for four samples are listed. As described in section 3.8, the thin-film deposition into these devices was achieved by using the spin-coating technique. In order to protect the polymer thin-film from any degradation or contamination due to its contact with dust and air, these devices were laterally sealed by using some *torr-seal*. We have observed that well-sealed devices remain in perfect condition (physical and optical) for a long time, at least two years after preparation. However, unsealed devices are only useful for a few months.

Table 7.1: Characteristics of the Fabry-Perot devices.

Sample	Poly-DCHD microcrystals Concentration	Mirrors Reflectivity R (%)	Wavelength Range
F-P1	**3wt%**	**95**	**700-800nm**
F-P2	**3wt%**	**99**	**700-800nm**
F-P3	**9wt%**	**95**	**700-800nm**
F-P4	**20wt%**	**95**	**700-800nm**

7.3 Linear transmission in nonabsorbing Fabry-Perot etalons

The Fabry-Perot is the simplest of all interferometers, consisting of two partially transmitting mirrors facing each other. Depending on the application, these mirrors may be flat or spherical, and the distance between them can range anywhere from micrometers to meters [15]. The Fabry-Perot mirrors form an optical cavity in which successive reflections create multiple beam interference fringes. The Fabry-Perot etalon, or interferometer, can be considered as the archetype of the optical resonator [16]. It consists

of two parallel mirrors separated a distance t. Let a plane wave be incident on the etalon at an angle θ' to the normal, as shown in Figure 7.2.

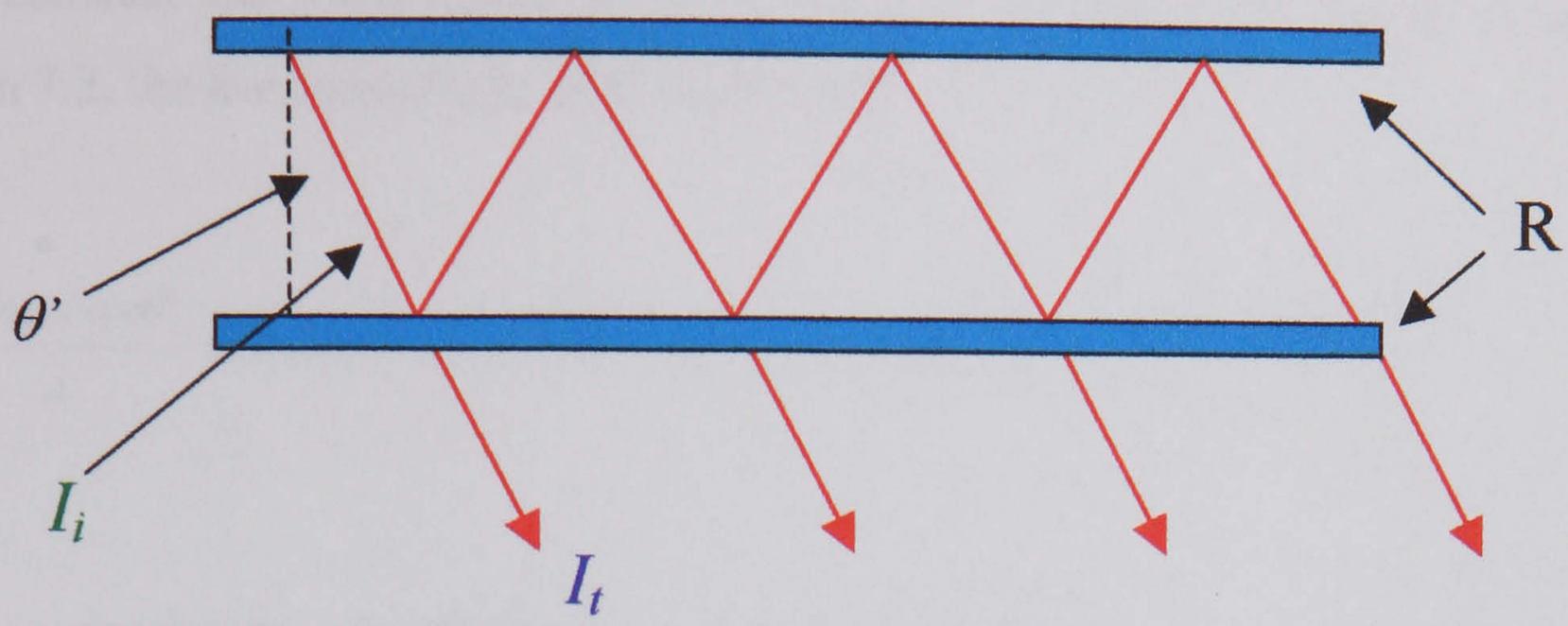

Figure 7.2: Multiple reflections in a Fabry-Perot cavity.

We can treat the problem of the transmission of the plane wave through the etalon by considering the infinite number of partial waves produced by reflections at the two mirror surfaces. The phase delay between two partial waves which is attributable to one additional round trip is given by [17]

$$\delta = \frac{4\pi n_0 t \cos\theta'}{\lambda} \tag{7.1}$$

Where λ is the vacuum wavelength of the incident wave, θ' is the internal angle of incidence and n_0 is the vacuum refractive index. Assuming no losses in the cavity, the expression for the fraction of the incident intensity that is transmitted is given by

$$\frac{I_t}{I_i} = \frac{(1-R)^2}{(1-R)^2 + 4r\sin^2(\delta/2)} \tag{7.2}$$

Where I_i and I_t are the incident and transmitted intensities, respectively. R is the reflectivity of the mirrors.

Let us consider the transmission characteristics of a Fabry-Perot etalon. According to equation 7.2, the transmission is unity whenever

$$\delta = \frac{4\pi n_0 t \cos\theta'}{\lambda} = 2\pi m \tag{7.3}$$

where m = any integer identifying the order of interference.

Using equation 7.1, the condition 7.3 for maximum transmission can be written as

$$\nu_m = m\frac{c}{2n_0 t\cos\theta'} \tag{7.4}$$

where $c = \nu\lambda$ is the velocity of light in vacuum and ν is the optical frequency. For a fixed t and θ', equation 7.4 defines the unity transmission (resonance) frequencies of the etalon. These are separated by the so-called free spectral range

$$\Delta\nu_0 \equiv \nu_{m+1} - \nu_m = \frac{c}{2n_0 t\cos\theta'} \tag{7.5}$$

In the presence of losses in the etalon medium, we find that the peak transmission is less than unity. This case is what occupies the study reported in the present chapter; the absorbing medium will be a polymer thin-film (poly-DCHD microcrystals).

7.4 Linear transmission in absorbing Fabry-Perot etalons

The transmission of a Fabry-Perot etalon is characterised by a series of peaks or fringes, the positions of which depend on the parameters of the cavity. For a cavity without any absorbing medium inside, the transmission at the maximum of each peak is equal to one, and if the separation between the mirrors is fixed, the peak position will depend on the separation distance and the incident wavelength. However, if an absorbing medium is placed between the mirrors, the intensity of the peaks will depend on the absorption coefficient of such a medium. In this section I present a theoretical model to describe the transmission of a Fabry-Perot cavity filled with an absorbing medium. This model will be used to fit the experimental data for all the samples.

7.4.1 Theoretical model for the linear transmission

A theoretical model for a Fabry-Perot etalon containing a thin-film medium was used to carry out the analysis of the experimental linear transmission obtained from these samples. The model is derived by introducing the mirrors reflectance R, thin-film linear absorption coefficient α_0, linear refractive index n_0, the angle θ' of the propagating wave of wavelength λ from the surface normal and thin-film thickness t. In this work two cases were of interest, one in which the incident beam is weak enough to avoid producing nonlinear effects, and the other in which an additional intense beam is used to excite the medium and produce nonlinear effects.

In this section, only that case in which a weak beam passes through the etalon in the absence of a strong beam in order to avoid nonlinear effects within the film will be discussed. Under this condition, both absorption coefficient and refractive index are not modified (at fixed wavelength) and we can write the linear transmission T_l for a Fabry-Perot etalon [12], as follows:

$$T_l = \frac{I_t}{I_0} = \frac{(1-R)^2 (e^{-\alpha_0 t})}{(1-R_{\alpha_0})^2 (1 + F \sin^2 \delta)} \tag{7.6}$$

where

$$\delta = \frac{2\pi n_0 t \cos\theta'}{\lambda}, \quad F = \frac{4R_{\alpha_0}}{(1-R_{\alpha_0})^2}, \quad R_{\alpha_0} = R(e^{-\alpha_0 t}) \tag{7.7}$$

Since the spin-coating technique is based on the spreading of a material solution (poly-DCHD microcrystals) on the substrate while it spins at high speed, the thin films obtained are not uniform in thickness. This causes the optical density $\alpha_0 t$ of the poly-DCHD thin film to vary through the cavity. We can see in equation 7.6 that the linear transmission T_l in a Fabry-Perot with an absorbing medium depends on the optical density of the medium. In other words, the linear transmission depends on the medium thickness t. Hence the thickness of the poly-DCHD film across the area illuminated by the continuum-probe beam is not constant. This fact should be taken into account and equation 7.6 needs to be modified. In order to take into account the thickness variation let us assume that the thickness across the illuminated area has a Gaussian distribution ψ, which is given by

$$\psi = N \exp(-A(t-t_0)^2) \qquad \int_{-\infty}^{\infty} \psi dt = 1 \tag{7.8}$$

where N is a normalisation constant, $A^{-1/2}$ represents the thickness uniformity, t is the film thickness and t_0 is the estimated one. Hence, the linear transmission is obtained by taking the average over the thickness distribution, then the expression becomes

$$\overline{T}_l(\lambda) = \frac{1}{\sqrt{\pi}} \int_{-\infty}^{\infty} \frac{(1-R)^2 (e^{-\alpha_0 t}) e^{-A(t-t_0)^2}}{(1-R_{\alpha_0})^2 (1+F\sin^2\delta)} dt \qquad (7.9)$$

this equation is used in the next section to fit the experimental data and obtain some of the parameters of the samples such as the thin-film thickness and the order of the fringes (Fabry-Perot peaks).

7.4.2 Linear transmission in Fabry-Perot etalons containing poly-DCHD

The linear transmission spectra of these four samples are shown in Figures 7.3, 7.4, 7.5 and 7.6 (already reported in [14] and [18]). In these figures we can see the typical Fabry-Perot peaks. From these spectra we can also see that in all the etalons the transmission of each peak is different from peak to peak due to the variation in the polymer absorption coefficient value along the spectral range.

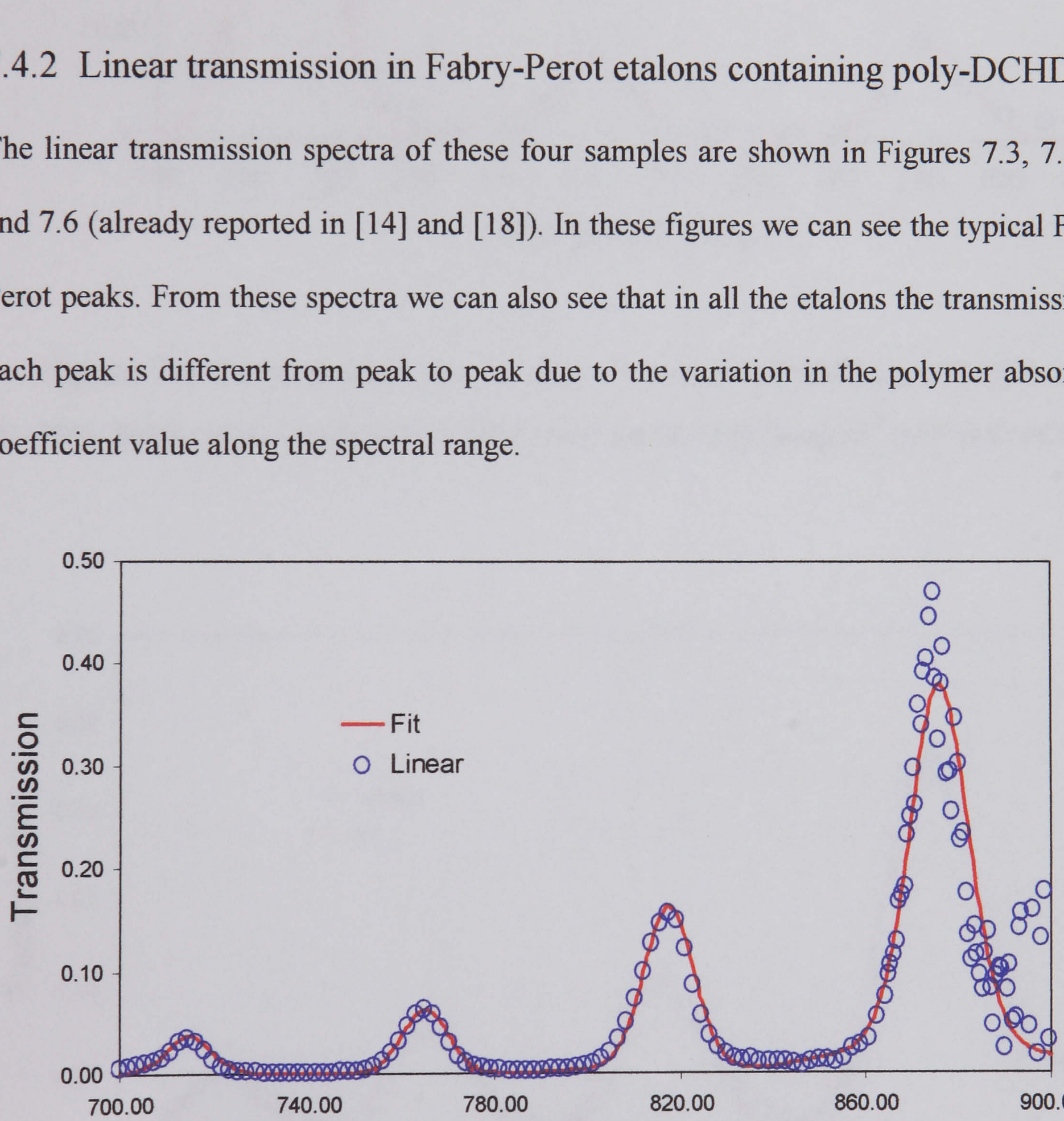

Figure 7.3: Linear transmission for the *F-P1* with poly-DCHD (3wt%). Mirrors, R=95%. Solid curve corresponds to the fit made to the data using $A^{1/2}$=0.3 and t=3.7 μm.

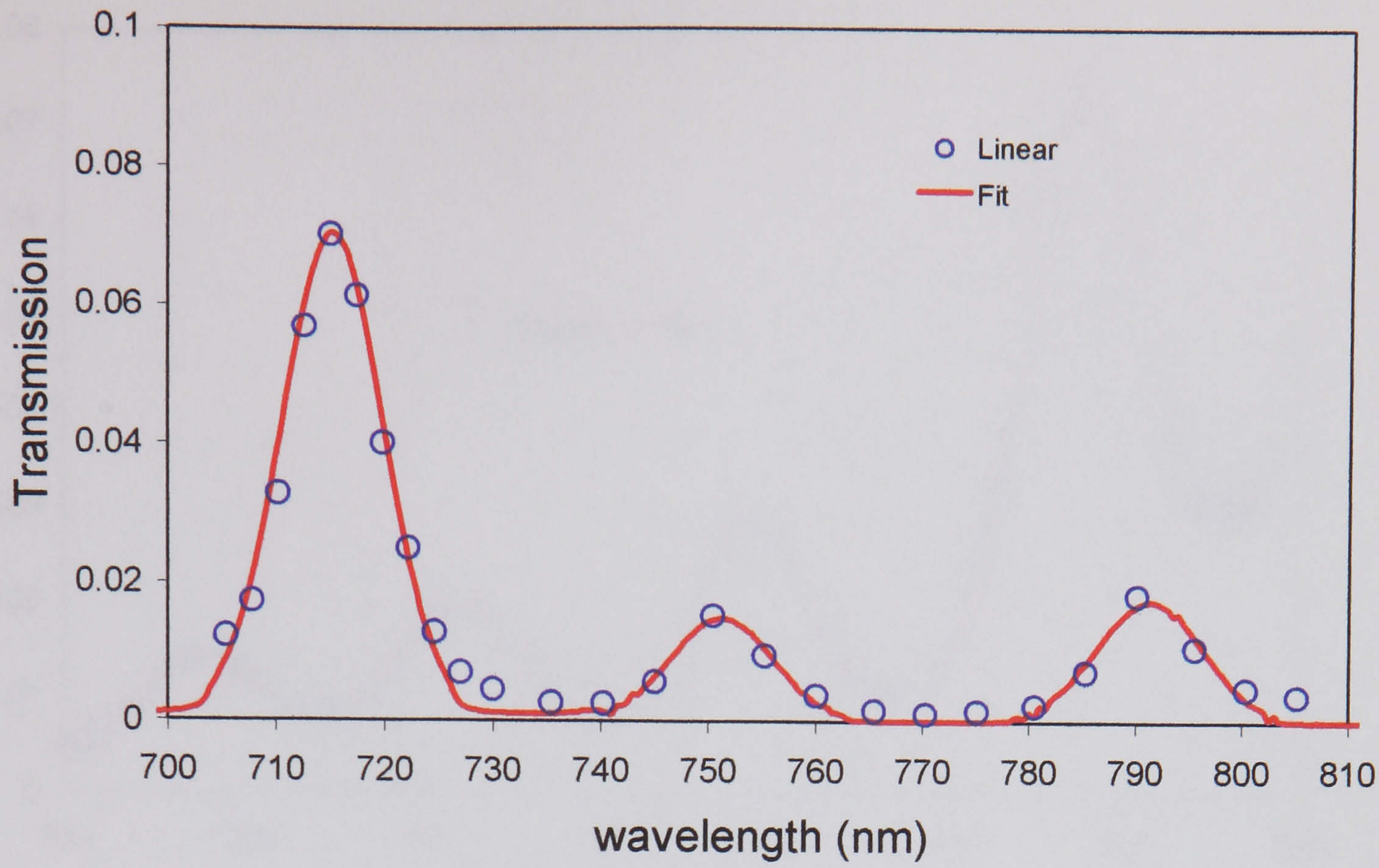

Figure 7.4: Linear transmission for the *F-P2* with poly-DCHD (3wt%). Mirrors, R=99%. Solid curve corresponds to the fit made to the data using $A^{1/2}$=0.5 and t=4.6 μm.

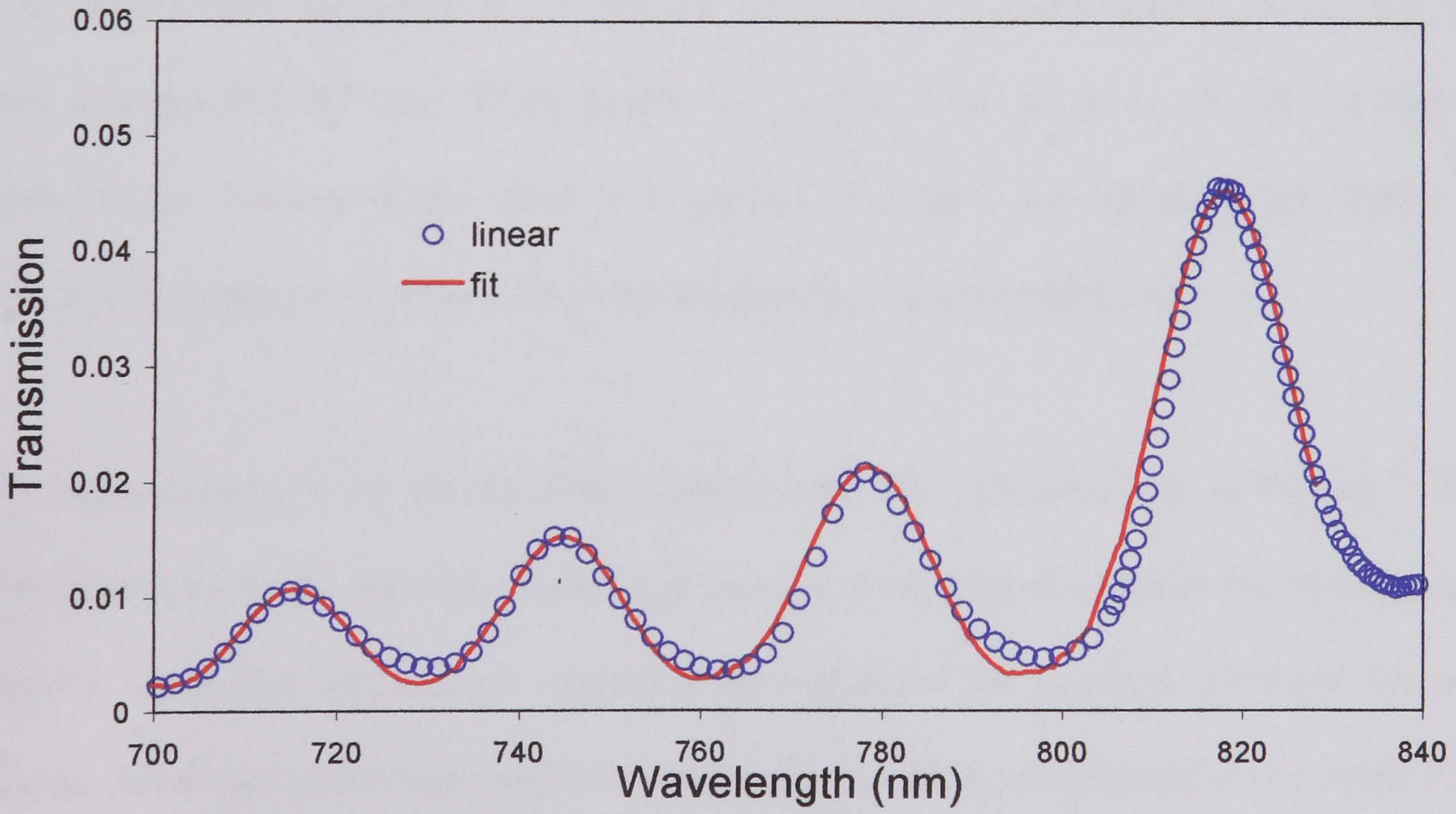

Figure 7.5: Linear transmission for the *F-P3* with poly-DCHD (9wt%). Mirrors, R=95%. Solid curve corresponds to the fit made to the data using $A^{1/2}$=0.7 and t=6.5 μm.

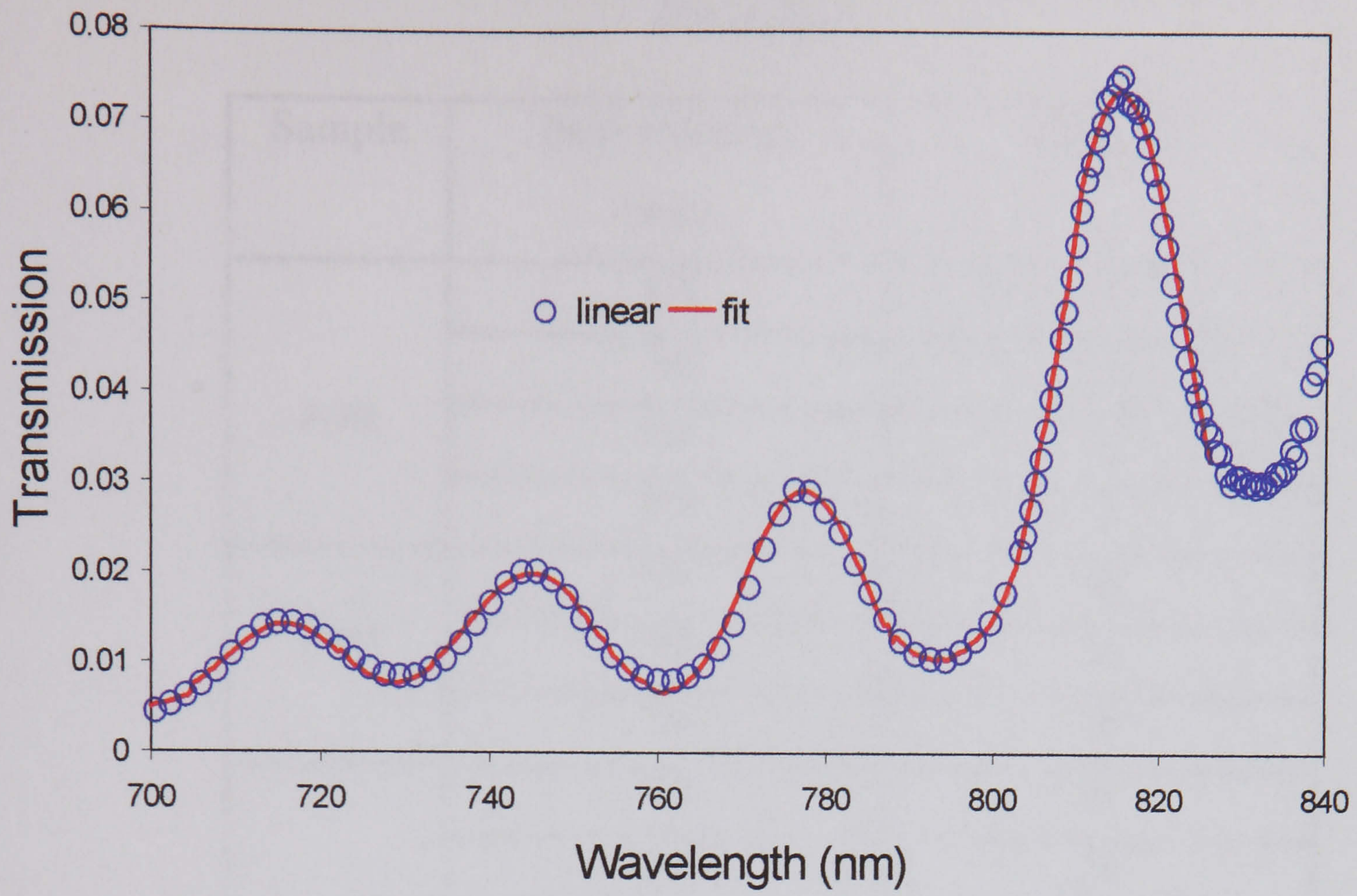

Figure 7.6: Linear transmission for the *F-P4* with poly-DCHD (20wt%). Mirrors, R=95%. Solid curve corresponds to the fit made to the data using $A^{1/2}$=0.7 and t=6.5 μm.

The transmission spectrum of *F-P1* etalon shows four well-defined peaks at 714 nm, 765 nm, 818 nm and 875 nm. These peaks correspond to the order m, 16, 15, 14 and 13, respectively. Spectra of the other *F-P* etalons also show the typical peaks. Table 7.2 contains a summary with the peak positions and the corresponding order m.

By using equation 7.11, we fitted the experimental data. The solid lines in Figures 7.3-7.6 correspond to the fit, showing a good agreement between the theoretical and experimental results. From this analysis we extracted the values of the polymer thickness for each etalon. All these values along with the uniformity variation are summarized in Table 7.3.

Table 7.2: Position and order *m* of the peaks for the linear transmission in *F-P* etalons.

Sample	Peak Position (nm)	Order *m*
F-P1	**714**	**16**
	765	**15**
	818	**14**
	875	**13**
F-P2	**715**	**20**
	751	**19**
	791	**18**
F-P3	**716**	**26**
	744	**25**
	777	**24**
	815	**23**
F-P4	**716**	**26**
	744	**25**
	777	**24**
	815	**23**

Table 7.3: Fitted parameters for the linear transmission in *F-P* etalons.

Sample	Mirrors Reflectivity R (%)	Poly-DCHD thickness (μm)	$A^{1/2}$
F-P1	**95**	**3.7 ± 0.1**	**0.3**
F-P2	**99**	**4.6 ± 0.1**	**0.5**
F-P3	**95**	**6.5 ± 0.1**	**0.7**
F-P4	**95**	**6.5 ± 0.1**	**0.7**

7.5 Time-resolved experiments in Fabry-Perot etalons containing poly-DCHD

The irradiance-dependent refractive index change $\Delta n = n_2 I$ derived from the nonlinear refractive index n_2 can be observed in several kinds of processes. It can be measured in a Fabry-Perot etalon; the transmission of the cavity depends on the phase relationships of the standing waves in the cavity and the irradiance-dependent refractive index can change these relationships in a light-intensity-dependent manner. If the refractive index of the medium is irradiance-dependent, then the resonance condition will be different at low irradiance and high irradiance. In other words, from an irradiance-dependence study of the resonance conditions, one can determine the change in the refractive index of the medium. This method provides the sign of nonlinearity by observing the direction in which the peaks move while the intensity is changed from low to high. In our time-resolved experiments the irradiance (of the excitation pulse) was changed from zero to high values around 50 $GWcm^{-2}$.

As was discussed above in section 7.3, in a Fabry-Perot cavity the phase delay between two partial waves is defined as δ and given by equation 7.1. Changes in phase delay δ can be achieved by inducing a change in the medium refractive index and/or by tuning the incident wavelength [19].

In this section I present the deduction of the expression that relates the peak-shift (fringe-shift) $\Delta\lambda$ and the change of the refractive index Δn induced in the medium (poly-DCHD) by an excitation pulse in a Fabry-Perot cavity. This expression will be used to analyse the data obtained in the time-resolved experiments performed in all the samples. Since these experiments allow us to measure the transmission peak-shift, we will be able to calculate the change in the refractive index.

Taking for simplicity the case of normal incidence (θ'=0°), we obtain the following expression [20] for the change $d\nu$ in the resonance frequency of a given transmission peak due to a variation in the refractive index (dn) of the medium

$$\frac{d\nu}{dn} = -\frac{2t\Delta\nu_0}{\lambda_0} \tag{7.10}$$

where $\Delta\nu_0$ (free spectral range in absence of the excitation) is given by equation 7.5, t is the medium thickness and λ_0 is the given transmission peak wavelength in absence of the excitation pulse (linear transmission). Rewriting equation 7.10 as

$$d\nu = -\frac{2t\Delta\nu_0}{\lambda_0} dn \tag{7.11}$$

then integrating both sides of this equation, we arrive at the next expression

$$(\nu - \nu_0) = -\frac{2t\Delta\nu_0}{\lambda_0}(n - n_0) \tag{7.12}$$

where ν and ν_0 are the peak transmission frequency in presence and absence of excitation, respectively; n and n_0 are the refractive index of the medium in presence (nonlinear) and absence (linear) of excitation, respectively. Using $\nu=c/\lambda$ we can write equation 7.12 as follows

$$\frac{(\lambda - \lambda_0)}{\lambda_0} = \frac{(n - n_0)}{n_0} \tag{7.13}$$

but if $\Delta n = (n - n_0)$ and $\Delta\lambda = (\lambda - \lambda_0)$ we obtain the relationship between the refractive index change Δn and the transmission peak-shift $\Delta\lambda$

$$\frac{\Delta n}{n_0} = \frac{\Delta\lambda}{\lambda_0} \tag{7.14}$$

Hence, by measuring the fringe-shift for a particular Fabry-Perot peak, the change in the refractive index Δn can be obtained by

$$\Delta n = n_0 \frac{\Delta\lambda}{\lambda_0} \tag{7.15}$$

7.5.1 Induced peak-shift in Fabry-Perot etalons containing poly-DCHD microcrystals

Time-resolved experiments were performed in all the etalons. In all the etalons we observed a clear fringe-shift and a fast fringe-shift recovery within 10 ps. Figure 7.7 which corresponds to the *F-P1* sample (3wt%) shows the Fabry-Perot peaks before (curve in blue) and 700 fs after (curve in red) excitation by a pump pulse at 640 nm with a duration of 800 fs and a peak irradiance of 52 $GWcm^{-2}$. A blue-shift of all the peaks due to a negative refractive index n_2 induced by the pump pulse is clearly observed.

We also observe an induced absorption, which takes place at 722, 770 and 822 nm peaks and a bleaching effect at the 680 nm peak. This is consistent with the nonlinearity measurements performed in poly-DCHD already reported in Chapter 6. Results of the third-order nonlinear coefficients (β and n_2) reported in Chapter 6 (Table 6.1) showed that within the spectral range 510-710 nm a saturable absorption ($\beta<0$) effect was observed. Induced absorption ($\beta>0$) was observed within the spectral range 710-800 nm. The

nonlinear refractive index n_2 showed to be negative ($n_2<0$) within 670-800 nm. The maximum peak-shift was observed to occur 700 fs after exitation at the 680 nm peak, its measured value was found to be $\Delta\lambda_{max}$= -3.3 nm. Now we can use equation 7.15 to calculate the change in refractive index Δn that produces this peak shift $\Delta\lambda$. Therefore if we take the value of the linear refractive index n_0 of poly-DCHD reported in section 6.2 (Chapter 6) as 1.535 at 680 nm, the maximum refractive index change (Δn_{max}) that corresponds to the maximum fringe shift $\Delta\lambda_{max}$ is Δn_{max} = -7.4 x 10^{-3}.

Figures 7.8-7.10 shows the maximum blue fringe-shift observed in the samples *F-P2* (3wt%), *F-P3* (9wt%), and *F-P4* (20wt%), respectively. In all of these figures we can see a clear fringe-shift occurring. As was mention above, an induced absorption effect, which was measured in poly-DCHD within the spectral 710-800 nm is also observed.

Excitation at 640 nm, with pulses of a duration of 800 fs and a peak irradiance of 52 GWcm^{-2}, was also used in these samples. In sample *F-P2* the maximum peak-shift was observed 990 fs after excitation at the 751 nm peak. A maximum peak-shift of $\Delta\lambda_{max}$ = -3.6 nm was observed and corresponds to a maximum refractive index change of Δn_{max} = -7.3 x 10^{-3}. In samples *F-P3* and *F-P4* the maximum peak-shift was observed 860 fs after excitation at the 744 nm peak. The maximum peak-shift of $\Delta\lambda_{max}$ = -6.6 nm observed in *F-P3* corresponds to a maximum refractive index change of Δn_{max} = -13.5 x 10^{-3}. In sample *F-P4* the maximum peak-shift of $\Delta\lambda_{max}$ = -6.1 nm, which corresponds to a maximum refractive index change of Δn_{max} = -12.3 x 10^{-3}. Table 7.4 summarizes all these results.

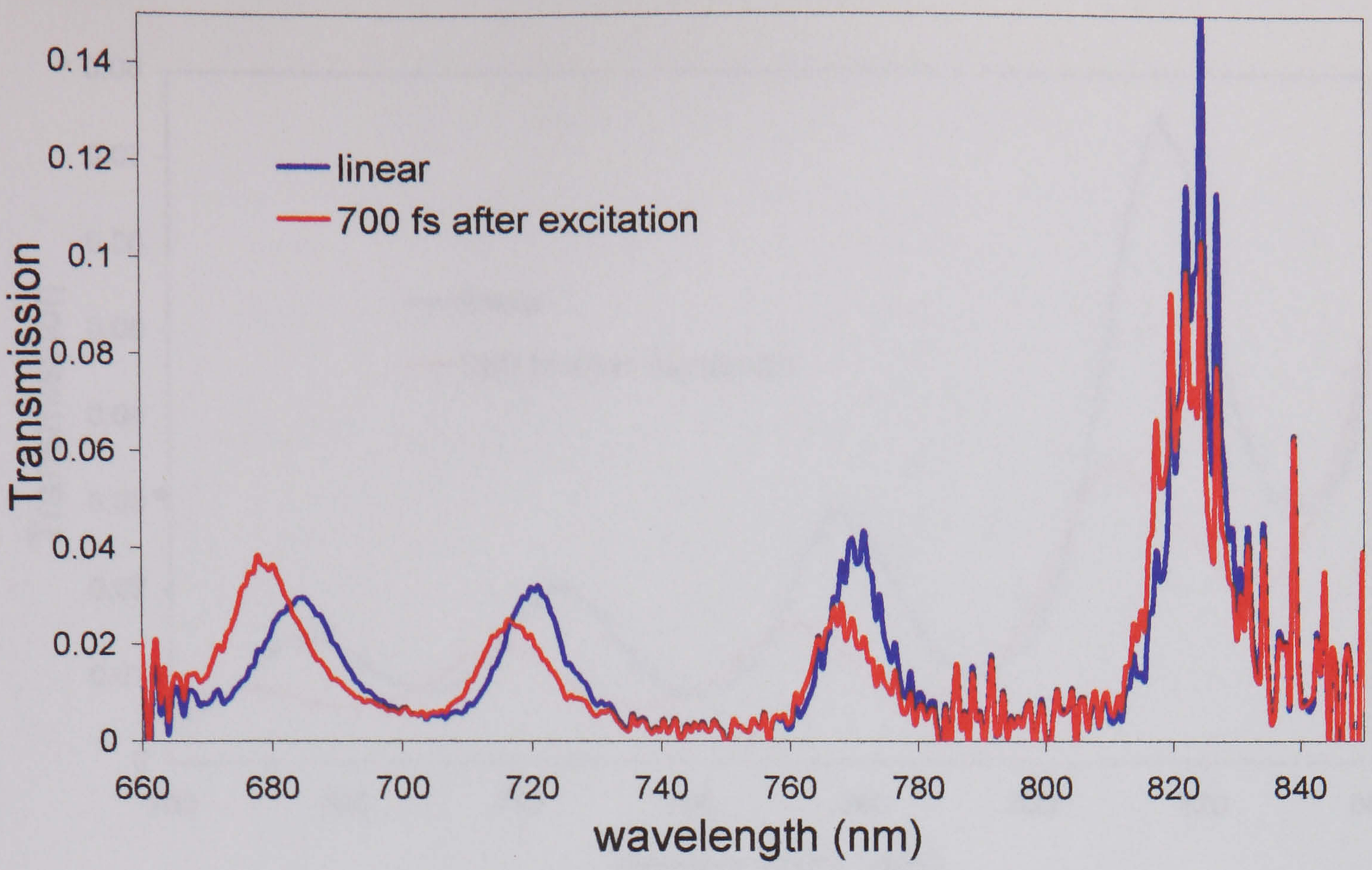

Figure 7.7: Fabry-Perot fringes in *F-P1* before (blue-line) and 700 fs after (red-line) excitation by a pump pulse at 640 nm with a duration of 800 fs and a peak irradiance of 52 GWcm^{-2}.

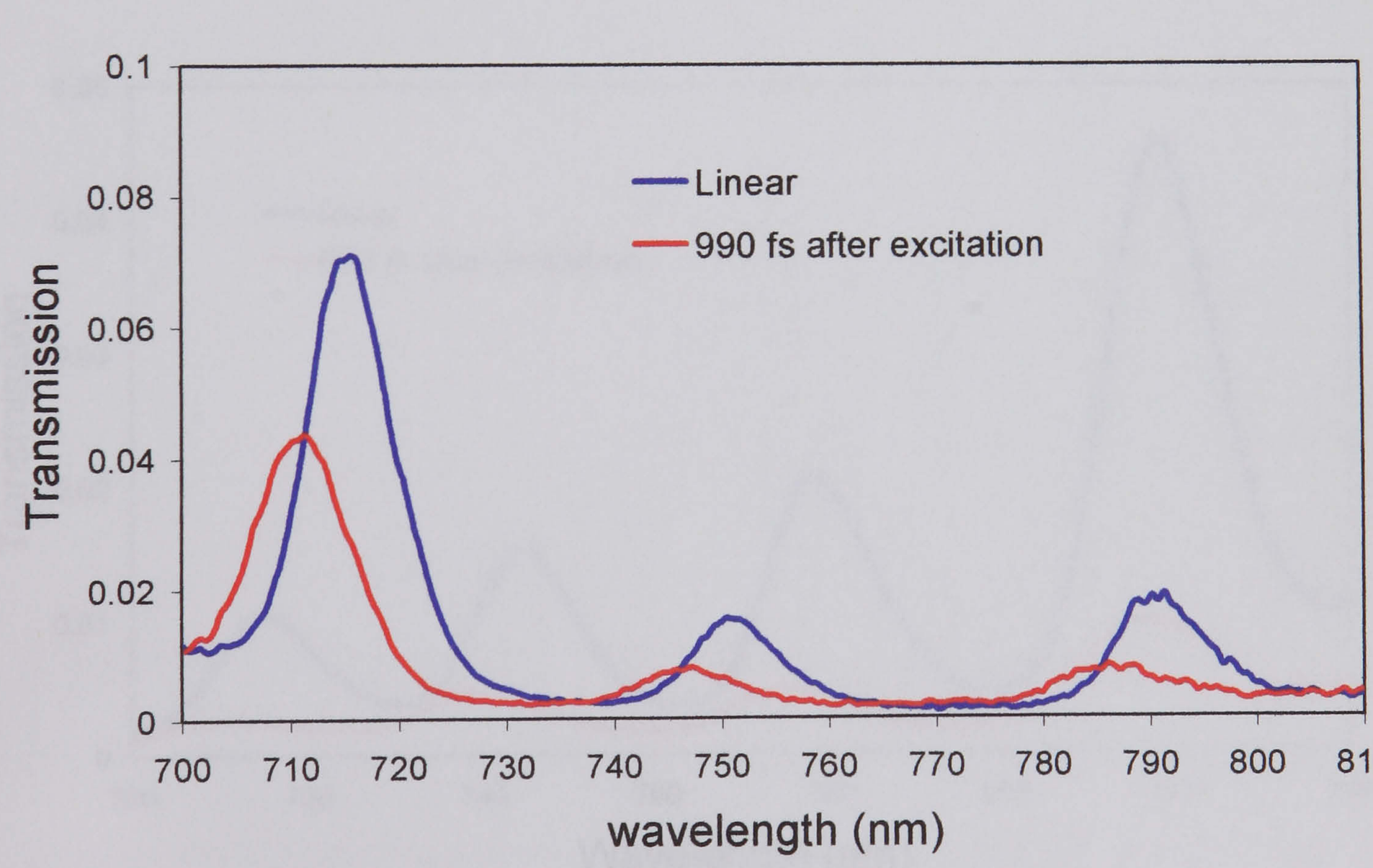

Figure 7.8: Fabry-Perot fringes in *F-P2* before (blue-line) and 990 fs after (red-line) excitation by a pump pulse at 640 nm with a duration of 800 fs and a peak irradiance of 52 GWcm^{-2}.

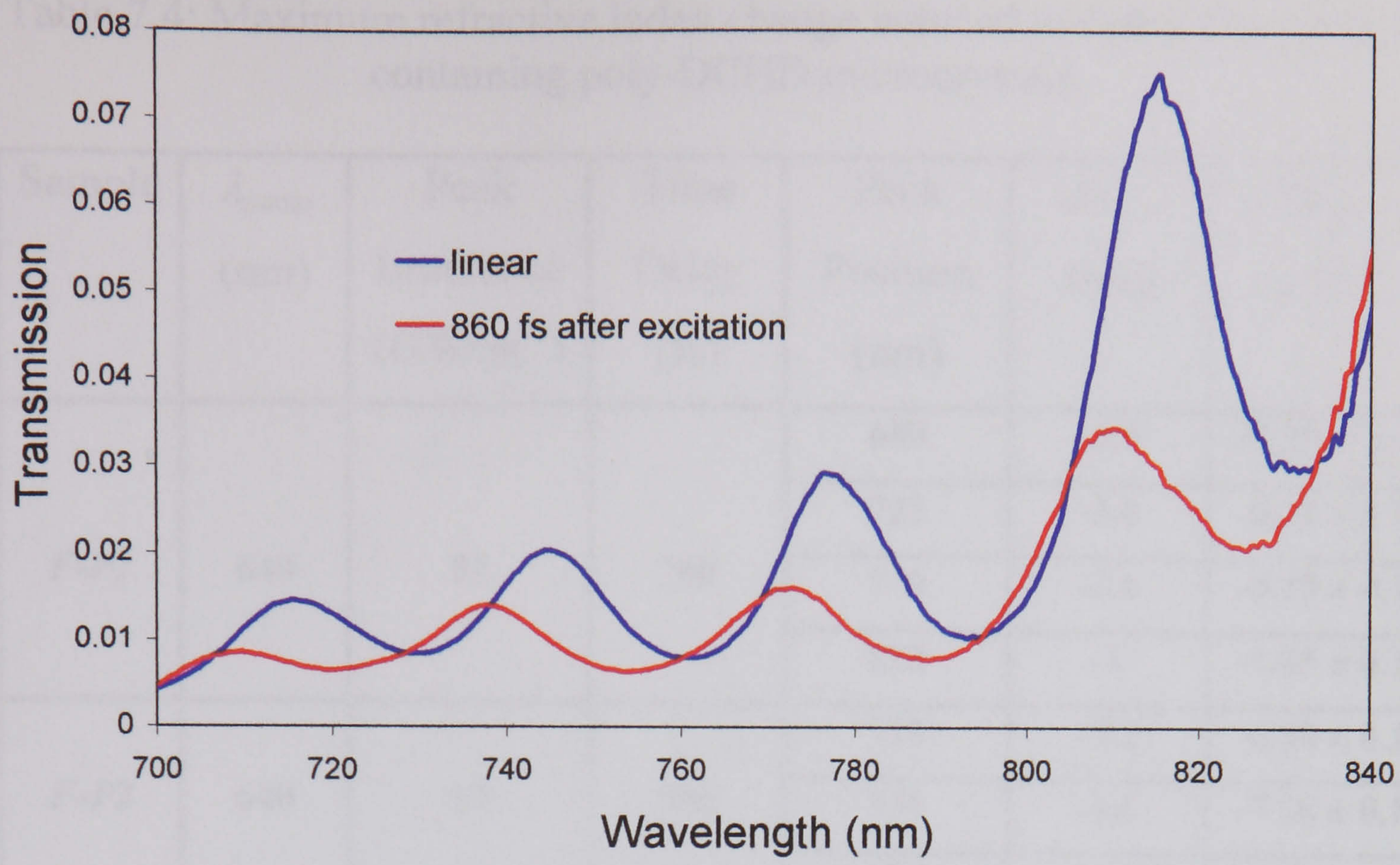

Figure 7.9: Fabry-Perot fringes in *F-P3* before (blue-line) and 860 fs after (red-line) excitation by a pump pulse at 640 nm with a duration of 800 fs and a peak irradiance of 52 $GWcm^{-2}$.

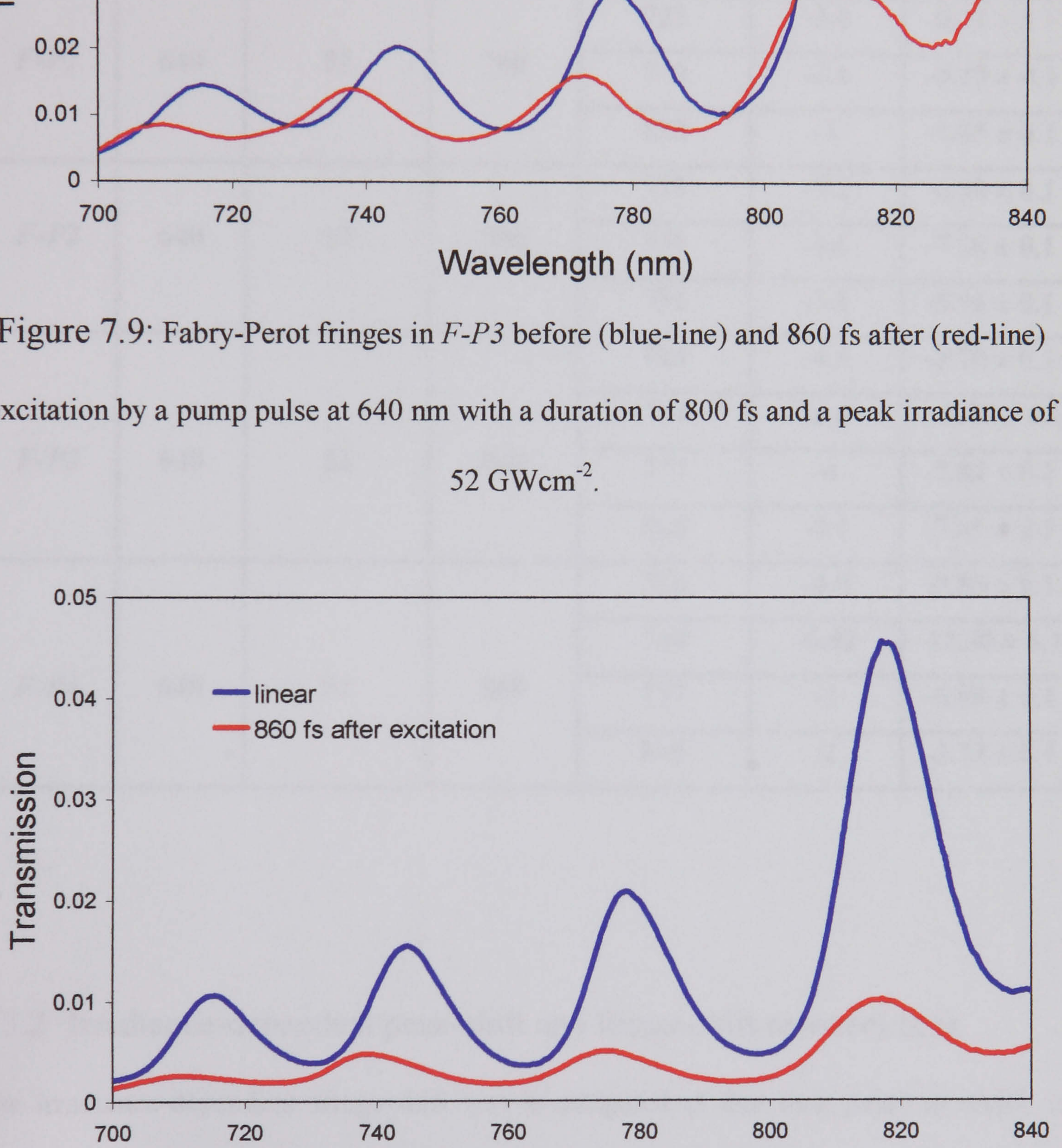

Figure 7.10: Fabry-Perot fringes in *F-P4* before (blue-line) and 860 fs after (red-line) excitation by a pump pulse at 640 nm with a duration of 800 fs and a peak irradiance of 52 $GWcm^{-2}$.

Table 7.4: Maximum refractive index change induced in Fabry-Perot etalons containing poly-DCHD microcrystals.

Sample	λ_{pump} (nm)	Peak Irradiance ($GWcm^{-2}$)	Time Delay (fs)	Peak Position (nm)	$\Delta\lambda_{max}$ (nm)	Δn_{max} x 10^{-3}
F-P1	**640**	**52**	**700**	**680**	**-3.3**	**-7.37 ± 0.1**
				722	**-3.0**	**-6.31 ± 0.1**
				770	**-2.6**	**-5.13 ± 0.1**
				822	**-1**	**-1.85 ± 0.1**
F-P2	**640**	**52**	**990**	**715**	**-3.2**	**-6.80 ± 0.1**
				751	**-3.6**	**-7.28 ± 0.1**
				791	**-3.1**	**-5.96 ± 0.1**
F-P3	**640**	**52**	**860**	**716**	**-4.1**	**-8.70 ± 0.1**
				744	**-6.6**	**-13.48 ± 0.1**
				777	**-4**	**-7.82 ± 0.1**
				815	**-4.1**	**-7.65 ± 0.1**
F-P4	**640**	**52**	**860**	**716**	**-4.5**	**-9.55 ± 0.1**
				744	**-6.02**	**-12.30 ± 0.1**
				777	**-3**	**-5.88 ± 0.1**
				815	**-2**	**-3.73 ± 0.1**

7.5.2 Irradiance-dependent peak-shift and fringe-shift recovery time

The irradiance-dependent fringe-shift was investigated at that time delay at which the maximum peak-shift occurs. Experiments were conducted in all the samples within the irradiance range 0-52 $GWcm^{-2}$.

(a)

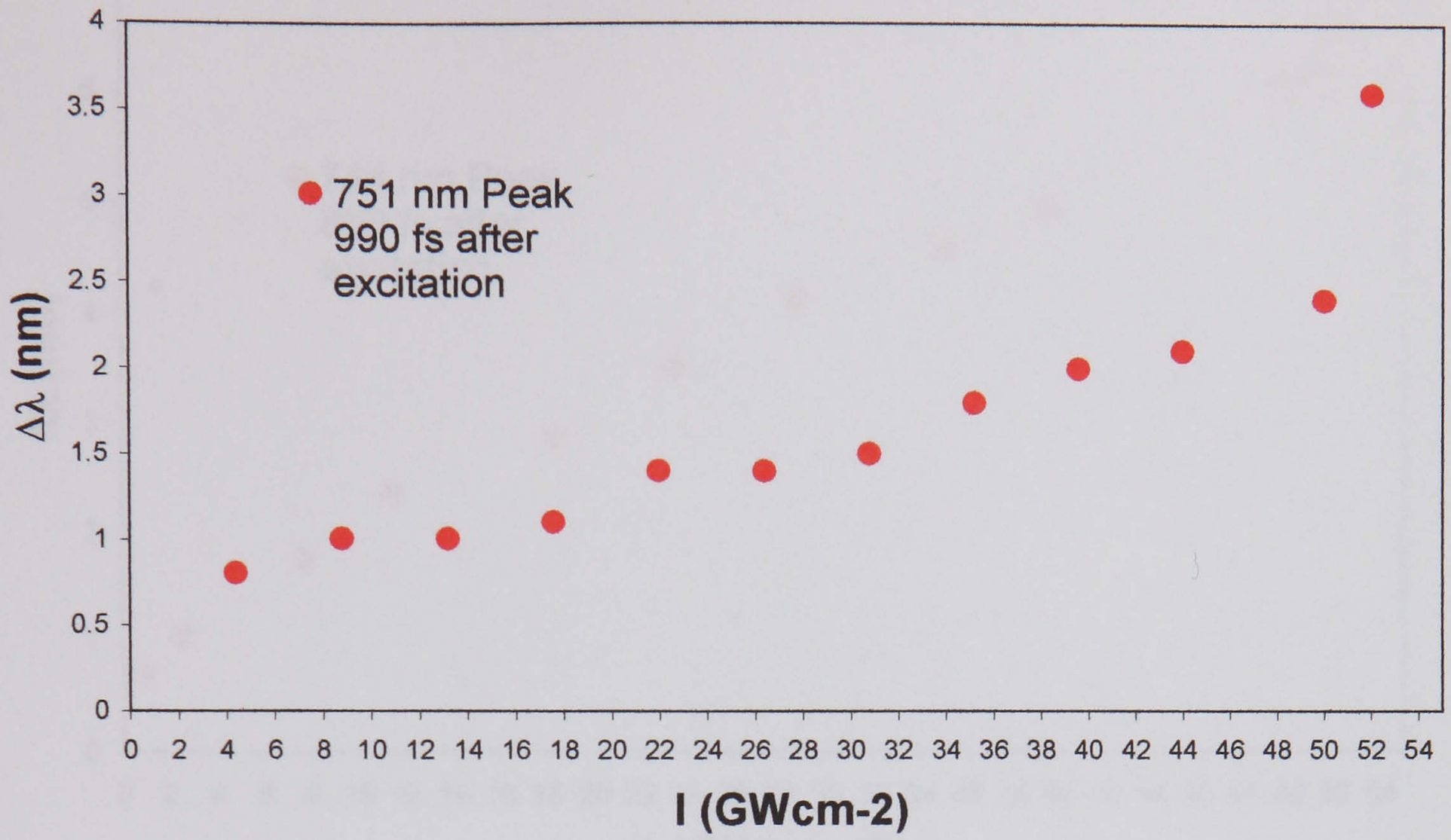

(b)

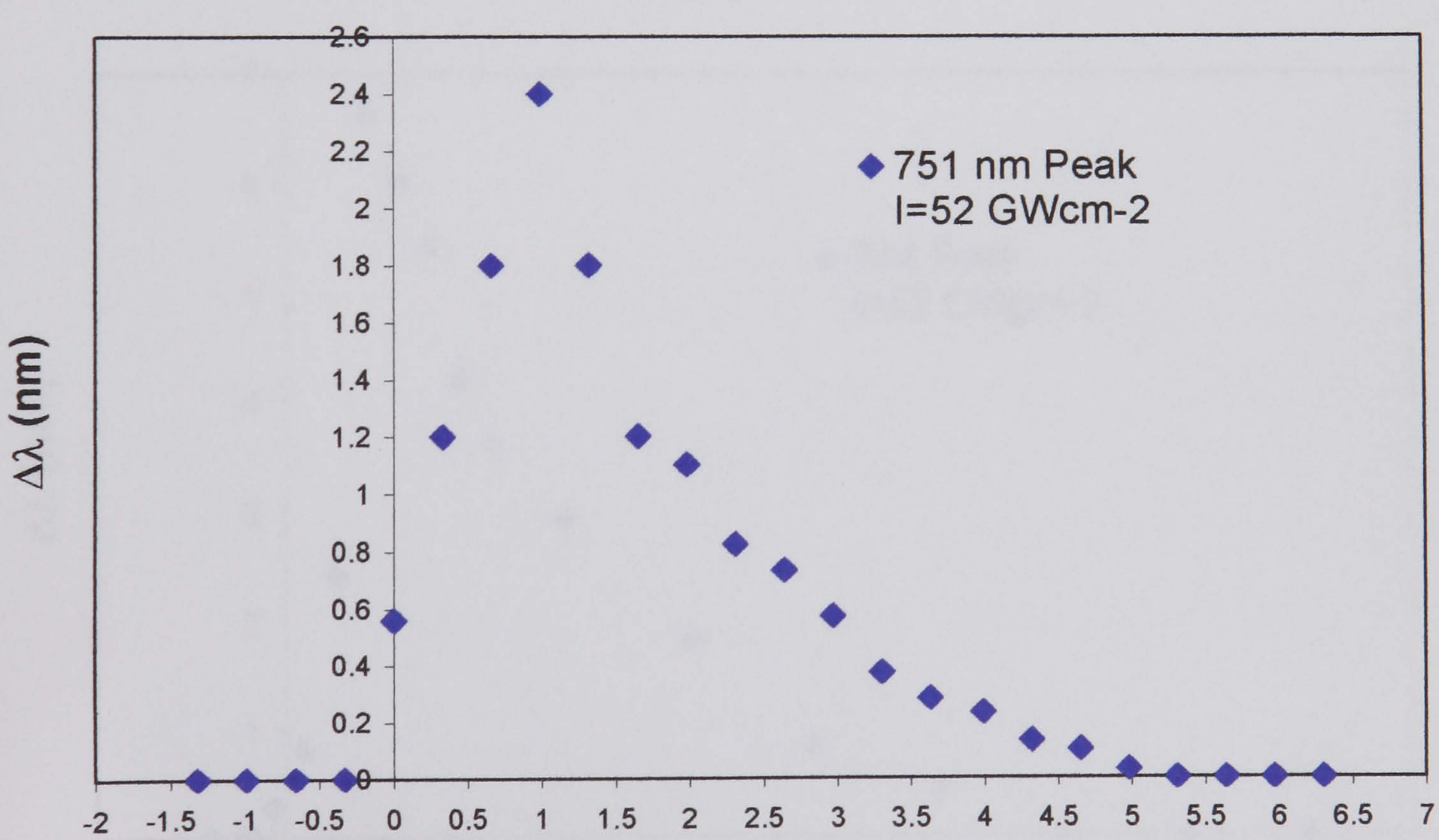

Figure 7.11: (a) Irradiance-dependent fringe-shift and (b) recovering time of the 751 nm peak-shift in the *F-P2* with poly-DCHD (3wt%) after excitation.

(a)

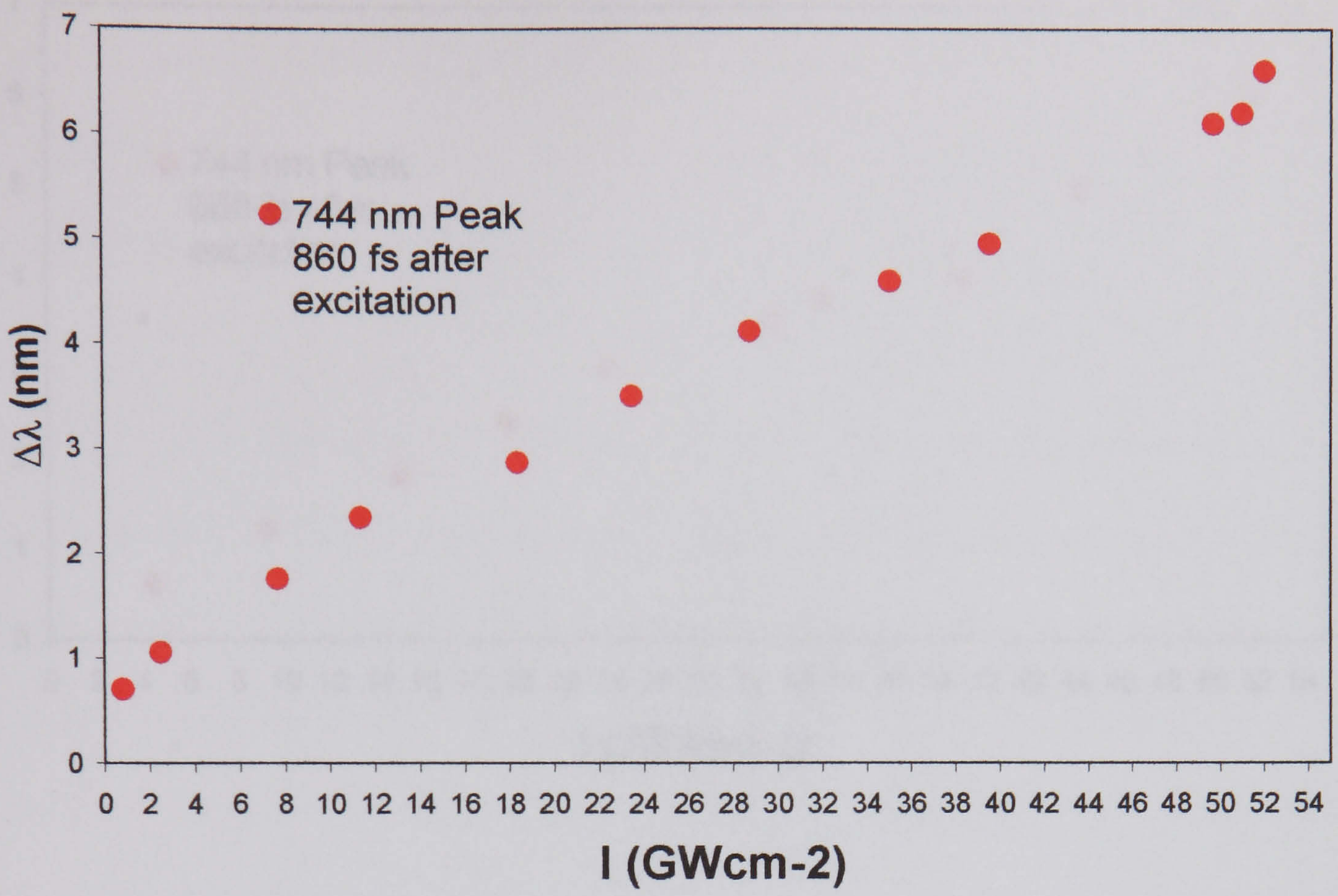

(b)

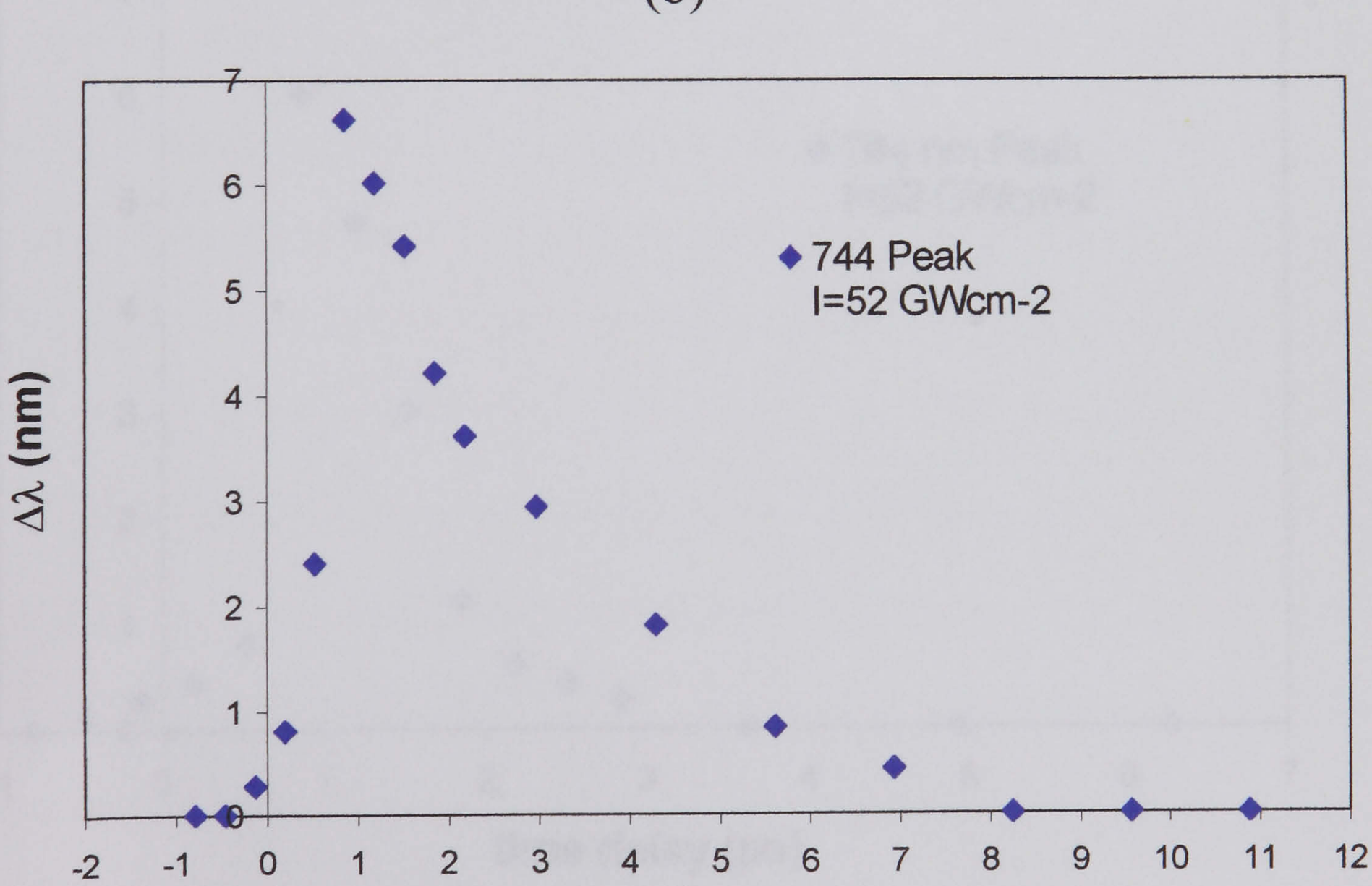

Figure 7.12: (a) Irradiance-dependent fringe-shift and (b) recovering time of the 744 nm peak-shift in the *F-P3* with poly-DCHD (9wt%) after excitation.

(a)

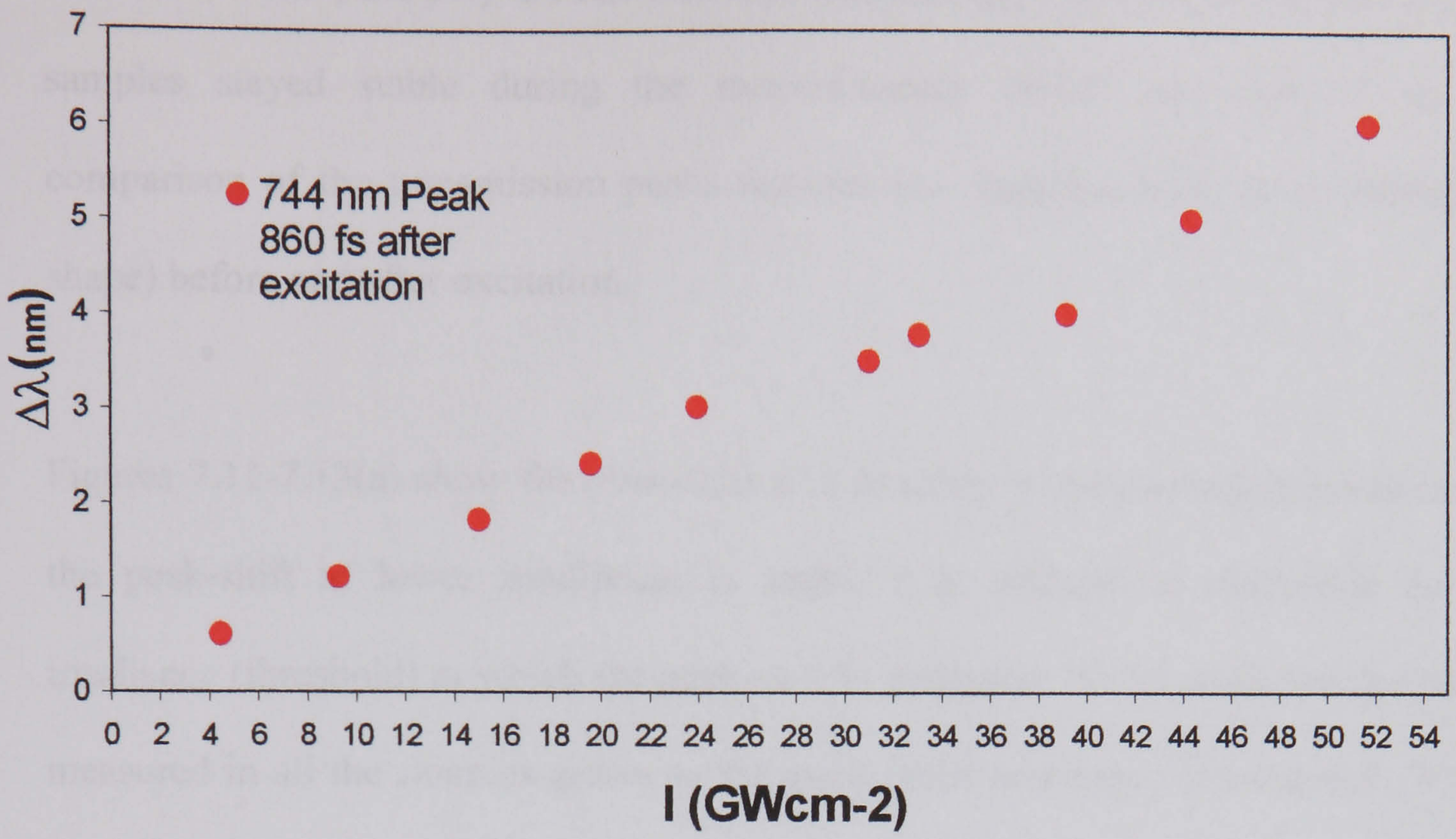

(b)

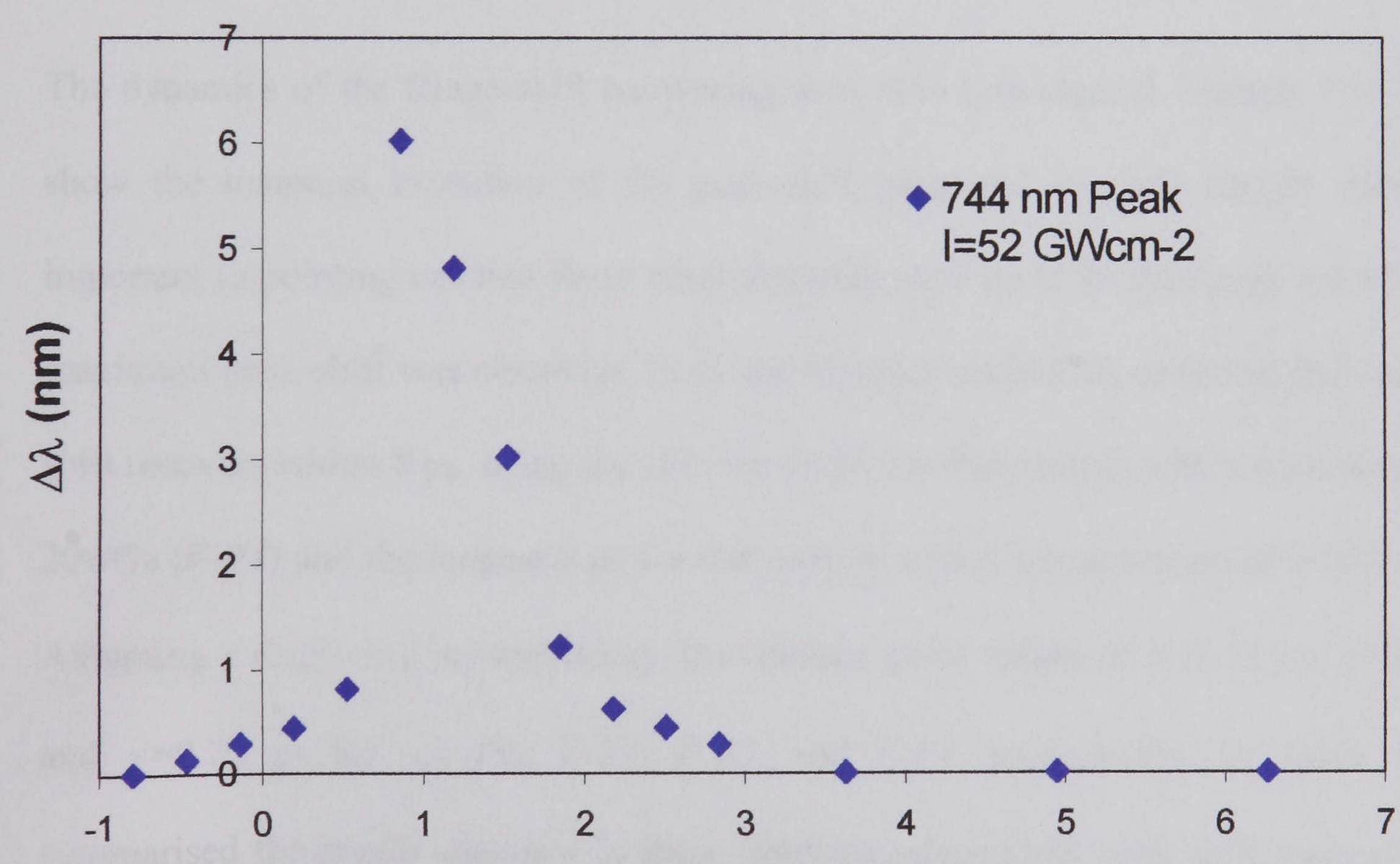

Figure 7.13: (a) Irradiance-dependent fringe-shift and (b) recovering time of the 744 nm peak-shift in the *F-P4* with poly-DCHD (20wt%) after excitation.

We observed that pumping the samples (*F-P* devices) with pulses of irradiances higher than 52 $GWcm^{-2}$, the poly-DCHD thin film was damaged. Below this irradiance level the samples stayed stable during the measurements, which was checked by simple comparison of the transmission peaks features (*i.e.* peak position, peak intensity, peak shape) before and after excitation.

Figures 7.11-7.13(a) show the peak-shift as a function of the excitation irradiance. Since the peak-shift at lower irradiances is small, it is difficult to determine the lowest irradiance (threshold) at which the peak-shift is produced. We observe that the peak-shift measured in all the samples grows as the pump pulse irradiance is increased. Within the irradiance range 0-52 $GWcm^{-2}$ we did not observe saturation effects in the irradiance-dependent peak-shift measurements.

The dynamics of the fringe-shift recovering were also investigated. Figures 7.11-7.13(b) show the temporal evolution of the peak-shift measured in each sample. Here it is important to pointing out that these measurements were done for that peak for which the maximum peak-shift was observed. In all the samples studied we observed that the peak-shift recovers within 8 ps, being the shortest (4 ps) for that sample with a concentration of 20wt% (*F-P4*) and the longest 8 ps for that sample with a concentration of 9wt% (*F-P3*). Assuming a single exponential decay, the lifetime gives values of τ=1.21 ps, τ=2.24 ps, and τ=0.75 ps for samples *F-P2, F-P3*, and *F-P4*, respectively. In Table 7.5 are summarised the results obtained in these irradiance-dependent peak shift measurements, along with the lifetimes of the peak-shift recovery.

Table 7.5: Maximum refractive index change and recovery time measured in Fabry-Perot devices containing poly-DCHD of different concentrations.

F-P2 751 nm F-P Peak		*F-P3* 744 nm F-P Peak		*F-P4* 744 nm F-P Peak	
Peak Irradiance ($GWcm^{-2}$)	Δn_{max} x 10^{-3}	Peak Irradiance ($GWcm^{-2}$)	Δn_{max} x 10^{-3}	Peak Irradiance ($GWcm^{-2}$)	Δn_{max} x 10^{-3}
4.4	**1.6 ± 0.1**	**0.75**	**1.2 ± 0.1**	**4.47**	**1.2 ± 0.1**
8.8	**2.0 ± 0.1**	**2.48**	**1.2 ± 0.1**	**9.27**	**2.5 ± 0.1**
13.2	**2.0 ± 0.1**	**7.73**	**2.5 ± 0.1**	**15.01**	**3.7 ± 0.1**
17.6	**2.2 ± 0.1**	**11.43**	**2.5 ± 0.1**	**19.58**	**4.92 ± 0.1**
22	**2.8 ± 0.1**	**18.39**	**2.5 ± 0.1**	**23.96**	**6.1 ± 0.1**
26.4	**2.8 ± 0.1**	**23.46**	**3.7 ± 0.1**	**31.01**	**7.2 ± 0.1**
30.8	**3.0 ± 0.1**	**28.83**	**3.7 ± 0.1**	**33.10**	**7.7 ± 0.1**
35.2	**3.6 ± 0.1**	**35.09**	**3.7 ± 0.1**	**39.16**	**8.2 ± 0.1**
39.6	**4.0 ± 0.1**	**39.56**	**6.1 ± 0.1**	**44.33**	**10.2 ± 0.1**
44	**4.2 ± 0.1**	**49.70**	**7.4 ± 0.1**	**------**	**------**
50	**4.9 ± 0.1**	**51**	**12.3 ± 0.1**	**------**	**------**
52	**7.3 ± 0.1**	**52**	**13.5 ± 0.1**	**52**	**12.3 ± 0.1**
Peak-shift recovering Lifetime (ps)	5		8		4

Pump-probe experiments performed at 596, 642 and 709 nm in polydiacetylene 9BCMU thin films [10] have shown that the lifetime of the excitation associated with the nonlinear refractive index n_2 has a value of $\tau \sim 1.6$ ps within this spectral range. Studies have been conducted in poly-DCH thin single crystals [21]. In degenerate four-wave mixing (DFWM) performed within the spectral range 700-730 nm an exciton lifetime of 1.7 ps was observed, along with a slow decay which may be due to excited charge carriers. In polydiacetylene single crystals the conduction band exists just above the exciton band. In poly-DCH the band gap energy between the conduction band and the valence band is

reported to be 2.3 eV (539 nm) by photo-current measurement [22]. Therefore, the long lifetime observed in poly-DCH may have come from a grating formed by trapped charge carriers, from which induced absorption would not be seen.

7.6 Optical switching criteria in Fabry-Perot Devices

There are a number of criteria to be met before a material is suitable for all-optical switching applications, depending on the specific application in mind. There are two types of all-optical switching geometries, the nonlinear Fabry-Perot cavity [23] and the nonlinear directional coupler [24]. Here only the first type is treated and its figures of merit W and T will be determined.

In order to compare the switching energy ε_s (defined later) of our device based on a Fabry-Perot etalon containing poly-DCHD microcrystals with that offered by other materials it is of interest to calculate the refractive cross section σ_n (change in refractive index per generated excitation per unit volume) and given by [25]

$$\sigma_n = (\pi w_0^2 th\nu)\frac{|\Delta n_{\max}|}{E_{abs}} \tag{7.16}$$

where Δn_{max} is the maximum possible induced index change (already defined above in section 7.5), $(\pi w_0^2 t)$ is the volume of poly-DCHD inside the *F-P* etalon that is excited by the pump pulse, $(h\nu)$ is the photon energy of the pump pulse, and E_{abs} is the energy absorbed by the material (poly-DCHD).

In the time-resolved experiments conducted in our Fabry-Perot etalons and described above we measured the maximum refractive index change. By using equation 7.16 we are able to calculate the refractive cross section at all the Fabry-Perot peaks.

Figures of merit W and T defined in section 5.4 (Chapter 5) are also evaluated. Values of the nonlinear absorption coefficient β and the nonlinear refractive index n_2 measured in poly-DCHD microcrystals (reported in Chapter 6) are used to evaluate the figure of merit T.

Table 7.6: Refractive cross section and figures of merit for Fabry-Perot etalons containing poly-DCHD microcrystals.

Sample	**Peak Position** (nm)	Δn_{max} x 10^{-3}	σ_n x 10^{-22} cm^3	E_{abs} (nJ)	β* ($cmGW^{-1}$)	n_2* x 10-5 cm^2GW^{-1}	**W**	**T**
F-P1	**680**	**-7.38**	**0.83**	**850**	**-80.0 ± 10%**	**-17 ± 10%**	**4.1**	**5**
	722	**-6.32**	**0.71**					
	770	**-5.13**	**0.58**					
	822	**-1.85**	**0.21**					
F-P2	**715**	**-6.80**	**0.76**	**850**	**1.6 ± 10%**	**-1.4 ± 10%**	**8.1**	**0.67**
	751	**-7.29**	**0.82**					
	791	**-5.96**	**0.67**					
F-P3	**716**	**-8.70**	**0.81**	**942**	**1.3 ± 10%**	**-2.6 ± 10%**	**4.0**	**0.35**
	744	**-13.48**	**1.25**					
	777	**-7.82**	**0.72**					
	815	**-7.65**	**0.71**					
F-P4	**716**	**-9.55**	**0.64**	**1436**	**1.3 ± 10%**	**-2.6 ± 10%**	**3.2**	**0.40**
	744	**-12.30**	**0.82**					
	777	**-5.89**	**0.40**					
	815	**-3.73**	**0.25**					

* Values of β and n_2 were measured by Z-scan and reported in Chapter 6. These values correspond to the 751and 744 nm F-P peaks, where the maximum peak-shift occurs.

Table 7.6 contains the values of the figures of merit W and T for all the cavities studied here, as well as the corresponding refractive cross section σ_n calculated using equation 7.16.

The key point in the all-optical switching field is not only to achieve the desirable figures of merit values, but also the energy necessarily to produce such optical switching. The desired properties of an optical switch for serial processing applications are that it is fast, with a switching time of order of 1 ps, and that it does not require much energy to switch, about 1 pJ. For parallel optical processing the switching time is less of an issue, although the switching energy is still important.

The switching speed depends on both the switching device geometry, particularly the proximity to switching threshold at which the device is held, and on the material relaxation time τ, or optical pulse duration τ_p, whichever is the longer. The switching energy is also dependent on device geometry, and a relationship has been derived for the minimum achievable switching energy ε_s for a nonlinear Fabry-Perot cavity [26];

$$\varepsilon_s \sim \frac{hc\lambda^2}{\sigma_n} \tag{7.17}$$

Where h is the Planck's constant (h = 6.626 x 10^{-34} Jsec), c is the speed of light and λ is the wavelength of the pump pulse. By introducing the values of σ_n reported in table 7.6 we obtain the switching energies for all the Fabry-Perot peaks. The minimum switching energy is achieved at that peak in which the maximum peak-shift was observed. Switching energies with values around 1 pJ were obtained in our *F-P* etalons. A switching energy of 0.9 pJ was achieved in the *F-P3* etalon. These values are of the same order of

those calculated in other materials. A minimum switching energy of 3 pJ was achieved in a Fabry-Perot device based on an MBE-grown ZnSe thin film [27]. As far as I know, the lowest switching energy has been obtained in C_{10}, with a value of 0.015 pJ at 595 nm [28]. Values of 8.8 (at 690 nm) and 0.1 pJ (at 640 nm), have been obtained in pTS and poly-9BCMU, respectively [29]. This means that our Fabry-Perot devices are suitable for all-optical switching. Table 7.7 contains the switching energy values for all our devices.

Table 7.7: Switching energy for all-optical switching in Fabry-Perot devices containing poly-DCHD microcrystals.

Sample	Peak Position (nm)	Switching energy $\mathcal{E}_s$ (pJ)
F-P1	**680**	**1.1**
	722	**1.4**
	770	**2.0**
	822	**6.4**
F-P2	**715**	**1.3**
	751	**1.3**
	791	**1.8**
F-P3	**716**	**1.2**
	744	**0.9**
	777	**1.6**
	815	**1.8**
F-P4	**716**	**1.6**
	744	**1.3**
	777	**3.0**
	815	**5.3**

Conclusions

Fringe-shift has been demonstrated in Fabry-Perot etalons containing poly-DCHD microcrystals. Symmetric Fabry-Perot devices were fabricated with concentrated poly-DCHD microcrystals and mirrors whose reflections were 95% and 99% from 700 to 800 nm. Using a subpicosecond pulse laser, the transmission property of the Fabry-Perot devices was measured by pump-continuum probe geometry. These time-resolved experiments have allowed us to obtain the spectral behaviour of the Fabry-Perot transmission for etalons built with different characteristics. A theoretical model for the linear Fabry-Perot transmission was developed and used to fit the experimental data. From this fit we can see that the model gives a good description in all the etalons and it was possible to obtain the polymer thickness as well as the order *m* of the fringes. Clear blue-shifts were observed in all the samples and the corresponding refractive index changes were estimated. A significant increment in the value of the maximum refractive index change Δn_{max} has been observed when the concentration of poly-DCHD microcrystals is increased from 3wt% (*F-P2*) where $\Delta n_{max} = -7.28 \times 10^{-3}$ to 9wt% (*F-P3*) where $\Delta n_{max} = -13.48 \times 10^{-3}$. However, no significant change was observed when the concentration was increased to 20wt% (*F-P4*) where $\Delta n_{max} = -12.3 \times 10^{-3}$. In all the samples a very fast recovery time of the fringe-shift, related to the refractive index change induced in the poly-DCHD, was observed. Figures of merit *W* and *T* for all the samples were met, indicating that those devices are suitable for all-optical switching applications. The corresponding switching energy has also been estimated in all the devices, the values obtained were around 1.0 pJ, which is enough to produce optical switching.

References

[1] M Thakur and D M Krol, *Appl. Phys. Lett*. **56**, 1213, 1990.

[2] G Stegeman and W Torruelas, *Nonlinear Materials for Information processing and Communications*, *Philos. Trans. R. Soc. Lond. Phys. Sci. Eng*., 354: 745-756, 1996.

[3] J F Heffernan, M H Moloney, J Hegarty and J S Roberts, *Electron. Lett.* **27**, 659, 1991.

[4] P W Smith, *Bell Syst. Tech. J.* **61** (8) 1975, 1982.

[5] J Bolger, T Harvey, W Ji, A Kar, S Molyneux, B Wherrett, and D Bloor, *J. Opt. Soc. Am*. **B9**, 1552, 1992.

[6] E Wright, B Lawrence, W Torruelas, and G Stegeman, *Opt. Lett*., **20**, 2481, 1995.

[7] D Bloor, D Ando, J Ohbi, S Mann, and M Worboys, *Makromol. Chem*., **7**, 665, 1986.

[8] S Hambir, G Blanchard, G Baker, *J. Chem. Phys*., **102**, 2295, 1995.

[9] R Crook, J Sambles, R Rangel-Rojo, G Spruce, and B Wherrett, *J. Phys D: Appl. Phys*., **28**, 269, 1995.

[10] S Molyneux, A Kar, B S Wherrett, T Axon, and D Bloor, *Opt. Lett*., **18**, 2093, 1993.

[11] D Cotter, J Lucek, and D Marcenac, *IEEE Commun. Mag*., 90, 1997.

[12] R Quintero-Torres and M Thakur, *Appl. Phys. Lett*., **66**, 1310, 1995.

[13] R Rangel-Rojo, S Yamada, H Matsuda, H Kasai, H Nakanishi, A K Kar and B S Wherrett, *J. Opt. Soc. Am. B*, 15, 2937 (1998).

[14] M Bakarezos, M A Camacho, A K Kar, B S Wherrett, H Matsuda, T Fukuda, S Yamada, R R Rangel-Rojo, H Katagi, H Kasai, S Okada, and H Nakanashi., *Electron. Lett.*, **35**, pp. 1078 (1999).

[15] W S Gornall, *Laser & Applications*, 47, 1983.

[16] Q B He, P Yeh and C Gu, *Optics Letters*, **17**, 664, 1992.

[17] See, for example, Yariv, *Optical Electronics*, Wiley, 1985.

[18] H Matsuda, T Fukuda, S Yamada. R Rangel Rojo, H Kasai, S Okada, H Nakanishi, E Bakarezos, M A Camacho, A K Kar, B S Wherrett, *Nonlinear Optics*, **22**, 311, 1999.

[19] Charles A. Eldering, Andre Knoesen and Stephen T. Kowel, *J. Appl. Phys.* **69**, 3676, 1991.

[20] Yariv, *Optical Electronics*, Wiley, 1985.

[21] S.Molyneux, H. Matsuda, A.K. Kar, B.S. Wherret, S. Okada, and H. Nakanishi, *Nonlinear Opt.*, **4**, 299, 1993.

[22] K Lochner, H Bassler, B Tieke, and G Wegner, *Phys. Stat. Sol. B*, **88**, 653, 1978.

[23] B S Wherrett and D C Hutchings. In R W Eason and A Miller, editors, *Nonlinear Optics in Signal Processing*, Page 145. Chapman & Hall, London, 1993.

[24] I Bennion and M J Goodwin. In R W Eason and A Miller, editors, *Nonlinear Optics in Signal Processing*, Page 145. Chapman & Hall, London, 1993.

[25] See, for example A E Siegman, *Lasers* , 1986.

[26] A A Said, M Sheik-Bahae, D Hagan, T Wei, J Wang, J Young, and E Van Stryland, *J. Opt. Soc. Am. B* **1992**, 405, 1992.

[27] J Bolger, I Galbraith, A Kar, J Simpson, S Wang, K Prior, B Cavenett and B Wherrett, *Appl. Phys. Lett.*, **63**, 709, 1993.

[28] F Meyers, S Marder, B Pierce, and J Bredas, *J. Am. Chem. Soc*. **116**, 703, 1994.

[29] A Kar, *Polym. Adv. Technol.*, **11**, 553, 2000.

Chapter 8

Conclusions

8.1 Introduction

The results of research into third-order nonlinear optical properties of several metal-complexated polydiacetylenes (PDA's) and optical switching in Fabry-Perot devices containing poly-DCHD microcrystals have been reported. All the experiments were carried out using a subpicosecond tuneable laser system and the z-scan and pump-continuum probe techniques.

In Chapter 5, the near-resonant third-order nonlinear optical response of Cu-, Ni, Ru, and Mo-complexed PDA's was studied by the Z-scan technique with picosecond pulses at 532 nm. This allowed us to obtain the third-order nonlinear optical coefficients, such as the two-photon absorption coefficient β and the nonlinear refractive index n_2 of all the samples. Figures of merit W and T, which determine the material suitability in all-optical switching applications, were also evaluated.

In Chapter 6 the on- and near-resonant third-order nonlinear optical response of poly-DCHD microcrystals in suspension was studied by the Z-scan technique. With tuneable picosecond pulses the absorptive and refractive contributions to the excitonic-dominated nonlinearity were fully resolved at several wavelengths within the spectral range 510-800 nm. A three-level model for the nonlinear response was presented, showing good agreement with the experimental data. The imaginary component (related to the nonlinear

absorption) of the third-order nonlinear susceptibility $\chi^{(3)}$ was found to change sign in the exciton absorption tail. Figures of merit, W and T, were also evaluated.

In Chapter 7, ultra-fast nonlinear refraction in integrated Fabry-Perot devices containing poly-DCHD was studied. These devices contained concentrations of 3, 9 and 20wt% of poly-DCHD. The pump-continuum probe technique was used to study the Fabry-Perot peak-shifts induced by a pump pulse at 640 nm with a duration of 800 fs. A spectral-broadband (ranging from 650 to 900 nm) produced by pumping a water cell was used as the probe beam. Time-resolved experiments were performed to measure the peak-shifts relaxation time.

Section 8.2 contains a summary of the results reported in this thesis for all the samples studied. In section 8.3 an evaluation of the nonlinear switching performance of the Fabry-Perot devices reported in Chapter 7 is presented. Here the switching parameters of the metal-complexed PDA's are also presented if they are used in a Fabry-Perot geometry. Finally, section 8.4 contains some suggestions for further work.

8.2 Summary of results

8.2.1 Chapter 5

We have studied the third-order nonlinear optical coefficients of a set of metal-complexed PDA's using picosecond pulses at 532 nm (near-resonance) and the z-scan technique. At this wavelength all the samples showed very low linear absorption. These polydiacetylenes have been shown to have a large nonlinearity, with values for the third-order nonlinear susceptibility $\chi^{(3)}$ of the order of 10^{-11} esu, in most samples. The values obtained in our samples are of the same order as those values reported for related polydiacetylenes in solution for the same wavelength used here (λ = 532 nm) [1], [2]. The work by Nunzi *et. al.* reports $\chi^{(3)} = 10^{-11}$ esu for solutions of poly-4BCMU [1], which is a

urethane substituted polydiacetylene. Poly-4BCMU has a similar absorption peak at λ_{max} = 469 nm.

The nonlinear absorption β and nonlinear refractive index n_2 coefficients measured in the Cu- and Ni-complexated samples were of the same order as that measured in the metal free (uncomplexed PDA) sample. Cu- and Ni-complexed samples with a metal:nitrogen [M:N] ratio of [1:1] showed values of β and n_2 slightly higher than similar samples with a [1:2] ratio. The ruthenium-complex sample showed saturation absorption ($\beta < 0$) and the molybdenum-complex sample showed a positive nonlinear refractivity ($n_2 > 0$). In Table 8.1 all these values are summarized.

The combination of a large nonlinear refractive index and very low absorption coefficient, such as those observed in the metal-complexated samples studied here, make them suitable candidates to be employed into the all-optical switching field. Their figures of merit T and W have been evaluated and their corresponding values are summarized in Table 8.2. In all the samples (except that ruthenium complex) the figure of merit W was found to be $W > 1$ which meets the switching requirements in a Fabry-Perot geometry. Figures of merit within a value range of 0.9 - 1.5 for T and 0.08 - 6.4 for W were estimated. This meets the switching requirements in a Fabry-Perot geometry in which $W > \sqrt{3}/2\pi$ (~0.3) and $T < 2\pi/\sqrt{3}$ (~3.5).

8.2.2 Chapter 6

The nonlinear coefficients β and n_2 at several wavelengths for poly-DCHD microcrystals (average size of 100 nm) in aqueous solution have been measured by using the z-scan technique. Their signs have also been obtained. The imaginary component (related to the nonlinear absorption) of the third-order nonlinear susceptibility $\chi^{(3)}$ was found to change

sign across the exciton peak ($\lambda \sim 645$ nm). The nonlinear refractivity was found to be three times larger in the 100 nm crystals than that reported for crystals 30 nm [3], one possible explanation is that smaller microcrystal sizes imply a higher degree of topological disorder of the polymer backbone, which would reduce the exciton delocalisation and hence the exciton oscillator strength.

It also was found that dominant nonlinearity arises from the excitonic absorption peak. A strong nonlinear absorption was measured around the exciton peak; such absorption could limit its application in the all-optical switching field. At $\lambda = 610$ and 630 nm the nonlinear absorption was found to be negative ($\beta < 1$), which is due to a saturable absorption. However at $\lambda = 760$ nm induced absorption was observed which, means that a crossing point (Im $\chi^{(3)} = 0$) should appear between 630 and 760 nm. The fits to the experimental data using the simple three-level model presented in Chapter 6 showing that the position of this crossing point occurs at 710 nm in poly-DCHD. The existence of this crossing point has also been observed in poly-9BCMU thin films [4] and poly-DCH [5] by S. Molyneux *et. al*. In Table 8.1 the values of β and n_2 are summarized.

Figures of merit W and T were estimated through the spectral range studied, near the crossover point (at 680 nm), W (>1) met the required value for Fabry-Perot and nonlinear directional-coupler geometries. Since the absorptive nonlinearity at this wavelength (680 nm) was dominated by a bleaching effect, the correspondent figure of merit T becomes irrelevant, and hence it does not represent a limiting factor for its application in all-optical switching. This constitutes an interesting regime for potential optical processing applications. The values of the figures of merit W and T of poly-DCHD are contained in Table 8.2.

Table 8.1: Summary of results of the third-order nonlinear coefficients in different materials.

Material	λ (nm)	α_0 (cm^{-1})	$\mathbf{n_2}$ ($x\ 10^{-4}\ cm^2GW^{-1}$)	β ($cmGW^{-1}$)
Poly-DCHD	510	16.9	0.4 ± 10%	-15 ± 10%
	532	21.5	1.5 ± 10%	-51 ± 10%
	550	25.9	2.6 ± 10%	-68 ± 10%
	570	31.9	1.9 ± 10%	-140 ± 10%
	590	35.5	0.3 ± 10%	-187 ± 10%
	600	37.3	-2.0 ± 10%	-337 ± 10%
	610	30.1	-8.4 ± 10%	-227 ± 10%
	620	26.9	------	-19 ± 10%
	630	34.4	8.6 ± 10%	-213 ± 10%
	635	39.7	12.6 ± 10%	-334 ± 10%
	640	45.6	------	-592 ± 10%
	650	52.2	------	-1076 ± 10%
	655	47.9	------	-1195 ± 10%
	660	38.4	------	-1034 ± 10%
	670	15.2	-29 ± 10%	-447 ± 10%
	680	4.38	-17 ± 10%	-80.0 ± 10%
	740	0.45	-0.2 ± 10%	1.3 ± 10%
	760	0.31	-0.2 ± 10%	1.6 ± 10%
	800	0.19	-0.1 ± 10%	1.2 ± 10%
No complex	514	2	1.7 ± 10%	-6.2 ± 10%
**Cu-complex*		2.3	1.8 ± 10%	-6.3 ± 10%
***Cu-complex*		0.8	1.2 ± 10%	-5.3 ± 10%
**Ni-complex*		1.8	1.6 ± 10%	-8.0 ± 10%
***Ni-complex*		0.7	1.1 ± 10%	-5.0 ± 10%
Ru-complex		25.8	-6.5 ± 10%	-5.9 ± 10%
Mo-complex		1.1	0.5 ± 10%	2.8 ± 10%
Poly-9BCMU thin films [4] [6]	596	--	5000 ± 10%	--
	642	--	1900 ± 10%	--
	709	--	320 ± 10%	--
	1064	--	-2.6 ± 10%	30 ± 10%
Poly-4BCMU [1]	1064	--	-1.5	10 ± 10%
AlGaAs [7]	1545	--	~1	--

*M:N=1:1 and ** M:N=1:2

Table 8.2: Figures of merit (FOM) T and W for various materials.

Material	λ (nm)	$\lvert \mathbf{W} \rvert$ $\left(W > \sqrt{3}/2\pi\right)$	$\lvert \mathbf{T} \rvert$ $\left(T < 2\pi/\sqrt{3}\right)$
Poly-DCHD	510	18.81	20.73
	532	35.46	18.36
	550	59.50	14.57
	570	33.71	42.20
	590	4.13	425.12
	600	20.64	101.21
	610	75.47	16.40
	620	------	------
	630	102.84	15.64
	635	115.80	16.85
	640	------	------
	650	------	------
	655	------	------
	660	------	------
	670	10.23	30.59
	680	2.72	9.88
	740	------	17.09
	760	------	14.82
	800	------	20.69
No complex	514	3	1.5
**Cu-complex*		2.6	1.5
***Cu-complex*		6.4	1.2
**Ni-complex*		3.8	1.1
***Ni-complex*		6.2	1.2
Ru-complex		0.08	---
Mo-complex		2.4	0.9
Poly-9BCMU thin films [4] [6]	596	--	--
	642	36	0.14
	709	--	0.43
	1064	160	13
PTS [8]	690	0.64	--
C_{10} [8]	595	17	--

8.2.3 Chapter 7

Ultrafast nonlinear refraction in Fabry-Perot devices containing poly-DCHD microcrystals has been demonstrated. Fabry-Perot etalons containing poly-DCHD microcrystals with concentrations of 3, 9 and 20wt% have been fabricated and linearly and nonlinearly characterised in a pump-continuum probe experimental arrangement. Their linear spectral transmission showed various well-defined Fabry-Perot peaks (fringes) within the high-reflectivity range (700-800 nm) of the component mirrors.

A theoretical model for the linear Fabry-Perot transmission was developed and used to fit the experimental data. From this fit we can see that this model gives a good description of the linear transmission in all the etalons, and it was possible to obtain the polymer thickness as well as the order *m* of the fringes. The estimated thickness of these samples was 3.7 μm for the 3wt%, and 6.5 μm for those with 9 and 20wt%.

Using a subpicosecond pulse laser system, time-resolved experiments on-resonance (λ = 640 nm) were conducted in these devices to obtain their spectral nonlinear transmission characteristics. As clear blue-shift and induced absorption were observed in all the samples, the corresponding refractive index change was estimated. This blue-shift means that the nonlinear refractive index n_2 is negative. A polymer concentration-dependent refractive index change was observed. The maximum refractive index change (Δn_{max}) was observed in that sample in which the concentration was 9wt%, its value was Δn_{max} = -13.6 x 10^{-3} at the irradiance I = 52 GWcm^{-2}, and corresponding to a maximum fringe-shift of $\Delta\lambda_{max}$= -6.6 nm. Table 8.3 contains a summary with all these results, corresponding to the maximum fringe-shift achieved.

Table 8.3: Results in Fabry-Perot etalons containing poly-DCHD of different concentrations. Maximum refractive index change and recovery time.

Poly-DCHD (Concentration)	λ_{pump} (nm)	λ_{probe} (nm)	$\Delta\lambda_{max}$ (nm)	Δn_{max}	$\Delta\sigma_n$ x 10^{-22} cm^3	Recovery time τ
3 wt%	640	751	-3.6	-0.0073	0.82	~5 ps
9 wt%		744	-6.6	-0.0136	1.25	~8 ps
20 wt%		744	-6.02	-0.0124	0.82	~4 ps

The irradiance-dependent refractive index change was also investigated, and showed a near linear behaviour, and it was seen that the poly-DCHD thin film is damaged when the irradiance reached around 55 $GWcm^{-2}$. The time-resolved experiments showed that the fringe-shift recovers very fast. The fastest recovery time was observed in the 20wt% sample and the slowest was observed in that with 9wt%. Their corresponding values were estimated to be 4 and 8 ps, respectively.

In order to estimate the switching energy ε_s of our devices based on a Fabry-Perot etalon containing poly-DCHD microcrystals and compare its performance with that offered by others materials, the refractive cross section σ_n (change in refractive index per generated excitation per unit volume) was calculated from the maximum refractive index change Δn_{max} achieved in all the etalons. A value of 1.25 x 10^{-22} cm^{-3} was obtained at the 744 nm peak in the sample with 9wt%.

8.3 Switching performance

All-optical switching has been demonstrated [7] [9] [10] and individual materials appear useful for specific applications, but the operating conditions and applications are limited. Ultrafast all-optical switching in an AlGaAs nonlinear–directional coupler structure was demonstrated [7] operating at 1.545 μm, with n_2 values of the order of 10^{-13} cm^2W^{-1}. These n_2 values are one order of magnitude larger than those ($\sim10^{-14}$ cm^2W^{-1}) obtained in our metal-complexated PDAs studied in Chapter 5, and of the same order of those ($\sim10^{-13}$ cm^2W^{-1}) measured in poly-DCHD microcrystals studied in Chapter 6. It has been known for some time that certain requirements of all-optical processing, e.g. fast response times, low scattering loss, stability and processability, could be met by the PDA materials and since the initial reports of the large third-order nonlinearity in polydiacetylene pTS, considerable efforts have been made in order to establish a combination of parameters suitable for useful devices. For PDA's, the limiting factors have included high linear absorption on resonance and large two-photon absorption off resonance. Excited-state absorption can also restrict the device potential.

Finally, it is the first time that "ultrafast optical switching" has been demonstrated in Fabry-Perot devices containing poly-DCHD microcrystals. All the devices studied here have shown a good performance. Figures of merit W and T meet the required values for this geometry. The corresponding switching energy has also been estimated in all the devices. The values obtained were around 1.5 pJ, which is enough to produce optical switching. This energy is just one order of magnitude larger than that needed in poly-9BCMU at 642 nm [4]. Table 8.4 contains the switching energy values obtained in our devices along with the values obtained in other materials. All this confirms that the PDA materials can be successfully engineered into suitable device formats and switching can be achieved.

Table 8.4: Switching energy for all-optical switching in Fabry-Perot devices containing poly-DCHD microcrystals and for other materials.

Material	Switching Energy ε_s (pJ)
Poly-DCHD 3 wt%	0.16
Poly-DCHD 9 wt%	1.95
Poly-DCHD 20 wt%	1.40
C_{10}*	0.015
DEMI*	330
PIP*	180
ULTRA*	68
Poly-9BCMU*	0.1
PTS*	8.8
* Taken from [8]	

8.4 Future work

Ultrafast all-optical switches are crucial components for future high-bit-rate time division-multiplexing, optical communication systems or free-space optical–digital computing systems. So far, many types of ultrafast all-optical switches have been studied and demonstrated using optical nonlinearities in optical fibres and semiconductor materials [11]–[16]. Due to the limits imposed by the properties of materials used for all-optical switches, to our knowledge, it is very hard to achieve subpicosecond all-optical switches at the optical communication wavelength of 1.55 μm [13] [14].

PDAs, such as those studied and reported in this thesis, are expected to exhibit large off-resonant values of $\chi^{(3)}$ in the telecommunication windows. Poly-DCHD exhibits high

solubility in common organic solvents that make possible fabrication of high quality optical waveguides. It would be interesting to explore the nonlinear optical properties of poly-DCHD in the optical communications wavelength range 1.3-1.5 μm. For this purpose, the characterization can be started with the well-established z-scan technique at 1.5 μm. A characterization around this wavelength is mandatory with a view to applications for the operating devices. This also will permit useful comparisons with other materials.

References

[1] J M Nunzi, J L Ferrier and R Chevalier, *Picosecond phase conjugation in yellow polydiacetylene solution*, in *Nonlinear Optical Effects in Organic Polymers*, ed. J. Messier, F. Kajzar, P.N. Prasad and D. Ulrich, Kluwer Academic Publishers, Netherlands, p. 365 (1989).

[2] W M Dennis, W Blau and D J Bradley, *Op. Eng.* **25**, 538, 1986.

[3] R Rangel-Rojo, S Yamada, H Matsuda, H Kasai, H Nakanishi, A K Kar and B S Wherrett, *J. Opt. Soc. Am.* B, **15**, 2937, 1998.

[4] S Molyneux, A Kar, B S Wherrett, T Axon, and D Bloor, *Opt. Lett.*, **18**, 2093, 1993.

[5] S Molyneux, H Matsuda, A K Kar, B S Wherret, S Okada, and H Nakanishi, *Nonlinear Opt.*, **4**, 299 (1993).

[6] R Crook, J Sambles, R Rangel-Rojo, G Spruce, and B Wherrett, *J. Phys D: Appl. Phys.*, **28**, 269, 1995.

[7] A Villeneuve, C C Yang, P G Wigley, G I Stegeman, J S Aitchison and C N Ironside, *Appl. Phys. Lett.*, **61**, 147, 1992.

[8] A Kar, *Polym. Adv. Technol.*, **11**, 553, 2000.

[9] V S Williams, Z Z Ho, N Peyghambarian, W M Gibbons, R P Grasso, M K O'Brien, P J Shannon and S T Sun, *Appl. Phys. Lett.*, **57**, 2399, 1990.

[10] D J Westland, V Skarda, W Blau, and L Costa, *Electron. Lett.*, **27**, 1327, 1991.

[11] J. Paye and D. Hulin, *Appl. Phys. Lett.* **62**, 1326, 1993.

[12] S. G. Lee, B. P. McGinnis, R. Jin, J. Yumoto, G. Khitrova, H. M. Gibbs, R. Binder, S. W. Koch, and N. Peyghambarian, *Appl. Phys. Lett.* **64**, 454, 1994.

[13] S. Nakamura, K. Tajima, and Y. Sugimoto, *Appl. Phys. Lett.* **65**, 283, 1994.

[14] Y. Nishikawa, A. Tackeuchi, S. Nakamura, S. Muto, and N. Yokoyama, *Appl. Phys. Lett.* **66**, 839, 1995.

[15] R. Takahashi, Y. Kawamura, and H. Iwamura, *Appl. Phys. Lett.* **68**, 153, 1996.

[16] M. Asobe, *Opt. Fiber Technol.: Mater., Devices Syst.* **3**, 142, 1997.

Appendices

Appendix A. List of Publications

- "Synthesis and nonlinear optical properties of functionalised polydiacetylenes and their complexes with transition metals" **M.A. Camacho**, Ajoy K. Kar, W. Edward Lindesell, Christopher Murray, Peter N. Preston and Brian S. Wherrett., J. Mater. Chem., **9**, pp.1251-1256, 1999.
- "Ultrafast nonlinear refraction in integrated Fabry-Perot etalon containing polydiacetylene" M. Bakarezos, **M.A. Camacho**, Ajoy K. Kar, Brian S. Wherrett, H. Matsuda, T. Fukuda, S. Yamada, R.R. Rangel-Rojo, H. Katagi, H. Kasai, S. Okada, and H. Nakanashi., Electron. Lett., **35**, pp. 1078-1079, 1999.
- *"Ultrafast optical switching in polydiacetylene Fabry-Perot devices"* H. Matsuda, T. Fukuda, S. Yamada. R. Rangel Rojo, H. Kasai, S. Okada, H. Nakanishi, E. Bakarezos, **M.A. Camacho**, A.K. Kar, B.S. Wherrett, *Nonlinear Optics*, **22**, pp. 311-314, 1999.

Appendix B. Attended Conferences

- **CONFERENCE ON LASERS AND ELECTRO-OPTICS (CLEO'99)**, *"Ultrafast nonlinear refraction in an integrated Fabry-Perot etalon containing polydiacetylene"* M. Bakarezos, **M.A. Camacho**, I.J. Blewett, A.K. Kar, B.S. Wherrett, H. Matsuda, T. Fukuda, S. Yamada, R.R. Rangel-Rojo, H. Katagi, H. Kasai, S. Okada, and H. Nakanashi, Baltimore, Maryland, USA, May 1999.
- **NATIONAL QUANTUM ELECTRONICS CONFERENCE (QE-14)**, *"Fabry-Perot fringe-shift in an etalon containing polydiacetylene"* **M.A. Camacho**, M.

Bakarezos, I.J. Blewett, A.K. Kar, B.S. Wherrett, H. Matsuda, T. Fukuda, S. Yamada, R.R. Rangel-Rojo, H. Katagi, H. Kasai, S. Okada, and H. Nakanashi, Manchester, Inglaterra, *UK*, September, 1999.

- **CONFERENCE FOR POSTGRADUTE RESEARCH IN ELECTRONICS AND PHOTONICS (*PREP-2000*)**, Notthingham, Inglaterra, *UK*, April 2000.

- **FIRST INTERNATIONAL WILHELM AND ELSE HERAEUS SUMMER SCHOOL**, *"Mesoscopics between Photonic and Electronic Systems"*, Wittenberg, Germany, July 2000.